



HAL
open science

Development of high-power laser diodes emitting at 975nm with enhanced wall-plug efficiency and wavelength stabilization for optical pumping of doped fibers and realization of fiber lasers

Roberto Mostallino

► **To cite this version:**

Roberto Mostallino. Development of high-power laser diodes emitting at 975nm with enhanced wall-plug efficiency and wavelength stabilization for optical pumping of doped fibers and realization of fiber lasers. Other. Université de Bordeaux, 2018. English. NNT : 2018BORD0132 . tel-02102847

HAL Id: tel-02102847

<https://theses.hal.science/tel-02102847>

Submitted on 17 Apr 2019

HAL is a multi-disciplinary open access archive for the deposit and dissemination of scientific research documents, whether they are published or not. The documents may come from teaching and research institutions in France or abroad, or from public or private research centers.

L'archive ouverte pluridisciplinaire **HAL**, est destinée au dépôt et à la diffusion de documents scientifiques de niveau recherche, publiés ou non, émanant des établissements d'enseignement et de recherche français ou étrangers, des laboratoires publics ou privés.

THÈSE PRÉSENTÉE
POUR OBTENIR LE GRADE DE
DOCTEUR DE
L'UNIVERSITÉ DE BORDEAUX

ÉCOLE DOCTORALE DES SCIENCES PHYSIQUES ET DE L'INGENIEUR
SPÉCIALITÉ LASERS, MATIERE ET NANOSCIENCES

Par Roberto MOSTALLINO

Développement de diodes laser émettant à 975nm de très forte puissance, rendement à la prise élevé et stabilisées en longueur d'onde pour pompage de fibres dopées et réalisation de lasers à fibre.

Development of high-power laser diodes emitting at 975nm with enhanced wall-plug efficiency and wavelength stabilization for optical pumping of doped fibers and realization of fiber lasers.

Sous la direction de : Laurent BECHOU, Professeur
(co-directeur : Yannick DESHAYES, Maître de Conférences HDR)

Soutenue le 05 septembre 2018

Membres du jury :

Mme AUPETIT-BERTHELEMOT Christelle
M. LANDESMAN Jean-Pierre
M. JIMENEZ Juan
M. KRAKOWSKI Michel
M. GARCIA Michel
M. TOMM Jens W.
M. LE FLOHIC Marc
M. GILARD Olivier

Professeure, Université de Limoges
Professeur, Université de Rennes
Professeur, Université de Valladolid
Ingénieur, GIE III-V lab, Palaiseau
Docteur, GIE III-V lab, Palaiseau
Senior Researcher, Max Born Institute
Docteur, Président de LUMIBIRD, Lannion
Docteur-Ingénieur, CNES, Toulouse

Présidente
Rapporteur
Rapporteur
Examineur
Examineur
Examineur
Invité
Invité

Titre : Développement de diodes laser émettant à 975nm de très forte puissance, rendement à la prise élevé et stabilisées en longueur d'onde pour pompage de fibres dopées et réalisation de lasers à fibre.

Résumé :

Cette thèse CIFRE adresse le développement de diodes laser, émettant à 975nm, de très forte puissance, rendement à la prise élevé, et stabilisées en longueur d'onde pour pompage de fibres dopées Er/Yb et réalisation de lasers à fibre. La thèse a été développée dans le cadre d'un partenariat étroit entre le Laboratoire IMS, le GIE III-V Lab, principal fondeur français de composants à semiconducteurs III-V pour des applications électroniques et photoniques, et THALES Research & Technology à Palaiseau en région parisienne. Un travail en profondeur de caractérisation et d'analyse a porté sur les aspects thermiques qui contribuent, en particulier, à limiter les niveaux de puissance optique de sortie. Dans ce cadre, nous avons réalisé un ensemble de caractérisations complémentaires au GIE III-V lab et à l'IMS nous permettant d'envisager des solutions correctives d'optimisation technologique portant en particulier sur la profondeur de gravure définissant la largeur de la zone d'émission et la nature du substrat dissipateur. Ces solutions ont été proposées à partir de modélisations physiques mises en œuvre avec un simulateur dédié, propriété de III-V Lab et de simulations par éléments finis thermiques et thermomécaniques (approche multiphysique) de la structure microassemblée définitive. Ces travaux se sont prolongés par la fabrication et la caractérisation électro-optique et thermique de plusieurs structures verticales : LOC (Large Optical Cavity), SLOC (Super Large Optical Cavity) et AOC (Asymetrical Optical Cavity). Les diodes laser de type LOC et SLOC sont stabilisées en longueur d'onde en intégrant un réseau de Bragg (DFB). Une puissance optique de 8W avec une efficacité de 60% a été obtenue ; ce qui permet de situer ces travaux à l'état de l'art international notamment vis-à-vis de ceux publiés par l'Institut Ferdinand-Braun. L'originalité des travaux menés dans cette thèse nous a permis d'avoir accès à une bourse du Cluster européen « Laserlab » (The Integrated Initiative of European Laser Research Infrastructures), pour conduire des campagnes d'expérimentation à l'Institut Max Born à Berlin dans le groupe du Dr J.W. Tomm. Les travaux ont porté sur la caractérisation thermique de ces diodes laser de forte puissance émettant à 975nm, à double hétérostructure symétrique et asymétrique (SLOC et AOC), en utilisant des techniques complémentaires (micro-photoluminescence, photoluminescence résolue en temps, spectroscopie de photocourant et mesures L-I pulsées) et permettant d'évaluer le type de contraintes résiduelles apportées par les étapes de report de la diode Laser ainsi que la cinétique de dégradation catastrophique de type COD.

Mots clés :

Optoélectronique, diode laser, caractérisation électro-optique, DFB, 975nm, simulation par éléments finis, thermique, thermomécanique, résistance thermique, micro-photoluminescence.

Title : Development of high-power laser diodes emitting at 975nm with enhanced wall-plug efficiency and wavelength stabilization for optical pumping of doped fibers and realization of fiber lasers.

Abstract :

This PhD addresses the development of high-power laser diodes emitting at 975nm with high efficiency and wavelength stabilized using a Bragg grating. This thesis was conducted in the framework of a close partnership between IMS Laboratory, the GIE III-V lab, who is the main French founder of III-V semiconductor devices for electronic and photonic applications, and THALES Research & Technology in Palaiseau. An in-depth characterization and analysis work has addressed thermal aspects that contribute, in particular, to limit the optical output power of a laser diode. In such a context, we have carried out a set of complementary characterizations both at III-V lab and IMS allowing us to provide some corrective solutions for technological optimization concerning the etching depth of the grooves that defines the emitting stripe of the laser diode and the nature of the submount acting as a thermo-compensator. These solutions have been proposed from optical modelling implemented with a dedicated simulator, property of III-V lab, and thermal and thermomechanical (multiphysics approach) finite element simulations of the overall microassembled structure. All this work has resulted in the fabrication as well as electro-optical and thermal characterizations of three vertical structures namely LOC (Large Optical Cavity), SLOC (Super Large Optical Cavity) and AOC (Asymmetrical Optical Cavity). The LOC and SLOC vertical structures have been processed with a Fabry-Perot cavity and also including a Bragg grating (DFB architecture) while the AOC one was only fabricated with a Fabry-Perot cavity. State-of-the-art results are demonstrated since in particular an optical power of 8W with an efficiency of 60% has been obtained that can be compared to those recently published by the Ferdinand-Braun Institute. The originality of the work carried out in this PhD has allowed us to receive a grant from the European Laserlab Cluster (The Integrated Initiative of the European Laser Research Infrastructures), to conduct dedicated experiments at the Max-Born Institute (Berlin) in the group of Dr. J.W. Tamm. The work aimed to characterize mechanical strain of the laser diode induced by the soldering process. Two vertical structures (SLOC and AOC) were investigated using complementary techniques (microphotoluminescence, time-resolved photoluminescence, photocurrent spectroscopy and pulsed L-I measurements), allowing to quantify the level of residual stress provided by the laser diode mounting process as well as the kinetics of the catastrophic degradation process (COD).

Keywords : Optoelectronics, laser diode, electro-optical characterization, DFB, 975nm, finite element simulation, thermal, thermomechanical, thermal resistance, micro-photoluminescence.

Unité de recherche

Laboratoire de l'Intégration du Matériau au Système (IMS), Université de Bordeaux, CNRS
UMR 5218, Bordeaux INP, 351 Cours de la libération, 33405 Talence Cedex, France

REMERCIEMENTS

Ce manuscrit est l'aboutissement de trois années de recherche menées en partenariat entre l'équipe « Evaluation des Dispositifs Micro et Nano-Assemblés » (EDMiNA) du laboratoire de l'Intégration du Matériau au Système (IMS) de l'Université de Bordeaux et le Groupe « Composants Optroniques » du Groupement d'intérêt économique (GIE) III-V lab. Je tiens ici à remercier toutes les personnes qui, par leurs conseils et leur amitié, ont fait de ces années de thèse des moments inoubliables.

Je souhaite tout d'abord remercier le Directeur de l'IMS, Monsieur Yann DEVAL, pour m'avoir accueilli au sein du laboratoire durant le déroulement de mes travaux.

Je tiens à remercier tous les membres du jury de thèse : merci aux rapporteurs, Monsieur Jean-Pierre LANDESMAN et Monsieur Juan JIMENEZ, d'avoir pris de leur temps précieux pour évaluer et analyser avec attention mon manuscrit. Merci aux examinateurs, Madame Christelle AUPETIT-BERTHELEMOT et Monsieur Jens TOMM, et aux membres invités, Monsieur Marc LE FLOHIC et Monsieur Olivier GILARD d'avoir accepté de participer au jury et d'examiner ce travail.

Je remercie particulièrement Monsieur Laurent BECHOU, Professeur des Universités, qui a proposé et encadré ma thèse. Sa rigueur dans ses enseignements, et le caractère très pratique, m'ont, entre autres, conforté dans mon choix de spécialisation en filière optoélectronique. Je lui suis très reconnaissant pour ses enseignements, ses conseils constructifs, fructueux et son encadrement exemplaire sur les différents aspects de ma thèse. Sa disponibilité tout au long de ce cheminement et son honnête intellectuel est d'inspiration.

Je remercie mon co-directeur de thèse Monsieur Yannick DESHAYES.

Je remercie Monsieur Michel KRAKOWSKI, qui m'a encadré tout au long de ces trois années passées à III-V lab.

Je remercie Monsieur Michel GARCIA, responsable de l'équipe Back-end, de la technologie GaAs qui m'a accueilli dans son équipe. Toujours plein d'idées, ses compétences scientifiques, sa bonne humeur, son côté chaleureux et l'allergie à toutes les raisons "historiques" étaient d'inspiration. J'ai énormément appris à ses côtés sur plusieurs aspects ; en particulier de la physique du composant optronique jusqu'à la « plomberie ».

Je tiens également à remercier chaleureusement les personnes suivantes :

Borge VINTER, Ingénieur Conseil à Thales, pour tous les aspects de simulation et physique du diode laser. Malgré les quelques semaines seulement par an passées avec lui, sa patience, ses connaissances et compétences dans le domaine m'ont été extrêmement utiles pendant les trois années de thèse.

Vojtech OLLE (dit « warrior »), arrivé en post-doc au sein de III-V lab. Un « hurricane » toujours hyperactif et également très allergique à toutes les raisons “historiques”, son extrême compétence et son habileté sur les mesures m’ont aidé à implémenter et maîtriser le banc de caractérisation pour les diodes laser.

Alexandre LARRUE, Expert technologue au III-V lab. Alexandre est une personne très rigoureuse, qui m’a toujours poussée à lire les publications les plus récentes et à en discuter. Avec sa rigueur et son « fort » caractère, il appartient à l’équipe des “Bounty hunters”. Tout comme Michel et Vojtech, il est l’allergique aux raisons “historiques”.

Monsieur Jens W. TOMM, chercheur sénior au Max Born Institut de Berlin, m’a accueilli dans son équipe pendant quelques semaines dans le cadre du programme européen LaserLab. J’ai eu l’opportunité de travailler avec lui et apprendre une petite partie de ses compétences scientifiques. D’une honnête intellectuelle inégalable, il m’a fait aussi découvrir une partie de Berlin et notamment la culture culinaire allemande.

Joseph Patient BEBE MANGA LOBE, doctorant en troisième année quand je suis arrivé au III-V lab. Toujours souriant avec son rire contagieux. Tu m’as aidé et appris comment me débrouiller au sein du III-V lab. Ton enthousiasme et ta motivation étaient comme ton rire, contagieux.

Andrzej JANKOWSKI, doctorant que j’ai rencontré à la fin de ma deuxième année de thèse. Toujours souriant et prêt à rigoler, il a réussi à me donner l’habitude de la vitamine C. Plus qu’un collègue, nous sommes devenus des amis.

Nicolas VON BANDEL doctorant avec qui j’ai partagé le bureau pendant toute ma thèse. Très respectueux et prêt à aider. Rigoureux et passionné dans son travail, nous avons réussi à remettre à neuf nos setups LIV, pour mettre à point ce qui se faisait jusqu’alors, de façon « historique ».

Hugues, apprenti ingénieur, nous avons partagé le laboratoire plusieurs fois. C’était très sympa, je testé les lasers et toi tu travaillé sur ton ordi.

Patrick RESNEAU, quel plaisir j’ai eu à échanger avec toi !

Yannick ROBERT et Eric VINET (responsables du clivage et du montage des puces). Sans vous, je n’aurais pas eu la possibilité de tester mes dispositifs.

Je tiens également à te dire merci Maryline BEGUET pour ta réactivité, ta disponibilité et ta bonne humeur. Merci pour ton support fournitures et aux ordres de mission. Tu as toujours tout mis en œuvre, pour nous faciliter la vie, entre nos multiples reçus de mission.

Je remercie également toutes les autres personnes sympathiques et motivées, avec lesquelles j'ai eu plaisir d'échanger : Andrea CASTELLANO, Gaël KERVILLA, Anaëlle MAHO et Louise JUMPERTZ, Clément GILLES, Simon FERRE et Florian LEGOFF, Western Bolanos RODRIGUEZ.

Un merci spécial à Andrea, Elena, Wendy, Silvia, Marco, Manuela et Claudia, avec qui j'ai partagé des très bons moments conviviaux en dehors du travail. Les repas de dimanche, les « bons » endroits sur Paris et tous les échanges que nous avons eus, sont des souvenirs que je vais garder pour toute la vie.

E l'ultimo grazie lo farò nella mia lingua madre. Ci tengo a ringraziare la mia famiglia, i miei due fratelli Francesco e Luca, e i miei genitori Paolo e Maria e tutti i miei zii e zie e cugine. Il loro costante supporto mi è stato d'aiuto in tutti questi anni. Quattro anni fa sono partito per iniziare la mia avventura in Francia e nonostante le difficoltà incontrate, mi hanno sempre spinto a continuare sulla mia strada. I miei genitori sono il mio punto di riferimento, loro mi hanno passato valori come l'onesta intellettuale e il duro lavoro, se sono arrivato qui è soprattutto grazie a loro.

Grazie mamma e grazie papà per tutti i sacrifici che avete fatto per noi, sono fiero di avere due genitori come voi.

CONTENT

I. GENERAL INTRODUCTION	13
References:	17
Chapter I.....	18
High-power laser diodes: physical background and technologies – Motivation of the study	18
I. Introduction	18
1.1 Brief state-of-the-art of infrared high-power laser diode technologies.....	19
1.2 General background on semiconductor heterostructures and optical resonators including Bragg grating.....	24
1.3 Global market overview of gallium-arsenide laser diodes.....	42
1.4 State-of-the-art performances review of high-power laser diodes emitting at 975nm.....	45
1.5 Motivation and objectives of the study	50
Conclusion.....	55
Chapter I References:	57
Chapter II.....	61
Description of the vertical structures and assessment of electro-optical performances	61
II. Introduction	61
2.1 Description and comparison of the III-V lab vertical laser structures	62
2.1.1 Optical simulations: FIMMWAVE® tool capabilities, material properties and main results.....	64
2.1.2 Technological description of the III-V lab vertical structures.....	69
a. Theoretical calculations of the optical losses and series resistance for each vertical structure	73
b. Simulated far field divergence for each vertical structure.....	75
c. Estimation of the DFB coupling factor for the LOC and SLOC structures.....	76
2.1.3 Effects of a Non-Injected-Mirror (NIM) window	79
2.1.4 Comparison of optical performances for the three structures.....	84
2.2 Fabrication process of the vertical structure	85
2.3 Electrical and optical characterizations.....	96
Conclusion.....	110

Chapter II References:.....	113
Chapter III	117
Thermal management issue	117
III. Introduction	117
3.1 Brief overview of heat sources in a high power LD	118
3.1.1 Joule effect - Ohmic heating.....	118
3.1.2 Heating from Auger and Shockley-Read-Hall processes	119
3.1.3 Heating from optical re-absorption and scattering processes	121
3.2 Thermal and optical analytical models	122
3.3 Description of the modelling conditions in Comsol Multiphysics® environment.....	133
3.4 Thermo-electrical fem simulations - comparison between F-P and DFB vertical structures.....	135
Conclusion.....	157
Chapter III References:	159
Chapter IV	161
Laser diode thermal resistance measurement and packaging-induced stress analysis	161
IV. Introduction	161
4.1 Measurement of thermal resistance derived from optical spectrum.....	163
4.1.1 Principle of measurement.....	165
4.1.2 Experimental results and discussion.....	166
4.2 Measurement of thermal resistance derived from transient thermal testing	167
4.3 Packaging-induced stress analysis: simulations and experiments.....	181
Conclusion.....	213
Chapter IV References:	217
GENERAL CONCLUSION.....	221
APPENDIXES.....	229
References	237
Publications	238
Résumé.....	239

LIST OF SYMBOLS AND ABBREVIATIONS

2D	Two dimensions
3D	Three dimensions
AOC	Vertical structure Asymmetrical Optical Cavity
AR	Anti-Reflection
c	Vacuum velocity of light
CI	CORNING Inc.
COD	Catastrophical Optical Damage
COMD	Catastrophical Optical Mirror Damage
C _p	Heat capacity at constant pressure
CTE	Coefficient of Thermal Expansion
C _{th}	Thermal capacity
CuW	Copper Tungsten
CW	Continuous wave Operation
DBR	Distributed Bragg Reflector
DCD	Diamond Copper Composite
DFB	Distributed Feedback
E _f	Energy Fermi level
E _g	Energy GAP
FBH	Ferdinand-Braun-Institut
FEM	Finite Element Method
FI	Fraunhofer-Institute
F-P	Fabry-Perot
FWHM	Full Width at Half Maximum
f _{red}	Reduction factor
g _{mat}	Material gain
g _{mod} (Γg ₀)	Modal gain
g _{th}	Threshold gain
H _A	Re-absorption and scattering heat
H _j	Joule Heat
HR	High-Reflection
H _R	recombination heat
hν	Photon energy
I _{COD}	Value of the current at the COD
ICP	Inductive Coupled Plasma
IET	Institute of Electron Technology
I _{th}	Current threshold
J _{COD}	Current density at the COD
J _{injected}	Current density injected into the laser diode
J _{n/p}	Electron/Hole current density
J _{simul}	Current density used in Thermo-electro-mechanical simulation
J _{tr}	Current density at the Transparency
K	Coupling coefficient of the optical modes with the Bragg grating
K	Thermal conductivity

k_B	Boltzmann constant
κL	DFB Coupling factor
L	Length of the laser diode
LD	Laser Diode
L-I-V	Light current voltage
LOC	Vertical structure Large Optical Cavity
m	Order of the Bragg grating
MBE	Molecular Beam Epitaxy
MBI	Max-Born-Institut
MOCVD	Metal-Organic Chemical Vapour Deposition
N	Doping level
NAM	Non Absorbing Mirror
n_{eff}	Effective index
$n_{gr,eff}$	Group effective index
NIM	Non Injecting Mirror
N_t	Trap density
OOS	OSRAM Opto Semiconductors
OSA	Optical Spectrum Analyser
$P_{absorption+scattering}$	Dissipated power due to Absorption and scattering heating
$P_{below_threshold}$	Dissipated power due to Shockley -Read-Hall and Auger heating
$P_{carrier_leakage}$	Dissipated power due to Electron-hole recombination heating
PCS	Photocurrent spectroscopy
$P_{diss\ exp}$	Experimental value of dissipated electrical power
$P_{diss\ theor}$	Theoretical value of dissipated electrical power
P_{ele_diss}	Dissipated electrical power
P_{hj}	Dissipated power due to Thomson heating
P_{joule}	Dissipated power due to Joule heating
P_{opt}	Output Optical Power
P_{tot_diss}	Dissipated electrical power
PW	Pulsed wave Operation
q	Elementary charge
Q	Heat flux
QW	Quantum Well
$R_{1/2}$	Mirror reflectivity
R_{aug}	Auger recombination
R_c	Contact resistance
R_s	Series Resistance
R_{SRH}	Shockley-Read-Hall Recombination
R_{th}	Thermal Resistance
S	Section
SCH	Separate Confinement Heterostructure
SLOC	Vertical structure Super Large Optical cavity
SMSR	Signal Noise Suppression Ratio
SRH	Shockley-Read-Hall
$T_{0/1}$	Characteristic temperatures of the LD
T_a	Environment temperature
$T_{\alpha i}$	Characteristic temperature of α_i
TE	Transverse Electric (polarisation of the electromagnetic field)

T_g	Characteristic temperature of Γ_{g0}
T_{HS}	Heatsink Temperature
T_j	Junction temperature
T_n	Characteristic temperature of η_i
TRPL	Time-Resolved Photoluminescence
T_{tr}	Characteristic temperature of J_{tr}
VBG	Volume Bragg Grating
V_{dri}	Drift voltage
V_F	Energy difference corresponding to the laser transition
V_S	Sensing voltage
V_{th}	Threshold voltage
w	Width of the ridge
W	Lattice thermal resistivity
WPE	Wall Plug Efficiency
$\mu_{n/p}$	Electron/hole mobility
μPL	Micro photoluminescence
η_D	Differential quantum efficiency
η_E	Slope efficiency
η_i	Internal quantum efficiency
α_i	Internal losses
α_m	Mirror losses
β_0	Bragg propagation constant
Γ	Fill factor
ϵ_r	Relative permittivity
θ_H	Horizontal divergence
θ_V	Vertical divergence
λ	Wavelength
λ_B	Bragg wavelength
Λ_m	length of mark (Bragg grating)
n_g	Group velocity in the medium
ρ	Resistivity
$\sigma_{n/p}$	Electron and hole absorption cross-sections
τ	non equilibrium carriers recombination lifetime
Φ_{ph}	Photon flux density
Ψ	Transverse optical energy density

GENERAL INTRODUCTION

This “CIFRE” PhD study, supervised by IMS Laboratory and III-V lab, takes part of a large project, funded by the French Ministry of Defense (DGA), namely “LAFIP SOMUST” (Laser à Fibre Pulsé à base de SOurce semi-conductrice Multimode STabilisée en longueur d’onde). The main objective of this project was to develop a pulsed fiber laser Er/Yb at 1.55 μ m through an active collaboration between Thales Research and Technology (TRT), III-V lab for the development of the pump source and the KEOPSYS company in charge of the integration of the pump source in the fiber laser.

High-power laser diodes (LDs) emitting near of 980nm are more and more used to provide the optical power for fiber lasers or amplifiers pumping mainly addressing LIDAR and micro-machining applications. The Yb, Er and Yb/Er doped optical fibers have a very narrow absorption line close to 975nm but a higher absorption compared to the 915nm-940nm surrounding wavelength region. Most Yb or Er/Yb doped fibre lasers currently use 915nm-940nm emitting devices. It is due to the broad absorption spectrum of Yb or Yb/Er glasses in this range and to the properties of current F-P pump LDs spectral properties. However, the three times higher absorption at 976nm permits to reduce fiber length and avoids non-linear effects as far as possible. For that, the spectral width of the pump source needs to be lower than 1nm [4].

Multimode 975nm Fabry Perot (F-P) pump LDs are still the best candidates as pump source for these applications and their wavelength stabilization as a function of temperature is now possible. However, the global market pressure drives the unit price down while maintaining high levels of performances and reliability, needing continuous improvement in terms of optical power output and slope efficiency (η_E). Regarding intrinsic performances of the LDs, high optical power front facet output (10W for a 4mm cavity length) and high value of η_E ($\sim 0,9$ W/A) are now achievable, particularly due to efforts carried out on reduction of internal losses and series resistance but above all on robustness of laser facet to well-known Catastrophic Optical Mirror Damage (COMD) failure [3]-[2]. Nevertheless, due to temperature shifting, high-cost temperature stabilization setup or external wavelength-lock devices such as Volume Bragg Gratings (VBG) are mandatory to maintain pumping efficiency and stability [5]. In order to reduce such additional high cost and the inconvenient use of external devices in particular for their sensitivity to mechanical disturbances, high-power monolithically wavelength-stabilized lasers such as distributed Bragg reflector (DBR) and DFB lasers are today under active investigations to achieve the best compromise between optical output power versus temperature drift [1].

A 10W pumping source operating in CW regime is mandatory for the development of pulsed fiber laser Er/Yb at 1,55 μ m delivering a pulsed peak optical power over 1KW at 25°C. But because of the narrow spectral absorption of Er/Yb fiber, the pump source must have a narrow spectral width, typically $\Delta\lambda < 1nm$, with a thermally stabilized central wavelength of 975nm ($< 0,1nm/K$). At this wavelength, the absorption is three times bigger than at 915nm, hence the fiber length can be reduced and consequently can avoid non-linear effects in the fiber. The fiber laser must operate without thermal regulation but a high level of WPE ($> 60\%$) is mandatory and a spectral stability is required for the pump source. These requirements must be fully covered with a LD pump source including DFB grating and some dedicated performances are detailed at the beginning of this manuscript.

This PhD study aims to develop, fabricate and characterize a new technology of DFB high-power LD (with a 90 μ m width over 2, 3 and 4mm cavity length including a patterned 2nd order grating layer) emitting at 975nm to fulfil the requirements of the “LAFIP SOMUST” project. However, the momentum for increasing performances of such devices is still present in particular to operate at the highest level of emission power and reject the Catastrophic Optical Damage (COD) level threshold as far as possible. It is well documented now to consider that failure due to a change in optical properties can arise from two main failure mechanisms both largely activated by temperature:

- Enhanced optical loss due to a localized (at the facet) degradation of the active region (QW) itself which leads to optical absorption and/or scattering (Catastrophic Optical Mirror Damage COMD).
- Bulk damage or defects of material around the active region which absorbs and/or scatters light.

COD-like failure corresponds to a sudden degradation mechanism that affects edge-emitting LDs in particular when operated at elevated levels of emission power. In most cases, COD starts at one of the cavity mirrors, i.e. laser facets, while sometimes defects within the gain medium inside the cavity also initiate the COD process. There are numerous reports on COD effects and kinetics, most of them relying on the analysis of the resulting damage pattern after the COD is triggered. For high-power broadband LDs, works have been initiated since few years ago in particular by the research group of Dr J. W. Tomm from the Max-Born Institut in Berlin. His Group has produced many background and reference papers on experimental and theoretical study of temperature distributions inside the bulk and at the facets. Nevertheless and although these huge improvements,

COD is still a major concern thus limiting performances and operating reliability of such devices since the COD threshold is more and more rejected towards high current values and COD sensitivity is more and more difficult to predict on fresh devices.

This PhD manuscript is divided into four main chapters.

- **Chapter I** will give a brief state-of-the-art of infrared LD technologies and in particular, the different vertical structures reported by the major research and industrial leaders in the field. The objective is to emphasize on the advantages offered by the III-V lab technology regarding the other competitors. Then, a second section is devoted to the general background on semiconductor Laser diode heterostructures and description of optical resonators including a distributed feedback structure (DFB). The different electro-optical parameters and in particular related to DFB laser resonators are presented and discussed. From an exhaustive evaluation of literature, a last section addresses a brief overview of the LDs global market and in particular, a state-of-the-art performances review of high-power LDs emitting at 975nm will be given over the last 20 years. Finally, the context and the motivation as well as the objectives of the study will be described. Regarding the targeted application, we will demonstrate that most of the requirements must be fully covered with a LD pump source including DFB grating and the expected specifications will be summarized.

- **Chapter II** lies in the technological description of the proposed LDs and the results of electrical and optical characterizations to determine their main intrinsic performances. An opening section will compare the three vertical structures developed at III-V lab from a technological point of view: Large Optical Cavity (LOC), Super Large Optical Cavity (SLOC) and Asymmetric Optical Cavity (AOC). These structures will be particularly studied and analyzed regarding their specific properties: optical confinement, far field divergence, DFB coupling factor, optical losses and spectral width using optical simulations via FIMMWAVE® tools. A second section deals with the complete description of the vertical structure fabrication process including in particular the core emissive structure, the patterning of the grating with the e-beam technique and the facets coating preventing from the well-established failure mode (COD). The device mounting process will be also detailed representing a key step to optimize the heat flow across the whole device that depends on the overall thermal resistance and its thermal management allowing to reduce the junction temperature. Lastly, a third section will be devoted to the electrical and optical characterizations based on the measurement of the L-I-V curves in pulsed and CW regimes enabling to extract the internal parameters for each vertical structure and compared with simulation results.

- **Chapter III** aims to bring a comprehension of the heat propagation in our LD technology through different tools using analytical calculations and FEM simulations. A first section will give a brief overview of the different heat sources in a high-power LD including well-established

processes. In a second section, we will describe the implementation methodology of a relevant analytical model used to estimate these heat sources. This model enables to predict any L-I curve of a LD over a large range of bias current, knowing external and internal parameters as well as establishing a simple relationship between the structure design of the LDs and their optical performances. The development of high-power LDs capable to reach high levels of optical power (10W) needs to accurately analyse their optical power limitations and optimize its packaging. The packaging process of such devices requires overcoming both optical, mechanical and electrical issues. Despite the great interest of such analytical models, some local effects can only be understood through 2D or/and 3D FEM simulations. We will describe, analyze and discuss the results achieved from 2D stationary thermo-electrical simulations to predict the thermal flow distribution in FP and DFB LDs under a specific bias current.

An important parameter to quantify thermal management of the fabricated devices operating in CW regime, lies in the determination of the thermal resistance of the micro assembled device since a low value of this parameter allows to reduce the junction temperature by an optimized thermal dissipation path (1D conduction and spreading effect), ensuring long-term operation especially when high output optical power is foreseen ($> 10\text{W}$). Moreover, the surface mounting of a high-power LD by solder joint represents a critical step since it has been already demonstrated that the soldering process induces residual mechanical stress and strain in particular due to CTE mismatch between the different materials and their temperature-dependent thermomechanical behavior (i.e. stress-strain curves versus temperature).

• **Chapter IV** deals with a methodology enabling to extract the thermal resistance not only of the overall assembly but also of each material using transient thermal testing. Indeed, recent progress on long length cavity DFB chip structures makes difficult to use optical spectrum analyzer due to the intrinsic multimodal nature of the LD and expected resolution. This can lead to a wrong extraction of the thermal resistance measurement (so the junction temperature) and accordingly the lifetime of the micro assembled device in operating conditions. From transient thermal testing, we will propose an optimized procedure to ensure repeatability and reproducibility of measurements that remains a key point in the case of very low thermal resistance ($< 2\text{K/W}$). We will point out the results and we will conclude on the added value provided by the transient technique compared with the one derived from the optical spectrum. A second part will investigate on two mechanical configurations used to mount the LD onto the C-mount heatsink consisting in different locations of the chip. Thermo-electro-mechanical FEM simulations will be performed to analyze the stress distribution on the front facet (transversal section) as well as along the cavity length (longitudinal section). Finally, stress distribution analysis as well as Catastrophic Optical Damage (COD) threshold determination will be achieved and discussed on LDs with different vertical structures

(mainly SLOC and AOC) using four dedicated techniques in collaboration with the Max-Born-Institut in Berlin.

We do believe that such a study will represent a useful approach and a significant part of **the general Design for Reliability (DfR) effort** carried out to produce efficient and reliable high-power devices at the industrial level.

REFERENCES:

- [1] Gotz Erbert, Arthur Barwolff, Jurgen Sebastian, and Jens Tamm, "High power Broad area diode laser and laser bars" In *SPIE proceeding High-Power diode lasers*, pp. 173–223, 2000.
- [2] M. Hempel, J. W. Tamm, D. Venables, V. Rossin, E. Zucker, and T. Elsaesser, "Long-term aging and quick stress testing of 980nm single-spatial mode lasers", in *Journal of Light Technology*, pp. 4450–4456, 2015.
- [3] B. Köhler, T. Brand, M. Haag, and J. Biesenbach, "Wavelength stabilized high-power diode laser modules" In *SPIE proceedings High-power diode laser technology and applications VII*, pp. 01–12, 2009.
- [4] M. Krakowski, M. Lamponi, M. Lecompte, M. Maria, P. Resneau, Y. Robert, E. Vinet, M. Garcia, and O. Parillaud, "Very high-power broad area laser diode with internal wavelength stabilisation at 975 nm for Yb fibre laser pumping" in *SPIE proceedings OPTO*, pp. 51–60, 2014.
- [5] G. Xueqin, F. Shiwei, Y. Yuan, Y. Junwei, and L. Junwei, "Thermal analysis in high power GaAs-based laser diodes" in *Thermal analysis in high power GaAs-based laser diodes*, pp. 044011-1/044011-5, 2016.

CHAPTER I

HIGH-POWER LASER DIODES: PHYSICAL BACKGROUND AND TECHNOLOGIES — MOTIVATION OF THE STUDY

INTRODUCTION

This chapter is divided into three main sections. A **first section** aims to give a brief state-of-the-art of infrared Laser diode (LD) technologies and in particular the different vertical structures reported by the major research and industrial leaders in the field. The objective is to emphasize on the advantages offered by the III-V lab technology regarding the other competitors.

A **second section** is devoted to the general background on semiconductor Laser heterostructures and a brief description of optical resonators including a distributed feedback structure (DFB). Indeed, multimode Fabry Perot (F-P) laser diodes are still the best candidates as pumping sources for high-power applications and their wavelength stabilization as a function of temperature is now possible. However, high-cost temperature stabilization setup or external wavelength-lock devices such as Volume Bragg Gratings (VBG) are mandatory to maintain pumping efficiency and stability. In order to reduce such an additional high cost and the inconvenient use of external devices in particular for their sensitivity to mechanical disturbances, high power monolithically wavelength-stabilized lasers such as distributed Bragg reflector (DBR) and DFB lasers are today under investigations to achieve the best compromise between optical output power versus temperature drift. So, the different electro-optical parameters and more specifically related to DFB laser resonators are presented and discussed.

A last **section** addresses a brief overview of the Laser diodes (LDs) global market and in particular, a state-of-the-art performances review of high-power LDs emitting at 975nm is given over the last 20 years. From an exhaustive evaluation of literature, we have reported the different values of the main electro-optical parameters over the year for LD with 4mm cavity length and for comparison,

the values obtained with the different III-V lab technologies and devices are also indicated ahead of time. Chapters II, III and IV will detailed accurately the assessment procedures. Finally, the context and the motivation as well as the objectives of the study are also given. Regarding the targeted application, we will demonstrate that most of the requirements must be fully covered with a LD pump source including DFB grating and the expected specifications will be summarized.

1.1 BRIEF STATE-OF-THE-ART OF INFRARED HIGH-POWER LASER DIODE TECHNOLOGIES

Ordinary doped single-mode fibers are able to generate a limited output and the available pump sources are those with diffraction-limited beam quality and low optical power. During the 1990s, specific optical fibers based on the double sheath technology raised in the market and this kind of fiber allowed to increase the pump source up to high levels of output optical power (10W) over a long distance. In these fibers, the laser light propagates in a multimode core that is surrounded by an inner cladding in which the pump light propagates. Thanks to the double sheath, an outer cladding (with lower refractive index) restricts the pump light into the inner cladding. The inner cladding has a significantly larger area (compared with that of the core) and a higher numerical aperture. Hence, it can support a large number of propagation modes. Yb-doped fiber lasers have reached nowadays an output power >20 kW. However, absorption spectrum, gain, losses are dependent on the length of the fiber and in order to reduce this length, the pump source must emit at the maximum of the absorption spectrum. This last point is detailed in a next section entitled “*Chapter I-Motivation and objectives of the study*”. This gives the opportunity to develop high-power Laser Diodes (LDs) at 975 nm as pump source for optical pumping of Er/Yb fibers used currently for high-power fiber Laser applications. A first remarkable achievement on such a technology was achieved in 1996s from D. Botez and al. [1]. It was the first Fabry-Perot (F-P) LD with a cavity length of 4mm and a 100 μ m width ridge reaching an output power more than 8W. Then, this team studied different architectures and in particular in 2002 an asymmetric broad waveguide and they first introduced a Non Absorbing Mirror (NAM) at the facet in 2003 [2]-[3]. This allows avoiding the surface recombination and increases the lifetime of the LDs. In 2006, this team reported on the first broad area LD including a distributed feedback architecture reaching an output optical power near of 5W [4].

Table I-1 shows the typical vertical Al-free structure developed by D. Botez et al. from the Reed Center.

Layer	Material	Thickness [μm]
Substrate	$GaAs$	150
Cladding	$In_{1-x}Ga_xP$	1
LOC	$Ga_xIn_{1-x}As_yP_{1-y}$	0,65
2 QWs	$Ga_xIn_{1-x}As$	0,007
LOC	$Ga_xIn_{1-x}As_yP_{1-y}$	0,65
Cladding	$In_{1-x}Ga_xP$	1
Contact	$GaAs$	0,13

Table I-1: Vertical structure of the Al-free F-P LD developed by the Reed Center [5].

In 2004, JDS Uniphase exhibited a high-power F-P LD at 975nm with a 4mm cavity length but not Al-free [6]. In particular, JDS has optimized the epitaxial stack in order to reduce the thermal resistance, the series resistance and the modal loss. Table I-2 gives F-P vertical structure with cladding and LOC elaborated in $Al_{1-x}Ga_xAs$.

Layer	Material	Thickness [μm]
Substrate	$GaAs$	No information
Cladding	$Al_{1-x}Ga_xAs$	No information
LOC	$Al_{1-x}Ga_xAs$	No information
QW	$Ga_xIn_{1-x}As$	No information
LOC	$Al_{1-x}Ga_xAs$	No information
Cladding	$Al_{1-x}Ga_xAs$	No information
Contact	$GaAs$	No information

Table I-2: Vertical structure of the F-P LD developed by JDS Uniphase [6].

In 2007, the Institute of Electron Technology (IET) in Poland also proposed a high-power F-P LD emitting at 975nm (not Al-free too) [7]. The vertical structure developed is an F-P LD with an optical cavity with graded composition of $Al_{1-x}Ga_xAs$ and an inner optical cavity layer in Al-free. Table I-3 summarizes the developed vertical structure.

Layer	Material	Thickness [μm]
Substrate	$GaAs$	100
Cladding	$Al_{1-x}Ga_xAs$	1,2
LOC_graded	$Al_{1-x}Ga_xAs$	0,45
LOC	$GaAs$	0,005
QW	$Ga_xIn_{1-x}As$	0,008
LOC	$GaAs$	0,005
LOC_graded	$Al_{1-x}Ga_xAs$	0,45
Cladding	$Al_{1-x}Ga_xAs$	1,2
Contact	$GaAs$	No information

Table I-3: Vertical structure of the F-P LD developed by IET [7].

In 2012, JENOPTIK published their works on achievement of high-power LDs but did not provide any information regarding the vertical structure of the LD [8].

A particular mention to the works of the Ferdinand-Braun-Institut (FBH) since 1990s they continuously developed architectures of high-power LDs. Indeed in 1996, the first high-power LD structure emitting at 915nm based on an “Al-free” optical cavity structure for a broad area LD with 50 μm ridge was presented [9]. Then in 2000, performances of an “Al-Free” optical cavity structure of high-power LD emitting at 950nm were reported [10]. In 2001, they studied different mounting techniques for such LDs using Boron Nitride or Copper Tungsten heat spreader [11]. In 2004, the first DFB design for high-power LD of 1,5mm cavity length (< 1W) is published [12] and then a tapered waveguide high-power LD at 975nm with an output optical power of 6,7W [13].

From 2005 to 2008, additional significant improvements have been highlighted:

- High-power LDs reaching more than 10W in the range of 940nm [14], [15].
- High-power LDs fabricated with distributed feedback (DFB) grating, emitting less than 1W at 980nm [16].
- The first successful development of “Al-Free” high-power LDs based on a F-P cavity emitting at 975nm and reaching a maximum optical power of 20W [17]- [18]. For the first time, the width of the emitting zone was lower than 100 μm (96 μm) and comparable to results reported in literature.

Since 2009, constant progresses by this leader in the field have been realized in terms of output power, thermal resistance, optical losses... and in 2010, a surface Distributed Feedback laser (DFB) grating has been processed [19]-[20]. Reliability has been also investigated [21] as well as in-situ etching in order to avoid layer oxidation [22]. Continuous efforts have been made for the development of Distributed Bragg Reflector (DBR) surface grating [23], fabrication of internal grating to obtain high-power LDs operating in a DFB mode [24] and limits of output optical power in CW regime [25]. In 2013, a new vertical laser structure has been proposed [26] as well as the most important factor that limits the overall efficiency [27], $\eta_U \eta_D \eta_{th}$ (see *Chapter I-Main electro-optical parameters of a high-power Laser diode* for more details). Since 2014, works are currently made on extreme asymmetric waveguide in order to reduce the series resistance of the LDs as far as possible [28] and to increase the beam quality to achieve the best coupling efficiency for the optical pumping of Er/Yb fiber around 980nm [29]-[30]-[31]. Finally in 2015, they developed the theoretical background and reported on the performances of high-power DFB LDs with surface grating enable to reach an optical output power higher than 5W [32].

Table I-4 shows the typical vertical structure for a DFB LD proposed by FBH. Some variations in the thickness may occur depending on the graded LOC (or asymmetrical) structure or the use of surface grating.

Layer	Material	Thickness [μm]
Substrate	<i>GaAs</i>	100
Cladding	<i>Al_{1-x}Ga_xAs</i>	No information
LOC_graded	<i>Al_{1-x}Ga_xAs</i>	0,25
LOC	<i>GaAs</i>	No information
2 QWs	<i>Ga_xIn_{1-x}As</i>	No information
LOC	<i>GaAs</i>	No information
LOC_graded	<i>Al_{1-x}Ga_xAs</i>	0,25
Cladding	<i>Al_{1-x}Ga_xAs</i>	No information
Grating	<i>In_{1-x}Ga_xP</i>	No information
Cladding	<i>Al_{1-x}Ga_xAs</i>	No information
Contact	<i>GaAs</i>	No information

Table I-4: Vertical structure of the DFB LD developed by FBH [12].

The LD structure developed by III-V lab consists in an “Al-free” based optical cavity with a two-steps epitaxy process in order to implement the grating layer. Although such a structure is more difficult to process, it leads to a higher facet stability and can reduce generation of defects [3]. Moreover, reliability is improved [33] and it prevents from layer oxidation when a grating layer is implemented with a regrown epitaxy (*Table I-5*).

Layer	Material	Thickness [μm]
Substrate	<i>GaAs</i>	100
Cladding	$Al_{1-x}Ga_xAs$	1,5
LOC	$Ga_xIn_{1-x}As_yP_{1-y}$	0,55
QW	$Ga_xIn_{1-x}As$	0,0085
LOC	$Ga_xIn_{1-x}As_yP_{1-y}$	0,55
Grating	$In_{1-x}Ga_xP$	0,01
Cladding	$Al_{1-x}Ga_xAs$	1,5
Contact	<i>GaAs</i>	0,2

Table I-5: Vertical structure of the DFB LD developed by III-V lab.

Most of the published works referred to high-power LDs with Al-based compounds composing the optical cavity. With this technology, reliability remains an issue since it has been observed a faster aging process of the device due to Al oxidation [33]. From literature, only the FBH has demonstrated reliable high-power LDs with insertion of a grating layer. The Reed Center has reported on performances obtained from LDs using Al-free structures but they failed in grating layer implementation. **This PhD study clearly aims to bring a step-forward in the realization of Al-free high-power LDs operating in a DFB mode and capable to reach at least 10W with a Wall-Plug Efficiency (WPE) higher than 50%.**

Table I-6 summarizes the main characteristics of the high-power LDs developed by the different research centers and companies.

Team	F-P	DFB	Al-free
Reed Center	✓	-	✓
JENOPTIK	✓	-	-
JDS Uniphase	✓	-	-
IET	✓	-	-
FBH	✓	✓	-
III-V lab	✓	✓	✓

Table I-6: Main characteristics of the high-power LDs developed by the different research centers and companies.

Our study is justified regarding the technology of IR high-power LDs reported by the main leaders in the field. In the next section, we will introduce the general background of a LD including the concept of resonant cavity, gain and threshold conditions as well as the design of the vertical structure. Such a background is necessary to understand and compare their performances with the state-of-the-art.

1.2 GENERAL BACKGROUND ON SEMICONDUCTOR HETEROSTRUCTURES AND OPTICAL RESONATORS INCLUDING BRAGG GRATING

This section presents the typical structure of high-power LD and its main electro-optical parameters that will be extracted from analytical calculations and/or monitored from experiments. Basically, this optoelectronic device consists in a p-n junction with an active region where electrons and holes recombine, resulting in an emitted light with specific properties. The active region of the device is a gain medium together with optical confinement, within a resonant optical cavity where the stimulated emission, the spontaneous emission and the absorption processes take place. The gain medium is a material that can amplify the output power and the gain refers to the amplification level. This material absorbs incident radiation and if receives sufficient energy through the pumping process, by either electrical or optical energy, the electrons within the material can be excited to higher non-equilibrium energy levels. The incident radiation can be amplified rather than absorbed by stimulating the recombination of these electrons along with the generation of additional

radiation. The concept of the heterostructure-based LD was primary proposed by Kroemer, Alferov and Kazarinov in 1963 [34]. The LD incorporated a semiconductor heterostructure in which the active layer is surrounded by higher bandgap materials. These materials enable the transverse confinement of both the injected charge carriers and the optical field. Because of the paramount progress achieved with the introduction of the double-heterostructure LDs, modern LDs commonly basically incorporate now a semiconductor double heterostructure [34]. *Figure I-1* shows the energy-band diagram of an abrupt heterojunction between two semiconductors with different bandgap energies. The basic model for the description of an heterojunction assumes that the two semiconductors retain their bulk properties right up to the point where they join each other [34]. The E_c and the E_v between the two materials must be joined up and the Fermi level E_F must be continuous along the heterojunction.

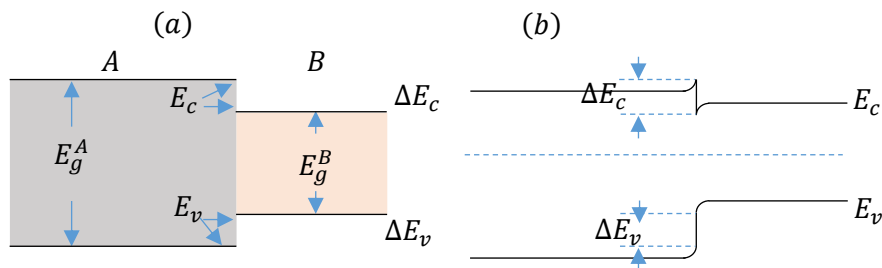


Figure I-1: (a) Semiconductor heterojunction between two semiconductors (A and B) with different bandgaps. (b) Energy band structure for an abrupt heterojunction.

In semiconductor heterojunction, the width of the depletion region is in the range of a few nanometers. So electrons may cross through the heterojunction by tunnel effect and the spikes in the band diagram may be neglected [34].

1.2.1 Design for carriers confinement

To get the well-known L.A.S.E.R. effect, a constant flow of charge carriers must be furnished to replenish the carriers that are being recombined and converted into photons in the optical cavity. The electrons are injected from the n-side with a higher bandgap energy material than the active region. Holes are injected from the p-side with a higher bandgap energy material than the active region. The active region is embedded in the high bandgap confinement layers and both the electrons and holes are forced to recombine inside it. The electrons and holes are converted into photons in the process of providing gain. The layers that induce the charge carrier confinement are called cladding layers.

The first LDs at homojunction had high optical and electrical losses, high threshold current and worked only at a very low temperature. An important step was made after the creation of the double heterostructure. The recombination, light-emitting, and population inversion zones are concentrated in the QW layer. Potential barriers and forbidden bands of different width for the semiconductors, avoid the through of electrons and holes currents even under strong forward voltages. There is no recombination in the emitters (in contrast to homostructures, in which the recombination plays the dominant role). Because of a considerable difference of the permittivity, the light is completely concentrated in the active layer, which acts as a high-grade waveguide, and thus there are low light losses in the passive regions [35].

1.2.2 Quantum well structure

In order to create an active area in a LD, a quantum well (QW) structure is currently implement. This structure derives from the double heterostructure (via epitaxial progresses). The threshold current is to a large part proportional to the thickness of the active region in the LD. The QW LD decrease the size of the active region down to quantum length scales and by that also the threshold current of the LD decrease [36]. The double heterostructure QW active regions have also improved efficiency compared to heterostructure LD [37]. Technically, this is achieved by growing very thin layers ($\sim 100\text{\AA}$) consisting of different crystal compositions. In the QW, it is possible to observe and control many quantum mechanical effects, in particular their properties occurring from the quantum confinement of charge carriers (electrons and "holes") of one semiconductor "well" material sandwiched between other semiconductor "barrier" layers. In other words, this layer is so thin that electrons and holes are confined in the direction perpendicular to the QW surface with quantization of their energy levels, while these particles are free to move in the 2D plane of the QW. In order to create an active area in a LD, it is common to implement a quantum well (QW) structure. In the domain of the quantum mechanics when the distance over which potential energy varies is approximately the so-called wavelength of "de Broglie", the classical electron trajectory loses its meaning:

$$\lambda = \frac{2\pi}{\sqrt{2me}} \hat{h} \quad [Eq. I-1]$$

where \hat{h} , m and e correspond to the Planck constant, the mass of the particle and its energy. The trajectory of a particle manifest the fundamental quantum-mechanical principle that states that all matter behaves as both waves and particle.

Indeed, the allowed states in this structure correspond to standing waves in the perpendicular direction of the layers. Because only particular waves are standing waves, the system is quantized justifying the name "quantum well".

Many modern LDs involve a more complex vertical structure for the carriers and photons confinement than the heterostructure or the QW. A strong confinement of the carriers wave function contrasts with the weak optical confinement using a QW as shown in *Figure I-2(a)*. To increase the optical confinement keeping a correct confinement, it is possible to use an additional optical waveguide around the QW as given in *Figure I-2(b)*. The corresponding structure is the Separate Confinement Heterostructure QW (SCH-QW). The electric field vector, E , shows that the photons are confined primarily by the inner QW. The wave function of carriers, Ψ , is confined by the outer heterointerfaces.

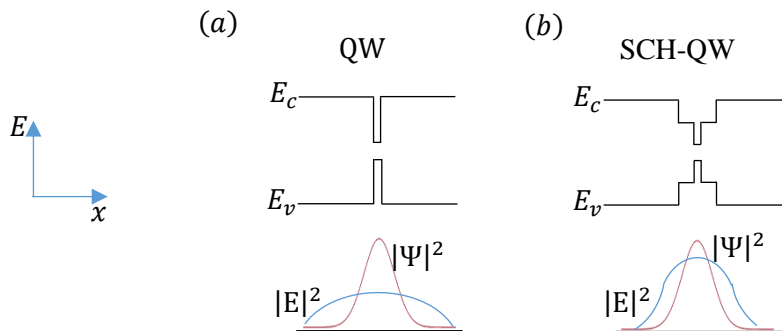


Figure I-2: Bandgap diagrams, optical fields and carriers distributions in a thin single QW, (a), and in a SCH-QW, (b). The blue and red lines represent the optical field and carriers distributions.

The development of the SCH-QW corresponds to a strained QW with a lattice constant material mismatched compared to that of the surrounding material. In the case of a GaAs substrate, a low percentage of Indium in the QW is added to increase the lattice constant. This allows for the fabrication of InGaAs/GaAs compressively strained QWs. This affects the light and heavy-holes distribution of the valence band (LH and HH respectively). Laser action usually occurs in the TE mode due to transitions to the HH band. The $E(k)$ curves are different in the growth plane and in the growth direction due to strain-induced tetragonal distortion of the unit cell and the LH and HH bands are separated in energy *Figure I-3*. The consequence is a change in the density of states. These two effects reduce the non-productive transitions and the carrier population at threshold [38]. The critical thickness at which the QW reverts back to its native state, causing high density of lattice defects, is in the range of a few hundred Å [39].

The mechanical strain of the QW has a consequence on the curvature of the valence and conduction bands structure as mapped in *Figure I-3*.

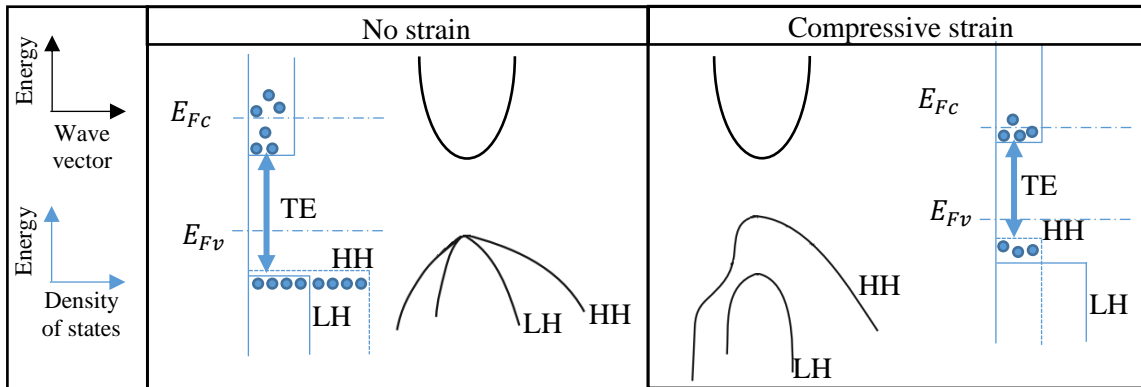


Figure I-3: Density of states and band diagram for strained and not strained QW. The quasi Fermi level, the edge energies and the densities of the states in the valence band are influenced by the mechanical strain.

For a given quasi-Fermi level separation, the electrons or holes density of the energy states diminishes introducing a strained QW. Such a drop reduces the carrier density required to reach the threshold. Hence, at the transparency, the strain QW has a lower carriers density and a strained QW significantly reduces the transparency current. Such a compressed strain QW also leads to a light emission into the direction parallel to the LD junction (TE polarization).

The strained SCH-QW represents the most modern design of LDs. In our study, all the theory and the calculations will be applied to compressed strained SCH-QW.

Two well-known techniques are used for SCH-QW fabrication: molecular beam epitaxy (MBE) and metal-organic chemical vapor deposition (MOCVD) [40], [41]. Both can achieve a layer thickness control to one atomic layer. MBE is essentially an ultra-high vacuum technique in which a beam of the constituent atoms or molecules (e.g., Ga, Al, or As) emerges from ovens, lands on the surface of a heated substrate and layers of material grow as a function of deposition time. Such a grown layer can be controlled by opening and closing shutters in front of the ovens. For example, with a shutter closed in front of the Al oven, but on contrary with open shutters in front of the Ga and As ovens, GaAs layers can be grown. By opening the Al shutter, the alloy AlGaAs can be grown with a relative proportion of Ga and Al elements controlled by temperature of the ovens. With additional ovens and shutters for the different dopant materials, structures of any sequence of GaAs, AlAs, and AlGaAs can be grown with essentially arbitrary doping levels. MOCVD is a gas phase technique at low pressure (e.g., 25 torr). In this case, the constituents are deposited using gasses (e.g., trimethylgallium and arsine) over a heated substrate with the resulting composition being controlled by the relative amount of the appropriated gasses. Hybrid techniques, using the gas sources of MOCVD in a high vacuum molecular beam system also exist and are known as gas-source MBE or chemical beam epitaxy (CBE). Typical structures grown by these techniques can reach a total thickness of a few microns, resulting from a stack of hundreds of layers.

1.2.3 Gain and threshold conditions

The optical mode originates from the spontaneous emission that is confined into the cavity by the waveguide. This optical mode is amplified by the gain medium. The active region represents the gain medium for optical field propagation that is of major importance for a LD.

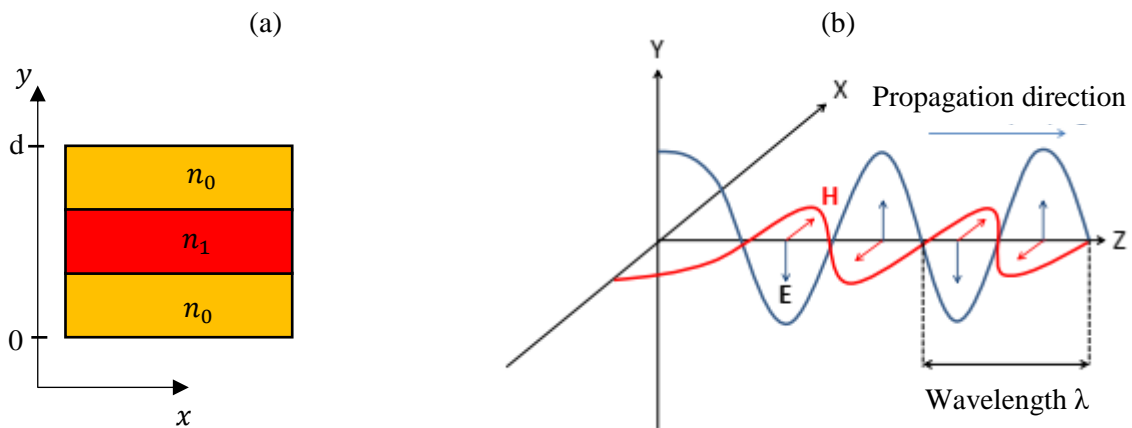


Figure I-4: Transversal cross-section view of a symmetrical waveguide (a) and propagation of the electromagnetic field (b).

Considering *Figure I-4* (a), the transversal cross-section of a symmetrical waveguide, the intensity of an optical plane wave, when passing through an absorption medium along the optical axis (z), can be described as:

$$J(z) = J_0 \cdot \exp(-\alpha z) \quad [\text{Eq. I-2}]$$

where J_0 represents the initial value of the optical mode and α is the absorption coefficient. The gain medium affects the absorption coefficient that drops from a positive value to a negative one. In *Figure I-5*, the material gain versus the wavelength for different carriers densities is shown [42].

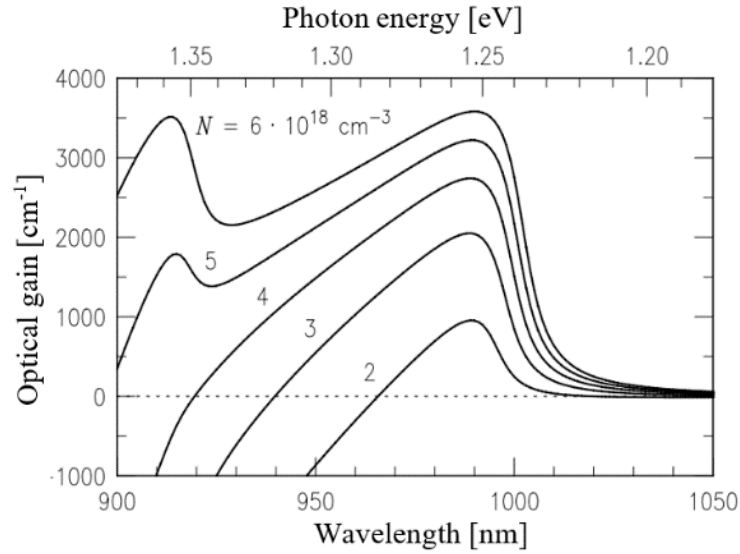


Figure I-5: Material gain spectrum versus carrier density in a InGaAs QW. Due to the high density of states in the QW, the maximum of the gain curve only shows a slight shift in wavelength [42].

For the LD design, a good estimate for the material gain g can be described by the following equation:

$$g_{mat} = g_0 \cdot \ln\left(\frac{J}{J_{tr}}\right) \quad [Eq. I-3]$$

where g_0 stands for the reference gain, J represents the current density applied to the device and J_{tr} is the transparency current density. The g_0 and J_{tr} are material-dependent constants depending on composition, thickness as well as strain value of the QW and barrier material respectively. [Eq. I-3] refers to the gain only in the QW layer. In order to consider the amplification of the optical wave within the resonator, the modal gain g_{mod} is introduced. This last depends on the degree of overlap of the optical wave within the QW and on the density of the injected carriers [42]. The modal gain depends on the material gain, multiplied with the overlap between the gain medium and the optical mode, namely the confinement factor Γ as detailed in appendix 5.3 of [37]:

$$g_{mod} = \Gamma g_{mat} \quad [Eq. I-4]$$

where:

$$\Gamma = \frac{\int_0^d J(y) dy}{\int_{-\infty}^{+\infty} J(y) dy} \quad [Eq. I-5]$$

The “d” parameter stands for the thickness of the active layer (the QW) and $J(y)$ describes the optical-intensity pattern of the fundamental optical guided TE mode propagating in the QW. For an efficient laser operation, high values of modal gain are required that means a high confinement factor. Since only a small part of the guided mode is confined into the QW ($\Gamma \ll 1$), the modal optical gain is much smaller than the material gain.

1.2.4 Structure and design parameters of an optical resonator with Bragg grating – Distributed Feedback architecture

In a LD, the stimulated emission is basically generated within an optical resonator structure. This lies in a QW sandwiched in waveguide layers and surrounded by claddings layers. This structure is located between two mirrors corresponding to crystal facets as shown in *Figure I-6*.

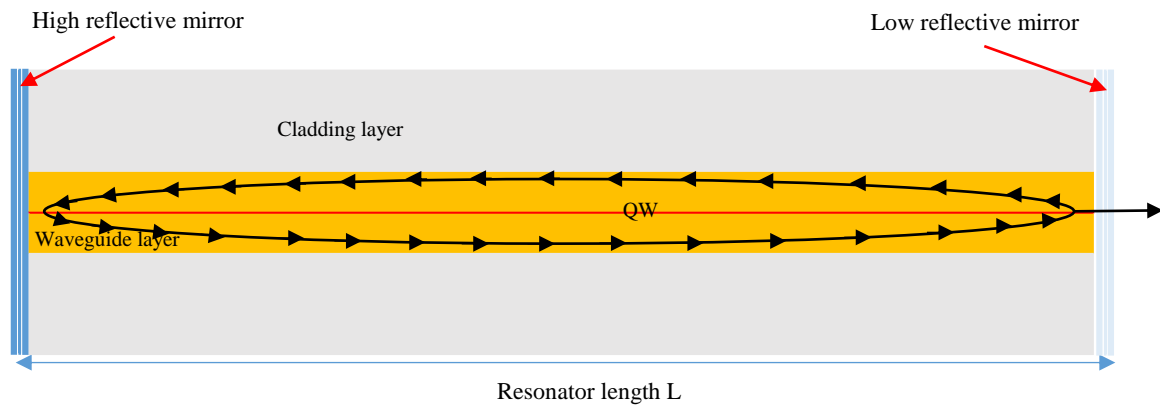


Figure I-6: Generic design of an optical resonator. The red line represents the QW. The optical field makes a roundtrip along the cavity length travelling between the two mirrors.

In an optical resonator, a mode travels along the optical waveguide. For each mode propagating into the cavity, it is possible to associate the intensity-absorption coefficient α , that is related to the modal gain by the following equation:

$$\alpha = \alpha_i - \Gamma g_{mat} \quad [Eq. I-6]$$

where α_i is the intrinsic modal absorption.

The α_i is caused by the scattering of the optical modes due to latent defects or rough interfaces and by free-carriers absorption. Hence, α_i gives important information about the quality of semiconductor layers and the overlap of the multiple optical modes (ideally confined into the optical cavity) into the cladding layers. The intensity of the optical mode entering into the optical cavity, after a roundtrip in the cavity becomes equal to J_1 :

$$J_1 = R_1 \cdot R_2 \cdot J_0 \cdot \exp[2(\Gamma g_{mat} - \alpha_i)L] \quad [Eq. I-7]$$

Based on [Eq. I-6] and [Eq. I-7], the amplification of the optical mode is reached when $g_{mod} > \alpha_i$. Lasing occurs when the gain, provided to the optical modes, compensates the intrinsic absorption and the mirror losses for a roundtrip. In these conditions, the optical plane wave after a roundtrip becomes $J_1 = J_0$. From [Eq. I-7] it is possible to obtain the laser threshold condition, substituting:

$$\begin{aligned} J_1 = J_0 &= R_1 \cdot R_2 \cdot J_0 \cdot \exp[2(\Gamma g_{th} - \alpha_i)L] \\ 1 &= R_1 \cdot R_2 \cdot \exp[2(\Gamma g_{th} - \alpha_i)L] \\ \Gamma g_{th} &= \alpha_i + \frac{1}{2L} \ln\left(\frac{1}{R_1 \cdot R_2}\right) = \alpha_i + \alpha_m \end{aligned} \quad [Eq. I-8]$$

where g_{th} represents the threshold gain that is the minimum gain necessary to achieve the lasing condition. The term α_m stands for the optical mirrors losses and it depends on both the cavity length L and the reflectivity of each mirror.

With respect to *Figure I-6*, it is possible to define the F-P resonator consisting in the two mirrors located at both ends of the optical waveguide. The optical modes must respect the resonance condition to achieve the laser condition. For high-power LDs, the optical resonator has multiple resonance frequencies called longitudinal modes. Under this standing wave condition, the repeatedly reflected rays are in phase with each other and positive interferences between them preserve the state of coherence. The standing wave condition represents the phase condition for the LD [42]:

$$1 = \exp\left(-\frac{i4\pi}{\lambda_0} n_{eff}L\right) \rightarrow \frac{4\pi}{\lambda_0} n_{eff}L = m2\pi \rightarrow m = \frac{2Ln_{eff}}{\lambda_0} \rightarrow L = m \frac{\lambda_0}{2n_{eff}} \quad [Eq. I-9]$$

where n_{eff} stands for the effective refractive index of an optical waveguide and m is an integer. Because $\frac{\lambda_0}{n_{eff}}$ is a wavelength in a material, a product of a positive integer “m” and half-wavelength $\lambda_0/2$ in a material is equal to the cavity length “L” at the resonance condition. In other words, the resonator length “L” equals an integer multiple of half of the center wavelength λ_0 . The total differential of [Eq. I-9] [Eq. I-10] gives the spectral separation between neighboring modes [42]:

$$\Delta\lambda_{F-P} \approx \frac{\lambda_0^2}{2L \left(n_{eff} - \frac{\partial n_{eff}}{\partial \lambda_0} \lambda_0 \right)} \approx \frac{\lambda_0^2}{2n_{gr,eff}L} \quad [Eq. I-10]$$

where $n_{gr,eff}$ is called group effective index and defined as $n_{gr,eff} = c/v_g$ with c and v_g speed of light in vacuum and group velocity in the medium. Because the study of the LD linewidth was not part of this thesis, we will not detail this part.

The group effective index is typically 20–30% larger than the effective refractive index depending on the specific photon energy relative to band-gap energy. The resonator length sets the longitudinal mode spacing while adjacent modes are typically separated of 0,05 nm from each other considering a 4mm cavity length.

The high-power LD with a ridge of $90\mu m$, experimentally, has a typical spectral width higher than $3nm$ and, for effectively pump an optical fiber doped Er/Yb, the spectral width must be lower than $1nm$. Moreover, for a F-P LD, the detuning of the spectrum as a function of temperature is in the range of $\frac{\delta\lambda}{\delta T} \approx 0,5 nm/^\circ C$.

For these reasons, the integration of an optical grating into the resonator is necessary allowing to reach a detuning of the spectrum as a function of temperature less than $0,1nm/^\circ C$. In DFB LDs, the optical feedback is distributed throughout the cavity length as a grating. Nakamura et al. [43] published in 1973 results showing that an optically pumped GaAs LD with built-in corrugation feedback has largely narrowed spectral emission compared to a F-P structure. In the following decades, high-power LDs delivering over 10W in CW regime and a Wall-Plug efficiency of more than 60% have been achieved using single emitters and Bragg grating (DFB or DBR) [22]-[12]-[44]. The optical feedback occurs by means of Bragg diffraction and couples the propagating waves in the forward and backward directions. The grating layer provides the feedback of the light by spatially modulating the complex refractive index in a region that delivers the optical gain. *Figure I-7* shows a DFB high-power LD developed in this study and processed with facilities of III-V lab. The grating layer is usually close to the p-side of the LOC structure. Details on the grating

parameters will be given in “*Chapter II*”. A DFB laser is typically defined as a device where the internal grating is actively and uniformly distributed between the output facets in an edge emitter as referred in [45].

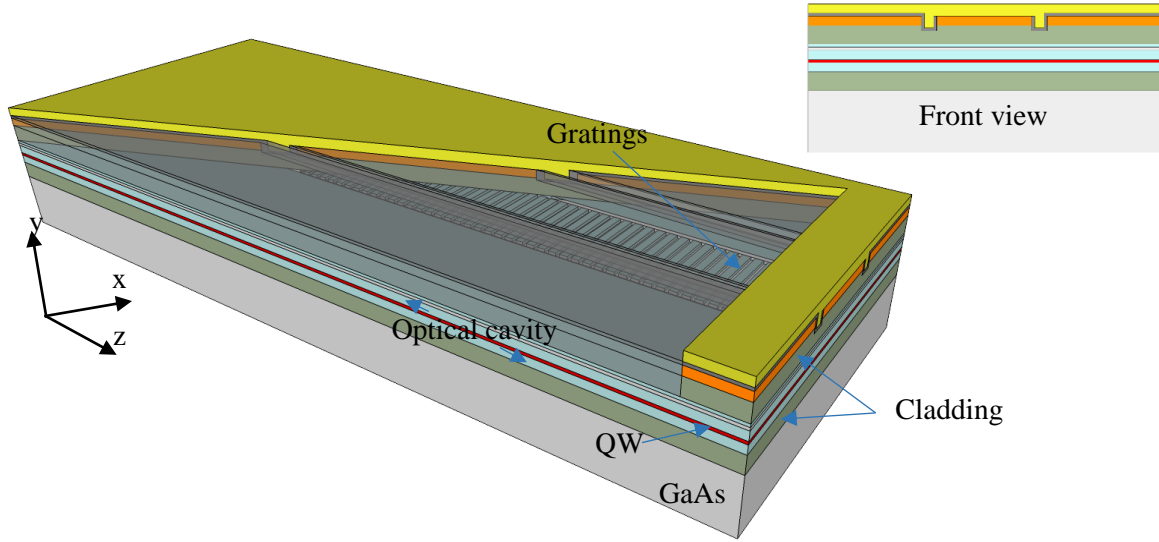


Figure I-7: 2D and 3D view of a DFB LD developed in this study and processed with facilities of III-V lab. The triangle cut highlights the DFB grating layer on top of the optical cavity layer.

The grating leads to a periodic variation of the refractive index along the optical axis (z-axis) as reported in the following equation:

$$n(z) = n'_{eff} + \frac{\Delta n}{2} \cos(2\beta_0 z) \quad [Eq. I-11]$$

With such an equation, it is supposed that the transverse and the lateral variations are neglected. The term n'_{eff} represents the real part of effective index without the grating and $\frac{\Delta n}{2}$ is the variation of the index amplitude (assuming that $\frac{\Delta n}{2} \ll n'_{eff}$) with and without grating. The parameter β_0 corresponds the Bragg propagation constant related to the spatial period of the structure Λ defined as follows:

$$\beta_0 = \frac{m\pi}{\Lambda} = \frac{2\pi}{\lambda_B} n'_{eff} \quad [Eq. I-12]$$

And the period Λ is linked to the Bragg wavelength:

$$\Lambda = m \frac{\lambda_B}{2n'_{eff}} \quad [Eq. I-13]$$

where λ_B and the parameter m represent the Bragg wavelength and the order of Bragg diffraction respectively [34].

Based on the coupled-modes theory, it is possible to model and analyze the optical wave propagation into periodic structures [46], [47] and the coupling coefficient “ κ ”:

$$\kappa = \frac{\pi \Delta n}{2\lambda} \quad [Eq. I-14]$$

The coupling factor equation depends on the grating shape. For our device, we choose to use square grating as shown in *Figure I-8*. However, for rectangular grating with unequal length of the mark and space a reduction factor f_{red} must be used. Therefore, from [46], [Eq. I-14] can be modified as follows:

$$\kappa = \frac{2\Delta n'}{\lambda_B} f_{red} = \frac{2\Delta n'}{\lambda_B} \cdot \frac{1}{m} \left| \sin \left(\pi \frac{\Lambda_m}{\Lambda} m \right) \right| \quad [Eq. I-15]$$

where f_{red} is the reduction factor, Λ_m and Λ are the length of mark, the period and m represents the order of the grating.

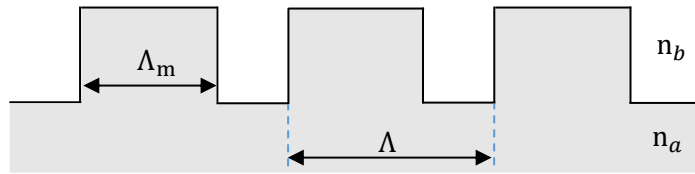


Figure I-8: Design of a rectangular grating with period Λ and mark length Λ_m (n_a and n_b represent the refractive indexes).

It is possible to write a relation between the coupling factor “ κ ” and the gain for the field g_f in the optical cavity [46]:

$$g_f L \approx \left(\frac{\pi}{\kappa L} \right)^2 \quad [Eq. I-16]$$

Part of the optical mode generated in the optical cavity travels through the grating but this coupled optical field intensity depends on the coupling factor κ . Hence, the laser gains both in temperature stability and spectral width. An increased feedback (higher κL) leads to lower mirror losses (lower $g_f L$) as the grating becomes efficient and more power travels around in the cavity. For values of κL and far from the Bragg wavelength (high values of $\Delta\beta L$), the feedback is less efficient and the mirror losses (α_m) is higher, [46]. There is no efficient methodology to control the exact position of the facets relative to the grating. A random phase angle is created for each LD and only a certain fraction of DFB LDs with a reflecting facet will have an acceptable SMSR. We can consider a vertical single mode selectivity (yield) related to this random phase angle. Usually, κ ranges from 0,5 to 2 and is directly connected to this yield [46]. This last depends on the κL and the facets reflectivity. Usually the coatings used are HR 95% and AR 1% and in order to maximize the yield, the κL must be close to one, [46]. Considering our LD technology, the vertical single mode operation is achieved. For modes with orders higher than the fundamental one, values of material gain are superior but are affected by larger losses. In other words, one can write: $g_{mat_{mod\ 1}} \ll g_{mat_{mod\ n}}$ with $n > 1$.

The “ κ ” directly depends on f_{red} assuming various values as a function of the Bragg order. For square grating, the f_{red} varies as a function of mark and space ratio (see *Figure I-9*). Particular attention must be paid to the choice of this ratio. For a first order Bragg grating, there is no zero-crossing. From second to higher orders, zero-crossing becomes relevant and the values of ratio $\frac{\Lambda_m}{\Lambda}$ must be accurately chosen.

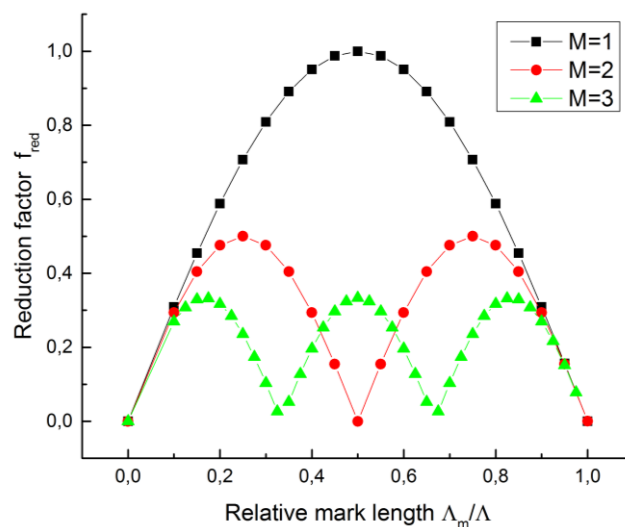


Figure I-9: Variations of the reduction factor f_{red} of κ coupling factor for a square grating versus $\frac{\Lambda_m}{\Lambda}$.

The LD linewidth is independent of the details of the vertical structure but depends on the number of photons in the laser. The number of photons in the laser is:

$$S' = \frac{\bar{S}}{\Gamma} V_a \quad [Eq. I-17]$$

where \bar{S}, V_a represent the average photon density and the active volume. Based on [46] it is possible to write the laser linewidth $\Delta\nu$:

$$\Delta\nu = \frac{\Delta\omega}{2\pi} = \frac{R_{sp}V_a}{4\pi S'} = \frac{h\nu v_g^2 (\alpha_i + \alpha_m) \alpha_m n_{sp}}{8\pi P_{out}} \quad [Eq. I-18]$$

where $R_{sp}, h\nu, v_g, n_{sp}, P_{out}$ represent the spontaneous emission rate, the photon energy, the group velocity, the spontaneous emission coefficient and the optical output power. Because the study of the LD linewidth was not part of this thesis, we will not delve deeper into this subject.

1.2.5 Main electro-optical parameters of a high-power Laser diode

No precise definition has been established between low and high-power LDs. It depends on the structure of the laser and the wavelength range as well as the spectral properties of the output beam. In this study, we will focus on multimode LDs that refer to high-power operation for an output optical power higher than 1W in CW regime. For such LD, the optical cavity is large enough ($\gg 10\mu m$) that allows the existence of multiple modes with similar effective index. Via Fimmwave® optical waveguide simulation, we estimate a difference of the effective index between two modes after the sixth decimal. For this reason, even using a DFB grating is not possible to obtain a mono-mode spectrum. Through an exhaustive review of literature and in order to compare the different technologies of high-power LDs, we must introduce and explain the external and internal parameters.

Below the threshold current, spontaneous emission mainly dominates and the light intensity emitted by the laser structure is very low. Above the threshold current, stimulated emission takes over and the output power (P_{out}) increases linearly as a function of the bias current as shown in *Figure I-10*. Therefore, the output optical power can be written as this:

$$P_{out} = \eta_i \cdot \frac{\alpha_m}{\alpha_i + \alpha_m} \cdot \frac{h\nu}{q} \cdot (I - I_{th}) = \eta_D \cdot \frac{h\nu}{q} \cdot (I - I_{th}) \quad [Eq. I-19]$$

where η_i , η_D , $h\nu$ represent the internal quantum efficiency, the differential quantum efficiency, the photon energy (of the modes) respectively and q is the elementary charge. The slope efficiency (η_E), dP/dI , is proportional to η_D .

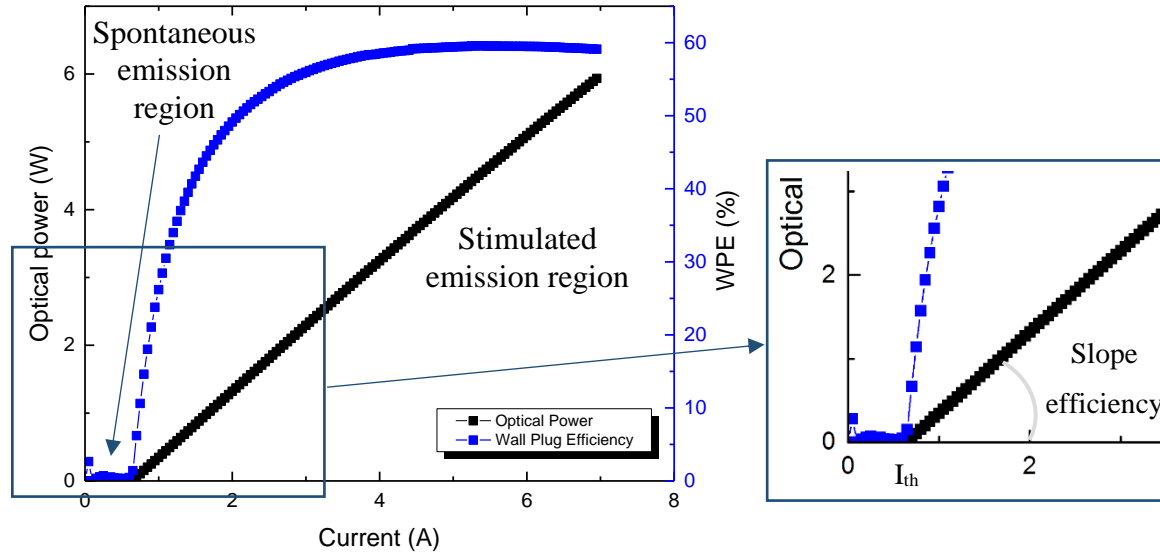


Figure I-10: Variations of the output optical power and Wall-Plug Efficiency (WPE) versus the applied bias current.

The η_i represents the fraction of the total current increment (ΔI) above threshold that, besides to the charge carriers located in the medium, results in the stimulated emission of photons. Of course, such a parameter is less than unity if part of ΔI is used for non-radiative recombination processes (ΔI_{n-r}), by vertical or lateral leakage ($\Delta I_v, \Delta I_l$) and can be written as follows [48]:

$$\eta_i = \frac{\Delta I_{stim}}{\Delta I} = \frac{\Delta I_{stim}}{\Delta I_{stim} + \Delta I_{n-r} + \Delta I_v + \Delta I_l} \quad [Eq. I-20]$$

Experimental studies have shown that the following various physical effects can play a role in broad-area lasers [27]:

- 1) carriers recombination in barrier or spacer layers,
- 2) carriers escape from the active region into the waveguide or cladding layers,
- 3) current spreading at the device edges,
- 4) non-uniform optical field within the stripe,
- 5) non-radiative defects centers within the active region that do not saturate at threshold.

Effects 1) to 4) can be managed with design changes using wider stripes ($\gg 90\mu\text{m}$) and by varying the layer compositions to minimize carriers escape. However, as for threshold current, losses due to non-radiative processes can only be addressed based on material quality improvements [48]. The slope efficiency, dP/dI , is one of the main performances of a LD. It is typically given W/A, and is derived from the linear part of the P-I curve above threshold. From this parameter, it is possible to calculate the differential quantum efficiency: $\eta_D = \frac{q}{h\nu} * \frac{dP}{dI}$, enabling to calculate the percentage of electrons injected above the threshold that allows generating stimulated photons. *Figure I-10* shows the Wall-Plug efficiency (WPE) for a LD. High values of WPE are crucial in many applications, for example to extend system life in portable range finders and in space applications or to reduce energy use in large systems such as industrial processing tools and for studies addressing laser-induced fusion. Even efficiency progression of a few percent can lead to added-value. In addition, increased WPE , especially at high P_{out} , reduces the level of current heating in the laser, [27]. This parameter can be written as a function of bias current from [Eq. I-19]:

$$WPE(I) = \frac{P_{\text{out}}}{P_{\text{in}}} = \frac{P_{\text{out}}}{I \cdot U} = \eta_D(I) \cdot \frac{h\nu}{qU} \cdot \frac{(I - I_{\text{th}})}{I} = \eta_D(I) \cdot \eta_U(I) \cdot \eta_{\text{th}}(I) \quad [\text{Eq. I-21}]$$

The terms η_U, η_{th} represent bias and threshold efficiency. In order to achieve lasing, the carrier population in the active region must be inverted and the necessary minimum external voltage corresponds to the photon energy (in eV): $U_{\text{ph}} = \frac{h\omega}{q}$. When $U = U_{\text{ph}}$, the bias efficiency η_U is equal to 1. By analogy to quantum defect solid-state lasers, a voltage in excess of U_{ph} can be termed as a voltage defect $U_d = U - U_{\text{ph}}$ [27]. For bias current largely above I_{th} , the threshold efficiency tends to the unity. Because ohmic losses increase as a quadratic function of the current, one can find a maximum for the WPE for a specific operating current. Typically for high-power LDs, it is possible to reach a WPE over 50%. The impact of temperature rise on threshold and differential quantum efficiency depends on the considered structure and the resonator quality of the LD. From a phenomenological point of view, the following parameters have an exponential temperature dependence:

$$I_{\text{th}2} = I_{\text{th}1} \exp\left(\frac{T_{j2} - T_{j1}}{T_0}\right)$$

$$\eta_{d2} = \eta_{d1} \exp\left(\frac{T_{j2} - T_{j1}}{T_1}\right) \quad [\text{Eq. I-22}]$$

where T_{j1}, T_{j2} , represent the junction temperatures and T_0 and T_1 are defined as characteristic temperatures.

It is very difficult to extract theoretical values of T_0 and T_1 while it is easier to determine them from experiments. For practical use, these constants are calculated for each type of LD. The characteristic temperature T_0 represents the dependence on the barrier height and the threshold current density. The T_1 temperature represents the dependence of non-radiative recombination and carrier overflow across hetero-interfaces that causes further free carrier loss within the cavity [49]. The I_{th} is strictly related to the QW and the resonator losses. In other words, the T_0 mainly depends on the material of the active region. Typical reported values of T_0 and T_1 range from 200K to 600K for high-power LDs emitting at 975nm [50]. The maximum output power can be also limited by the temperature rise of the active region, well-established as the thermal “roll-over” phenomenon. The decrease in the LD differential quantum efficiency as increases the current injection, comes across the thermal roll-over. The excess power not converted into light, can be converted into heat causing material heating and performance degradation. As the laser is driven at higher currents, the active region starts heating up significantly. In the same conditions when the dissipation of the generated heat becomes challenging, the temperature of the active region is very high causing a reduction of the output optical power. Excessive heat generation by ohmic heating leads to a significant temperature rise in the active layer resulting in carrier spreading, significant gain reduction, and an increase in non-radiative recombination [51]. Hence, another important parameter of LDs deals with the series resistance (R_s).

The applied voltage to the LD increases until the turn on diode voltage and, after the threshold, is considered as linear. This means that R_s can be calculated as the sum of each layer contribution. From the Ohm’s law, one can be written as follows:

$$R_i = \rho \cdot \frac{L}{A} \rightarrow R_s = \sum_{i=0}^n R_i \quad [Eq. I-23]$$

where R_i, ρ, L, A are the electrical resistance of the layer, the resistivity, the length along the current path, the section crossed by the electrical flow respectively and n represents the number of layers.

In order to minimize the thermal roll-over, the design must result from a compromise enabling to reduce the internal losses and the threshold current, maximize the WPE of the LD and finally minimize the series and the overall thermal resistance. Another power-dependent limiting process lies in the occurrence of two well-known failure modes, namely Catastrophic Optical Damage

(COD) or Catastrophic Optical Mirror Damage (COMD). Physical mechanisms of facet-related degradation are schematized in *Figure I-11*. A facet oxidation loop, a loop for dislocations at the facet and some related phenomena are physically connected with the overall COMD loop. When light is absorbed at the facet, electron-hole pairs are generated and this pair generation enhances the bond breaking. The generated electrons and holes recombine through a non-radiative way and the temperature is increased at the facet. Therefore, the band gap energy is reduced, the light absorption at the facet and the number of electron-hole pairs increase. Finally, the temperature rise reaches the melting point of the laser material and a COMD occurs.

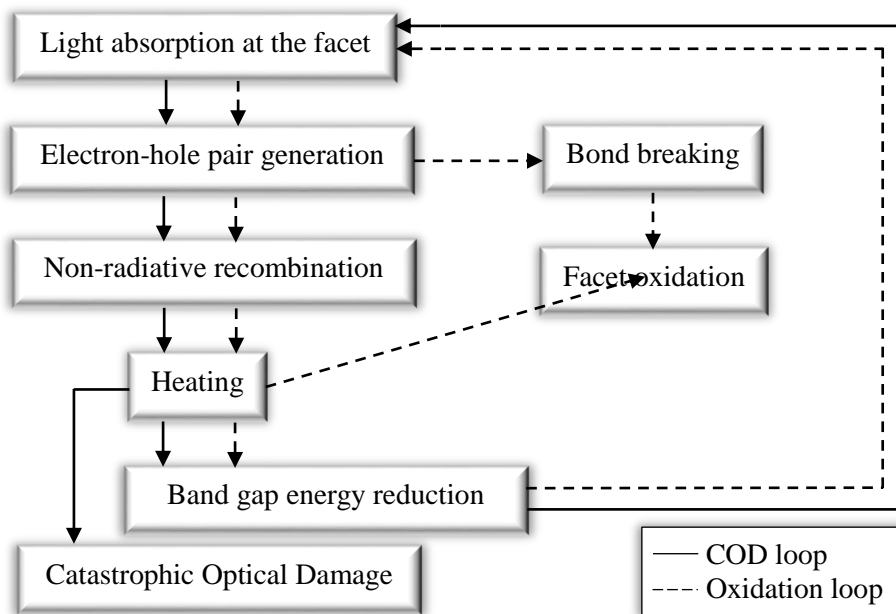


Figure I-11: Scheme of physical processes leading to a COD occurring at the laser facets [52].

The maximum output power achievable in CW regime is directly proportional to the COMD power density limit as reported in [53]. The maximum CW output power can be written as follows:

$$P_{max} = W \cdot \frac{d}{\Gamma} \cdot \left(\frac{1 - R_1}{1 - R_2} \right) \cdot P_{COMD} \quad [Eq. I-24]$$

where P_{COMD} , W , d , Γ , R_1 and R_2 stand for the internal optical power density at COMD, the central ridge width, the thickness of the optical cavity, the confinement factor and the reflectivity of the front and rear facet of the LD.

As a fact, the P_{COMD} decreases as the Al concentration in the active region increases. This is due to an increased sensitivity to oxidation of the Al-containing active regions [51]. In order to increase the maximum optical power achievable, the d/Γ ratio must be high but a high confinement factor results in high thermal facet load and larger beam divergence. In the case of high-power LDs, these parameters are crucial regarding reliability aspects.

We have studied the general principle of the LD that converts electrical energy into light and we have also introduced the main electro-optical parameters of an LD. After a brief introduction of the GaAs LDs global market, we will compare the electro-optical parameters of our LDs with the state-of-the-art.

1.3 GLOBAL MARKET OVERVIEW OF GALLIUM-ARSENIDE LASER DIODES

Nowadays, the LDs cover a wide range of application in different areas. From industry to military applications and scientific fields, the role and the use of LDs is clearly highlighted. Industrial grade LDs are exceeding a power of 120W in CW regime from a standard 10 mm bar or 10W from a single 100 μ m width stripe at 9xx nm wavelength. QCW devices at 808nm already exceed 300W per bar, enabling several kW of pump power with the smallest footprints. The efficiency of state-of-the-art materials for LDs already overcomes 60% and is scratching the 70% mark. All these improvements made LDs a well-proven instrument for:

- The industrial reality, e.g. in the soldering of car bodies in mass production for automotive.
- Spacecraft instrumentation, e.g. the intra-satellite communication
- Basic equipment in many research Laboratories and Research Centers all over the world.

Figure I-12 shows the market sectors for industrial material processing. The low-power (< 1kW) and high-power (1-100kW) are described by submarkets such as macro (metal cutting, welding brazing with optical power in the range of 1kW or more), micro (application using LDs with optical power lower than 500W) and marking. The low-power segment represents nearly half of the market and includes lower power macro, micro, marking and engraving. The volume of global market for laser and material processing is estimated in 6B\$ for 2009 and until now, the expansion rate reaches 3.8%. In 2016, the forecast was established about 10,5B\$ [54]-[55].

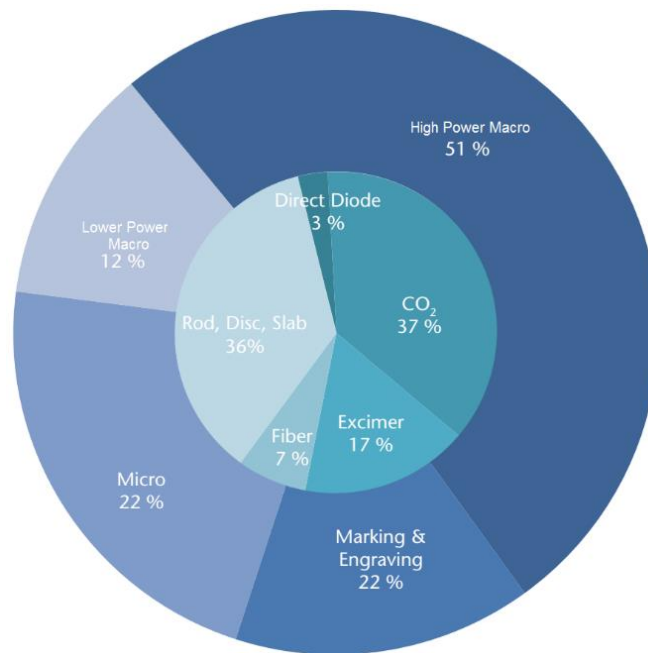


Figure I-12: LDs are mainly used for industrial materials processing. This market is usually divided into high-power (1–100kW) and low power (< 1kW) macro, micro and marking [54]-[58].

The main applications of LDs address:

- Optical storage
- Telecommunications
- Solid-state laser pumping
- Medical therapeutics
- Image recording
- Barcode scanning
- Inspection, measurement & control
- Material processing
- Sensing
- Basic research

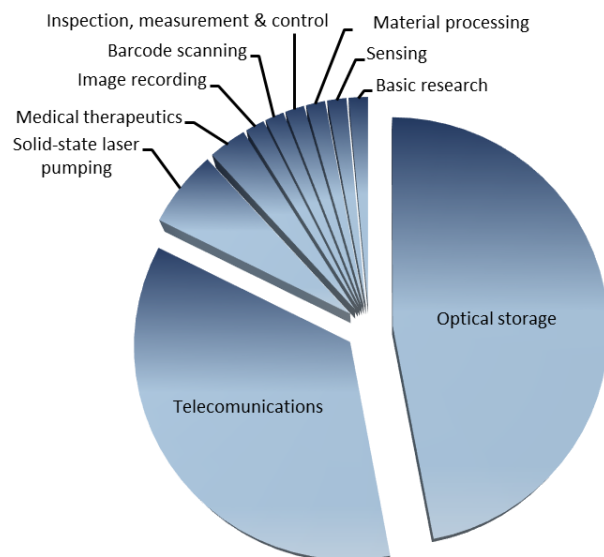


Figure I-13: Main applications of LDs [2]- [51].

Figure I-13 shows the market repartition for the LDs applications. Optical storage is clearly the major segment followed by telecommunications. Figure I-14 shows the main international leaders in the market of LD-based systems. Among these eleven manufacturers, 90% use LDs in their products, more than 50% are vertically integrated in their manufacturing lines. In addition, among

the companies holding less than 1% market share, there are at least five major manufacturers of LDs [54].

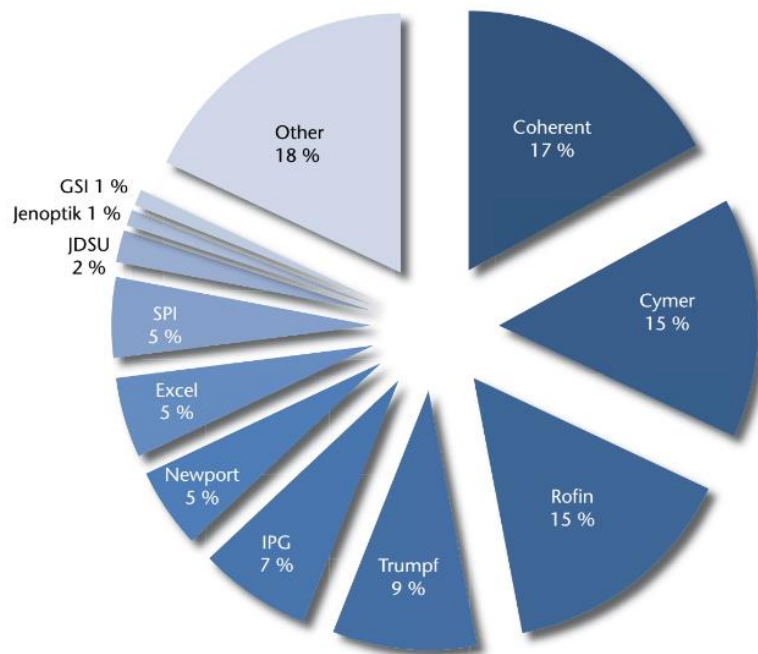


Figure I-14: The main international leaders developing LD-based systems [54].

In the 1980s, low-power laser diodes were extensively developed for communication and data-storage purposes. The next step in exploring semiconductor laser technology has focused on the development of high-power LDs as key devices for laser system and their vast application potential in production processes such as welding, soldering, polymer joining, cutting, surface treatment and medical application. The breakthrough came early in the 1990s when the power lifetime of 1cm x 0,06cm laser bars reached more than 20W and 10.000h taking into account that the lifetime of a basic lamp does not exceed 1000h [50]. In the late 1990s, optical power levels of 50W for 1 cm bar with efficiency over 50% were demonstrated and first applications in polymer welding were publicized. Then, their first large-scale deployment for industrial applications was realized at that time [56]. The question arose whether – and if so how – those lasers could someday complement classical CO₂ and solid-state lasers, possibly even in a near future. The main advantages of laser systems based on high-power LDs compared to lamp pumping or gas discharge for coherent light generation, are their smaller size, electro-optical conversion efficiency, simpler power and cooling supply as well as their higher reliability.

Fiber lasers have been consistently a growing part of this market for several years. In 2014, fiber lasers overtook CO₂ as the leading revenue producer for industrial laser systems. The major component in a fiber laser lies in the optical pumping part basically provided by a LD. The pumping device can also be used as a stand-alone system for many industrial applications and in particular marking. The direct diode market (such as material processing) also shows strong growth. *Figure I–15* highlights that more than 60% of the market for laser-powered materials processing is based on high-power GaAs-based LDs technologies. This trend is expected to going-on with diode-based systems progressively replacing solid-state and CO₂ lasers.

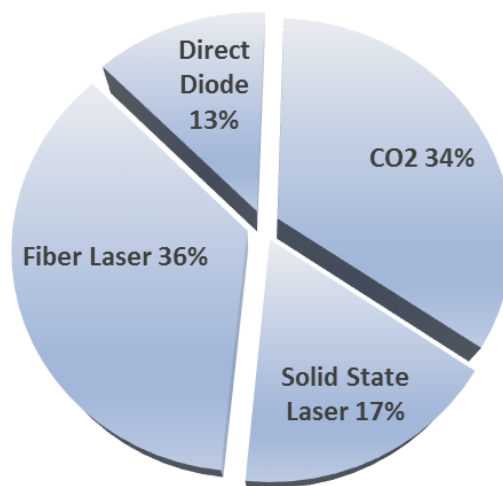


Figure I–15: Market share of high-power optical systems, high-power lasers for industrial manufacturing, market segments and development for CO₂ lasers, Solid State Lasers and LDs [57].

1.4 STATE-OF-THE-ART PERFORMANCES REVIEW OF HIGH-POWER LASER DIODES EMITTING AT 975NM

Recently, high-speed and high-power fiber lasers have emerged not only as a workhorse for information technology but also as a viable alternative to current generation of main-frame lasers for industrial and scientific applications [58]. Laser machining and processing of materials, e.g., welding, drilling and precision cutting, are among the most important conventional applications. High-power LDs emitting at 975nm are used in various fields [59]-[58]:

- Direct diode laser
- DPSS laser pumping
- Fiber laser pumping

- Graphic art and printing
- Illumination, night-adapted vision
- Material processing
- Medical and dental
- Micro plastic welding

Infrared laser pointer emitting at 975nm is widely used in night vision devices. Near infrared illumination allows observation of people or animals without being detected by an enemy or other people. Soldiers use 975nm IR laser for military and civilian purpose such as target acquisition, surveillance, night vision targeting goal surveillance, home safeguard and tracking etc. The fiber laser at 1,55 μ m, pumped by a LD at 975nm, can be used for telemetry, obstacle detection and drone driving. Moreover, it is a valuable optoelectronic countermeasure against rockets. All those applications can be accomplished using the Light Imaging, Detection, And Ranging (LIDAR) technology [60].

In a previous section of this chapter, we have introduced the different electro-optical parameters of a LD (η_E , I_{th} , R_S , WPE , α_i , η_i , J_{tr} , G_0 , T_0 , T_1) allowing to assess its performance. Now, it is interesting to make a review of state-of-the-art performances along the last twenty years. From *Figure I–16* to *Figure I–21* and an exhaustive evaluation of literature in the framework, we have reported the different values of the main electro-optical parameters over the years for LDs with 4mm cavity length and finally for comparison, values obtained with the different III-V lab technologies and devices are indicated ahead of time. Chapters II, III and IV will detail accurately the measurement procedures. In the next figures, different acronyms are used:

- F-P is a LD without spectral filtering layer (DFB or DBR).
- SQW stands for a LD with one single QW.
- DQW represents a LD with two QWs.
- Bragg_270/135/80 represents the Bragg order of the grating.

In *Figure I–16*, values of slope efficiency obtained over 20 years are reported. There is not a real tendency because the slope efficiency was quite high in particular due to Alphalight technology who reached 1W/A with a 4mm DQW F-P device since 1996. The FBH shows also a constant progression in the slope efficiency performance since 2007. The values obtained at III-V lab

(around 0,9-1 W/A) are in the range of the best ones published by FBH and n-Light (1,05-1,15 W/A).

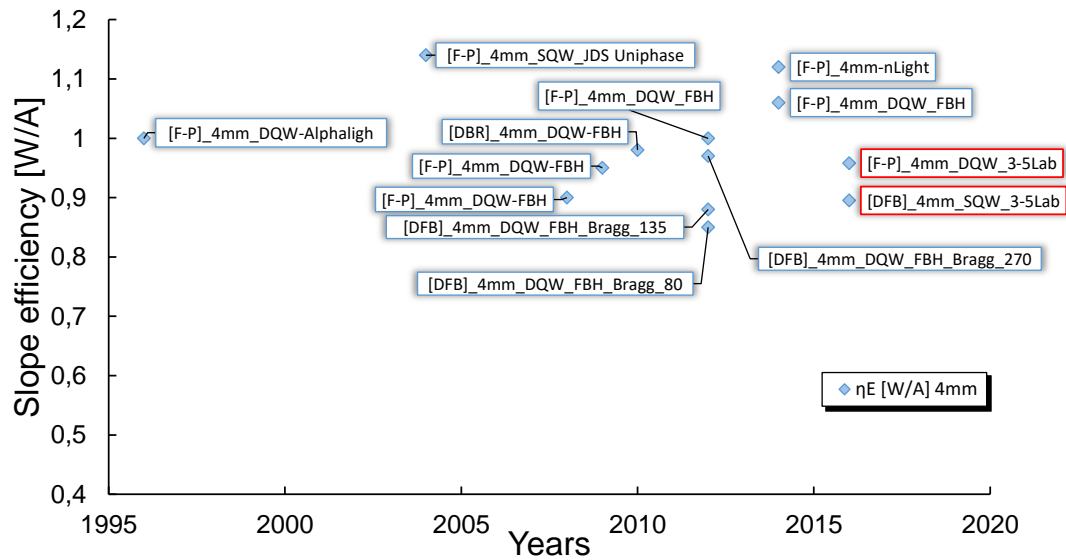


Figure I-16: Values of slope efficiency since 1995 extracted from [1]-[2]-[3]-[4]-[7]-[8]-[17]-[18]-[19]-[20]-[21]-[22]-[23]-[24]-[26]-[61].

Figure I-17 shows the values of the series resistance reported in literature and since 2005, one can see an incessant decrease. Undoubtedly, the constant improvements carried out by epitaxy and lithography processes have permitted to significantly reduce series resistance (> 70%) as well as Joule effect.

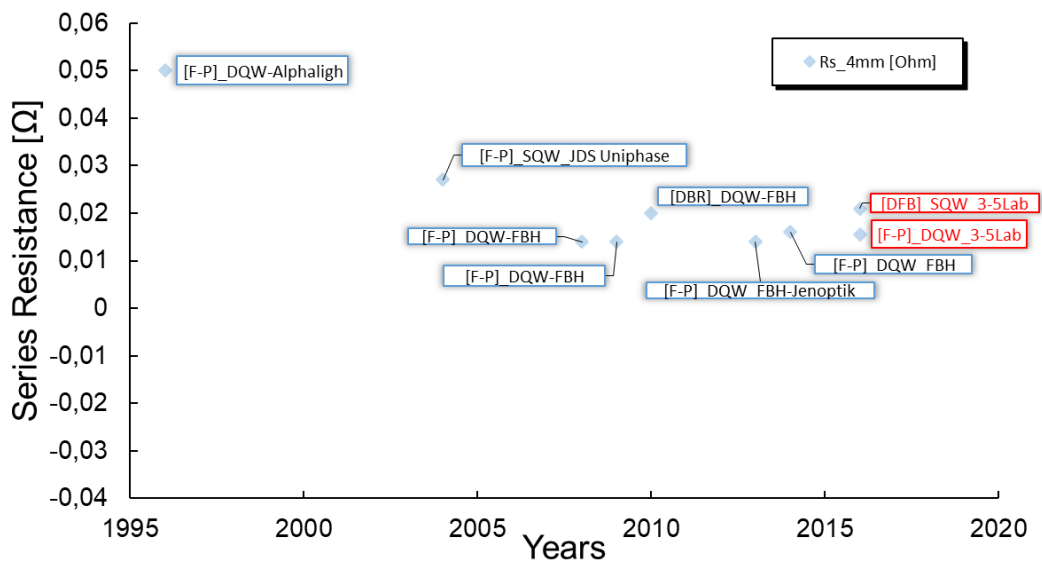


Figure I-17: Values of series resistance since 1995 extracted from [1]-[2]-[3]-[4]-[7]-[8]-[17]-[18]-[19]-[20]-[21]-[22]-[23]-[24]-[26]-[61].

Values displayed in *Figure I–18*, *Figure I–19* and *Figure I–20* are also of interest giving the main electro-optical parameters regularly characterized on LDs technology: threshold current, WPE and internal quantum efficiency. Usually a double QW structure should have (approximately) a threshold current density almost double respect to the single QW. Here, one can highlight the remarkable effort of the FBH. In particular, they have optimized the structure of a DQW F-P LD in order to obtain a threshold current density divided by two (300 A/cm^2 to 150 A/cm^2) in less than 5 years. This optimization lies in the in-situ lithography in order to avoid oxidation of Al layer. Because of the Al-free active area, the developed III-V lab structures are not affected by such a phenomenon.

Figure I–19 and *Figure I–20* demonstrate that the devices of III-V lab reach the WPE and internal quantum efficiency state-of-the-art values. Up to 2008, the WPE remains constant ranging from 55 to 65% whatever the technology considered, though we need to remind that an increase of few percent is worthy. Since 2010, higher values of WPE have been achieved with a world-record for FBH-JENOPTIK ($\sim 75\%$) in 2013. The FBH has worked on the performance increase of their DFB laser technology and, in a relatively short period, they obtained almost the same values of WPE (62-64%) for DFB (2 steps epitaxy) and F-P (1 step epitaxy) LDs. In contrast, the III-V lab devices reach rather lower values for F-P (58-59%) and DFB (56-57%) architectures. Regarding the internal quantum efficiency, clearly the III-V lab devices (DFB architecture) is one of the main leaders with 93%. Such values are mostly achieved by an ability to produce layers with a very low concentration of residual defects.

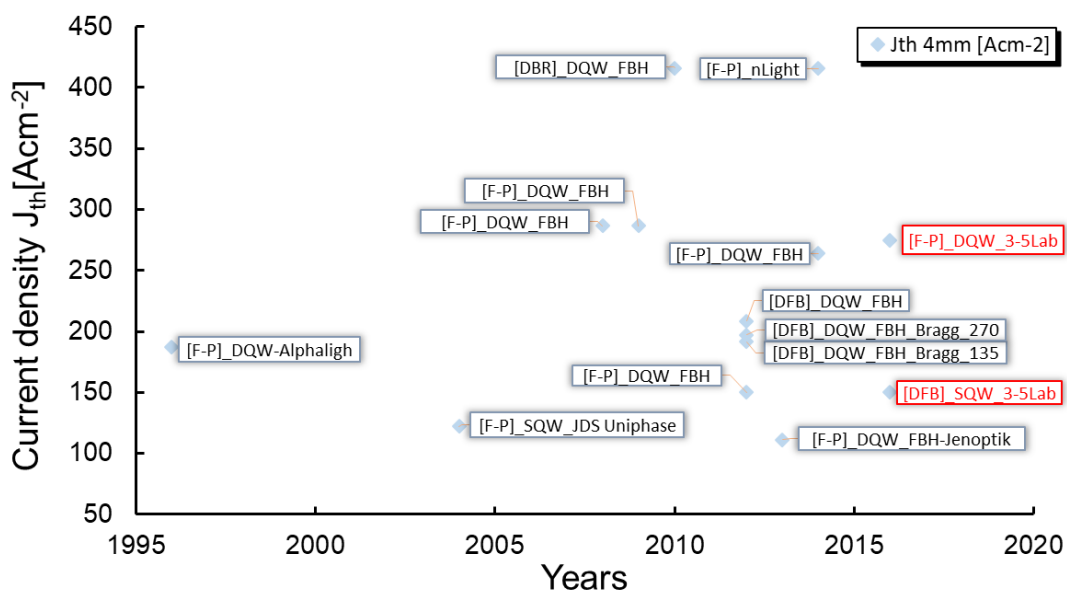


Figure I–18: Values of threshold current density since 1995 extracted from [1]-[2]-[3]-[4]-[7]-[8]-[17]-[18]- [19]- [20]-[21]-[22]-[23]-[24]-[26]-[61].

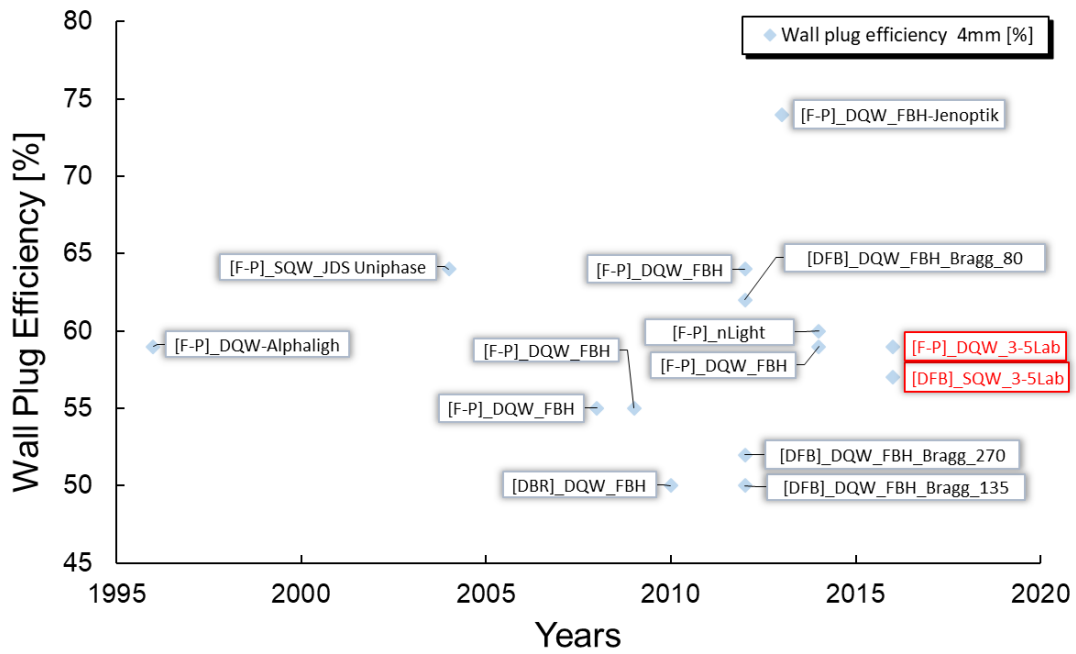


Figure I-19: Values of WPE since 1995 extracted from [1]-[2]-[3]-[4]-[7]-[8]-[17]-[18]- [19]-[20]-[21]-[22]-[23]-[24]-[26]-[61].

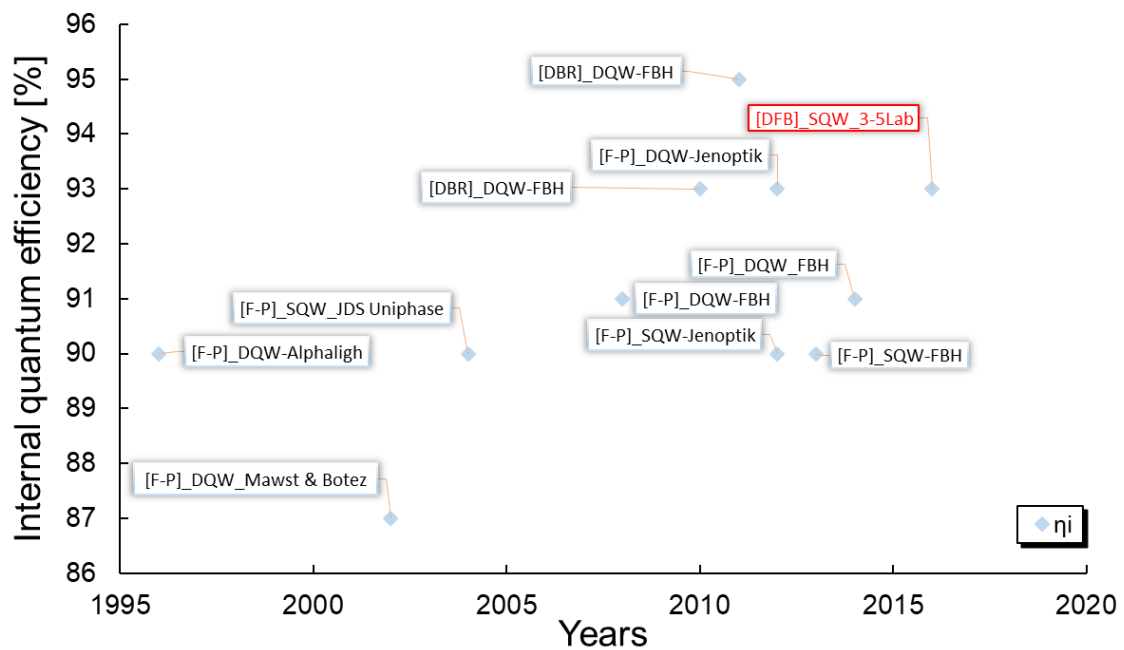


Figure I-20: Values of internal quantum efficiency since 1995 extracted from [1]-[2]-[3]-[4]-[7]-[8]-[17]-[18]- [19]-[20]-[21]-[22]-[23]-[24]-[26]-[61].

Characteristic temperatures are of great interest in particular to assess thermal sensitivity of LDs that finally affects their long-term reliability. Small values of T_0 indicate a larger dependence on temperature (see [Eq. I-25]). Because of huge technological improvements in particular addressing the differential quantum efficiency, values reported in *Figure I-21* show a quite linear decrease of T_1 since 1995 while in contrast the values of T_0 did not change drastically since this parameter is more dependent on the physical properties of the heterostructures that are well-mastered. One can see that the data obtained from the III-V lab devices show excellent results for the both characteristic temperatures ($> 200\text{K}$).

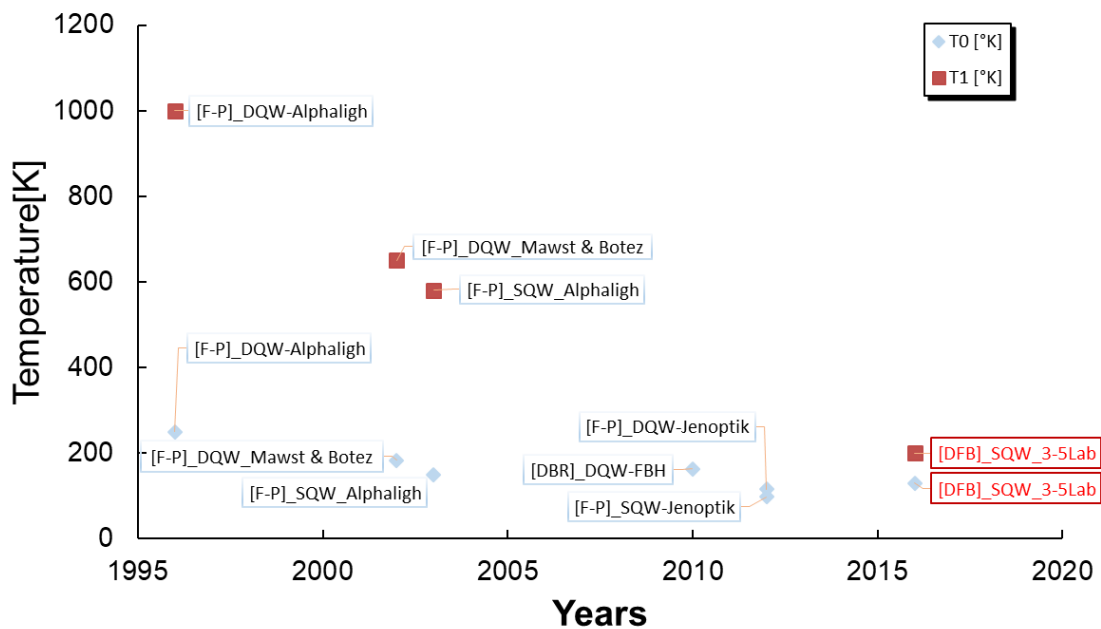


Figure I-21: Values of characteristic temperatures (T_0, T_1) extracted from [1]-[2]-[3]-[4]-[7]-[8]-[17]-[18]- [19]- [20]-[21]-[22]-[23]-[24]-[26]-[61].

1.5 MOTIVATION AND OBJECTIVES OF THE STUDY

This PhD study takes part of a **large project**, funded by the French ministry of defense (DGA), namely “LAFIP SOMUST” (**L**aser à **F**ibre **P**ulsé à base de **S**ource semi-conductrice **M**ultimode **S**Tabilisée en longueur d’onde). **The main goal of this project is to develop a pulsed fiber laser Er/Yb at 1,55 μm through an active collaboration between:**

- Thales Research and Technology (TRT),
- The III-V lab for the development of the pump source,

- The KEOPSYS company in charge of the integration of the pump source in the laser fiber at $1,55\mu\text{m}$.

Optical amplification technique by EDFA (Erbium-doped fiber amplifier) is based on the process of stimulated emission. *Figure I–22* shows the three lowest-lying energy levels of the Erbium ion in a silica matrix. A pump laser at 975 nm, excites the Erbium ions from the ground state to the level marked E_3 . The level E_3 is a short-lived level and the ions jump down to the level marked E_2 after a time lasting less than a microsecond. The lifetime of level E_2 is much larger and is about 12 ms. Hence, ions brought to the level E_2 stay there for a long time. Thus, by pumping hard enough, the population of ions in the level E_2 can be larger than the population of ions in the level E_1 and achieve a population inversion between the levels E_1 and E_2 . In such a situation, if a light beam at a frequency $\nu_0 = \frac{(E_2 - E_1)}{h}$ falls on the collection of Erbium ions, it will be amplified. For Erbium ions, the frequency ν_0 fits with the 1550nm band and then can be considered as an ideal amplifier for wavelengths in this window that is the lowest-loss window of silica-based optical fibers.

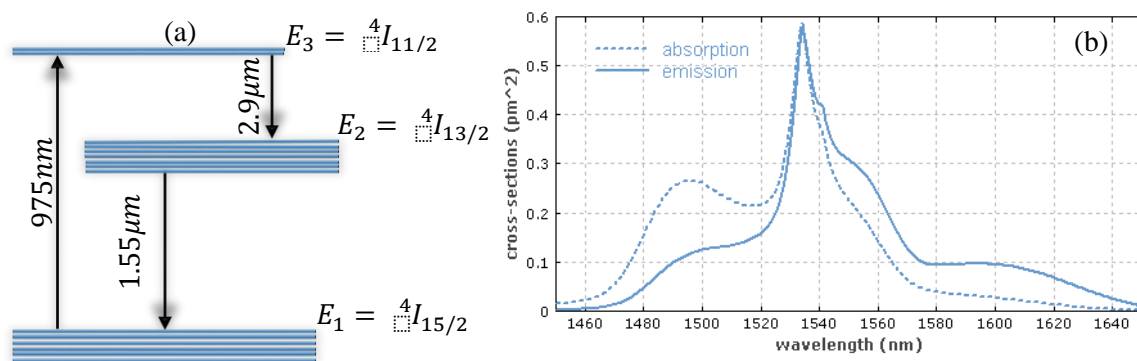


Figure I–22: (a) Energy level structure of the trivalent Erbium ion and the optical transition. (b) Absorption and emission cross-sections for Erbium ions [58].

Ytterbium (Yb)-doped fiber-based laser systems are currently the laser system chosen for the applications mentioned above. This is primarily due to their efficiency, broad gain bandwidth and operating wavelength near 1060nm (preferred for Nd: YAG lasers). *Figure I–23* shows the energy level diagram of Yb-doped silica fiber and the corresponding absorption and emission spectra. The laser transitions occur between the sub-levels of ${}^2F_{5/2}$ and ${}^2F_{7/2}$ states in Yb-doped silica. Ytterbium (Yb)-doped fiber has a very broad absorption and emission band and can be efficiently pumped by 915nm or 975nm wavelengths. Absorption at 975nm is stronger than at 915 nm, though its

bandwidth is comparatively narrow. As a result, relatively sophisticated temperature stabilization schemes are required for the pumping device (LD) emitting at 975nm.

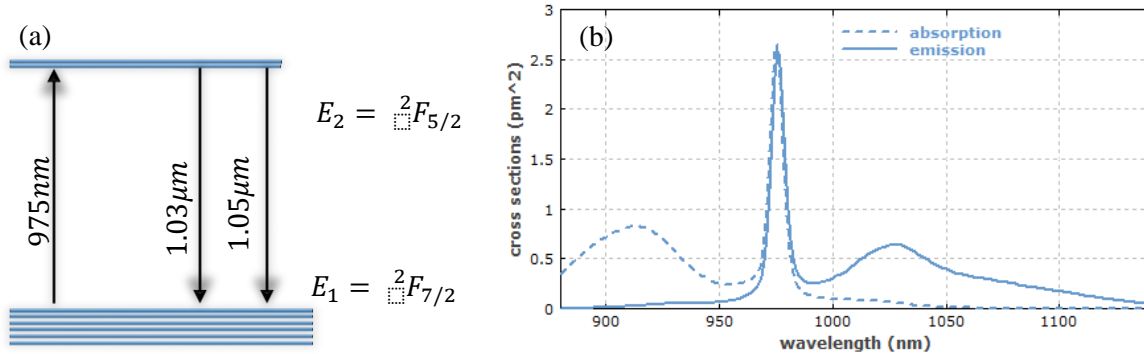


Figure I-23: (a) Energy level of Yb^{3+} in Yb:YAG and the usual pump and laser transition. (b) Absorption and emission cross sections of Ytterbium-doped germanosilicate glass, as used in the cores of Ytterbium-doped fiber [58].

Figure I-24 shows the general architecture of a fiber laser emitting at $1,55\mu\text{m}$. A seed laser combined with an amplifier forms a master oscillator power amplifier configuration. It is used for generating an output with high-power. The LD at 975nm pumps the fiber laser $\text{Er}^{3+}/\text{Yb}^{3+}$ in order to reach the highest level in terms of output optical power.

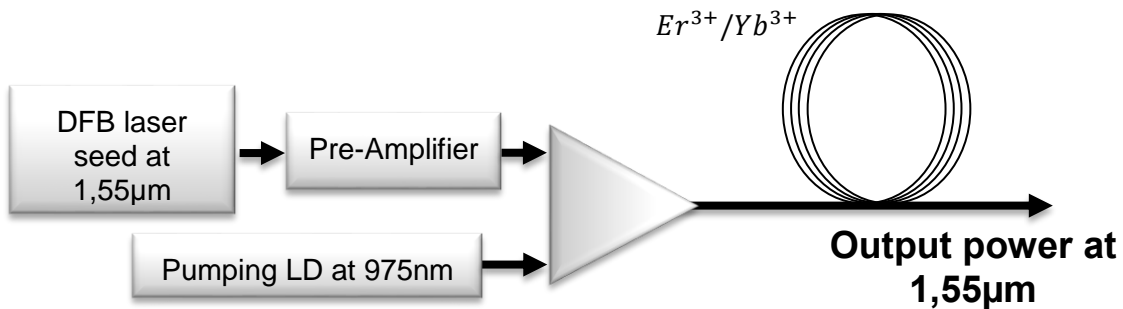


Figure I-24: General architecture of an Er/Yb fiber laser. The pumping LD is combined with a DFB laser seed into the Er/Yb fiber in order to obtain the highest output optical power at $1,55\mu\text{m}$.

A 10W pumping source operating in CW regime is mandatory for the development of this pulsed fiber laser delivering a pulsed peak optical power over 1KW at 25°C . But because of the narrow spectral absorption of Er/Yb fiber, Figure I-22(b), the pump source must have a narrow spectral width, typically $\Delta\lambda < 1\text{nm}$, with a thermally stabilized central wavelength of 975nm. At this wavelength, the absorption is three times bigger than at 915nm, hence the fiber length can be

reduced and consequently can avoid non-linear effects in the fiber. The fiber laser must operate without thermal regulation but a high level of WPE ($> 60\%$) is mandatory and a spectral stability is required for the pump source.

These requirements must be fully covered with a LD pump source including DFB grating and the expected specifications are the following:

- Optical power: $> 10W$
- Reliability: >10 years
- Emission wavelength: $975nm$
- Wall Plug Efficiency: $> 60\%$
- Spectral wavelength stabilized: $< 0,07nm/K$
- Spectral width at half height: $\Delta\lambda < 1nm$

The multimode 975nm Fabry Perot (F-P) LDs are still the best candidates as pumping sources for these applications and their wavelength stabilization as a function of temperature is now possible. However, the global market pressure drives the unit price down while maintaining high levels of performances and reliability, needing continuous improvement in terms of optical power output and differential quantum efficiency. Regarding intrinsic performances of the LDs, high optical power front facet output (10W for a 4mm cavity length) and high value of differential quantum efficiency ($\sim 0,9$) are now achievable particularly due to efforts carried out on reduction of internal losses and series resistance but above all on robustness of laser facet to well-known Catastrophic Optical Mirror Damage (COMD) failure. Nevertheless, due to temperature shifting, high-cost temperature stabilization setup or external wavelength-lock devices such as Volume Bragg Grating (VBG) are mandatory to maintain pumping efficiency and stability. In order to reduce such an additional high cost and the inconvenient use of external devices (i.e. multiple optical lenses) in particular for their sensitivity to mechanical disturbances, high power monolithically wavelength-stabilized lasers such as distributed Bragg reflector (DBR) and DFB lasers are today under investigations to achieve the best compromise between optical output power versus temperature drift.

Thermal resistance remains also a critical issue leading to a reduced junction temperature rise within the chip. This could be reduced up to 40% by an appropriate design of the laser chip and the use of epi-down bonding meaning that both the constant reduction of the thermal resistance (R_{th}) and thermal management optimization are also a concern especially for higher targeted optical output power such as 20W. Indeed, some Research Centers and Companies are currently on the way to

obtain reliable optical output power up to 20W delivered from a 100 μ m width stripe laser and especially enabled by an efficient heat transfer from the laser active region to the basic heat-spreading element. The extremely high density of heat sources inside the active layers of the heterostructure is still the fundamental item that must be considered. Indeed, when radiative recombination of injected carriers takes place, it is required to manage a heat density close to 3GW/cm³ and generated inside the active region for the same stripe laser width operating at 10W. Such an issue represents a record value for semiconductor optoelectronic devices and having in mind that extending the reliable optical power range up to 20W will be associated to a heat density elevation up to 10 GW/cm³ in the active region. Basically, thermal resistance represents one the most useful indicator of the thermal performance of such devices and intensive works have been conducted to decrease it from an appropriate design of the epitaxial chip process, the use of epi p-side down bonding and/or new solder materials. Furthermore, an erroneous thermal resistance measurement can lead to a wrong extraction of the junction temperature and accordingly an underestimated lifetime of the micro assembled device in operating conditions.

This PhD study aims to develop high-power DFB LDs with Al-free optical cavity enabling to fulfill the previous requirements, through a collaborative partnership **between III-V lab and the Laboratoire de l'Intégration du Matériau au Système (IMS) from the University of Bordeaux** which has a strong and well-established experience in reliability of optoelectronic and photonic technologies. Different technologies will be described and characterized through the next chapters specifically considering electrical, optical, thermal and thermomechanical aspects including:

- Three vertical structures derived from the well-established Large Optical Cavity (LOC).
- The developed process for the fabrication of a DFB grating layer in the vertical structure. Up to now, no results have been reported of high-power LDs with an Al-free active region including such a layer.
- The implementation of an optimized Non-Injected Mirror (NIM) window in order to push forward the Catastrophic Optical Damage (COD) threshold at the front facet of the LD.

We do believe that such a study represents a significant part of the general Design for Reliability (DfR) effort carried out to produce efficient and reliable high-power devices at the industrial level.

CONCLUSION

This chapter has introduced the general context, the motivation and the objectives of **this PhD study**. **Firstly**, a brief state-of-the-art of infrared LD technologies has been given and in particular the different vertical structures reported by the major research and industrial leaders in the field. The objective was to emphasize on the advantages bringing by the III-V lab technology regarding the other competitors. Indeed, most of the published works referred to high-power LDs with Al-based compounds composing the optical cavity. With this technology, reliability remains an issue since a faster aging process of the device has been observed due to Al oxidation. From literature, only the FBH has demonstrated reliable high-power LDs with a grating layer. The Reed Center has reported on performances obtained from LDs using Al-free structures but no data have been reported in grating layer implementation. **With this PhD study, we clearly aim to bring a step-forward in the realization of Al-free high-power LDs operating in a DFB mode and capable to reach at least 10W in CW regime with a Wall-Plug Efficiency (WPE) higher than 50%.**

General background on semiconductor Laser heterostructures and description of optical resonators including a distributed feedback structure (DFB) have been given in a **second part**. Indeed, the different electro-optical parameters and in particular related to DFB laser resonators have been presented and discussed. The high-power LD with a ridge of $90\mu\text{m}$ has a typical spectral width higher than 3nm but regarding the application, the spectral width must be lower than 1nm . Moreover, for a F-P LD, the detuning of the spectrum as a function of temperature is in the range of $0,5\text{nm}/^\circ\text{C}$. For these reasons, the integration of an optical grating into the resonator is necessary allowing to reach less than $0,1\text{nm}/^\circ\text{C}$. The different technological parameters have been presented and the coupling factor as well as the reduction factor (depending on the geometry of the grating) are crucial parameters since directly related to the vertical single mode selectivity. The main electro-optical parameters have been also stated for a high-power LD. We demonstrated that the output optical power and the Wall-Plug Efficiency (WPE) are related to internal quantum efficiency (at the first order) depending on physical effects that play a major role in performance drift (carriers recombination, current spreading, non-uniform optical field, non-radiative centers). The maximum output power can be also limited by the temperature rise of the active region, well-known as the thermal “roll-over” phenomenon. Excessive heat generation by ohmic heating leads to a significant temperature rise in the active region resulting in carrier spreading, significant gain reduction and an increase in non-radiative recombination. Moreover, important parameters of LDs deal with the

series resistance (R_s) and a power-dependent limiting process resulting in the occurrence of two well-known failure modes: Catastrophic Optical Damage (COD) or Catastrophic Optical Mirror Damage (COMD). The power threshold decreases as the Al concentration in the active region increases that is due to an enhanced sensitivity to oxidation of the Al-containing active region. Thus, different trade-offs need to be considered for the optimal design (geometry of the cavity, confinement factor...) of high-power LDs ensuring to push back their COD limit and increase as far as possible their operating lifetime.

A last **section** addresses a brief overview of the LDs global market and in particular, a state-of-the-art performances review of high-power LDs emitting at 975nm is given over the last 20 years. From an exhaustive evaluation of the literature, we have reported the different values of the main electro-optical parameters over the year only for LDs with 4mm cavity length and for comparison, the values obtained with the different III-V lab devices are also indicated ahead of time.

This PhD study takes part of a large project, funded by the French ministry of defense (DGA). A 10W pumping source operating in CW regime is mandatory for the development of this pulsed fiber laser Er/Yb at 1,55 μ m delivering a pulsed peak optical power over 1KW at 25°C. But because of the narrow spectral absorption of Er/Yb fiber, the pump source must have a narrow spectral width with a thermally stabilized central wavelength of 975nm. At this wavelength, the absorption is three times bigger than at 915nm, hence the fiber length can be reduced and consequently can avoid non-linear effects in the fiber. The fiber laser must operate without thermal regulation but a high level of WPE (> 60%) is mandatory and a spectral stability is required for the pump source. Regarding the targeted application, it is demonstrated that most of the requirements must be fully covered with a LD pump source including DFB grating and the expected specifications are summarized below:

- $P_{OUT} : > 10W$ (CW regime)
- Lifetime : >10 years
- Emission wavelength = 975nm
- WPE : > 60%
- Spectral wavelength stabilized : < 0,07nm/K
- $\Delta\lambda < 1nm$ @ FWHM

The next chapters will present the structure of the devices developed and optimized with the help of analytical and FEM models, their electro-optical characterization and finally, phenomenological analysis regarding their thermal and thermomechanical behavior.

CHAPTER I REFERENCES:

- [1] L. J. Mawst, A. Bhattacharya, J. Lopez, and D. Botez, D. Z. Garbuzov, L. DeMarco, and J. C. Connolly, M. Jansen, F. Fang, and R. F. Nabiev, “8 W continuous wave front-facet power from broad-waveguide,” *Applied Physics Letters*, vol. 69, no. 11, pp. 1532–1534, 1996.
- [2] J. J. Lee, L. J. Mawst, and D. Botez, “Asymmetric Broad Waveguide Diode Lasers ($\lambda = 980$ nm) of Large Equivalent Transverse Spot Size and Low Temperature Sensitivity,” *IEEE Photonics Technology Letters*, vol. 14, no. 8, pp. 1046–1048, 2002.
- [3] M. Kanskar, M. Nesnidal, S. Meassick, A. Goulakov, E. Stiers, Z. Dai, T. Earles D.Forbes, D. Hansen, P. Corbett, L. Zhang, T. Goodnough, L. LeClair, N. Holehouse, D. Botez and L.J. Mawst, “Performance and Reliability of ARROW Single Mode & 100 μ m Laser Diode and the Use of NAM in Al-free Lasers,” *SPIE proceedings Novels in-plane semiconductor lasers II*, vol. 4995, pp. 196–208, 2003.
- [4] M. Kanskar, Y. He, J. Cai, C. Galstad, S.H. Macomber, E. Stiers, D. Botez and L.J. Mawst, “53% wallplug efficiency 975 nm distributed feedback broad area laser,” *Electronics Letters*, vol. 42, no. 25, 2006.
- [5] A. Al-Muhanna, L. J. Mawst, D. Botez, D. Z. Garbuzov, R. U. Martinelli, and J. C. Connolly, “High-power (>10 W) continuous-wave operation from 100- μ m-aperture 0.97- μ m-emitting Al-free diode lasers”, *Applied Physics Letters*, vol. 73, no. 9, pp. 1182–1184, 1998.
- [6] V. Rossin, E. Zucker, M. Peters, M. Everett, and B. Acklin, “High power High efficiency 910-980 nm broad area laser diodes,” in *SPIE proceedings High power Laser Technology and applications*, vol. 5336, pp. 196–203, 2004.
- [7] K. Kosiel, J. Muszalski, A. Szerling, and M. Bugajski, “High power (>1 W) room-temperature (300 K) 980 nm continuous-wave AlGaAs/InGaAs/GaAs semiconductor lasers,” *Optica Applicata*, vol. 37, no. 4, pp. 423–431, 2007.
- [8] M. Zorn, R. Hülsewede, O. Hirsekorn, J. Sebastian, and P. Hennig, “High-Power single emitters and Diode Laser bars with improved performance developed at Jenoptik,” in *SPIE proceedings High power diode laser Technology and applications X*, vol. 824, 2012.
- [9] G. Erbert, F. Bugge, A. Knauer, J. Sebastian, K. Vogel, and M. Weyers, “High power diode lasers based on InGaAsP spacer- and waveguide-layers with AlGaAs cladding layer,” in *SPIE proceedings*, vol. 2683, pp. 136–145, 1996.
- [10] G. Erbert, G. Beister, A. Knauer, J. Maege, W. Pittroff, P. Ressel, J. Sebastian, R. Staske, H. Wenzel, M. Weyers, and G. Tränkle, “Al-free 950nm BA diode lasers with high efficiency and reliability at 50°C ambient temperature,” in *Laser Diodes and LEDs in Industrial, Measurement, Imaging, and Sensors Applications II; Testing, Packaging, and Reliability of Semiconductor Lasers V*, vol. 3945, pp. 301–307, 2000.
- [11] W. Pitroff, G. Erbert, G. Beister, F. Bugge, A. Klein, A. Knauer, J. Maege, P. Ressel, J. Sebastian, R. Staske, G. Traenkle, “Mounting of high power laser diodes on boron Nitride Heat Sinks Using an Optimized Au/Sn Metallurgy,” in *IEEE Transactions on Advanced Packaging*, vol. 24, pp. 4, 2001.
- [12] H. Wenzel, A. Klehr, M. Braun, F. Bugge, G. Erbert, J. Fricke, A. Knauer, P. Ressel, B. Sumpf, M. Weyers and G. Tränkle, “Design and realization of high-power DFB lasers,” in *Physics and applications of optoelectronic devices*, vol. 5594, pp. 110–123, 2004.
- [13] K. Paschke, B. Sumpf, F. Dittmar, G. Erbert, J. Fricke, A. Knauer, S. Schwertfeger, H. Wenzel, G. Tränkle, “Nearly-diffraction limited 980nm tapered diode lasers with an output power of 6.7 W,” in *Semiconductor Laser Conference*, vol. 1, pp. 43–44, 2004.
- [14] G. Erbert, “High power diode laser – physics and technology of key elements for modern laser applications,” in *Óptica Pura y Aplicada*, vol. 28, pp. 3, 2005.
- [15] M. Weyers, “GaAs-based high power laser diodes,” in *GaAs-based high power laser diodes*, vol. 1, pp. 273–278, 2005.

- [16] H. Wenzel, J. Fricke, A. Klehr, A. Knauer, and G. Erbert, “High-Power 980-nm DFB RW Lasers With a narrow vertical far field,” in *IEEE Photonics Technology Letters*, vol. 18, no. 6, pp. 737–740, 2006.
- [17] K. Paschke, S. Einfeldt, A. Ginolas, K. Häusler, P. Ressel, B. Sumpf, H. Wenzel, G. Erbert, “15-W reliable operation of 96- μm aperture broad-area diode lasers emitting at 980 nm,” in *Lasers and Electro-Optics/Quantum Electronics and Laser Science Conference and Photonic Application System Technologies*, vol. CMN4, 2008.
- [18] P. Crump, G. Blume, K. Paschke, R. Staske, A. Pietrzak, U. Zeimer, S. Einfeldt, A. Ginolas, F. Bugge, K. Häusler, P. Ressel, H. Wenzel, and G. Erbert, “20W continuous wave reliable operation of 980nm broad-area single emitter diode lasers with an aperture of 96 μm ,” in *High-Power diode laser technology applied VII*, vol. 7198, no. 14, pp. 9, 2009.
- [19] J. Fricke, A. Ginolas, F. Bugge W. John, A. Klehr, M. Matalla, P. Ressel, H. Wenzel, and G. Erbert, “High-Power 980 nm Broad Area Laser Spectrally Stabilized by Surface Bragg Gratings,” in *IEEE Photonics Technology Letters*, vol. 22, no. 5, pp. 284–286, 2010.
- [20] C. M. Schultz, P. Crump, H. Wenzel, O. Brox, A. Maaßdorf, G. Erbert and G. Trankle., “11W broad area 976 nm DFB lasers with 58% power conversion efficiency,” in *Electronics Letters*, vol. 46, no. 8, pp. 580–581, 2010.
- [21] P. Crump, C. M. Schultz, H. Wenzel, S. Knigge, O. Brox, A. Maaßdorf, F. Bugge and G. Erbert, “Reliable operation of 976nm High Power DFB Broad Area Diode Lasers with over 60% Power Conversion Efficiency,” in *SPIE proceedings Novel in-plane semiconductor lasers X*, vol. 7953, pp. 1, 2011.
- [22] A. Maaßdorf, C.M. Schultz, O. Brox, H. Wenzel, P. Crump, F. Bugge, A. Mogilatenko, G. Erbert, M. Weyers, G. Trankle, “In-situ etching of patterned GaAs/InGaP surfaces for highly efficient 975nm DFB – BA diode lasers,” in *Journal of Crystal Growth*, vol. 370, pp. 226–229, 2012.
- [23] J. Fricke, H. Wenzel, F. Bugge, O. P. Brox, A. Ginolas, W. John, P. Ressel, L. Weixelbaum, G. Erbert, “High-Power Distributed Feedback Lasers With Surface Gratings,” in *IEEE Photonics Technology Letters*, vol. 24, no. 16, pp. 1443–1445, 2012.
- [24] P. Crump, J. Fricke, C. M. Schultz, H. Wenzel, S. Knigge, O. Brox, A. Maaßdorf, F. Bugge and G. Erbert , “10W-reliable 90 μm -wide broad area lasers with internal grating stabilization,” in *SPIE proceedings High-Power diode laser technology and applications X*, vol. 8241, pp. 10, 2012.
- [25] P. Crump, H. Wenzel, G. Erbert, and G. Trankle, “Progress in increasing the maximum achievable output power of broad area diode lasers,” in *SPIE proceedings High-Power diode laser technology and applications X*, vol. 8241, pp. 1, 2012.
- [26] A. Pietrzak, R. Hülsewede, M. Zorn, O. Hirsekorn, J. Sebastian, J. Meusel, P. Hennig, P. Crump, H. Wenzel, S. Knigge, A. Maaßdorf, F. Bugge, G. Erbert, “Progress in efficiency-optimized high-power diode lasers,” in *SPIE proceedings Technologies for optical countermeasures X and High power lasers*, 2013, vol. 8898, pp. 08–22.
- [27] P. Crump, G. Erbert, H. Wenzel, C. Frevert, C. M. Schultz, K. H. Hasler, R. Staske, B. Sumpf, A. Maaßdorf, F. Bugge, S. Knigge, G. Trankle , “Efficient High Power Laser Diodes,” *IEEE Journal of Quantum Electronics*, vol. 19, no. 4, 2013.
- [28] K. H. Hasler, H Wenzel, P Crump, S Knigge, A Maasdorf, R Platz, R Staske and G Erbert, “Comparative theoretical and experimental studies of two designs of high-power diode lasers,” *Semiconductor Science and Technology*, vol. 29, no. 045010, pp. 01–06, 2014.
- [29] P. Crump, J. Decker, M. Winterfeldt, J. Fricke, A. Maaßdorf, G. Erbert and G. Tränkle, “Development of high power diode lasers with beam parameter product below 2 mm \times mrاد within the BRIDLE project,” in *SPIE proceedings High-power diode laser technology and applications XIII*, vol. 9348, pp. 9348D1-9348D1, 2015.

- [30] P. Crump, M. Winterfeldt, J. Decker, M. Ekterai, J. Fricke, A. Maaßdorf, G. Erbert and G. Tränkle , “Limitations to brightness in high power laser diodes,” in *IEEE Photonics conference*, vol. 1, pp. 553–554, 2015.
- [31] J. Decker, P. Crump, J. Fricke, A. Maaßdorf, M. Traub, U. Witte, T. Brand, A. Unger, G. Erbert, and G. Tränkle, “25-W Monolithic Spectrally Stabilized 975-nm Minibars for Dense Spectral Beam Combining,” *IEEE Photonics Technology letters*, vol. 27, no. 15, pp. 1675–1678, 2015.
- [32] H. Wenzel, J. Fricke, J. Decker, P. Crump, G. Erbert, “High-Power Distributed Feedback Lasers With Surface Gratings Theory and Experiment,” *IEEE Journal of Quantum Electronics*, vol. 21, no. 6, pp. 1–8, 2015.
- [33] M. Ott, “Capabilities and Reliability of LEDs and Laser Diodes,” in *Capabilities and Reliabilities of LEDs Laser Diodes*, vol. Internal NASA Parts and Packaging Publication, pp. 1–7, 1996.
- [34] J. Buus, M.-C. Amann, and D. J. Blumenthal, *Tunable Laser Diodes and Related Optical Sources*, 2nd Edition. A John Wiley & Sons, Inc., Publication, 2005.
- [35] I. A. Zhores, “Nobel Lecture: The double heterostructure concept and its applications in physics, electronics, and technology,” in *Review of Modern Physics*, vol. 73, pp. 767–782, 2001.
- [36] E. Rosencher, B. Vinter, and P. G. Piva, “Quantum well laser diodes,” in *Optoelectronics*, Cambridge University press, pp. 637–652, 2004.
- [37] L. A. Coldren, S. W. Corzine, and M. L. Mashanovitch, *Diode lasers and photonic integrated circuits*, 2nd Edition. A Wiley-Interscience publication, 2012.
- [38] M. Fallahi and R. Bedford, “Gain–current relations,” in *Semiconductor lasers: Fundamentals and application*, 2nd Edition, Woodhead, pp. 33, 2013.
- [39] L. A. Coldren, S. W. Corzine, and M. L. Mashanovitch, “Active materials and their characteristics in Gain and current relations,” in *Diode lasers and photonic integrated circuits*, 2nd Edition, A Wiley-Interscience publication, pp. 218–240, 2012.
- [40] A. Y. Cho, “Advances in molecular beam epitaxy (MBE),” in *Journal of Crystal Growth*, vol. 111, no. 1, pp. 1–13, 1991.
- [41] P. Dasté, Y. Miyake, M. Cao, Y. Miyamoto, S. Arai, Y. Suematsu, K. Furuya, “Fabrication technique for GaInAsP/InP quantum wire structure by LP-MOVPE,” in *Journal of Crystal Growth*, vol. 93, no. 1–4, pp. 365–369, 1988.
- [42] P. Unger, “Introduction to Power Diode Lasers,” in *High-Power Diode Lasers. Fundamentals, Technology, Applications*, Roland Diehl, vol. 78, Springer-Verlag Berlin Heidelberg, pp. 420, 2000.
- [43] M. Nakamura, A. Yariv, H. W. Yen, S. Somekh, and H. L. Garvin, “Optically pumped GaAs surface laser with corrugation feedback,” in *Applied Physics Letters*, vol. 22, no. 10, pp. 515–516, 1973.
- [44] R. Mostallino, M. Garcia, Y. Deshayes, A. Larrue, Y. Robert, E. Vinet, L. Bechou, M. Lecomte, O. Parillaud, M. Krakowski, “Thermal investigation on high power DFB broad area lasers at 975nm, with 60% efficiency,” in *SPIE proceedings High-Power Diode Laser Technology and Applications XIV*, vol. 9733, 2016.
- [45] P. Crump, O. Brox, F. Bugge, J. Fricke, C. Schultz, M. Spreemann, B. Sumpf, H. Wenzel, G. Erbert, “High-Power, High-efficiency Monolithic edge-emitting GaAs-Based lasers with narrow spectral widths,” in *Advances in semiconductor lasers*, Academic press publication, 2012.
- [46] J. Buus, M.-C. Amann, and D. J. Blumenthal, “Single-mode laser diode,” in *Tunable Laser Diodes and Related Optical Sources*, 2nd Edition, A John Wiley & Sons, Inc. Publication, 2005.
- [47] M. Takahiro, “Optical Resonators,” in *Fundamentals of semiconductor Laser*, 2nd Edition, William T. Rhodes, pp. 40, 2015.

- [48] J. Piprek, “Edge-emitting laser,” in *Semiconductor Optoelectronic devices Introduction to physics and simulation*, Academic press publication, pp. 151–169, 2003.
 - [49] E. Farsad, S. P. Abbasi, A. Goodarzi, and S. Zabihi, “Experimental Parametric Investigation of Temperature Effects on 60W-QCW Diode Laser,” in *Journal of Electronics Communications Engineering*, vol. 5, no. 11, pp. 1467–1472, 2011.
 - [50] G. Erbert, A. Barwolff, J. Sebastian, and J. Tomm, “High power Broad area diode laser and laser bars,” in *High-Power Diode Lasers*, vol. 78, Springer Berlin Heidelberg, pp. 173–223, 2000.
 - [51] M. Fallahi and R. Bedford, “High-power semiconductor lasers,” in *Semiconductor lasers: Fundamentals and application*, 2nd Edition, Woodhead, p. 662, 2013.
 - [52] M. Fukuda, *Reliability and Degradation of Semiconductor Lasers and LEDs*, 1st ed., vol. 1. Artech House, 1991.
 - [53] D. Botez, “Design considerations and analytical approximations for high continuous wave power, broad-waveguide diode lasers,” in *Applied Physics Letters*, vol. 74, no. 21, pp. 3102–3104, 1998.
 - [54] G. Bonati, “Prospects for the diode laser market: from science to coveyers,” *Wiley Blackwell (John Wiley & Sons)*, vol. 7, no. 2, pp. 37–40, 2010.
 - [55] “Annual laser market review & forecast; can laser market trump a global slowdown?,” in *www.laserfocusworld.com*, vol. 52, no. 01, pp. 01–08, 2016.
 - [56] B. Martin, G. Erbert, M. Reinhard, B. Konstantin, T. Jens W., and K. Mark, “High-Power Diode Laser: Fundamentals, Technology, Application,” in *High-Power diode lasers*, Springer/Verlag., vol. 128, pp. 5–74, 2007.
 - [57] C. Lee, “European laser ecosystem 9 March 2015.” EPIC, 2015.
 - [58] D. F. Welch, “A Brief History of High-Power Semiconductor Lasers,” in *IEEE Journal of Quantum Electronics*, vol. 6, no. 6, pp. 1470–1477, 2000.
 - [59] G. Romanos and G. H. Nentwig, “Diode Laser (980 nm) in Oral and Maxillofacial Surgical Procedures: Clinical Observations Based on Clinical Applications,” in *Journal of Clinics Laser Medical Surgery*, vol. 17, no. 5, pp. 193–197, 1999.
 - [60] S. Wei, F. Qiang, Z. Xiushan, R.A. Norwood, N. Peyghambarian, “Fiber lasers and their applications,” in *Applied Optics*, vol. 53, no. 28, pp. 6554–6568, 2014.
 - [61] V. Rossin, E. Zucker, M. Peters, M. Everett, and B. Acklin, “High power High efficiency 910-980 nm Broad area laser diodes,” in *SPIE proceedings High power laser technology and applications*, vol. 5336, pp. 27–35, 2004.
-

CHAPTER II

DESCRIPTION OF THE VERTICAL STRUCTURES AND ASSESSMENT OF ELECTRO-OPTICAL PERFORMANCES

INTRODUCTION

The main goal of this PhD work is to develop a high-power Er/Yb-doped fiber laser and the key part of such a laser consists in the pump source and we demonstrate that the best choice is a LD emitting at 975nm. **The general objective of this chapter** lies in the technological description of the proposed LDs and the results of electrical and optical characterizations to determine their main intrinsic performances. This chapter is divided into three main parts. **An opening section** describes and compares the three vertical structures developed at III-V lab from a technological point of view, namely Large Optical Cavity (LOC), Super Large Optical Cavity (SLOC) and Asymmetric Optical Cavity (AOC). These structures have been particularly studied and analyzed regarding their specific properties: optical confinement, far field divergence, DFB coupling factor, optical losses and spectral width using optical simulations via FIMMWAVE® tools. Though the Non-injected Mirror (NIM) structure with a current block layer near the mirror has been already proposed for ultra-reliable laser diodes used for high-rate and long-haul telecommunication applications, its effects are discussed by considering the impact of length variations and vertical position, aiming an optimal implementation for this high-power LD technology.

A second section deals with the complete description of the vertical structure fabrication process including in particular the core emissive structure, the patterning of the grating with the e-beam technique and the facets coating preventing from the well-established failure mode (COD) occurring in laser diodes at high output power. The device mounting process is also detailed representing a key step to optimize the heat flow across the whole device that depends on the overall thermal resistance and its thermal management allowing to reduce the junction temperature.

Finally, a **third section** is devoted to the electrical and optical characterizations based on the measurement of the L-I-V curves in pulsed and CW regimes enabling to extract the internal parameters for each vertical structure and compared with simulation results. Our characterizations also address the wall-plug efficiency, the far field and vertical divergence playing a significant role in the coupling efficiency during the beam collimation as well as the spectral properties. Particularly the spectral width and the temperature stability of the wavelength achieved with a DFB LD are identified as crucial parameters to reach the performances required by the targeted application.

2.1 DESCRIPTION AND COMPARISON OF THE III-V LAB VERTICAL LASER STRUCTURES

The III-V lab has a strong experience in the development of high-power LDs and some highlights have been already reported in different papers published since 2009 [1], [2]. Thanks to our knowledge on both performances, robustness and failure analysis, design for reliability rules are of interest starting from the fabrication of the LD since this last takes positive feedback from characterization to epitaxial process improvement and a particular attention must be paid to reliability since the early steps of the chip fabrication and development. Basis of high reliability must integrate level of design, technological choices, process control and physical modelling of failure mechanisms; one of the goals being to guarantee failure distributions as tightened as possible at the end of the lifetime. In the next sections, three specific vertical structures are investigated and advantages and drawbacks are stated for each of them. The considered structures are grown in one (for F-P LD) or two (for DFB LD) steps using a metal-organic vapor phase epitaxy (MOVPE) on 2" GaAs wafers. *Figure II-1* shows the overall structure of the LD that is based on the edge double trench planar structure. After the epitaxy grown, the LD is then processed using standard techniques with a 90 μm wide strip.

- Metal
- Oxyde
- [P] Contact GaAs
- [P] Cladding AlGaAs
- [P] Grating GaInAsP
- [P] Spacer GaInP
- [P] Optical cavity GaInAsP
- QW GaInAs
- [N] Optical cavity GaInAsP
- [N] Cladding AlGaAs
- [N] Substrate GaAs

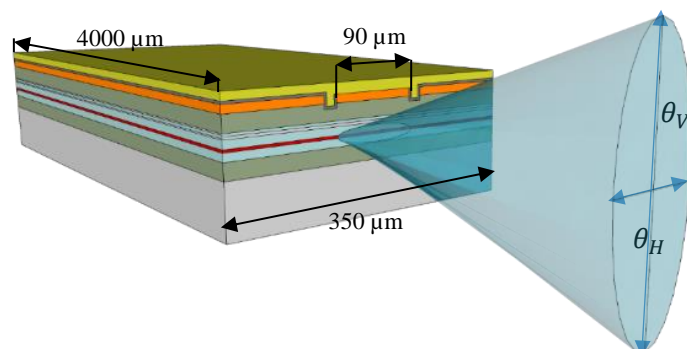


Figure II-1: Generic vertical structure of the LD showing the different layers obtained by epitaxy.

The vertical structure for high-power LDs must fulfill contradictory requirements expecting to reach a final compromise. Indeed, a low series resistance is necessary to avoid Joule effect, meaning that high doping levels are necessary for all the layers in the vertical structure. However, ideally, the internal losses by free carrier absorption must be lowered as possible leading to a low doping profile especially on the p-side and at least in the area where the optical field is confined (GaInAsP layer). Therefore, the design of high-power LDs emitting at 975nm must address the following main issues:

- Such high-power LDs aim to be used as a reliable pump source for Er/Yb optical fiber laser. Hence, the coupling factor between the LD and such a fiber source must be taken into consideration during the development.
- The maximum absorption spectrum peak of the Er/Yb optical fiber is centered at 975nm with a bandwidth of $\Delta\lambda \approx 3nm$. Therefore, the pump source must have an emission wavelength at 975nm with low $\Delta\lambda$ and a strong wavelength stabilization as a function of temperature. For that, a DFB structure is proposed.

To implement a DFB-based LD vertical structure, we will particularly investigate on the coupling factor of the grating that represents a key issue. Moreover, we will analyze the influence of the grooves depth (used to define the emissive central ridge of the index guided LD) at each side of the stripe (see *Figure II-2*) and its consequence on the confinement of the optical modes as well as the coupling factor.

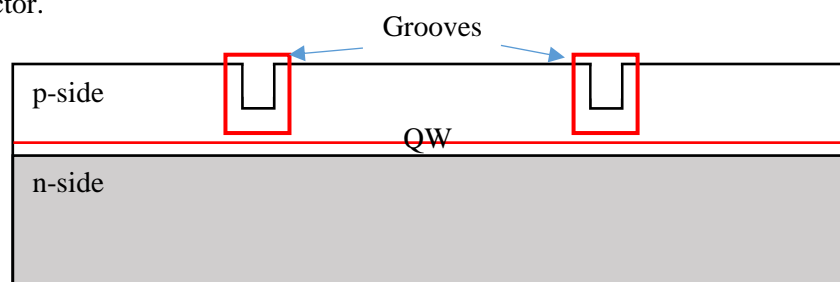


Figure II-2: Front facet cross section view of the LD. The emissive zone is in the middle of the two grooves.

The next sections will detail the III-V lab vertical structures that are derived from an “Al-free” optical cavity highlighting several advantages compared to the well-known GaAs/AlGaAs structure [3] given below:

- the low reactivity of InGaP to oxygen facilitates regrowth for the fabrication of index-guided structures,

- an higher electrical and thermal conductivity compared with AlGaAs, that can improve reliability by pushing up the COD threshold [3].

The first considered LD vertical structure corresponds to the Large Optical Cavity (LOC) that represents the first step in the high-power LD development. As a higher optical confinement is required, then we focused on the Super Large Optical Cavity (SLOC) vertical structure and finally the Asymmetrical Optical Cavity (AOC) vertical structure representing the last achievement of our study. This last vertical structure allows obtaining a high optical confinement while maintaining the lowest series resistance compared to other vertical structures processed by the competitors of III-V lab: FBH, JDS Uniphase and IET.

2.1.1 Optical simulations: FIMMWAVE® tool capabilities, material properties and main results

Optical properties of the three LDs vertical structures have been investigated using the software FIMMWAVE® tool that uses the well-known approximate method of effective index mode solver [4]. This method is a fast and reliable way to determine estimates for the guided optical modes, where the waveguide refractive index cross-section can be well approximated by the expression: $n_{eff} = f(x)g(y)$.

Figure II-3 represents the 1D refractive index variations of a waveguide where W and h are the width of the central ridge strip and the depth of each groove around this last respectively. It is assumed that the optical wave propagates along the z direction.

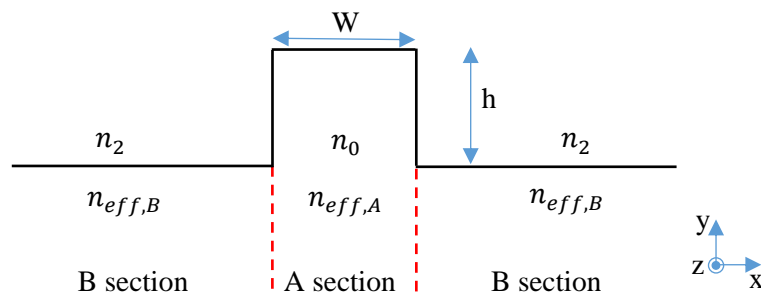


Figure II-3: Method of effective index solver basically applied to a waveguide.

When the “ h ” dimension increases, the evanescent field is reduced in the lateral sections (B). Hence, the effective index in these sections decreases. Because of the lower confinement factor of the modes in the lateral sections, the effective index of the modes on the left and right sides of the ridge are also reduced.

In this case and using the method of effective modes, the solver of FIMMWAVE® calculates the electrical field distribution along the x direction. From this distribution, it is possible to calculate the effective index in the A section and the waveguide structure namely $n_{eff}(x)$. Then, the solver finds the results for 1D+z, which corresponds to the entire waveguide. Using FIMMWAVE®, it is possible to simulate the 2D cross-section of the LD as shown in *Figure II-4*.

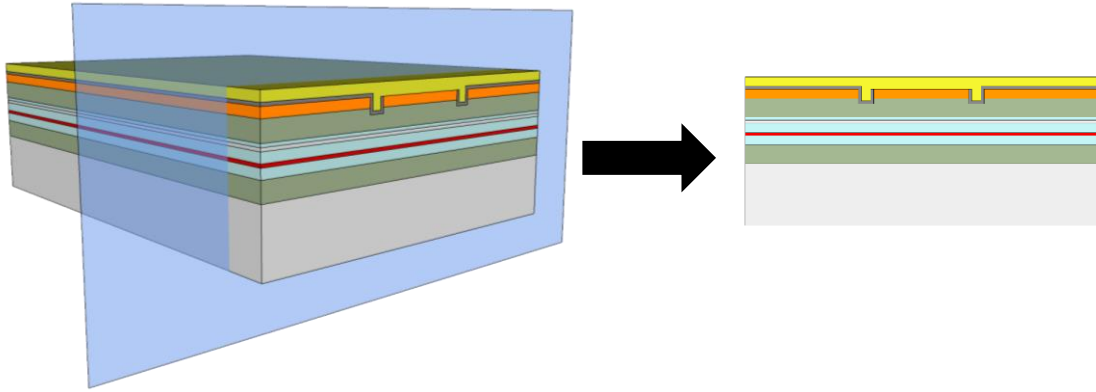


Figure II-4: Cross-section view of the device considered in FIMMWAVE® (the blue plane) to predict the 2D index profile variations.

With such optical simulations, we can study the properties of the DFB vertical structure. It is possible to predict the theoretical coupling factor and the spectral width as well as analyze the influence of the grooves depth on the optical confinement.

We simulated the waveguide without and with the DFB grating layer and we calculate the effective index for both cases. In the paragraph “*Chapter I- Structure and design parameters of an optical resonator with Bragg grating – Distributed Feedback architecture*”, part of the DFB theory is recalled. Starting from [Eq. I-15], $\left\{ \kappa = \frac{2\Delta n'}{\lambda_B} f_{red} = \frac{2\Delta n'}{\lambda_B} \cdot \frac{1}{m} \left| \sin \left(\pi \frac{\Lambda_m}{\Lambda} m \right) \right| \right\}$, it is possible to calculate the coupling factor κ . According the difference between the two effective indices (without and with DFB grating), namely $\Delta n'$, and knowing the DFB order grating, the theoretical value of the coupling factor κ can be predicted.

With such optical simulations, an estimation of the spectral width is possible since the solver calculates the different values of the effective index for each optical mode in the optical cavity. Reminding that $\Lambda = m \frac{\lambda_B}{2n'_{eff}}$ and knowing the period of the structure “ Λ ”, the DFB order “ m ”, as well as the difference between the effective index without the DFB grating (n_{eff}) and with the DFB grating (n'_{eff}), it is possible to calculate the Bragg wavelength λ_B for each guided mode.

As input parameter, the software needs details not only of the vertical structure geometry but also the refractive index for each layer. Hence, an exhaustive literature review of the proposed models has been necessary for calculations of refractive index corresponding to each layer.

Hereafter, different analytical models are compared in order to calculate the refractive index for each layer of the vertical structure of the LDs. Starting with the GaAs layer, AlGaAs, GaInAsP and GaInP layers are principally considered:

- **GaAs layer:** The model takes part from the well-established equation of W. Sellmeier [5]:

$$n = \sqrt{A + \frac{B}{1 - \left[\frac{C}{\lambda}\right]^2}} \quad [Eq. II-1]$$

where A, B and C are empirical coefficients according to [5] and λ is the wavelength.

- **Al_xGa_{1-x}As layer:** Different approaches allow to calculate the refractive index. One is based on the works of S. Adachi [6] while another derived from the works of V. Cardinal [7].

We choose to use the model of M.A. Afromowitz [8] because is the one who gives the lower deviation between the theoretical and experimental effective index for the LD:

$$n(x) = \sqrt{1 + \frac{E_d}{E_p} E^2 \cdot \frac{E_d}{E_p^2} \cdot \frac{\eta}{\pi} E^4 \ln\left(\frac{2E_p^2 - E_G - E^2}{E_G^2 - E^2}\right)} \quad [Eq. II-2]$$

$$E_p = 3,65 + 0,871x + 0,179x^2 \quad \dots \quad E_d = 36,1 - 2,45x$$

$$E_G = 1,424 + 1,266x + 0,26x^2 \quad \dots \quad E = \frac{1,2395}{\lambda[\mu m]} \quad \dots \quad \eta = \frac{\pi E_d}{2E_p^3(E_p^2 - E_G^2)}$$

where x represents the AlAs mole fraction, E_G , E_p and E_d stand for the band gap of the material, the oscillator energy and the dispersion energy respectively. The parameters E_G , E_D and E_p are known for many binary semiconductors alloy but can also be calculated for ternary and quaternary compounds [9].

- **Ga_xIn_{1-x}As_yP_{1-y} layer:** This layer represents the optical confinement of the LD and is of major interest. Since the refractive index must be calculated with a sufficient accuracy, the model established by S. G. Wallace has been considered [10]. It gives a rather good estimation of the refractive index and allows obtaining the minimum deviation between the theoretical and the

experimental effective index data. It is possible to predict the gap value as a function of the stoichiometry and thus, the refractive index:

$$n(\lambda) = -6,904 + 21,95E_g - 14,828E_g^2 + 3,2E_g^3 \quad [Eq. II-3]$$

$$E_g = 1,35 + 0,668x - 1,068y + 0,758x^2 + 0,078y^2 - 0,069xy - 0,332x^2y + 0,03xy^2$$

- **Ga_xIn_{1-x}As layer:** This layer represents the QW. The optical confinement of the modes depends primarily on the refractive index of the QW and the GaInAsP layer. In literature, two models are proposed for refractive index calculation. The first value is based on the equation given by W. Sellmeier for GaAs [11]. A model based on the shift of E_g depending on the mole concentration x :

$$n = \sqrt{A + \frac{B}{1 - \left[C \frac{E_{g_{GaAs}}}{\lambda E_g(x)} \right]^2}} \quad [Eq. II-4]$$

$$E_g(x) = E_{g_{GaAs}} - x \cdot 1,501 + 0,436x^2$$

The second model refers to the one proposed by M.S. Alam [12]:

$$n(\lambda) = \sqrt{A_0 \cdot \left[f(\chi) + \frac{1}{2} \left(\frac{E_0}{E_0 + \Delta_0} \right)^{\frac{3}{2}} \cdot f(\chi_{so}) \right] + B_0} \quad [Eq. II-5]$$

$$f(\chi) = \frac{2 - \sqrt{1 + \chi} - \sqrt{1 - \chi}}{\chi^2} \quad \chi = \frac{hc}{\lambda E_0} \quad \chi_{so} = \frac{hc}{\lambda(E_0 + \Delta_0)}$$

where E_0 and Δ_0 are referred to the fundamental band gap and spin orbit splitting energies. The term $\frac{hc}{\lambda}$ is the photon energy while A_0 and B_0 stand for the free electron hole pair contribution and the higher lying gaps contribution respectively.

The refractive index calculated from these two models only differs to the first decimal. Finally, we choose the model of M.S. Alam because it allows obtaining optical simulation results closer to the experimental ones.

- **Ga_xIn_{1-x}P layer:** Few data are available in literature and only experimental measurements are reported from works of M. Schubert [13]. As example, this measurement was done to extract the

refractive index but only up to 958nm. Assuming a linear behavior up to 980nm, we used a linear extrapolation to extract the value at 975nm as plotted in *Figure II-5*.

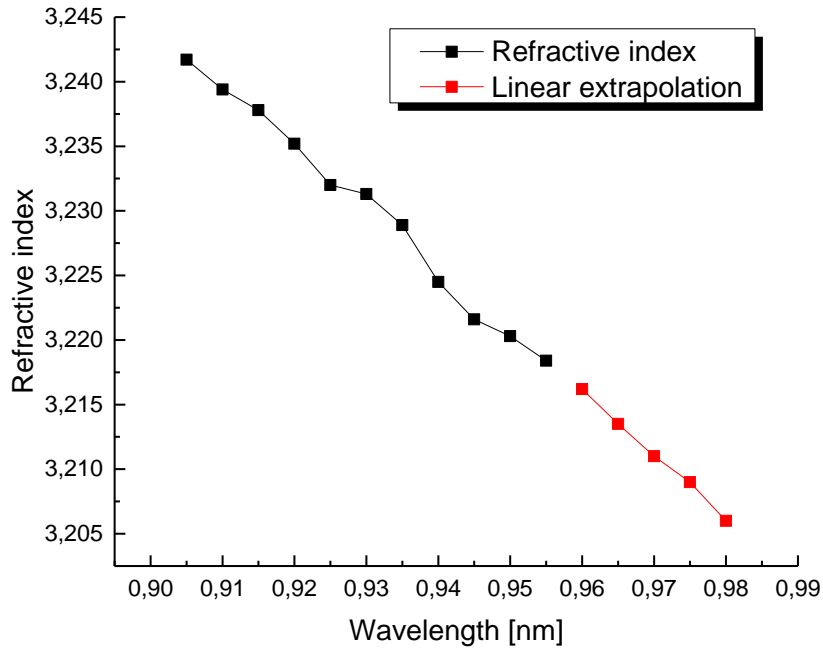


Figure II-5: Variations of the refractive index of GaInP material and the corresponding linear extrapolation from 955nm to 980nm.

Table II-1 summarizes the different models used to calculate the refractive index of each layer of the vertical structure.

Layer	Material	Model
[N] Substrate/ [P] Contact	$GaAs$	W. Sellmeier [5]
[N-P] Cladding	$Al_xGa_{1-x}As$	M.A. Fromowitz [8]
[N-P] LOC	$Ga_xIn_{1-x}As_yP_{1-y}$	S.G. Wallace [10]
QW	$Ga_xIn_{1-x}As$	M.S. Alam [12]
[P] Spacer	$Ga_xIn_{1-x}P$	M. Schubert [13]

Table II-1: The different models used to calculate the refractive index for each layer of the vertical structure.

From the refractive index calculations, one can estimate the confinement factor Γ that is a key parameter since it is possible to predict the theoretical optical losses for each region of the LD vertical structure as reported in [13]:

$$\alpha_i = \Gamma(\sigma_n n + \sigma_p p) \quad [Eq. II-6]$$

where $\sigma_{p,n}$ correspond to the free electron and hole absorption cross-sections and n, p are the doping levels of each layer.

The values of $\sigma_{p,n}$ have been extracted from experiments reported in literature [14], [15]:

$$\sigma_n \approx 4 \cdot 10^{18} \text{cm}^{-2}, \sigma_p \approx 12 \cdot 10^{18} \text{cm}^{-2}.$$

Based on the results of a proprietary simulation software specifically developed at III-V lab where input data are derived from many characterizations, the obtained and chosen values are the following ones:

$$\sigma_n \approx 3 \cdot 10^{18} \text{cm}^{-2}, \sigma_p \approx 11 \cdot 10^{18} \text{cm}^{-2}.$$

The waveguide optical simulations, provided in the next sections, have been performed mainly to determine the following parameters:

- The theoretical value of the coupling factor κ
- The effect of etching on the coupling factor
- The near and far fields
- The far field divergence
- The spectral width of the DFB versus F-P optical spectrum

In the next section, we will describe the vertical structures developed at III-V lab starting from the first developed the LOC vertical structure. Then, we will discuss this choice justifying the development of the two other vertical structures (SLOC and AOC). In each section, we will compare the vertical structures through their optical and electrical properties, mainly in terms of coupling factor, far field, spectral width, optical losses and series resistance.

2.1.2 Technological description of the III-V lab vertical structures

Aiming to develop a pump source LD for Er/Yb fiber laser, the vertical structures developed at the III-V lab are processed on a GaAs substrate including a GaInAs-based QW. Due to the lattice mismatch between the strained QW and the optical cavity in GaInAsP, the emission of such structures is mainly TE-polarized.

- **Large Optical Cavity (LOC) structure**

The first LD vertical structure developed, in the field of high-power DFB LD at 975nm, is the LOC based on a single QW. This last allows obtaining a monomodal emission along the fast-axis with both low internal losses and series resistance. *Table II-2* summarizes the main technological parameters of the whole structure. The photons are confined in the optical cavity because of the two quaternary layers that have a refractive index lower than the QW, corresponding to an index guided structure. The two grooves presented in *Figure II-2* confine the injected current in the central ridge. Thus, carriers are injected into the active region and only a little part diffuse laterally. The grooves confine the current inside the central ridge, and then the lateral structure refractive index is modified. The lateral index change, between the grooves and the central ridge, guides photons along the axis of the cavity. A LD structure where a recombination of current carriers and a population inversion occur only in the central ridge stripe through which the current flows is called gain-guided.

Aiming to develop a pump source with very high output optical power ($\gg 5W$ in CW regime), the width of the optical cavity is large by forming two separate heterojunctions in both sides of the homojunction. Such a structure can provide a small vertical far field angle, enabling to satisfy the requirements on the optical elements to shape the beam. It also increases the near field width that allows reducing the output facet load and it is possible to obtain a fill factor of the optical mode in the QW equals to 1,2%.

Layer	Material	Doping	Thickness [μm]
Substrate	$GaAs$	Confidential information	150
Cladding	$Al_xGa_{1-x}As$	Confidential information	
LOC	$Ga_xIn_{1-x}As_yP_{1-y}$	Confidential information	0,55
QW	$Ga_xIn_{1-x}As$	Confidential information	0,009
LOC	$Ga_xIn_{1-x}As_yP_{1-y}$	Confidential information	0,55
Spacer	$Ga_xIn_{1-x}P$	Confidential information	0,1
DFB Grating	$Ga_xIn_{1-x}As_yP_{1-y}$	Confidential information	0,05
Spacer	$Ga_xIn_{1-x}P$	Confidential information	0,1
Cladding	$Al_xGa_{1-x}As$	Confidential information	0,2
Cladding	$Al_xGa_{1-x}As$	Confidential information	1,3
Contact	$GaAs$	Confidential information	0,13

Table II-2: Main technological parameters of the overall LOC structure (doping level of each layer is a confidential information).

- **Super Large Optical Cavity (SLOC) structure**

The second vertical structure is the SLOC that derives from the LOC structure. Its main objective is to reduce the fast axis divergence by using an optical cavity with a higher thickness. A narrow beam divergence makes easier the coupling of the light into the optical parts but also reduces the power density within the optical cavity. *Table II-3* summarizes the main technological parameters of the whole structure.

Layer	Material	Doping	Thickness [μm]
Substrate	$GaAs$	Confidential information	150
Cladding	$Al_xGa_{1-x}As$	Confidential information	2,8
LOC	$Ga_xIn_{1-x}As_yP_{1-y}$	Confidential information	1,25
QW	$Ga_xIn_{1-x}As$	Confidential information	0,009
LOC	$Ga_xIn_{1-x}As_yP_{1-y}$	Confidential information	0,75
Spacer	$Ga_xIn_{1-x}P$	Confidential information	0,1
DFB Grating	$Ga_xIn_{1-x}As_yP_{1-y}$	Confidential information	0,01
LOC	$Ga_xIn_{1-x}As_yP_{1-y}$	Confidential information	0,5
Spacer	$Ga_xIn_{1-x}P$	Confidential information	0,1
Cladding	$Al_xGa_{1-x}As$	Confidential information	2,7
Contact	$GaAs$	Confidential information	0,18

Table II-3: Main technological parameters of the overall SLOC structure (doping level of each layer is a confidential information).

The SLOC presents a $2,5 \mu\text{m}$ thick optical cavity that is twice compared to the LOC structure thickness and so the number of guided modes increases inherently. The SLOC waveguide structure will support the propagation of many higher order vertical modes. The odd modes are supported by the waveguide but for a symmetric situation, there is a node at the QW. At this node, destructive interferences can occur and thus are not amplified. The higher even modes have higher losses than the fundamental ones and only the fundamental mode can have a resonance [16]. One can say that even if the vertical thickness of the optical cavity is bigger than that of the LOC, the transverse single-mode operation can propagate. For the SLOC vertical structure, the fill factor Γ in the QW is 0,7% that is lower compared to the LOC structure. A higher optical cavity thickness reduces the overlap of the optical modes in the highly-doped layers. Therefore, the optical losses by free carriers absorption linked to the doping level decrease and the COD threshold for this structure is higher compared to the LOC structure.

A major drawback with the SLOC structure lies in the increase of the R_s that negatively affects the Wall-Plug Efficiency (WPE).

- **Asymmetric Large Optical Cavity (AOC) structure**

The last vertical structure deals with the AOC. Such a structure allows reducing the series resistance using a high asymmetrical design by reducing the p-side optical cavity thickness. However, in the p-side of the optical cavity, the confinement of the modes is lower compared to that of the LOC and SLOC structures. For this reason, two QWs are included into the structure to obtain a higher gain and mitigate the lower confinement into the p-side optical cavity. *Table II-4* summarizes the main technological parameters of the whole structure.

Layer	Material	Doping	Thickness [μm]
Substrate	$GaAs$	Confidential information	150
Cladding	$Al_xGa_{1-x}As$	Confidential information	2,8
LOC	$Ga_xIn_{1-x}As_yP_{1-y}$	Confidential information	0,9
QW	$Ga_xIn_{1-x}As$	Confidential information	0,009
Barrier	$Ga_xIn_{1-x}As_yP_{1-y}$	Confidential information	0,012
QW	$Ga_xIn_{1-x}As$	Confidential information	0,009
LOC	$Ga_xIn_{1-x}As_yP_{1-y}$	Confidential information	0,1
Cladding	$Al_xGa_{1-x}As$	Confidential information	0,4
Cladding	$Al_xGa_{1-x}As$	Confidential information	1,1
Contact	$GaAs$	Confidential information	0,18

Table II-4: Main technological parameters of the overall AOC structure (doping level of each layer is a confidential information).

With such a vertical structure, it is possible to obtain a confinement factor (Γ_{AOC}) of the optical mode in the QWs equal to 2,2%. This value is almost twice of the LOC vertical structure ($\Gamma_{LOC} = 1,2\%$) and four times bigger than SLOC ($\Gamma_{SLOC} = 0,7\%$). Because of that, the COD threshold can be lower than the other structures. We must note that the fabrication of AOC structure-based LD including a DFB portion is not planned in the framework of this study. Accordingly, all the results reported for the AOC devices are only based on a F-P vertical structure.

- a. Theoretical calculations of the optical losses and series resistance for each vertical structure

The relative contribution to the series resistance and optical losses of the different regions of the vertical structures can be calculated. For the first parameter, [Eq. I-20] presented in “Chapter I- Main electro-optical parameters of a high-power Laser diode” is basically used:

$$R_i = \rho \cdot \frac{L}{A} = \frac{1}{q \cdot N \cdot \mu} \cdot \frac{L}{A} \rightarrow R_s = \sum_{i=0}^n R_i \quad [Eq. II-7]$$

where q, N, μ, ρ represent the elementary charge, the doping level of the layer, the mobility of the electron/hole within the layer respectively.

Considering the results described in the previous section “Chapter II - Optical simulations: FIMMWAVE® tool capabilities, material properties” the cross-section of the refractive index profile, the optical losses (α_i) as well as the series resistance (R_s) are predicted hereafter (see Figure II-6) for each layer of the three vertical structures considering the 975nm emission wavelength. For the calculations of the R_s , some important assumptions must be considered:

- The QW contribution is neglected. The doping level of the QW corresponds to the residual value of the last grown layer that is the n-side quaternary alloy GaInAsP. Indeed, a low doping level ($\approx 10^{14} cm^{-3}$) results in a high value of resistance. Because the QW has a very low thickness ($0,009 \mu m$), we assume no contribution to the overall series resistance.
- The contact resistance “ R_c ” is also neglected since it is assumed to be much lower than the series resistance.

Table II-5 summarizes the results concerning the overall series resistance and internal losses as a function of the cavity length for the three vertical structures.

Cavity length [mm]	LOC		SLOC		AOC	
	R_s [mΩ]	α_i [cm ⁻¹]	R_s [mΩ]	α_i [cm ⁻¹]	R_s [mΩ]	α_i [cm ⁻¹]
2	51		72		20	
3	34	0,35	48	0,29	13	0,58
4	25		36		10	

Table II-5: Calculated series resistance and optical losses for the three vertical structures versus the cavity length.

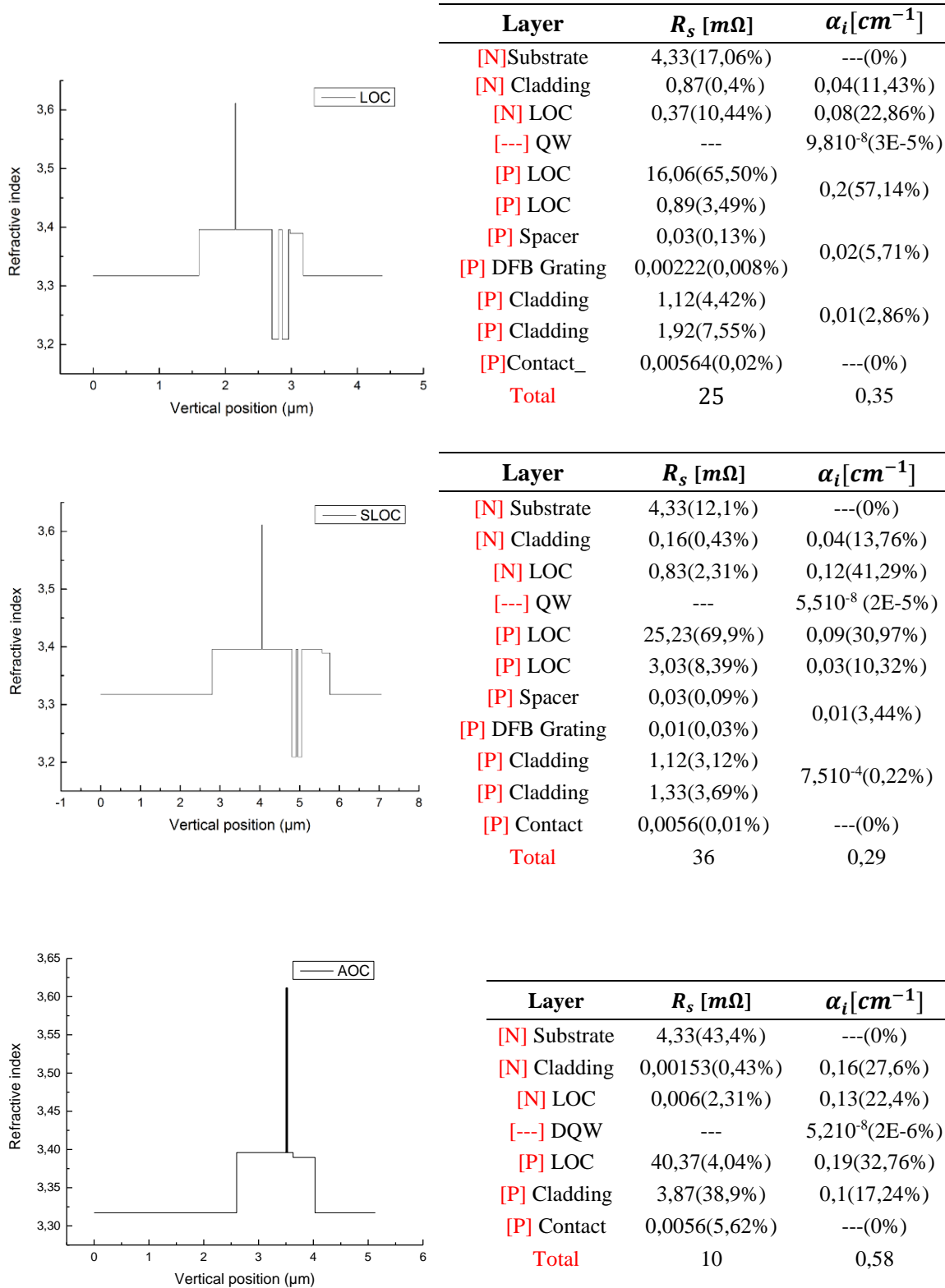


Figure II-6: Variations of the index profile versus the vertical position and predicted R_s as well as α_i for each layer of the three vertical structures considering a 4mm cavity length LD. The percentage refers to the total R_s and α_i .

The AOC structure clearly presents the higher optical losses (60% and 100% compared to the LOC and the SLOC structures respectively) and the lower series resistance (almost a half and one third compared to SLOC and LOC respectively).

b. Simulated far field divergence for each vertical structure

These optical simulations aim to provide information about the far field characteristics to investigate on the properties of the transversal single-mode emission (perpendicular to the layers plane) of the LD. The design of the vertical structure ensures the transversal confinement because only the fundamental mode is amplified; the other modes have a higher material gain. *Figure II-7* displays the simulated far field for each vertical structure at 975nm.

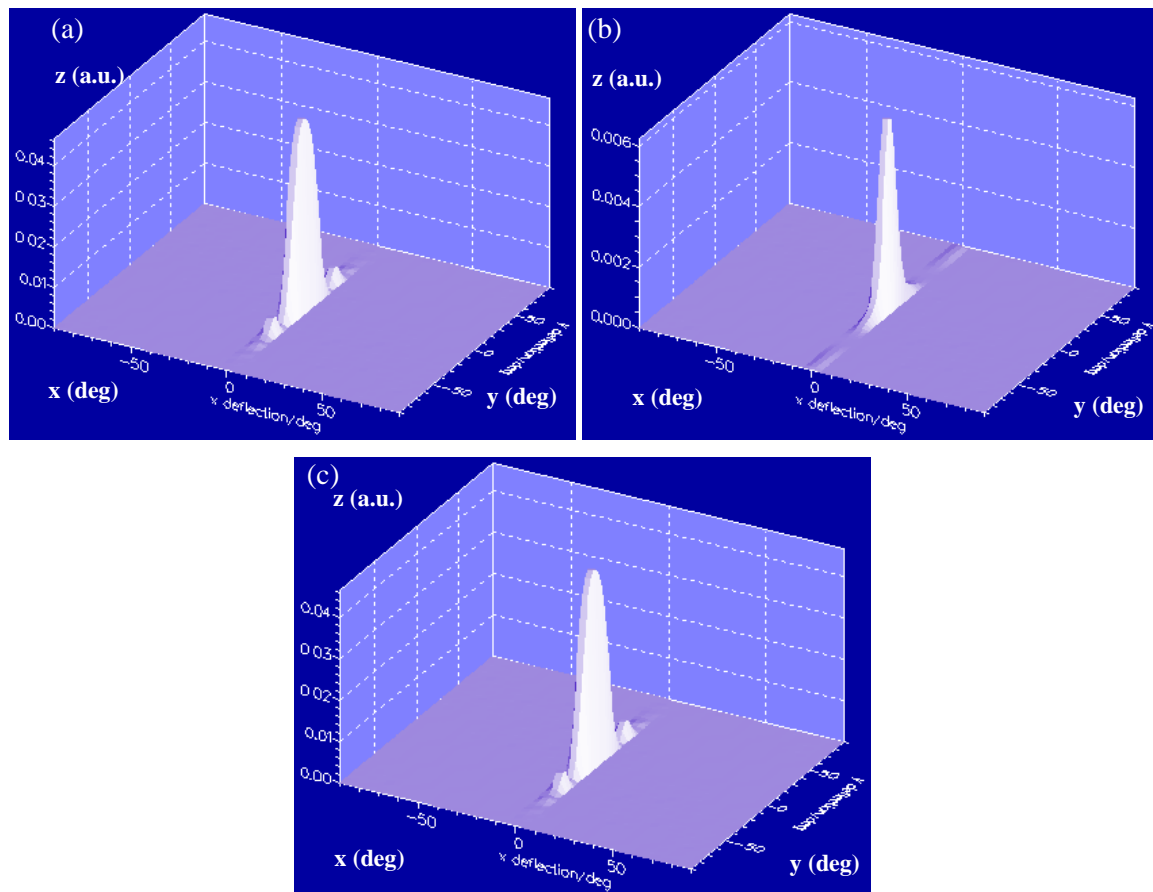


Figure II-7: Simulated far fields for each vertical structure LOC (a), SLOC (b) and AOC (c). The emissive facet of the LD is located at the bottom of the graph. Along the z-axis, an arbitrary scale of intensity is used and the x/y-axis (in degree) enables to predict the divergence of both the fast and slow axis.

The extracted values of the divergence for the fast (θ_V) and the slow axis (θ_H) at FWHM are given in *table II-6*.

Vertical structure	θ_V [°]	θ_H [°]
LOC	31	6,1
SLOC	18	6,1
AOC	30	6,1

Table II-6: Predicted fast (θ_V) and slow (θ_H) axis divergence for the three vertical structures.

The slow axis divergence is not a specific issue because the dimension of the fiber core and the LD emissive facet are almost the same and equal to $100\mu m$. In contrast, based on the expected performances of the LD, we must take care of both:

- The divergence of the fast axis because it is inversely proportional to the height of the optical cavity: $\theta_V \approx \arctan\left(\frac{2\lambda}{\pi \cdot 1,25 \cdot 10^{-6}}\right)$.
- The slow axis since it is inversely proportional to the width of the LD: $\theta_H \approx \arctan\left(\frac{2\lambda}{\pi \cdot 100 \cdot 10^{-6}}\right)$.

An experimental study has been performed on LOC and SLOC vertical structures, demonstrating that the coupling efficiency into an optical fiber of $100\mu m$ of inner core diameter (numerical aperture equal to 0,15) reaches 82% just above the threshold and 80% under an injected power of 1W for the LOC structure. For the SLOC structure, these performances are clearly improved since a coupling efficiency of 98% and 87% just above the threshold, under an injected power of 1W have been achieved respectively. We can conclude that the coupling efficiency considering both the performances of both LOC and SLOC vertical structures are good enough to consider our LD technology as pump source for high-power Er/Yb-doped fiber laser.

c. Estimation of the DFB coupling factor for the LOC and SLOC structures

Based on waveguide optical simulations, it is possible to estimate the coupling factor κ of the DFB grating layer. The section “*Chapter I-Structure and design parameters of an optical resonator with Bragg grating – Distributed Feedback architecture*” explains that the coupling factor must stay in a specific range ($0,5 < \kappa L < 2$) corresponding to a typical targeted value as reported in [17]. In literature, different values of κ have been extracted for high power LD at 975nm. In 2006, a value of 2 cm^{-1} is extracted for 1,5mm and 3mm cavity length high-power DFB LD at

975nm [18]. In 2010, this value was increased up to 3cm^{-1} for a 3mm cavity length LD [19]. In 2011, the team at FBH studied the impact of coupling factor κ on differential quantum efficiency (η_D) and modal gain (Γg_0), these are inversely proportional to κ . Hence, they chose to use 9cm^{-1} as given in [20]. In 2012, they published a work reporting values of κ ranging from 0,6 to 1cm^{-1} [21]. *Table II-7* summarizes the different values of the coupling factor reported in literature since the first developments of DFB structures in high-power LD in 2006.

Years	Research Center	Length [mm]	Order of the grating	κL	κ [cm^{-1}]
2006	FBH	1.5	2 nd	0,3	2
2006	FBH	3	2 nd	0,6	2
2010	FBH	3	2 nd	0,9	3
2011	FBH	3	2 nd	0,15	9
2012	FBH	3	2 nd	0,18-0,3	0,6-1
2014	III-V lab	3	1 st	1,4	4,66
2014	III-V lab	3	2 nd	0,7	2,33
2016	III-V lab	4	2 nd	1,3	3,25
2016	III-V lab	4	2 nd	0,92	2,31

Table II-7: Variations of the coupling factor for different technologies reported in literature since 2006 extracted from [2]-[18]-[19]-[20]-[21].

The κ value can be modified using a spacer layer and moving away the DFB grating from the LOC. At III-V lab, values of $\kappa \approx 4,66\text{cm}^{-1}$ and $\kappa \approx 2,33\text{cm}^{-1}$ were set [2].

The coupling factor mainly depends on the imperfection of the real shape of the grating. Thus, it is of interest to investigate on the influence of the relative mark length on the values of κL for a first- and second-order grating (see *Figure II-8*).

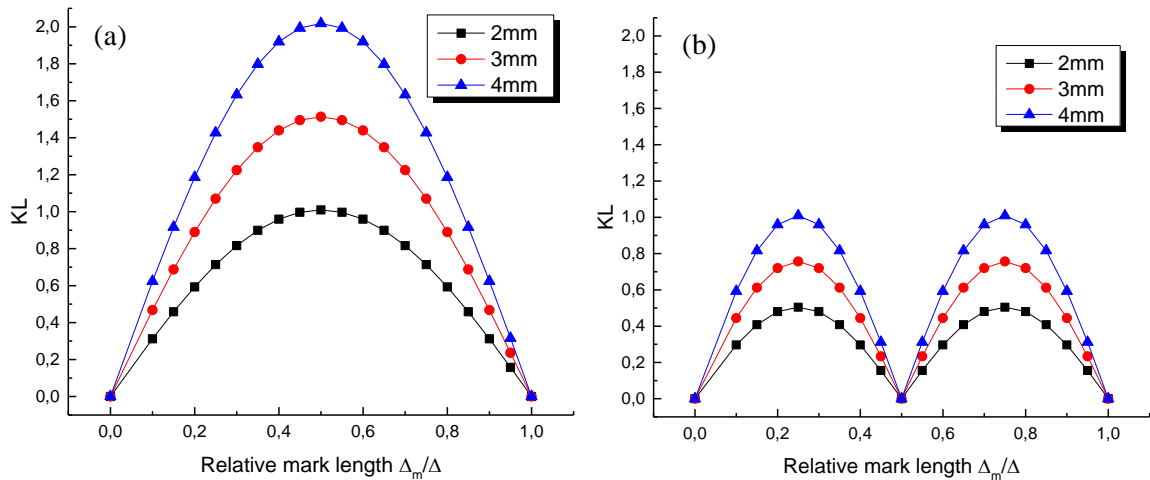


Figure II-8: Coupling factor variations for square grating as a function of the $\frac{\Delta_m}{\Delta}$ for a first- (a) and a second- (b) order grating.

Clearly, the second-order grating is the most affected by variations of the relative mark length compared to the first-order grating. However, a second-order grating was chosen because of the main difficulties to pattern a first-order grating that requires a very short pitch ($\Lambda \approx 100\text{nm}$) using the e-beam technique. To obtain a $\kappa L \approx 0,92$ or $\kappa L \approx 1,3$, we used the second-order square shape grating with $\frac{\Lambda_m}{\Lambda} = 25\%$. Assuming a value of κ equal to $0,92\text{ cm}^{-1}$ and [Eq. I-11] ($\Lambda = m \frac{\lambda_B}{2n'_{eff}}$), it is possible to obtain a grating pitch of 290nm , easier to pattern with III-V lab facilities.

Based on these considerations, one can calculate the theoretical spectral envelop width when a DFB structure is implemented. The optical simulation calculates the effective index of all the guided modes into the optical cavity. According to [Eq. I-13], it is possible to calculate the Bragg wavelengths " λ_B " for all the guided modes travelling along the optical cavity. Considering that Λ and m are equal to $287,5\text{ nm}$ and 2 , as well as using the calculated effective refractive index (n'_{eff}) of the guided modes, one can calculate the Bragg wavelengths for the first and the last index modes propagating within the waveguide. A maximum of 38 and 40 modes can propagate within the optical cavity for LOC and SLOC structures respectively. The difference between the first and the last guided modes allows giving the complete spectral line width equal to $0,55\text{nm}$ and $0,6\text{nm}$ for the SLOC and the LOC structures respectively.

It is important to consider that the depth of the grooves affects the optical confinement and consequently the total number of guided optical modes. This is mainly due to the difference of the refractive index of the grooves and the central ridge. For instance, based on optical simulations, with a depth of the grooves close to the epi p-side of GaInAsP layer, almost 80 modes can be guided. Indeed, the number of the guided modes is inversely proportional to the grooves depth. Hence, it is recommended to use a groove depth of $2,2\mu\text{m}$ and $2,8\mu\text{m}$ for the LOC and SLOC structures respectively. The depth will certainly affect the thermal management of the LD and so the final choice must result from a compromise between the expected optical confinement and the thermal management. Based on both optical and thermal simulations, an etching depth equal to $0,8\mu\text{m}$ and $1,3\mu\text{m}$ has been chosen for the LOC and SLOC structures respectively, corresponding to the middle of the epi p-side cladding layer.

To determine the optimal depth of the grooves, the influence of their etching in the coupling factor has been analyzed through optical simulations as reported in *Figure II-9*. An etching equal to $0,2\mu\text{m}$ of the GaAs contact thickness corresponds to the beginning of the cladding layer while values of $1,7\mu\text{m}$ and $2,2\mu\text{m}$ correspond to the beginning of the p-side GaInAsP layer for the LOC and SLOC structures respectively.

Clearly, one can conclude that the *coupling factor* remains strictly constant as a function of their depth as shown in *Figure II-9*.

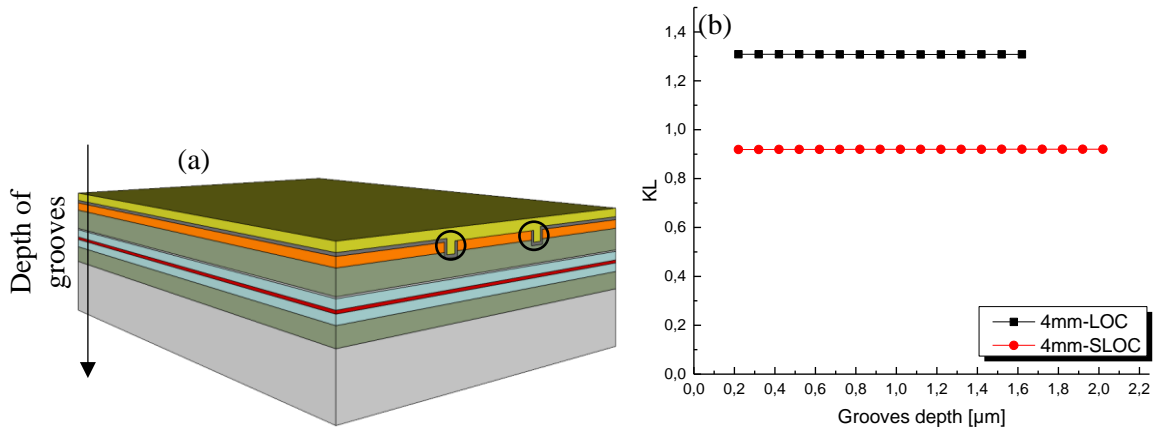


Figure II-9: (a) Grooves etched around the strip. (b) Variations of the coupling factor versus the etching depth of the grooves (4mm length cavity LOC and SLOC structures).

2.1.3 Effects of a Non-Injected-Mirror (NIM) window

The emission facet of the LD is subjected to a huge local heating effect due to a recombination process at the GaAs-Air interface and the reabsorption phenomenon of the emitted light particularly [22]. The first one is significant at low optical power while the last one dominates at high levels of optical output power. The surface recombination leads to a temperature rise and, as a consequence, an increase of the current threshold that can result in a catastrophic failure due to a very strong local heating at the front facet [23], [24]. The optical absorption increases linearly with the output power increasing the facet temperature [25]. Facet heating reduces the band gap energy, consequently increasing the absorption coefficient and concentrating the current, that lead to further non-radiative recombination process responsible of local heating. This “positive” feedback cycle undergoes a well-known effect known as thermal run-away, bringing a rapid increase of both the facet temperature resulting in a COD. The two contributions are shown in *Figure II-10*, considered as a qualitative estimation of the heat generation at the facet as a function of the optical output power.

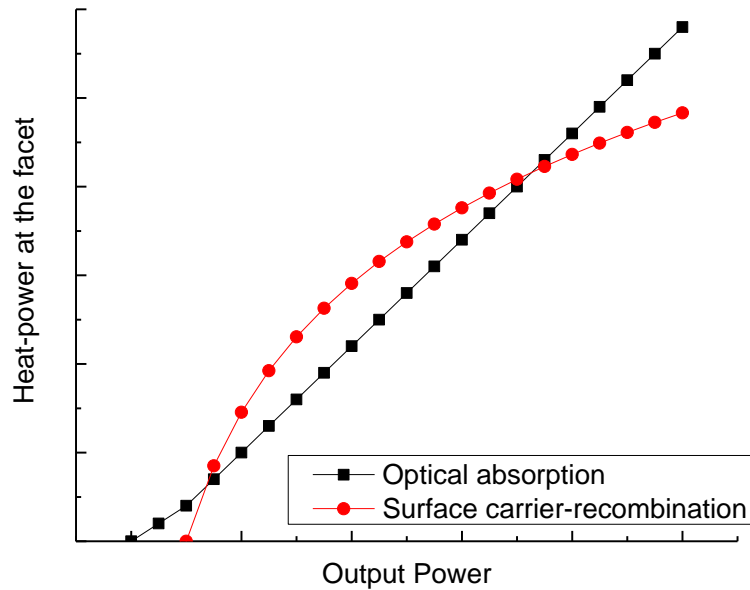


Figure II-10: General contributions of the optical absorption and the surface carrier-recombination process to the heat power variations at the front facet versus the optical output power of the LD [25]-[26].

The heat generated leads to a local reduction of the band gap estimated via the well-known equation reported by Y.P. Varshni [27]:

$$E_g = E_{0K} - \frac{\alpha T^2}{T + \beta} \quad [Eq. II-8]$$

where α, β are constants depending on materials while E_{0K} represents the energy gap at 0K and T stands for the temperature.

To reduce and even avoid such effects, different solutions have been proposed in literature:

- A non-pumped zone near the facet via segmented electric contacts [28].
- Different passivation processes [29]-[30].
- A non-absorbing mirror (NAM) due to a large band gap close to the facet using Ion beam implantation [31]-[32]-[33] or quantum well intermixing [34].
- A Non-Injecting mirror (NIM) with a current block layer near the mirror [26]-[35]-[36]-[37].

All these solutions are introduced after the overall epitaxial process allowing fabricating the vertical structure and modifying the bandgap without epitaxial regrowth. The top contact is divided in three parts. To influence the carrier density near the facets, which is responsible for the heating along the front facet, the voltage in the mirror region must be controlled separately. Thus, it is possible to

modify the bandgap at the facet. The ion implantation quantum well intermixing method uses a glass film etched with a mask. Neutral impurities are implanted into the semiconductor material through the glass film. The varying thickness of the film controls the amount of neutral impurities implanted in the region above the quantum well. Then, the wafer goes through an annealing process. At elevated temperatures, the generated vacancies diffuse from their high concentration region to a low concentration region further down into the wafer structure. The vacancies movement intermixes the different atoms in the quantum well structure. The effect of intermixing creates a graded quantum well structure, thereby increasing its bandgap energy profile at the intermixed region [38]. The NIM window consists in an insulator layer (in our case SiO_2) just above the metallization and close to the emissive facet of the LD (*Figure II-11*). This layer reduces the current injection at the facet. *Figure II-11* shows a schematic with a cutting section on the metallization layer (in yellow) of the LD. Such a view is used to show the SiO_2 NIM layer (in grey) between the metallization and the GaAs contact layer (in orange).

The manufacturers have implemented different structures of NIM. In 2003, Fraunhofer-Institute (FI) and Max-Born-Institut (MBI) demonstrated the temperature reduction using a current blocking layer of $30\ \mu\text{m}$ near the facet and under the metallization layer [26]. In 2006, CORNING Inc. (CI) reported on the use of a current block layer of $30\ \mu\text{m}$ near the facet and under the metallization layer [39]. In 2014, the FI and OSRAM Opto Semiconductors (OOS) published some relevant results on a specific implementation of a passivation layer. Moreover, using micro-optical structures on the facet, they were able to tailor the phase front of the slow axis modes inside the waveguide and the beam quality as well as the brightness have been improved [40]. In 2015, IMS laboratory, from the University of Bordeaux, has investigated on the influence of the unpumped window length on high-power LD emitting at 980nm with a current block layer of $30\ \mu\text{m}$ and even more [36]. *Table II-8* summarizes the different values of NIM reported in literature.

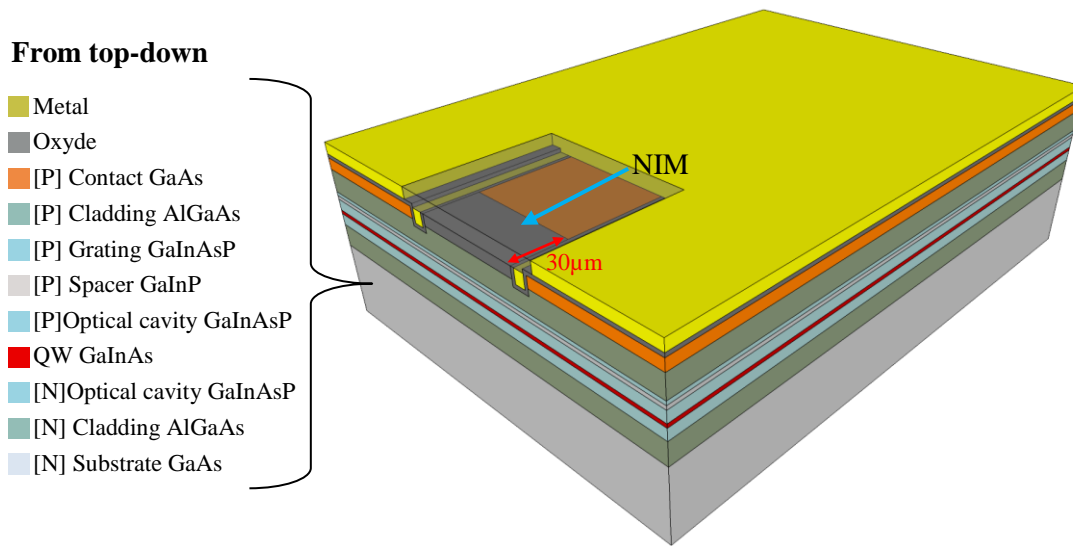


Figure II–11: Top view of a NIM. The oxide layer below the metallization reduces the current in the area close to the emissive facet.

Years	Laboratory	NIM Length [μm]	NIM position
2003	FI-MBI	30	Under the metallization [26]
2006	CI	30	Under the metallization [39]
2014	FI-OOS	----	---- [40]
2015	IMS	30 μm and more	---- [36]

Table II-8: NIM specifications reported in literature since 2003 extracted from [26]-[36]-[39]-[40].

To determine the optimal length of the NIM, optical simulations have been done. In particular, it was studied the impact of the vertical position of the NIM (from 0,1 to 1,8 μm) for two different lengths of blocking layers (30 and 50 μm) on the near and far field patterns. The vertical position of the NIM represents at which level in the vertical structure of the LD the NIM is located. The far field and the fast axis divergence variations as a function of the vertical position of the NIM are presented in *Figure II–12*. These results are quite similar for both 30 and 50 μm NIM length. Based on optical simulations, the main results are the following:

- The near field does not change significantly either according the implementation of a NIM or the variations of both its vertical position and length.
- In contrast, the far field is more affected since some changes clearly appear on both the intensity and the fast axis divergence as reported on *Figure II–12(b)*. These results are quite similar whatever the NIM length considered.

- The slow axis divergence is not affected by the vertical position of the NIM. However, the fast axis divergence increases and the far field intensity decreases as function of the NIM vertical position.

Based on simulation results, an optimized design of the NIM window has been proposed:

- We choose a NIM vertical position equal to $0,4\mu\text{m}$, keeping the fast axis divergence and the far field intensity quite unchanged.
- An etching depth equal to $0,5\mu\text{m}$ for both NIM length. With such an etching depth, the NIM reaches the p-side cladding layer ensuring an electrical insulation in the region of the emissive facet.

In the next chapter, we will describe the effects of the NIM window on the current density at the level of the front facet and its possible effect on COD.

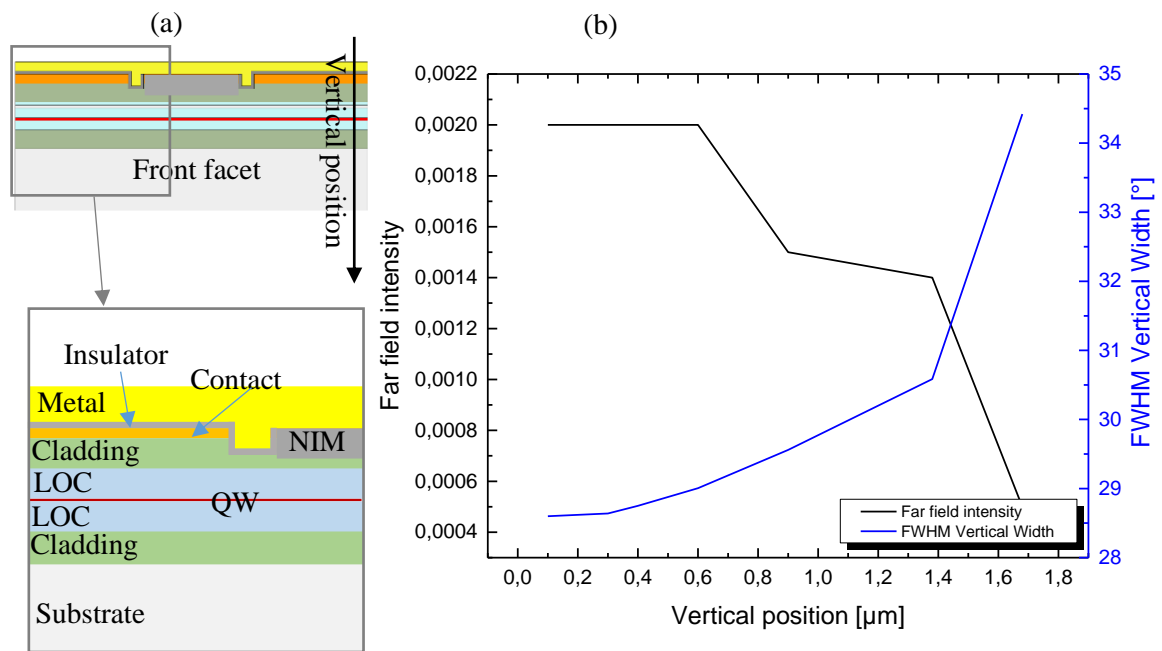


Figure II-12: (a) Cross-section view of the front facet with the NIM position. The grey square corresponds to an enlargement of the front facet showing the NIM position. (b) Influence of the vertical position of the NIM on the far field intensity and divergence for a length of $30\mu\text{m}$.

2.1.4 Comparison of optical performances for the three structures

The DFB LOC vertical structure has a coupling factor equal to 1,3 and a spectral linewidth of 0,6nm. The fast and slow axis divergence has been determined and optical simulations give a divergence of the fast (θ_V) and slow (θ_H) axis equal to 31° and 6,1°. The major drawback with such a structure lies in its vertical divergence. Because of the optical cavity thickness, it may be difficult to reach a high coupling efficiency (80% under 1W of injected power) between the LD and the Er/Yb optical fiber.

To overcome such a limitation, the DFB SLOC vertical structure has been developed. This structure has a $kL \approx 0,92$ that allows to obtain a spectral linewidth of 0,5nm. The fast and slow axis divergence has been investigated and the optical simulations show a divergence of the fast (θ_V) and slow (θ_H) axis equal to 18° and 6,1°. Hence, it is possible to reach a higher coupling efficiency between the LD and the Er/Yb optical fiber (87% under 1W of injected power). Moreover, the thickness of the optical cavity is twice compared to the one of the LOC structure enabling to reduce the overlap of the optical modes in the highly-doped layers. Therefore, the optical losses linked to the doping level decrease and the COD threshold is significantly pushing up compared to the LOC structure (14% more). However, the SLOC structure has a higher series resistance than the one obtained for the LOC structure (30% more), leading to an increase of Joule effect and, consequently, reduce the WPE.

Thanks to the high asymmetrical design, the developed AOC structure allows to strongly decrease the series resistance (60% less than LOC and 72% less than SLOC). The fast and slow axis divergence has been investigated through optical simulations and we obtain: $\theta_V = 30^\circ$ and $\theta_H = 6,1^\circ$. The double QWs structure results in a higher threshold current, almost twice compared to the LOC structure. Finally, a higher confinement reduces the COD threshold compared to the LOC and SLOC structures. *Table II-9* summarizes the main optical performances for each vertical structure based on a 4mm cavity length LD.

Structure	R_s [mΩ]	Γ [%]	Coupling efficiency	θ_v [°]	$k \cdot L$	α_i [cm ⁻¹]
LOC	25	1,2	80%	31	1,3	0,35
SLOC	36	0,7	87%	18	0,93	0,29
AOC	10	2,2	---	30	---	0,58

Table II-9: Comparison of the main electro-optical performances for each vertical structure (4mm cavity length).

The next section will give the detailed description of the fabrication process of the LDs starting from the epitaxy to the final device mounting.

2.2 FABRICATION PROCESS OF THE VERTICAL STRUCTURE

This section is dedicated to the description (step by step) of the fabrication process of the overall vertical structure. The first section addresses the epitaxy on the GaAs substrate and then, the lithography process is described. Finally, the last sections focus on the facet coating and the device mounting.

2.2.1 Epitaxial process background

The three vertical structures are fabricated using two main steps based on the Metal Organic Vapour Phase Epitaxy (MOVPE) technique. The first growth is performed on a N-type GaAs substrate. The first step consists in a deposition of N-type AlGaAs layer graded index. After that, the epitaxy of the AlGaAs cladding layer and then the GaInAsP/GaInAs/GaInAsP stack is processed.

Figure II–13 shows the photoluminescence of the GaInAs-based QW measured at 25°C, validating the homogeneity of the wavelength emission around 965nm. Since the LD will operate at high levels of current (12A), the drift of the gain will approach the targeted wavelength (975nm).

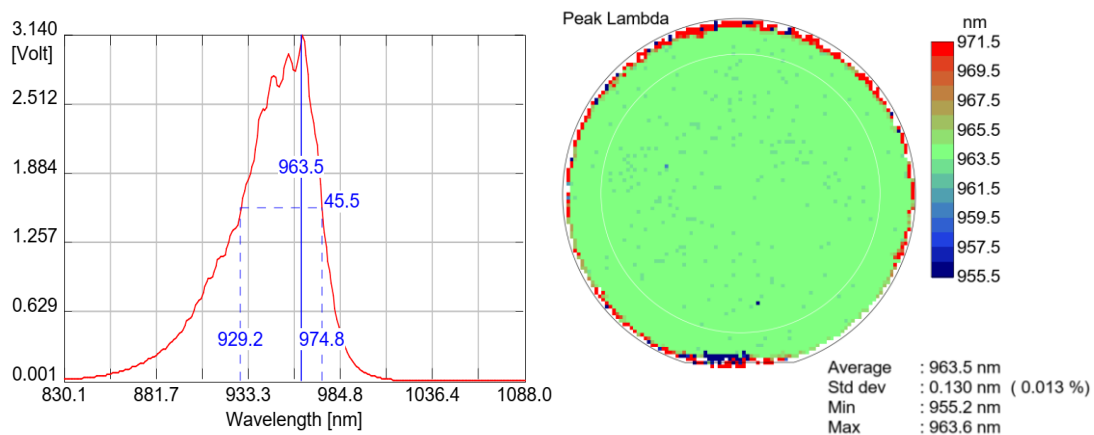


Figure II–13: Spectral-resolved photoluminescence distribution of the GaInAs-based QW measured at 25°C.

2.2.2 Main steps of lithography process and DFB grating fabrication

The LDs goes out of the epitaxy after the growth of the p-side GaInAsP layer because the next step corresponds to the patterning of the DFB grating layer. To fabricate the DFB grating, a spacer of GaInP is epitaxially grown after the P-type LOC layer as reported in *Figure II-14*.

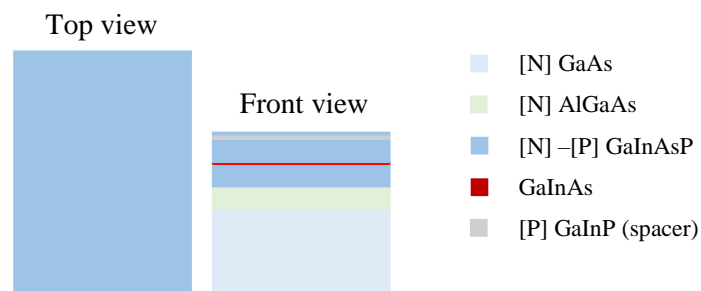
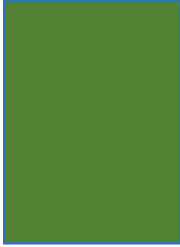
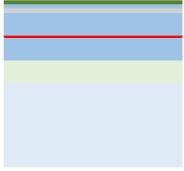
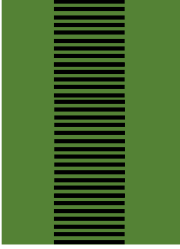
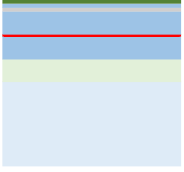
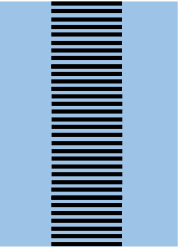
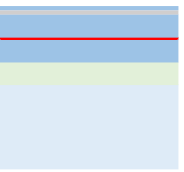


Figure II-14: First epitaxy growth with the deposition of the layer up to the grating. Then the device is ready for the grating patterning.

Table II-10 describes the main lithography steps used for the realization of the DFB grating and the ridge.

Step description	Views
Deposition of SiO ₂ used for the definition of grating via e-beam technique	<div style="display: flex; align-items: center;"> <div style="margin-right: 20px;"> <p>Top view</p>  </div> <div style="margin-right: 20px;"> <p>Front view</p>  </div> </div>
Patterning of the DFB grating via e-beam technique	<div style="display: flex; align-items: center;"> <div style="margin-right: 20px;"> <p>Top view</p>  </div> <div style="margin-right: 20px;"> <p>Front view</p>  </div> </div>
Etching of SiO ₂ and implementation of grating within the layer GaInAsP	<div style="display: flex; align-items: center;"> <div style="margin-right: 20px;"> <p>Top view</p>  </div> <div style="margin-right: 20px;"> <p>Front view</p>  </div> </div>

The DFB grating is defined in the photoresist using the e-beam technique, transferred in a SiO₂ layer and etched into the semiconductor via Inductive Coupled Plasma (ICP). *Figure II-15* shows a SEM view of the patterned second-order grating. The measured pitch ($\approx 290\text{nm}$) fully agrees with the predicted one.

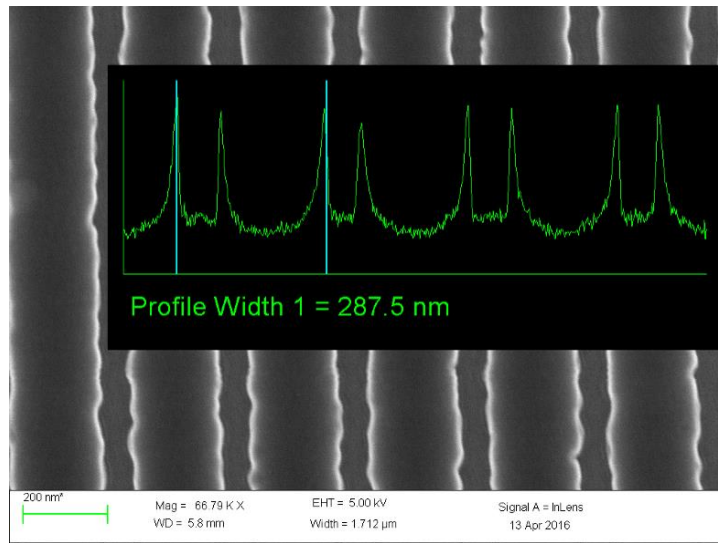
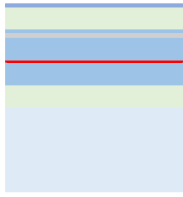
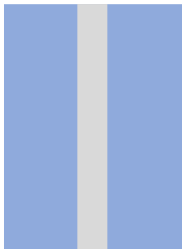
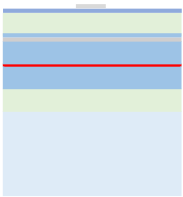
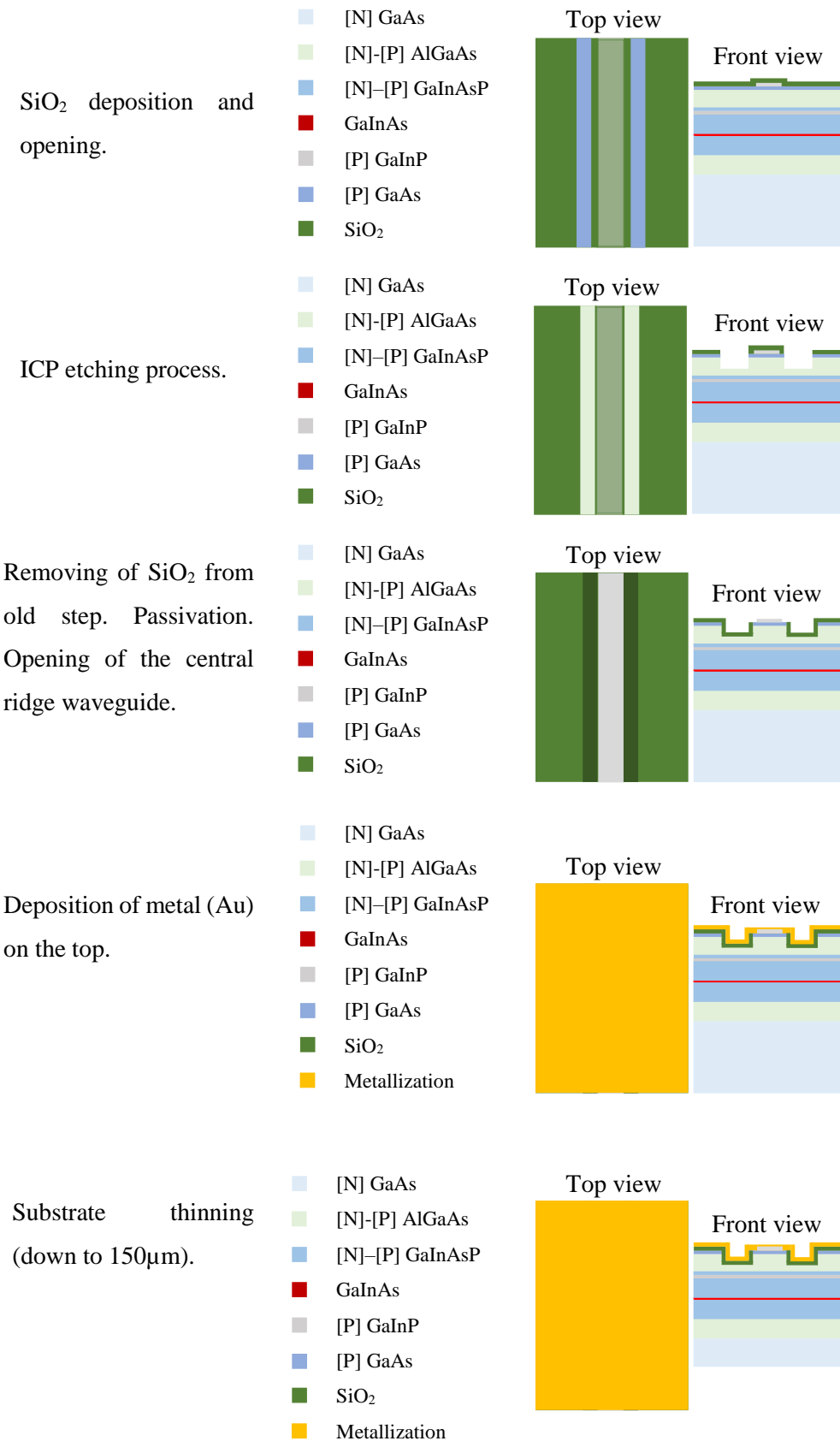


Figure II-15: SEM view of the patterned grating with the obtained period (inset).

Step description	Views
<p>After the grating patterning, the device is ready for the second growth epitaxy. In this step, the AlGaAs cladding and a deposition of P type AlGaAs layer graded index as strain compensation are processed. The last step corresponds to the deposition of P-type GaAs as contact layer.</p>	<div style="display: flex; align-items: center;"> <div style="margin-right: 20px;"> <ul style="list-style-type: none"> [N] GaAs [N]-[P] AlGaAs [N]-[P] GaInAsP GaInAs [P] GaInP [P] GaAs </div> <div style="text-align: center;"> <p>Top view</p>  </div> <div style="margin-left: 20px;"> <p>Front view</p>  </div> </div>
<p>After a de-oxidation of P-type GaAs layer with HCl/H₂O. Deposition of metal (Ti/Pt/Au) for the ohmic contact and lift-off of the metallization.</p>	<div style="display: flex; align-items: center;"> <div style="margin-right: 20px;"> <ul style="list-style-type: none"> [N] GaAs [N]-[P] AlGaAs [N]-[P] GaInAsP GaInAs [P] GaInP [P] GaAs </div> <div style="text-align: center;"> <p>Top view</p>  </div> <div style="margin-left: 20px;"> <p>Front view</p>  </div> </div>



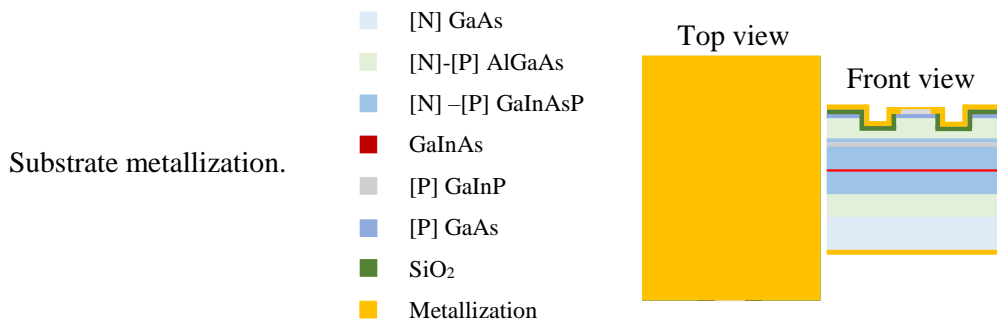


Table II-10: Main steps of the lithography process for the fabrication of the DFB grating and the ridge.

2.2.3 Properties of the facets coating

The section “*Chapter I -Structure and design parameters of an optical resonator with Bragg grating – Distributed Feedback architecture*” introduced the concept of mirror. To obtain a laser resonator architecture, the wafer is cleaved into bars and these last are cleaved into chips, whose facets are coated with dedicated dielectric materials. An issue of high-power LDs lies in the fabrication of robust mirrors at the facets. The energy heating the facet is concentrated in a small volume and the power density easily reaches values on the order of $10\text{MW}/\text{cm}^2$ [41]. The degradation of LD by facet oxidation, along with the other degradation modes, becomes more prevalent with higher Al fraction and the increasing of optical-power densities [42]. The process used to avoid facet oxidation is based on the passivation of facets. The LDs are cleaved in air and the facets are passivated with nitride and silicon barriers. In literature, it is reported different examples of the use of such a technique and it has been clearly established that a passivation process largely improves the reliability of high-power LDs [29]-[30]-[42].

Even though the LD has an “Al-free” optical cavity, part of the optical field propagates in the cladding ($\approx 10\%$), a layer with 33% Al-content. In *Figure II-16*, it is possible to highlight typical variations of the L-I curve for different LDs with 4mm cavity length without any coating or passivation on both facets (front and rear). These LDs were cleaved at the same time, then mounted on the same C-mount heatsink with the same conditions but the measurements were done at different times over a period of 4 months. It clearly appears that the COD threshold strongly decreases as a function of the measurement time assuming a larger thermal roll-over and COD sensitivity in operating conditions.

Thus, to avoid the oxidation process at the facets, a passivation layer is mandatory after the cleaving process. As this process is not realized in a vacuum chamber and to avoid oxidation of facets, the time between the cleaving and the passivation must be the lowest as possible.

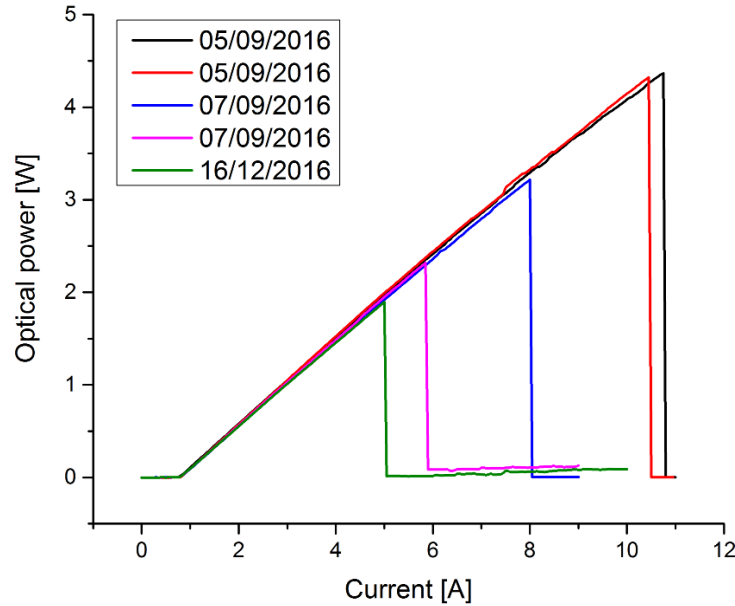


Figure II-16: COD threshold variations versus time measurement for LDs of a same batch without any coating or passivation layer applied on both facets.

The reflectivity of cleaved facet, with or without passivation, is nearly 33% and a coating of the facets with a layer or a stack of layers modifies this value. While the mirror on the rear side has a reflectivity over 90% (high reflectivity side/HR), the front mirror allowing for light extraction has a much lower reflectivity than 5% (anti-reflection side/AR). The value of AR reflectivity must be chosen carefully since the value of J_{th} depends mostly on it:

$$J_{th} = J_0 \exp\left(\frac{\alpha_i + \alpha_m}{\Gamma g_0}\right) \quad [Eq. II-9]$$

However, as reported in *Figure II-17*, the J_{th} strictly depends also on the AR coating. In “*Chapter I – Main electro-optical parameters of a high-power Laser diode*” we have analyzed the $WPE = \eta_D(I) \cdot \eta_U(I) \cdot \eta_{th}(I)$ and in this equation, there is a term that directly depends on the current threshold density, the $\eta_{th}(I)$. Because of that, in order to maximize the WPE, a particular attention must be paid to the choice of the AR reflectivity. For a DFB structure, the reflectivity and the optical losses at the mirror are modified. The equation $\Gamma g_{th} = \alpha_i + \alpha_m$ introduces the parameter α_m that

corresponds to the optical losses at the mirror, but the “true” losses can be achieved from the solution of a transcendental equation [43]. *Figure II–18* shows the relationship between the true mirror losses, the equivalent F-P reflectivity (at the emissive front facet of a LD) and the strength of the coupling factor “ κ ” for a DFB structure. A DFB LD vertical structure results from the fabrication of the grating layer and the true front facet reflectivity is never equal to the one experimentally measured via the spectrometer (*Figure II–18*). In our study, different materials and (HR, AR) coatings have been investigated (see *Table II-11*).

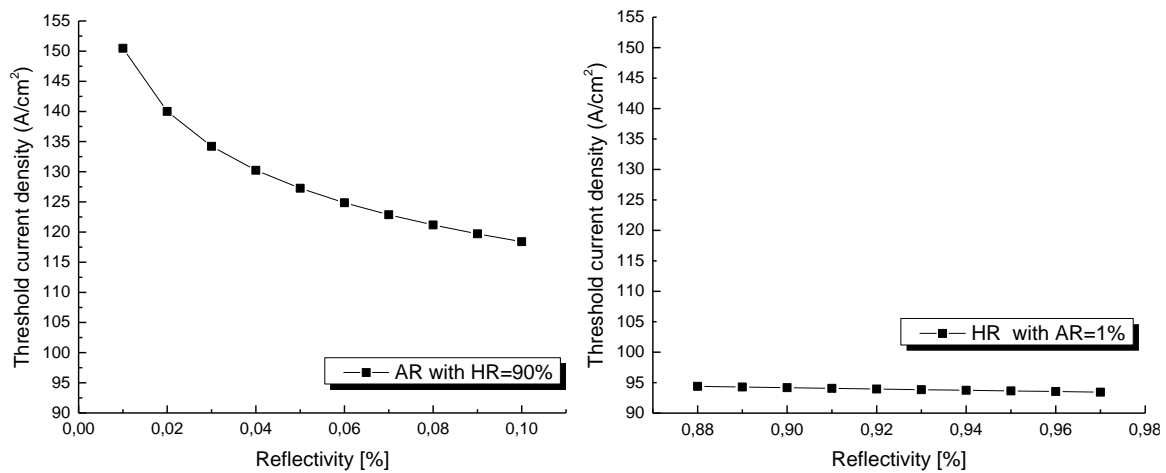


Figure II–17: Variations of J_{th} versus AR (assuming a 90% HR) or versus HR (assuming a 1% AR) reflectivity values. The AR reflectivity is clearly the predominant parameter.

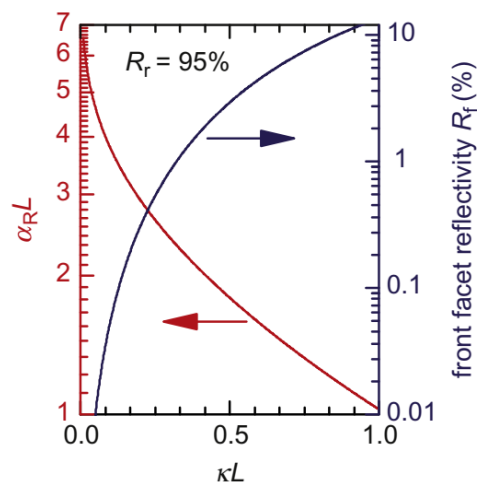


Figure II–18: Resonator losses of a DFB laser (left axis) and corresponding reflectivity of the front facet of an equivalent F-P laser (right axis) versus the coupling coefficient [44].

AR (1%)	HR (90%)
TiO ₂ /SiO ₂ (2 layers)	SiO ₂ /TiO ₂ (3 layers)
TiO ₂ /SiO ₂ (2 layers)	TiO ₂ /SiO ₂ (4 layers)

Table II-11: HR/AR facet coatings considered for this study (courtesy of III-V lab).

The AR mirror has a reflectivity of 1% with TiO₂/ SiO₂ (2 layers). A value of AR lower than 1% allows obtaining higher optical power but increases the threshold current.

Considering that the LD will be used as a pump source for the Er/Yb optical fiber, the highest value of optical power requires having an AR value lower than 1%.

For the HR facet, two different coatings have been considered: HR mirror of 90% with SiO₂/TiO₂ (3 layers) and 95% with SiO₂/TiO₂ (4 layers). The increase of HR reflectivity provides an increase of the optical output power (few %) at the front facet but can affect the LD robustness. Such an issue will be analyzed and discussed in the “*Chapter IV*”.

2.2.4 Device mounting process

Packaging is the ultimate but the most cost-consuming step. Packaging can cause mechanical strain on the active region and may lead to premature COD [45]. The soldering process needs to overcome two main issues:

- A high quality electrical contact,
- An optimized heat transfer coupled to the minimization of the strain and the stress induced by the different assembly process steps.

To improve heat transfer, recent literature reported on the effect of a microchannel liquid cooled assembly and for instance, X. Liu et al. demonstrated significant improvement in terms of thermal roll-over, WPE and thermal resistance [46].

The chip dimensions are relatively small compared to those of the heat sink and the submount, since the cavity is typically of few millimeters length and 350µm width. *Figure II-19* shows a picture of the final micro assembled device on the C-mount heat sink. As for all high power LD, the LD is soldered epi p-side down in order to increase the thermal dissipation. Different materials for the

submount can be used such as Copper-Tungsten (CuW) or Diamond- Copper composite (DCD) as well as different alloys such as Gold/Tin alloy or Indium as solder for the mounting of the chip.

It is well-established now that a CuW submount provides a much lower thermal expansion rate compared to pure copper while maintaining a necessary thermal conduction one [47]. In our case, it is possible to solder the CuW submount on top of the C-mount heatsink at III-V lab facilities or buy a CuW submount directly connected to the C-mount heat sink. In this last case, a dedicated soldering process is used at high pressure and temperature and part of the CuW can diffuse into the surface of the C-mount heatsink, creating an intermixing zone at the interface.

During the soldering operation or continuous wave operation, the micro assembled device heats up. In both cases, the different materials show different geometrical changes due to the Coefficient of Thermal Expansion (CTE) mismatch. In order to avoid thermomechanical failures of the LD, the CTE of the submount (around $6 \cdot 10^{-6} K^{-1}$), needs to be closer as possible to that of the GaAs substrate one. *Table II-12* gives the thermo-mechanical properties of the main materials constituting the micro assembled device.



Figure II-19: Optical view of the final micro assembled device on a C-mount heat sink.

Material	CTE [ppm/K]	Thermal conductivity @ 300K [$\frac{W}{m \cdot K}$]	Young's modulus [GPa]	Poisson's ratio
CuW	6,5	180	300	0,284
DCD	3	600	841	0,316
Au ₈₀ Sn ₂₀	16	58	59,2	0,405
In	32,1	82	11	0,4498
GaAs	5,73	55	85,5	0,314
Copper	16	401	117	0,355

Table II-12: Mechanical and thermal properties of the main materials constituting the microassembled device [9]-[48]-[49].

The Gold/Tin (AuSn) eutectic solder allows the absorption of the mechanical stress while Indium (In) is preferentially used as soft solder when the CTE mismatch is not considered as critical [50]. Even if the CTE mismatch is large between GaAs and Cu, it is possible to use Indium as a solder thanks to its strength and malleability. However, the thermomechanical stress and the elevated temperature when the LD operates at high output power, limit significantly the applicability of soft solders [46]. The nature and the quality of the die-attach solder can dramatically reduce the reliability of high-power LDs and a higher COD threshold can be obtained with AuSn solder compared to Indium solder. For high-power LDs (~10W in CW regime), the lifetime with indium solder reaches 500 hours while lifetime increases over 1600 hours with AuSn solder [46]. So, the CuW submount combined with AuSn solder appears as the best solution to provide both good thermal conductivity and thermal expansion matching those of GaAs. *Figure II–21* shows a cross-section view of the region surrounded by a red square in *Figure II–20*.

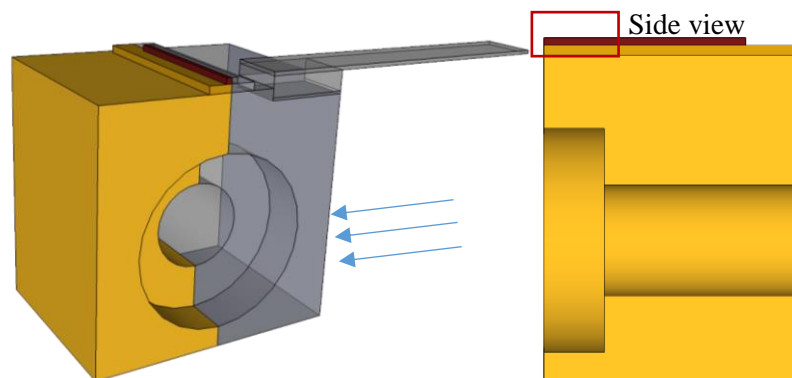


Figure II–20: 3D schematics and longitudinal section of LD mounted on C-mount heatsink.

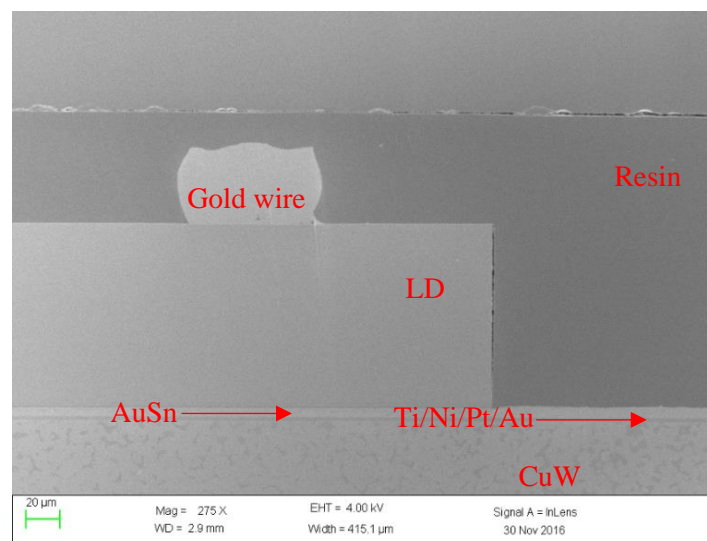


Figure II–21: SEM view of the longitudinal cross-section corresponding to an enlargement of the red square in Figure II–20.

Short summary

In this section, we described the overall process fabrication of the LD. Starting from the GaAs substrate, we detailed all the technological steps used to grow the different layers (AlGaAs, GaInAsP and GaInAs) and to define the ridge width. In “*Chapter II-Description and comparison of the III-V lab vertical laser structures*”, we have studied the DFB grating and calculated the pitch to operate in a DFB mode at 975nm. In this chapter, the grating structure has been processed and a DFB LD has been fabricated. We have analyzed the effects of facet coatings on the DFB coupling factor. Finally, we studied the device mounting and how different die-attach materials (AuSn or In) can affect the reliability of the LD.

In the following section, we will introduce the different test benches used for electro-optical characterizations of the LDs and the methodology for the extraction of the main internal/external parameters.

2.3 ELECTRICAL AND OPTICAL CHARACTERIZATIONS

In this section, the different experimental setups for the CW and pulsed L-I-V characteristics of high-power F-P LDs are described. All the test benches are used to extract the main parameters of our LDs enabling to assess performances of each vertical structure.

First, a detailed description of the setup dedicated to the CW L-I-V characterization is given. With this setup, it is possible to extract some external parameters such as η_E , η_D , I_{th} , R_S , V_{th} , and to perform spectral measurements. Secondly, a description of the setup developed for pulsed L-I-V measurements is given allowing to determine the internal parameters such as α_i , η_i , J_{tr} , G_0 , T_0 , T_1 . The pulsed L-I-V setup is used to avoid self-heating of the LDs and, therefore, to obtain accurate extrapolation of the external parameters. Third, in a final subsection, spectrum and far field measurements for each vertical structure are also performed.

2.3.1 L-I-V curves in CW and pulsed regime: setup and results

LDs of each vertical structure were tested with the C-mount heat sink mechanically contacted with a temperature-controlled gold-plated copper test fixture. The LDs have been characterized under CW conditions with a heat sink temperature maintained at 20°C using a temperature sensor

located in the rear edge of the C-mount. The optical power is measured with a calibrated photodiode connected to the integrating sphere. The detection head of the power meter has an aperture of 30,5mm and an accuracy of $\pm 3\%$ reading value. The optical spectrum is measured with an Optical Spectrum Analyser (OSA) MS9740A from Anritsu. The accuracy is estimated to be $\pm 1\text{pm}$ around 980nm. The calibration is done using a thermopile power meter from THORLABS as an “etalon”. The test bench is composed of a THORLABS current supply (ITC 4020) biasing both the LD and the thermoelectric cooler (TEC). The supply source of the LD has a maximal output current of 20A with a maximal voltage of 5V and a current accuracy of $\pm 0,1\%$ of the reading value + 8mA. The TEC current control has an accuracy of $\pm 0,2\%$ of the reading value + 8mA. The integrating sphere has two outputs (photodiode sensor and multimode fiber) to collect the received light. A multimeter 34401A from AGILENT reads the output voltage of the photodiode located in the integrating sphere and the other multimeter 34401A performs 4-wires measurement of voltage (see *Figure II–22*). The multimeter 34401A has an accuracy of $\pm 0,0035\%$ of the reading value + 0,0005% range, in this case 10V. All the setup is remotely controlled via a home-made LabView® software. This last automatically collects the L-I-V data and then generates an Excel file with all the extracted parameters and relevant plots.

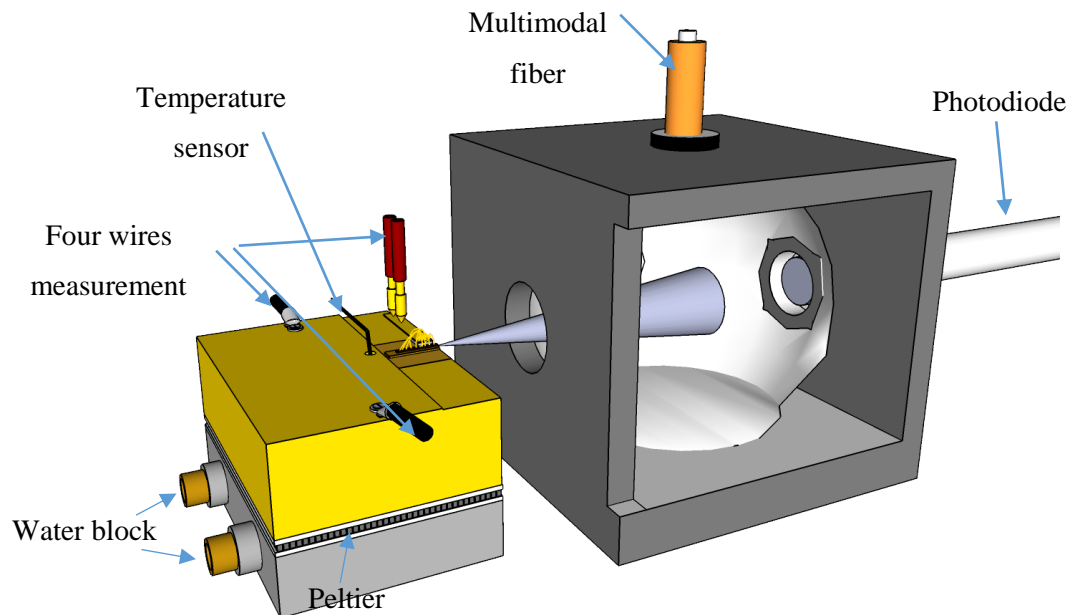


Figure II–22: Setup for the measurement of L-I-V curves in CW regime.

Figure II–23 shows a typical CW L-I-V curve obtained from a 4mm cavity length SLOC LD. From these curves, the software deduces some parameters such as: η_E , I_{th} , R_S , V_{th} . The value of η_E is

extracted from a linear interpolation at the beginning of the L-I curve above the current threshold and the value of R_s as well as V_{th} are extracted at high levels of current ranging from 7 to 10A.

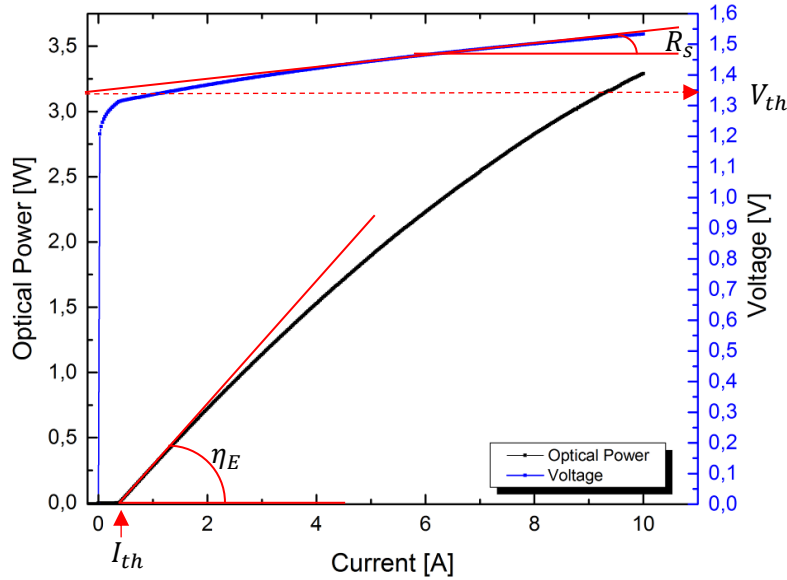


Figure II-23: Typical CW L-I-V curves obtained for a 4mm cavity length SLOC LD with 33% reflectivity for each facet.

Figure II-24(a) compares the L-I-V curves of three LDs from each vertical structure. The P(I) and WPE(I) curves are representative of the performances achieved with the structure. All the LDs are coated with $\text{SiO}_2/\text{TiO}_2$ HR equal to 95% and $\text{TiO}_2/\text{SiO}_2$ AR equal to 1%. The LOC structure has a lower threshold current and because of that, a maximum WPE is reached before the SLOC and AOC devices. The maximum of the term $\eta_{th}(I) = \frac{(I-I_{th})}{I}$, presented in [Eq. I-17]. ($WPE(I) = \frac{q}{h\nu} \cdot \eta_E(I) \cdot \eta_U(I) \cdot \eta_{th}(I)$), is strictly related to the values of I_{th} .

The SLOC structure has a slope efficiency higher than the previous structure, and consequently a higher WPE. For high values of current ($> 5A$), the WPE remains higher than for the LOC structure within the range 4-12A. The AOC has $\eta_E(I)$ almost equal to the values of SLOC or LOC, but because of the higher I_{th} , the $\eta_{th}(I)$ is lower as well as the WPE. Table II-13 summarizes the typical values of external parameters for the three vertical structures (4mm cavity length).

Vertical structure	Max WPE [%]	I_{th} [A]	R_s [mΩ]	Max η_E [W/A]	Max $\eta_{thmax}(I)$ [%]
LOC	52 @ 3,2A	0,9A	20,3	0,93	98 @ 10A
SLOC	55 @ 4A	0,55A	32,4	0,95	94 @ 9A
AOC	55 @ 8A	0,65A	16,5	0,93	90 @ 11,5A

Table II-13: External parameters obtained for each structure (4mm cavity length).

Nevertheless, because the optical power does not saturate, the WPE remains almost constant even at high values of current for the three vertical structures. At 12A, the WPE for the LOC, SLOC and AOC decreases respectively from 12%, 10% and 5%.

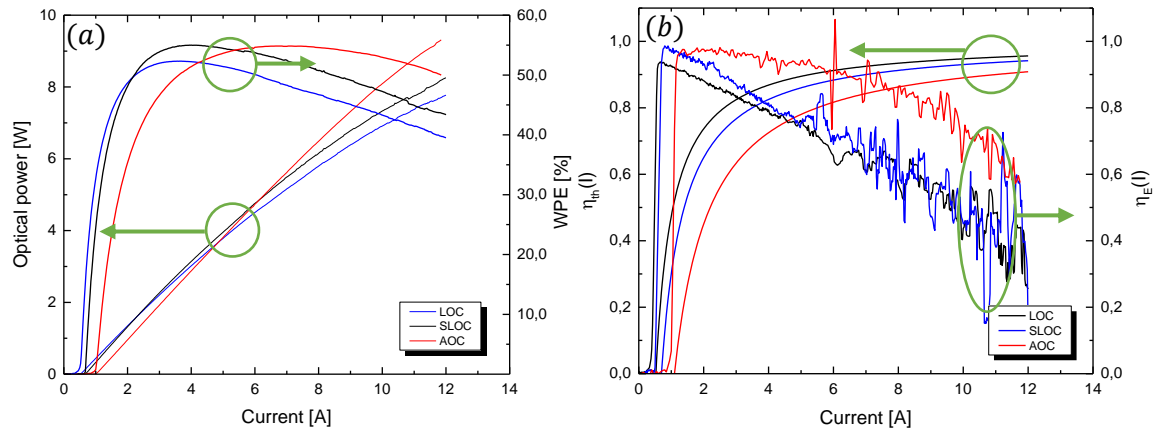


Figure II-24: CW L-I-V curves for the three vertical structures (4mm cavity length) with HR 95% and 5% AR coatings.

From *Figure II-24(b)*, the high values obtained for η_{th} and η_E at low values of current can be highlighted. When η_{th} reaches its maximum, η_E has already decreased. Such an effect is more obvious for the AOC structure. Because of that, the maximum value of WPE for the AOC structure cannot be higher than the one for the LOC structure.

The pulsed measurement is performed with the “2520 Pulsed Laser Diode Test System” developed by KEITHLEY, consisting in an integrated and synchronized system for testing LDs. This setup can perform pulsed L-I-V testing up to 5A (500ns pulse width) to deduce the internal parameters of a LD as described in *Figure II-25*.

The main interest of pulsed L-I-V measurements is to reduce as far as possible the self-heating phenomenon (or at least reducing it to become negligible) compared to the CW regime and responsible of an erroneous extraction of its intrinsic parameters. In addition, it is possible to calculate the characteristic temperature for the three vertical structures, as described in “*Chapter I – Main electro-optical parameters of a high-power Laser diode*”. *Figure II-26* shows typical pulsed L-I curves for the three vertical structures and *Table II-14* summarizes the experimental values of the characteristic temperature.

LD Structure	T_0 [K]	T_1 [K]
LOC	86	424
SLOC	128	754
AOC	171	659

Table II-14: Extracted characteristic temperatures of each vertical structure (4mm cavity length).

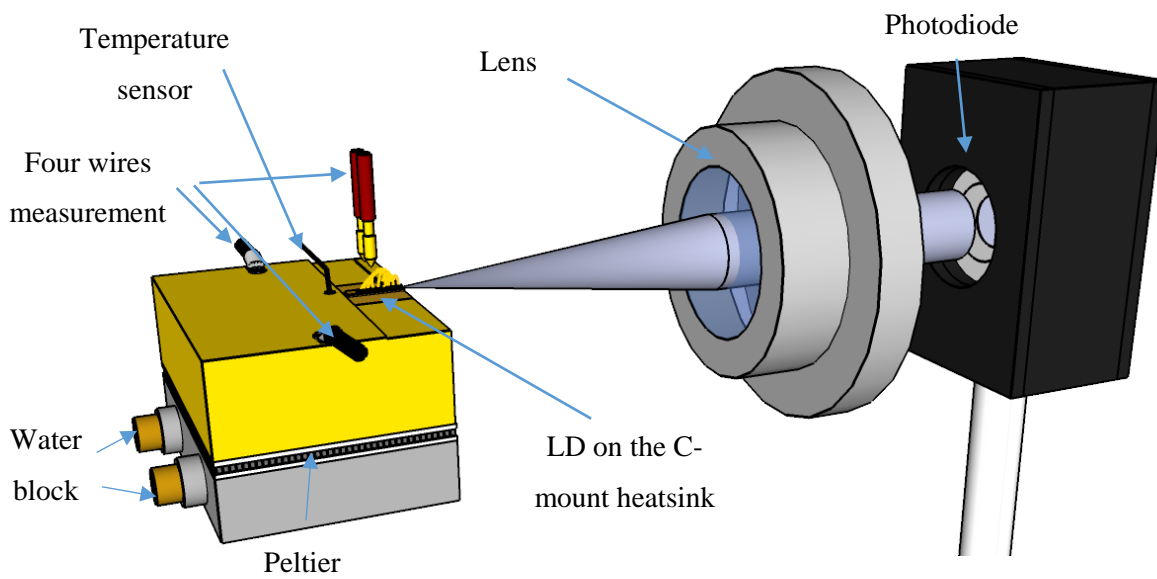


Figure II-25: Setup for pulsed L-I-V measurement.

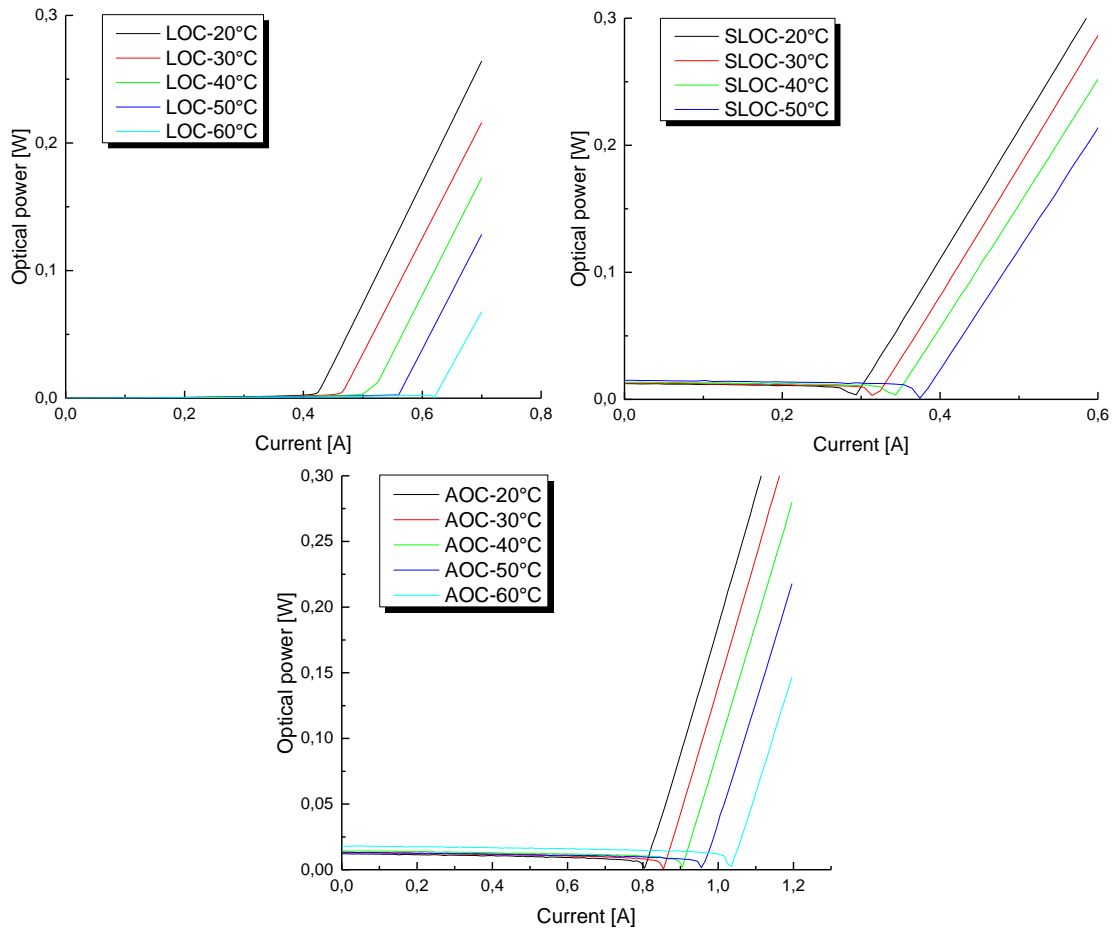


Figure II-26: Typical pulsed L-I curves for the three vertical structures measured at different temperatures. The 4mm cavity length LDs have a passivation layer to avoid facet oxidation but no facets coating.

Short summary

The SLOC structure highlights the best WPE regarding the three vertical structures but with the highest value of series resistance. The AOC structure gives the best values of characteristic temperature ($T_0=171$ K compared to 128 K and 86 K for the SLOC and LOC) and series resistance but reaches the maximum of WPE at high levels of current. Hence, the maximal value of WPE is lower than the other structures. Finally, the LOC structure reaches the maximal value of WPE before the one extracted from the other structures but gets the worst $\eta_E(I)$. Hence, the WPE does not remain constant for high values of bias current.

As we can conclude, all three structures have their own pros and cons and so the final choice of the suitable vertical structure will depend on the final targeted application.

2.3.2 Experimental extraction of internal parameters

In order to extract the internal parameters, it is necessary to use three different cavity lengths for each vertical structure. For the LOC and AOC structures, three cavity lengths have been used equal to 2, 3 and 4 mm respectively while for the SLOC structure, three other cavity lengths (1,6-2-2,5 mm) have been chosen and four LDs have been considered for each length.

With the setup given in *Figure II-25*, the measurement of pulsed L-I-V curves has been performed up to 2A. All LDs are mounted with CuW submount on a C-mount heatsink. The LDs are cleaved without coating; there is a passivation layer at both facet to avoid oxidation. The TEC sets a constant temperature of 20°C at the bottom of the C-mount heatsink. The internal parameters of each LD are calculated from the external parameters experimentally determined. In “*Chapter I – Main electro-optical parameters of a high-power Laser diode*” we have written $P_{out} = \eta_D \cdot \frac{h\nu}{q} \cdot (I - I_{th})$. From the differential quantum efficiency, it is possible to calculate the internal parameters of the LD. Hence, one can write:

$$\eta_D = \eta_i \cdot \frac{\alpha_m}{\alpha_i + \alpha_m} = \eta_i \cdot \frac{\frac{1}{2L} \cdot \ln\left(\frac{1}{R_1 R_2}\right)}{\alpha_i + \frac{1}{2L} \cdot \ln\left(\frac{1}{R_1 R_2}\right)}$$

$$\frac{1}{\eta_D} = \frac{1}{\eta_i} \cdot \frac{\alpha_i + \frac{1}{2L} \cdot \ln\left(\frac{1}{R_1 R_2}\right)}{\frac{1}{2L} \cdot \ln\left(\frac{1}{R_1 R_2}\right)} = \frac{1}{\eta_i} \cdot \left[\frac{2L\alpha_i}{\ln\left(\frac{1}{R_1 R_2}\right)} + 1 \right]$$

$$\frac{1}{\eta_D} = \frac{1}{\eta_i} \frac{2\alpha_i}{\ln\left(\frac{1}{R_1 R_2}\right)} \cdot L + \frac{1}{\eta_i}$$

[Eq. II-10]

From [Eq. II-10] and using the values of the differential quantum efficiency (η_D) as well as the reflectivity of the facets, it is possible to calculate the following parameters:

- Internal quantum efficiency (η_i)
- Internal losses (α_i)

Plotting the $\frac{1}{\eta_D}$ as a function of the cavity length (L) and through a linear regression, these parameters can be extracted based on the data reported in *Figure II-27*. Then, the results are summarized in *Table II-15*.

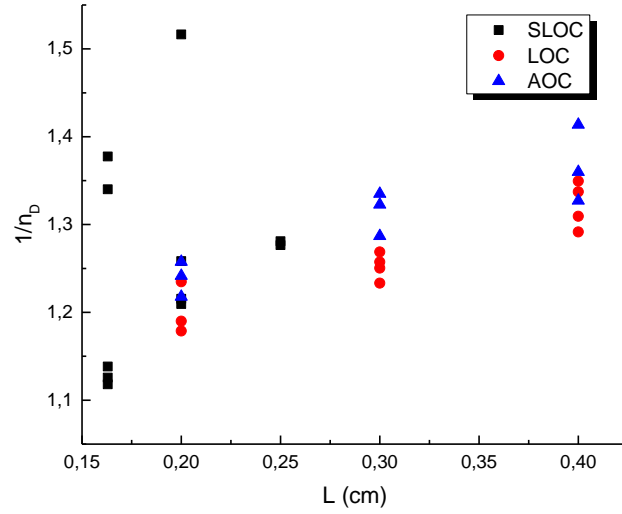


Figure II-27: Plot of experimental differential quantum efficiencies versus LD cavity length for extrapolation of internal parameters considering the three structures.

In chapter I, we have considered the [Eq. I-8] that establishes the amplitude condition providing the lasing effect of a LD and it is possible to substitute the value of g_{th} using the definition of the material gain, $g_{mat} = g_0 \cdot \ln\left(\frac{J}{J_{tr}}\right)$. Hence, we can write:

$$\begin{aligned}
 \Gamma g_{th} &= \Gamma g_0 \cdot \ln\left(\frac{j_{th}}{j_{tr}}\right) = \alpha_i + \frac{1}{2L} \ln\left(\frac{1}{R_1 \cdot R_2}\right) \\
 \Gamma g_0 \cdot \ln\left(\frac{j_{th}}{j_{tr}}\right) &= \alpha_i + \frac{1}{2L} \ln\left(\frac{1}{R_1 \cdot R_2}\right) \rightarrow \Gamma g_0 [\ln(j_{th}) - \ln(j_{tr})] \\
 &= \alpha_i + \frac{1}{2L} \ln\left(\frac{1}{R_1 \cdot R_2}\right) \\
 \ln(j_{th}) &= \ln(j_{tr}) + \frac{1}{\Gamma g_0} \left[\alpha_i + \frac{1}{2L} \ln\left(\frac{1}{R_1 \cdot R_2}\right) \right] \\
 \ln(j_{th}) &= \frac{1}{2\Gamma g_0} \ln\left(\frac{1}{R_1 \cdot R_2}\right) \cdot \frac{1}{2L} + \ln(j_{tr}) + \frac{\alpha_i}{\Gamma g_0} \tag{Eq. II-11}
 \end{aligned}$$

Plotting the $\ln(j_{th})$ as a function of $1/L$ and through a linear regression, we can extrapolate the parameters Γg_0 (modal gain) and the j_{tr} (current density transparency) by using the data of *Figure II-28*. The results are also given in *Table II-15*.

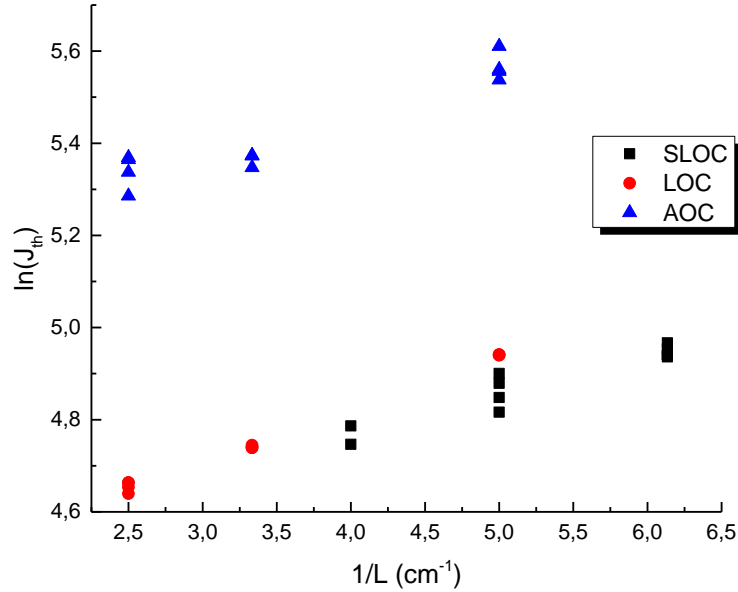


Figure II-28: Plot of current transparency density versus LD cavity length for extrapolation of internal parameters considering the three structures.

LD Structure	η_i	α_i [cm ⁻¹]	J_{tr} [A · cm ⁻²]	ΓG_0 [cm ⁻¹]
F-P LOC	0,92	0,62	73,6	9,76
F-P SLOC	0,91	0,6	82,5	13,90
F-P AOC	0,9	0,64	153	13,42

Table II-15: Internal parameters extracted for each vertical structure.

Each vertical structure shows a high internal quantum efficiency ($\eta_i > 0,9$) and very low internal losses ($\alpha_i < 0,7$ cm⁻¹) in very good agreement with the state-of-the-art results, recently published on high-power LDs and described in “*Chapter I*”.

The η_i represents the probability of a photon obtained from a transition of an electron from the conduction band to the valence band within the optical cavity and gives information about the percentage of the radiative recombination in the QW. Finally, a value close to one is related to a very low rate of non-radiative recombination.

The α_i , gives important information about the quality of semiconductor layers (in particular related to scattering [51]) and the overlap of the optical modes with the cladding layers (free carriers absorption). Considering the low values obtained with our technology whatever the considered structure, we do assume that our design of the three vertical structures is now optimized.

The modal gain ΓG_0 represents the material gain adjusted to take into account the poor overlap that always exists between the optical mode and the medium gain, as described in “*Chapter I–Quantum well structure*”. The modal gain is caused by the generation of a photon due to the transition of an electron from the conduction band to the valence band. A high value of the modal gain gives both a strong generation of stimulated photons and a high level of output optical power. One can note that vertical structure, having multiple QWs such as the AOC one, will present a higher modal gain. The values of ΓG_0 strongly differ from one vertical structure to another and in particular between the LOC and SLOC structures. Even if the AOC has an optical cavity thickness similar to the LOC, the modal gain value is quite similar to the SLOC because of two QWs.

The J_{tr} represents the optical gain threshold. It is sensitive to material quality such as defects, traps and non-radiative recombination sources and a low value of J_{tr} is better. The low values of transparency current are in good agreement with the obtained results for the LOC and SLOC vertical structures. The AOC vertical structure has a double QW, hence the J_{tr} is almost twice compared to the previous ones.

2.3.3 Far field measurements

Small vertical divergence angle (with at least 90% of optical power) allows minimizing the power loss and aberrations during the beam collimation. Most applications need a low vertical divergence angle. The reduction of the vertical divergence angle makes the beam shaping easier and more efficient. Finally, optical systems are less expensive and robust.

With the setup presented in *Figure II–29*, the far field has been measured for each vertical structure.

The setup is quite similar to the CW L-I-V setup given in *Figure II–22*, but instead of collecting the light with the integrating sphere, we use an automatic rotating camera from COHERENT, in order to extract the fast and slow axis of the far field divergence. The front facet of LD is aligned to the rotating camera. Then we choose to keep a distance equal to 1 cm between the front facet LD and the camera in order to obtain a propagation of the light from the front facet.

Figure II–30 compares the fast axis divergence for each vertical structure measured at 20°C and 1A bias current. These experimental results confirm the lowest fast axis divergence of the SLOC structure in particular due to the higher thickness of the optical cavity. Through the previous optical simulations, the predicted values of the vertical divergence (Θ_v @ FWHM) for the three structures are known and in *Table II-16*, a comparison between the theoretical and experimental fast axis divergence is reported for LDs with 4mm cavity length.

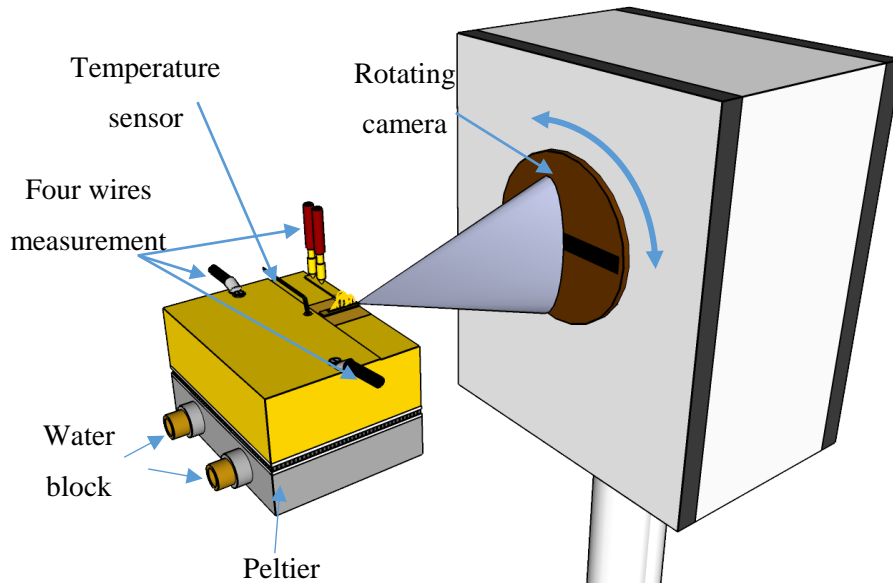


Figure II-29: Setup developed for far field measurement.

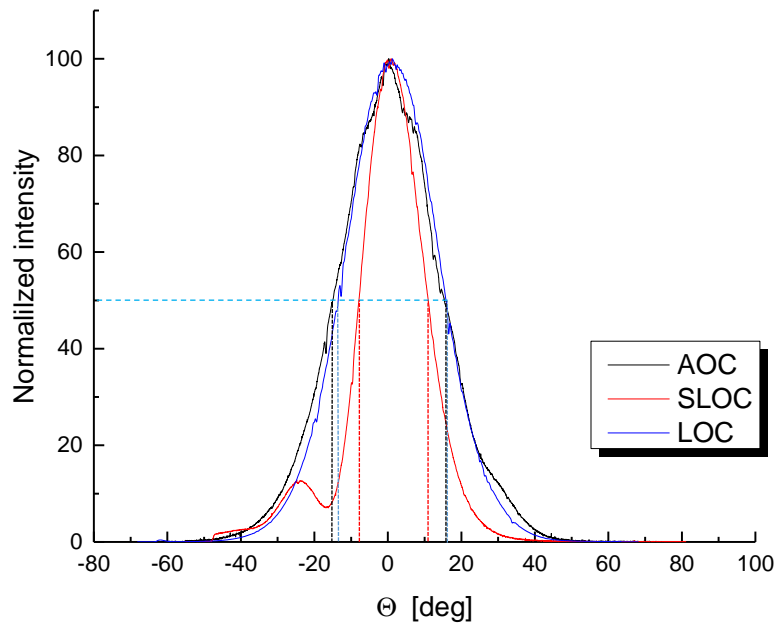


Figure II-30: Fast axis divergence for each vertical structure measured at 20°C and 1A.

Vertical structure	Theoretical Θ_v [°]	Experimental Θ_v [°]	Relative error [%]
F-P LOC	31	32	3,12
F-P SLOC	18	18	0
F-P AOC	30	33	0,09

Table II-16: Comparison between predicted and experimental values of Θ_v for each vertical structure.

2.3.4 Spectral properties

For the spectral measurement, the setup presented in “*Chapter II- L-I-V curves in CW and pulsed regime: setup and results*” is used and reported in *Figure II-22*. The optical spectrum analyser, Anritsu MS9740A, has a maximum accuracy of $\pm 1\text{pm}$ near 980nm. High-power LDs emitting near of 980nm are more and more used to provide the optical power for fiber lasers or amplifiers pumping mainly addressing LIDAR and micro-machining applications. The Yb, Er and Er/Yb doped optical fibers have a very narrow absorption line close to 975nm but a higher absorption compared to the 915nm-940nm surrounding wavelength region. Due to the large number of excited modes in broad area F-P LD, the spectral width is typically bigger than the optical absorption of an Er/Yb optical fiber (1 to 2 nm) as shown in *Figure II-31*. Nevertheless, due to temperature shifting, high-cost temperature stabilization setup or external wavelength-lock devices such as Volume Bragg Grating (VBG) are mandatory to maintain pumping efficiency and stability [52]. In order to reduce such additional high cost and the inconvenient use of external devices, in particular for their sensitivity to mechanical disturbances, nowadays are available different solutions. High-power monolithically wavelength-stabilized LDs such as distributed Bragg reflector (DBR) and DFB lasers are today under investigations to achieve the best compromise between optical output power versus temperature drift [41]. To validate the optical simulations, it is possible to calculate the effective index from the optical spectrum using $\Lambda = m \frac{\lambda_B}{2n_{eff}}$. *Table II-17* compares the simulated effective index and the experimental value. The experimental results confirm the good results obtained from optical simulations since a relative error lower than 0,04% is achieved.

	Simulation η_{eff}	Experimental η_{eff}	Relative Error
LOC	3,3839	3,3807	0,025%
SLOC	3,3906	3,3754	0,041%

Table II-17: Effective index for two different vertical structures (we remind that no DFB grating was realized with the AOC structure).

Due to the coupling of the optical field with the DFB grating, the spectral width is significantly reduced as displayed in *Figure II-32*. Based on a spectral width lower than 1nm, it is possible to efficiently pump the core of the optical fiber. Moreover, a DFB structure increases the wavelength stability of the LD spectrum as a function of the temperature.

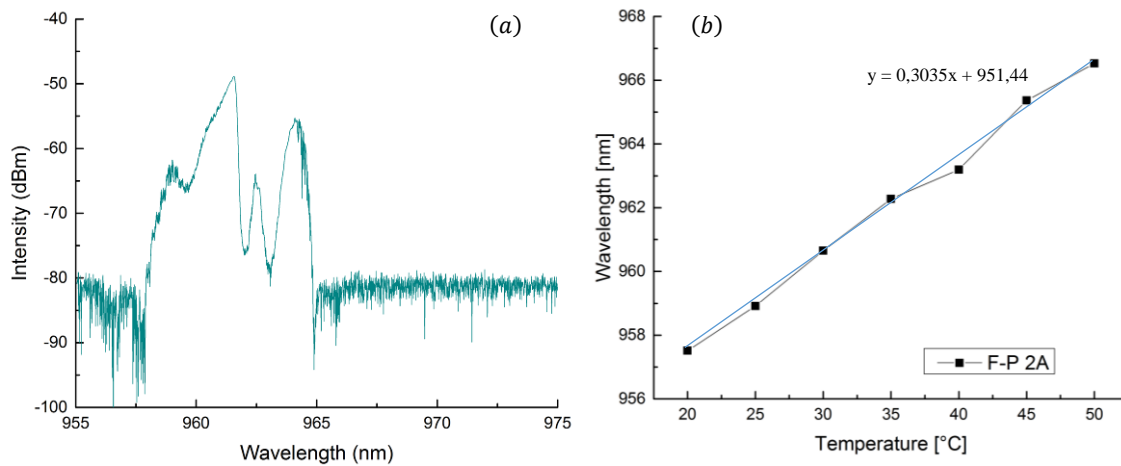


Figure II-31: (a) Optical spectrum for an F-P 4mm cavity length SLOC LD measured at 20°C and 1A. The spectral width is over 5nm. (b) Spectral drift versus temperature measured at 2A.

The spectral width of such a LD is larger than 5nm and because of the very narrow spectral absorption of the Er/Yb fiber, it is not suitable for the pumping. The obtained detuning with temperature is close to 0,3nm/°C. In comparison with the DFB structure, the spectral drift with the temperature is limited to 0,08nm/°C. For the LOC structure, it is possible to obtain the same results in terms of optical spectrum and spectral drift with the temperature. We remind that we have not design any AOC-based DFB structure. Finally, we demonstrate the possibility to fabricate DFB-LDs presenting high optical power and WPE as well as a narrow spectral width and operating up to 60°C.

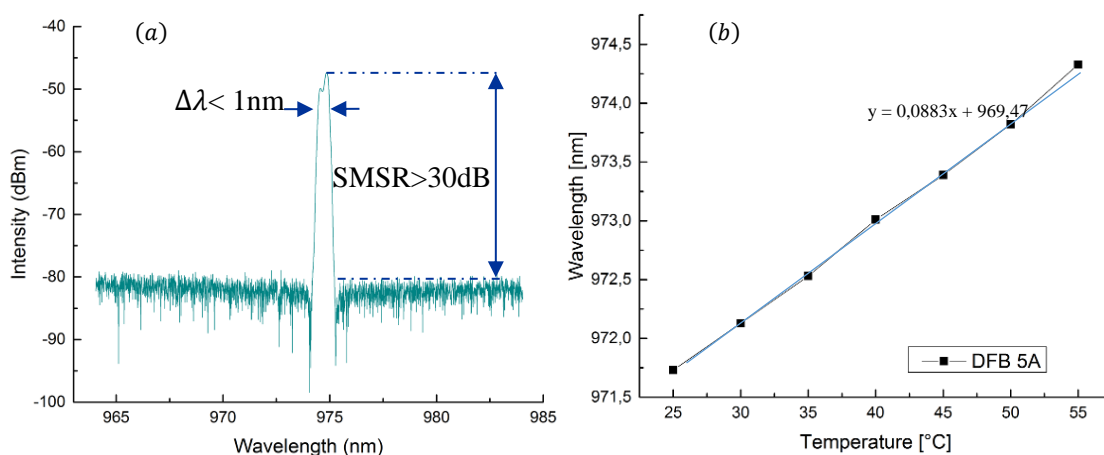


Figure II-32: (a) Optical spectrum for a DFB 4mm cavity length SLOC LD measured at 60°C and 5A. The spectral width is lower than 5nm. (b) Spectral drift versus temperature measured at 5A.

2.3.5 Comparison of main experimental electro-optical performances for the three vertical structures

Table II-18 summarized the main experimental electro-optical performances of each vertical structure (4mm cavity length) considering mainly the maximal WPE, the COD threshold, the vertical divergence and the internal losses.

Vertical structure	WPE max [%]	J_{COD} [A/cm ²]	θ_v [°]	α_i [cm ⁻¹]
F-P LOC	52	$8,5 \cdot 10^2$	31	0,35
F-P SLOC	55	$10 \cdot 10^3$	18	0,29
F-P AOC	55	$7,14 \cdot 10^2$	30	0,58

Table II-18: Main electro-optical performances for each vertical structure (4mm cavity length).

- The vertical divergence of the LOC structure, that was the first one considered in this study, allows obtaining 82% of the output power into an optical fiber around 1W in CW regime. Based on the current density J_{COD} , the experimental COD threshold, in CW operation, is observed to reach 12A.
- In order to increase the coupling efficiency into the Er/Yb optical fiber and to reach the highest COD threshold, a new vertical structure was proposed, namely the SLOC. Such a structure, for a 4mm DFB cavity length, reveals a COD threshold, in CW operation, near of 14A that is significantly higher compared to that of the LOC vertical structure. In addition, the coupled output power into the Er/Yb optical fiber increases up to 87%. The WPE reaches its maximum (55%) at 4A and then decreases for high values of bias current (up to 10% from the maximum at 10A). Unfortunately, the increase of the overall structure thickness compared to the LOC one results in a higher series resistance (30% more than LOC). In addition, the fill factor of modes in the quantum well is almost the half of the LOC structure ($\Gamma_{LOC} = 1,2\%$) resulting in a higher threshold current that consequently has a negative impact on the WPE. In this context, a new design of vertical structure (AOC) has been implemented. The optical losses in the cladding are not negligible and can decrease the COD threshold. For a 4mm cavity length, the COD threshold, in CW operation, reaches 10A. The WPE reaches its maximum (55%) at 8A and then decreases for high values of bias current (up to 5% from its maximum at 10A).

To provide a better heat exchange and whatever the considered vertical structure, all the high-power LDs are mounted epi p-side down. Because of the design of the vertical structure, the optical cavity of the AOC structure is located near of the heat sink compared to the LOC or SLOC ones that can irremediably provide a higher thermomechanical stress on the active region (so lower the COD threshold) and require an optimized thermal management of the micro assembled LD. The chapter III will address and discuss this issue.

CONCLUSION

This chapter aimed to describe the proposed LDs from a technological point of view and report on the results of electrical and optical characterizations enabling to determine their main intrinsic performances. This chapter has addressed three main parts.

In the first section, three vertical structures, developed in the cleanrooms of III-V lab (LOC, SLOC and AOC), have been studied. Taking benefit from its solid experience in the development of high-power LDs in the IR band, the considered devices are grown in one (for F-P LD) or two (for DFB LD) steps using a metal-organic vapor phase epitaxy (MOVPE) on 2" GaAs wafers. The overall structure of the LD is based on the edge double trench planar structure and an "Al-free" optical cavity with a 90 μm wide strip. Each design has been described with a specific emphasize on the main differences in terms of materials, thickness of layers and doping levels. Through dedicated optical simulations using both analytical models and FIMMWAVE® tools, some key parameters of the LDs have been determined: series resistance and optical losses, coupling factor, far field divergence and spectral width of the DFB versus F-P optical spectrum.

The effect of the cavity length is clearly shown on the series resistance of each structure that represents the main source of thermal dissipation at high levels of bias current. Considering this effect, the innovative AOC structure reveals one of its main advantage, demonstrating a very low series resistance (ex. 10m Ω for a 4mm cavity length) but the highest value of internal losses (0,6 cm^{-1}) whatever the cavity length, in comparison with the two other structures (LOC and SLOC). Their vertical refractive index profile has been also calculated, predicting an excellent optical confinement factor ($> 2\%$) of the AOC design.

Because of the performance requirements for the targeted application, the spectral envelop width needs to be reduced lower than 1nm. For that, a specific DFB structure has been processed (only for the LOC and SLOC structures) that remains a challenge for high-power LDs since only few

research centers succeeded in its development. With these optical simulations, the properties of the DFB vertical structure have been studied to predict the theoretical coupling factor and the spectral width as well as analyze the influence of the grooves depth on the optical confinement. The coupling factor depends on the imperfection of the real shape of the grating. Thus, it has been of interest to investigate on the influence of the relative mark length on the values of κL for a first- and second-order grating. Clearly, the second-order grating is the most affected by variations of the relative mark length compared to the first-order grating. However, a second-order grating was chosen because of the main difficulties to pattern a first-order grating using the e-beam technique that requires a very short pitch ($\Lambda \approx 100\text{nm}$). We used the second-order square shape grating with a relative mark length equal to 25% allowing to obtain: $\kappa L \approx 0,92$ or $\kappa L \approx 1,3$. Finally, a grating pitch equal to 290nm has been successfully implemented that is more compatible with e-beam resolution of III-V lab facilities.

The emission facet of the LD is subjected to a huge local heating effect due to a recombination process at the GaAs-Air interface and the reabsorption phenomenon of the emitted light particularly. The first one is significant at low optical power while the last one dominates at high levels of optical output power bringing a rapid increase of both the facet temperature resulting in the well-known COD. To prevent the LDs and enhance their robustness to COD, a Non-Injecting Mirror (NIM) window has been proposed and its effect on the far field divergence has been particularly analyzed since the near field does not change significantly. The slow axis divergence is not affected by the vertical position of the NIM while the fast axis divergence increases and the far field intensity decreases as function of the NIM vertical position. Based on simulation results, an optimized design of the NIM window has been proposed according the following recommendation:

- A vertical position equal to $0,4\mu\text{m}$ keeping the fast axis divergence and the far field intensity quite unchanged.
- An etching depth equal to $0,5\mu\text{m}$ for both NIM length. With such an etching depth, the NIM reaches the p-side cladding layer ensuring an electrical insulation in the region of the emissive facet.

A second section has given the complete description of the vertical structure fabrication process including in particular the core emissive structure, the patterning of the grating based on the e-beam technique in good agreement with the proposed one by simulations and the facets coating preventing from their oxidation and COD. The device mounting process is also detailed including

the study of different die-attach materials (Gold-Tin and Indium), the nature of the submount acting as a thermomechanical compensator (Copper-Tungsten and Composite-Diamond) and then mounted on a C-mount heat sink (in Copper). The mechanical mounting is a key step to optimize the heat flow across the whole device that depends on the overall thermal resistance and its thermal management allowing to reduce the junction temperature.

The last section was devoted to the electrical and optical characterizations based on the measurement of the L-I-V curves in pulsed and CW regimes enabling to extract the external and internal parameters for each vertical structure and compared with simulation results. After the development of dedicated setups, our characterizations have also addressed the extraction of the wall-plug efficiency, the far field and vertical divergence playing a significant role in the coupling efficiency during the beam collimation as well as the spectral properties. The experimental external parameters of the three structures have been compared with the literature showing state-of-the-art results. The calculation of internal parameters via pulsed L-I measurements allowed us to compare the experimental and simulated values of optical parameters as well as the series resistance. The measurements of the optical spectrum for a DFB LD validate the simulation results. The good agreement between the values of experimental effective index, determined from the DFB spectrum and optical simulations (error < 0,04%), validates our simulation models.

Finally, the following outcomes are highlighted:

- An optical output power and a WPE reaching 9,5W at 12A and 55% at almost 6A respectively for the AOC structure.
- Through the optical simulations, the predicted values of the vertical divergence for the three structures are in very good agreement with the characterizations. These results are dependent on the structure (from 18° for the SLOC to 30° for the AOC/LOC).
- The benefit of the DFB architecture since the spectral envelop is lower than 1nm with an SMSR higher than 30dB. For the SLOC-based design, the spectral drift versus temperature is limited to 0,08nm/°C instead of 0,3nm/°C for a F-P device. For the LOC structure, the results are quite similar.
- As required by the targeted application, the possibility to fabricate LDs emitting at 975nm, with high optical power and WPE reaching ~ 10W and ~ 60% respectively as well as temperature-stabilized DFB operating mode up to 60°C (< 0,1nm/°C).

CHAPTER II REFERENCES:

- [1] N. Michel, M. Calligaro, M. Lecompte, O. Parillaud, and M. Krakowski, "High wall-plug efficiency diode lasers with an Al free active region at 975nm," in *SPIE proceedings Photonics West Opto*, vol. Paper 7198-53, 2009.
- [2] M. Krakowski, Marco Lamponi, Michel Lecomte, Michaël Maria, Patrick Resneau, Yannick Robert, Eric Vinet, Michel Garcia, Olivier Parillaud, "Very high-power broad area laser diode with internal wavelength stabilisation at 975 nm for Yb fibre laser pumping," in *SPIE proceedings Photonics West Opto*, vol. 01, pp. 9002–51, 2014.
- [3] L. J. Mawst, A. Bhattacharya, J. Lopez, D. Botez, D. Z. Garbuzov, L. DeMarco, and J. C. Connolly, M. Jansen, F. Fang, and R. F. Nabiev "8 W continuous wave front-facet power from broad-waveguide," in *Applied Physics Letters*, vol. 69, no. 11, pp. 1532–1534, 1996.
- [4] A. Ivanova, R. Stoffer, and M. Hammer, "A variational mode solver for optical waveguides based on quasi-analytical vectorial slab mode expansion," pp. 19, 2013.
- [5] "Internet website, http://www.batop.de/information/n_InGaAs.html."
- [6] S. Adachi, *Properties of Aluminium Gallium Arsenide*, vol. 1, 1 vol. Inspec, the Institution of Electrical Engineers, 1993.
- [7] V. Cardinal, "Conception, élaboration sous contrôle optique et caractérisation de modulateurs à microcavité Fabry-Perot," in Thèse de doctorat, INSA Toulouse, Université Paul Sabatier, 1995.
- [8] M. A. Afromowitz, "Refractive index of GaAlAs," in *Solid State Communications*, vol. 15, pp. 59–63, 1974.
- [9] S. Adachi, *Properties of semiconductor alloy group IV, III-V, II-VI semiconductors*. John Wiley and Sons Inc. Publication, 2009.
- [10] S. G. Wallace, B. J. Robinson, P. Mascher, H. K. Haugen, D. A. Thompson, D. Dalacu and L. Martinu, "Refractive indices of InGaAsP lattice-matched to GaAs at wavelengths relevant to device design," in *Applied Physics Letters*, vol. 76, no. 19, pp. 2791–2793, 2000.
- [11] S. Adachi, *Properties of Group-IV, III-V and II-VI Semiconductors*, 2005th ed., vol. 1. John Wiley & Sons, Inc. Publication, 2005.
- [12] M. S. Alam, M. S. Rahman, M. R. Islam, A. G. Bhuiyan, and M. Yamada, "refractive index, absorption coefficient, and photo elastic constant: key parameters of ingaas material relevant to ingaas-based device performance," in *International Conference on Indium Phosphide and Related Materials*, vol. 1, pp. 343–346, 2007.
- [13] M. Schubert, V. Gottschalch, C. M. Herzinger, H. Yao, and P. G. Snyder, "Optical constants of GaIn_{1-x}P lattice matched to GaAs," in *Optical constants GaInP Lattice Matched GaAs*, vol. 77, no. 7, pp. 3416–3419, 1995.
- [14] A. Pietrzak, "Realization of High Power Diode Lasers with Extremely Narrow Vertical Divergence," in Thèse de doctorat, Elektrotechnik und Informatik Der Technischen Universität Berlin, 2011.
- [15] M. Peters, V. Rossin, and B. Acklin, "High Efficiency, High Reliability Laser Diodes at JDS Uniphase," in *SPIE proceedings High-power diode laser technology and applications III*, vol. 5711, pp. 142–152, 2005.
- [16] M. Weyers, "GaAs-based high power laser diodes," in *GaAs-based high power laser diodes*, vol. 1, pp. 273–278, 2005.
- [17] J. Buus, M.-C. Amann, and D. J. Blumenthal, "Single-mode laser diode," in *Tunable Laser Diodes and Related Optical Sources*, 2nd Edition, A John Wiley & Sons, Inc. Publication, 2005.
- [18] H. Wenzel, J. Fricke, A. Klehr, A. Knauer, and G. Erbert, "High-Power 980-nm DFB RW Lasers With a narrow vertical far field," in *IEEE Photonics Technology Letters*, vol. 18, no. 6, pp. 737–740, 2006.

- [19] C. M. Schultz, P. Crump, H. Wenzel, O. Brox, A. Maaßdorf, G. Erbert and G. Trankle, “11W broad area 976 nm DFB lasers with 58% power conversion efficiency,” in *Electronics Letters*, vol. 46, no. 8, pp. 580–581, 2010.
- [20] P. Crump, C. M. Schultz, H. Wenzel, S. Knigge, O. Brox, A. Maaßdorf, F. Bugge and G. Erbert, “Reliable operation of 976nm High Power DFB Broad Area Diode Lasers with over 60% Power Conversion Efficiency,” in *SPIE proceedings Novel in-plane semiconductor lasers X*, vol. 7953, p. 1G, 2011.
- [21] P. Crump, J. Fricke, C. M. Schultz, H. Wenzel, S. Knigge, O. Brox, A. Maaßdorf, F. Bugge and G. Erbert, “10W-reliable 90 μ m-wide broad area lasers with internal grating stabilization,” in *SPIE proceedings High-Power diode laser technology and applications X*, vol. 8241, p. 10N, 2012.
- [22] J. M. G. Tijero, H. Odriozola, I. Esquivias, A. Martin-Minguez, L. Borrueal, A. Gomez-Iglesias, M. Reufer, M. Bou-Sanayeh, P. Brick, N. Linder, M. Ziegler, J.W. Tomm, “Simulation of facet heating in high power red lasers,” in *SPIE proceedings physics and simulation of optoelectronic devices XVIII*, vol. 7597, pp. 11, 2010.
- [23] J. S. Yoo, H. L. Hong, and P. Zory, “Temperature Rise at Mirror Facet of CW Semiconductor Lasers,” in *IEEE Journal of quantum electronics*, vol. 28, no. 3, pp. 635–639, 1992.
- [24] J. Michaud, L. Béchou, D. Veyrié, F. Laruelle, S. Dilhaire, and S. Grauby, “Thermal behavior of high power GaAs-based laser diodes in vacuum environment,” *IEEE Photonics Technology Letters*, pp. 665–668, 2016.
- [25] F. Rinner, J. Rogg, N. Wiedmann, H. Konstanzer, M. Dammann, M. Mikulla, R. Poprawe, G. Weimann, “Carrier density dependence of the lifetime of InGaAs/AlGaAs high-power lasers,” in *SPIE Test measurement application of optoelectronics devices*, vol. 4648, 2002.
- [26] F. Rinner, J. Rogg, M. T. Kelemen, M. Mikulla, and G. Weimann, J. W. Tomm and E. Thamm, R. Poprawe, “Facet temperature reduction by a current blocking layer at the front facets of high-power InGaAs/AlGaAs lasers,” in *Journal of Applied Physics*, vol. 93, no. 3, pp. 1848–1850, 2003.
- [27] Y. P. Varshini, “Temperature dependence of the energy gap in semiconductors,” in *Physica*, vol. 34, pp. 149–154, 1967.
- [28] F. U. Herrmann, S. Beeck, G. Abstreiter, C. Hanke, C. Hoyler, and L. Korte, “Reduction of mirror temperature in GaAs/AlGaAs quantum well laser diodes with segmented contacts,” in *Applied Physics Letters*, vol. 58, pp. 1007–1010, 1991.
- [29] H. Horie, H. Ohta, and T. Fujimori, “Reliability improvement of 980-nm laser diodes with a new facet passivation process,” in *IEEE Journal of Selected Topics of Quantum Electronics*, vol. 05, no. 03, pp. 832–838, 1999.
- [30] P. Ressel, G. Erbert, U. Zeimer, K. Häusler, G. Beister, B. Sumpf, A. Klehr, G. Tränkle, “Novel passivation process for the mirror facet of Al-Free active region high power semiconductor diode lasers,” in *IEEE Photonics Technology Letters*, vol. 17, no. 05, pp. 962–964, 2005.
- [31] M. Kanskar, M. Nesnidal, S. Meassick, A. Goulakov, E. Stiers, Z. Dai, T. Earles D.Forbes, D. Hansen, P. Corbett, L. Zhang, T. Goodnough, L. LeClair, N. Holehouse, D. Botez, L.J. Mawst, “Performance and Reliability of ARROW Single Mode & 100 μ m Laser Diode and the Use of NAM in Al-free Lasers,” in *SPIE proceedings Novels in-plane semiconductor laser II*, vol. 4995, pp. 196–208, 2003.
- [32] P. G. Riva, S. Fafard, M. Buchanan, and S. Charbonneau, “Reduction of InGaAs/GaAs laser facet temperatures by band gap shifted extended cavities,” in *Applied Physics Letters*, vol. 70, no. 13, pp. 1662–1664, 1997.
- [33] C. L. Walker, A. C. Bryce, and H. Marsh, “Improved Catastrophic Optical Damage Level From Laser With Nonabsorbing Mirrors,” in *IEEE Photonics Technology Letters*, vol. 14, no. 10, pp. 1394–1396, 2002.

- [34] H. Taniguchi, H. Ishii, R. Minato, Y. Ohki, T. Namegaya, and A. Kasukawa, “25-W 915-nm Lasers With Window Structure Fabricated by Impurity-Free Vacancy Disorder (IFVD),” in *IEEE Journal of Selected Topics of Quantum Electronics*, vol. 13, no. 5, pp. 1176–1179, 2007.
- [35] H. C. Eckstein, M. Stumpf, U. D. Zeitner, C. Lauer, A. Bachmann, and M. Furitsch, “Mode shaping for enhanced brightness in broad area lasers using monolithically integrated microoptical structures,” in *IEEE International Semiconductor Laser Conference*, vol. 1, pp. 17–18, 2014.
- [36] J. Michaud, P. Del Vecchio, L. Béchou, D. Veyrié, M. A. Bettiati, F. Laruelle, S. Grauby, “Precise Facet Temperature Distribution of High Power Laser Diodes: Unpumped Window Effect,” in *IEEE photonics technology letters*, vol. 27, no. 09, pp. 1002–1004, 2015.
- [37] G. Yang, Gary M. Smith, M. K. Davis, D. A. S. Loeber, M. Hu, C. Zah, R. Bhat, “Highly Reliable High-Power 980-nm Pump Laser,” in *IEEE Photonics Technology Letters*, vol. 16, no. 11, pp. 2403–2405, 2004.
- [38] “<http://www.poet-technologies.com/quantum-well-intermixing.html>.”
- [39] X. Liu, M. H. Hu, C. G. Caneau, R. Bhat, and Chung-en Zah, “Thermal Management Strategies for High Power Semiconductor Pump Lasers,” in *IEEE Transactions on Components and Packaging Technologies*, vol. 29–2, pp. 268–276, 2006.
- [40] H. C. Eckstein, M. Stumpf, U. D. Zeitner, C. Lauer, A. Bachmann, and M. Furitsch, “Mode shaping for enhanced brightness in broad area lasers using monolithically integrated microoptical structures,” in *IEEE International Semiconductor Laser Conference*, vol. 1, pp. 17–19, 2014.
- [41] G. Erbert, A. Barwolff, J. Sebastian, and J. Tomm, “High power Broad area diode laser and laser bars,” in *High-Power Diode Lasers*, vol. 78, Springer Berlin Heidelberg, pp. 173–223, 2000.
- [42] R. W. Lambert, Tim Ayling, Alec F. Hendry, Joan M. Carson, David A. Barrow, Stuart McHendry, Crawford J. Scott, Andrew McKee, W. Meredith, “Facet-Passivation Processes for the Improvement of Al-Containing Semiconductor Laser Diodes,” in *Journal of Lightwave Technology*, vol. 24, no. 2, pp. 956–961, 2006.
- [43] W. Zheng and G. W. Taylor, “Determination of the photon lifetime for DFB Lasers,” in *IEEE Journal of Quantum Electronics*, vol. 43, no. 4, pp. 295–302, 2007.
- [44] P. Crump *et al.*, “High-Power, High-efficiency Monolithic edge-emitting GaAs-Based lasers with narrow spectral widths,” in *Advances in Semiconductor Lasers*, Academic press publication, 2012.
- [45] J. W. Tomm and J. Jimenez, “Strain measurement,” in *Quantum-well laser array packaging*, pp. 65–144, 2007.
- [46] X. Liu, L. C. Hughes, M. H. Rasmussen, M. H. Hu, V. A. Bhagavatula, R. W. Davis, C. G. Caneau, R. Bhat and C. Zah , “Packaging and Performance of High Power Semiconductor Lasers of High Heat Flux up to 2000 W/cm²,” in *IEEE Electronics Components and Technology Conference*, vol. 1, pp. 251–258, 2005.
- [47] G. Jiang, L. Diao, and K. Kuang, “Understanding Lasers, Laser Diodes, Laser Diode Packaging and Their Relationship to Tungsten Copper,” in *Advanced Thermal Management Materials*, Springer Science and Business Media, 2013, pp. 154.
- [48] S. V. Kidaliv and F. M. Shakhov, “Thermal Conductivity of Diamond Composites,” in *Materials*, vol. 2, pp. 2467–2495, 2009.
- [49] J. Wilson, “Thermal conductivity of common alloys in electronics packaging” in <https://www.electronics-cooling.com/2007/02/thermal-conductivity-of-common-alloys-in-electronics-packaging>, 2007.
- [50] W. Pitroff, G. Erbert, G. Beister, F. Bugge, A. Klein, A. Knauer, J. Maege, P. Ressel, J. Sebastian, R. Staske, G. Traenkle, “Mounting of high power laser diodes on boron Nitride

- Heat Sinks Using an Optimized Au/Sn Metallurgy,” in *IEEE Transactions on Advanced Packaging*, vol. 24, pp. 4, 2001.
- [51] L. V. Asryan and S. Luryi, “Effect of Internal Optical Loss on Threshold Characteristics of Semiconductor Lasers With a quantum-confined active region,” in *IEEE Journal Quantum Electronics*, vol. 40, no. 7, p. 11, 2004.
- [52] G. Xueqin, F. Shiwei, Y. Yuan, Y. Junwei, and L. Junwei, “Thermal analysis in high power GaAs-based laser diodes,” in *Thermal analysis high power GaAs-based laser diodes*, vol. 37, no. 4, pp. 044011-1/044011-5, 2016.
-

CHAPTER III

THERMAL MANAGEMENT ISSUE

INTRODUCTION

In the previous chapter, we have demonstrated the capability for a LD based on an AOC vertical structure to reach both a high optical output power ($> 9\text{W}$ @ 12A) and a WPE reaching 55% at almost 6A. To obtain such performances, a particular attention must be paid to the thermal dissipation in the micro-assembled device (from the LD to the C-mount heat sink). **This third chapter** aims to bring a comprehension of the heat propagation in our LD technology through different tools using analytical calculations and FEM simulations.

A first section gives a brief overview of the different heat sources in a high-power LD including well-established processes such as: Joule, Auger, SRH, re-absorption and scattering effects. But calculation of these heat contributions leads inevitably to some approximations. A typical example lies in the heat due to the Auger recombination since the Auger recombination coefficient is difficult to predict or even to measure and in literature. Only an estimation is often available.

In a second section, we will describe the implementation methodology of a relevant analytical model used to estimate these heat sources. For that, we will propose an analytical thermo-electrical model derived from three models already reported in literature, the data achieved by experimental measurements and theoretical L-I-V curves. This model enables to predict any L-I curve of a LD over a large range of bias current, knowing the external and the internal parameters as well as establishing a simple relationship between the structure design of the LDs and their optical performances.

The development of high power LDs emitting at 975nm capable to reach high levels of optical power (10W) needs to accurately analyse the LD optical power limitations and optimize its packaging. The packaging process of such devices requires overcoming both optical, mechanical and electrical issues. These last are often highly interactive and the stability of devices is an essential factor to ensure high performances and develop reliable solutions. In such a context, time dependent FEM-based Multiphysics simulations appear as a relevant tool.

Indeed, despite the great interest of these analytical models, some local effects can only be analyzed through 2D or 3D simulations in particular based on FEM. **The last section** will describe, analyse and discuss the results achieved from 2D stationary thermo-electrical simulations. These last have been performed with the COMSOL© software using a mandatory Multiphysics approach, to predict the thermal flow distribution in a F-P and DFB LDs under a specific bias current. Then, the effect of grooves etching depth defining the stripe width (90µm) and the length of Non-Injected Mirror (NIM) window are also discussed in terms of current density and heat distribution both at the emissive front facet and along the longitudinal axis of the LD.

3.1 BRIEF OVERVIEW OF HEAT SOURCES IN A HIGH POWER LD

It is well-established that heat generation limits LDs performance due to the free carriers displacement, responsible of the energy transfer to the crystal lattice and so the increase of temperature. The thermal energy is dissipated via lattice vibration and the phonons represent the smallest quantity of the energy portion of lattice waves.

Many works have been already published addressing modelling of heat generation in LDs [1]-[2]-[3]-[4]. The generation of heat in a LD, independently from the vertical structure, is directly connected to the physical processes of transfer energy to the crystal lattice. In other words, these processes are mainly related to transfer mechanisms such as:

- Heating by Joule effect due to the series resistance.
- Electron-hole recombination and Auger Shockley-Read-Hall heating processes.
- The heterojunction and the Thomson heating processes.
- Heating by optical re-absorption and scattering processes.

3.1.1 Joule effect - Ohmic heating

When a flow of carriers passes through a metal or a semiconductor, it establishes a process leading to energy loss. Such a flow leads to frequent carrier scattering by phonons, leading to a continuing energy loss to the lattice. The carriers move from the higher electrostatic voltage to a lower electrostatic one and the energy difference corresponds to the energy absorbed by the lattice as Joule heat H_j (Wm^{-3}) [2]. The general equation governing this phenomenon is the following:

$$H_j = \frac{\vec{j}_n^2}{q\mu_n n} + \frac{\vec{j}_p^2}{q\mu_p p} \quad [Eq. III-1]$$

where $J_{n/p}$ stands for the electron/hole current density, q is the elementary charge, $\mu_{n/p}$ is the electron/hole mobility and n/p represents the electron/hole concentration.

The Joule heating is known as dissipated power estimated from: $P_{ele_diss} = V \cdot I = R_s \cdot I^2$ where V and I are the voltage applied to the LD and the current passing through it. Hence, the Joule heating is proportional to the electrical resistance of each layer within the LD.

3.1.2 Heating from Auger and Shockley-Read-Hall processes

The photon can leave the semiconductor or be re-absorbed but in both cases, not contribute to a direct heating process. In contrast, the phonon contributes largely to the heating of the semiconductor crystal lattice. Because we focus on heat sources, only phonon contribution will be considered in this study. The two main recombination phenomena related to phonon emission are the Auger and Shockley-Read-Hall effects.

A brief theoretical survey of these phenomena is presented hereafter. The average heat released is proportional to the difference between the quasi-Fermi levels:

$$H_R = R(E_{Fn} - E_{Fp}) \quad [Eq III-2]$$

where H_R stands for recombination heat, R is the recombination rate and includes the Auger and Shockley-Read-Hall recombination processes.

The Auger recombination involves three particles: an electron and a hole that recombine in a band-to-band transition and give off the energy to another electron or hole as shown in *Figure III-1(a)*. When the energy is transferred to an electron in conduction band, this is pushed high into the conduction band and the first electron recombines with the hole within the conduction band. The third electron gradually gives off its energy thermally and relaxes to the band edges [2]-[5].

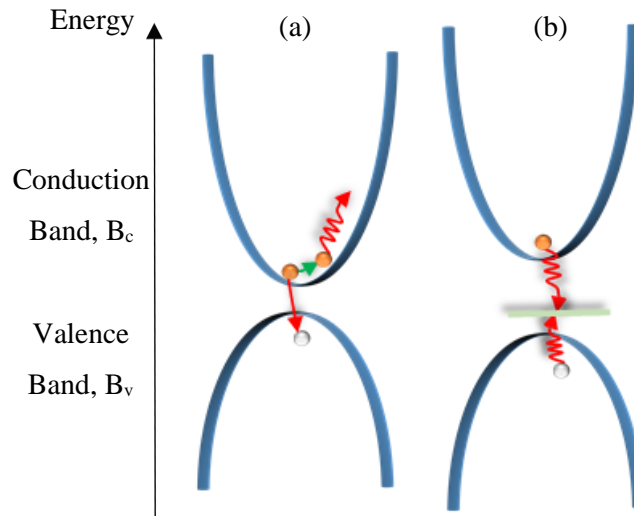


Figure III-1: (a) Auger recombination: an electron in B_c recombines with a hole in B_v and a third electron takes energy from the primary electron. The electron gives the excess of energy to the lattice, converted into heat, and comes back to its first energy. (b) SRH recombination: the green line represents the trap energy level located in the band gap.

The Auger recombination can be written as:

$$R_{Aug} = C_n n \cdot (np - n_i^2) + C_p n \cdot (np - n_i^2) \quad [Eq. III-3]$$

where n and p are the concentrations of free carriers, C_n and C_p are the Auger coefficients and n_i is the intrinsic concentration. At high levels of injection, it is assumed that $n \cong p \gg n_i^2$ and considering that $C_p = C_n = C$, one can write:

$$R_{Aug} \approx C n^3 \quad [Eq. III-4]$$

The value of the Auger coefficient (C) is quite difficult to determine through experiments. In literature, this coefficient is available for direct band gap compound semiconductors and in this case, this coefficient is near of $\cong 1 \cdot 10^{-28} \text{ cm}^6/\text{s}$ for InGaAs material [2]. Above the optical threshold, the value of free carriers concentration is constant. Based on electro-optical simulations via EDio, a software developed at III-V lab, our calculations give $n_{th} \cong 1,53 \cdot 10^{12} [1/\text{cm}^3]$ for our LD technology.

In a paper published in 1990, Y. C. Chen reported that the Auger rate saturates for $n > n_{th}$ [6]. In addition a PhD work, developed at TRT in 1998, has confirmed that Auger contribution to the heating process is clamped after the optical threshold [7]. A study carried out in 2004, shows a correlation between the stripe width and the injected current contribution to the Auger phenomena [8]. This paper has taken into consideration an InGaAs/GaAs single QW and studied the influence of the stripe width on Auger recombination. It has been highlighted that a greater fraction of the

injection current contributes to luminescence in a wide device ($\approx 90 \mu m$) compared to a narrower one ($20 \mu m$).

SRH recombination involves deep energy traps inside the semiconductor band gap that are generated by crystal defects (see *Figure III-1(b)*). Such deep-level defects are able to trap electrons from the conduction band as well as holes from the valence band. From [2], one can write:

$$R_{SRH} = N_t \frac{c_n c_p (np - n_0 p_0)}{c_n (n + n_1) + c_p (p + p_1)} = \frac{(np - n_0 p_0)}{\tau_p (n + n_1) + \tau_n (p + p_1)} \quad [Eq. III-5]$$

where N_t is the density of traps and c_n and c_p are the trap coefficients ($c_{n/p} N_t = 1/\tau_{n/p}^{SRH}$). If E_t represents the trap energy, the electron n_1 and hole p_1 concentrations are given by the following equations:

$$n_1 = N_c \exp\left(\frac{E_t - E_c}{k_B T}\right) \quad \dots \quad p_1 = N_v \exp\left(\frac{E_v - E_t}{k_B T}\right) \quad [Eq. III-6]$$

These two contributions are bound to the electrons density in the LD and this last is clamp above the optical threshold (see *Annex n°1*). Therefore, above the optical threshold, the Auger and Shockley-Read-Hall recombination give a constant contribution to heating generation into the LD.

3.1.3 Heating from optical re-absorption and scattering processes

Above the optical threshold, the carriers injected foster the photon production. The generated optical wave makes a round trip into the cavity. Some optical waves go out from the front facet of the LD while instead, some other optical waves penetrate the materials outside the optical cavity along the parallel direction of the epitaxial growth axis. In this case, the optical wave can be partially or fully absorbed. The absorption causes phonon generation and thus a quantity of heat via lattice vibrations. The law that describes this phenomenon is the following:

$$H_A = \alpha_0 \Phi_{ph} h\nu \quad [Eq. III-7]$$

where α_0 stands for the optical absorption coefficient, Φ_{ph} represents the photon flux density and $h\nu$ is the photon energy. It is obvious that such a generated heat depends proportionally on photon energy (see *Annex n°2*).

3.2 THERMAL AND OPTICAL ANALYTICAL MODELS

In the previous section, we reminded the analytical equations that quantify the main heat sources into a LD. In this section, we will describe the implementation methodology of a relevant analytical model used to estimate these heat sources. Such an easy and quick to solve analytical model can give important information to improve the design of the LDs whatever the considered vertical structure. Some parts are difficult to estimate and experimental comparisons are necessary to adjust such a model. The calculation of these heat contributions, only based on theoretical data, leads to some approximations. A typical example lies in the heat due to the Auger recombination. The Auger recombination coefficient is difficult to calculate or measure and, in literature, only an estimation is available. We propose an analytical thermo-electrical model derived from three models already reported in literature, based on data achieved by experimental measurements (α_i , η_i , J_{tr} , Γg_0) and theoretical calculations (R_s , I_{th} , T_0 , T_1). These models can establish a simple relationship between the structure design of the LDs and their output optical performances. From these last, it is possible to extract the internal parameters of the LDs but above all to use them as input for this analytical thermo-electrical model.

3.2.1 Modelling methodology of L-I curves

a. Model n° 1: The III-V lab approach

This analytical model aims to predict the L-I curve of our LDs technology taking into account its junction temperature. Since the optical power is affected by the heat generation, this model takes into account the heat generated within the LD using the experimental characteristic temperatures (T_0 and T_1).

The [Eq. III-8] allows to determine the junction temperature and it is possible to predict the optical power $P_{opt}(n)$ as a function of the bias current as follows:

$$T_j = T_a + R_{th} (V_{th}I + R_s I^2 - P_{opt}(n)) \rightarrow \Delta T(n-1) = T_j - T_a$$

$$\Delta T(n-1) = R_{th} (V_{th}I + R_s I^2 - P_{opt}(n)) \quad [Eq. III-8]$$

$T_j, T_a, V_{th}, I, R_{th}, R_s$ are the junction and environmental temperatures, the threshold voltage, the current, the thermal resistance and the series resistance of the LD respectively. The subscript “n” represents the iteration of the bias current (I) applied to the LD.

The final value of $P_{opt}(n)$ is extracted when the iteration converges to the third decimal value.

$$P_{opt}(n) = (V_{th}I + R_s I^2) - R_{th}/\Delta T(n - 1) \quad [Eq. III-9]$$

- For the first iteration (n=1), it is possible to use a generic value of $\Delta T(0) = T_1 - T_0$ and solve [Eq. III-8]. With such a value and using [Eq. III-9], it possible to calculate the value of $\Delta T(n - 1)$.
- For the second iteration, we report the value of $\Delta T(n)$ in [Eq. III-10]. Using this value, the optical power $P_{opt}(n + 1)$ becomes:

$$P_{opt}(n + 1) = \eta_E(I - I_{th}) = \frac{1,24}{\lambda} \eta_{D(0)} \cdot \exp\left(\frac{\Delta T(n)}{T_1}\right) \cdot \left[I - I_{th(0)} \cdot \exp\left(\frac{\Delta T(n)}{T_0}\right) \right] \quad [Eq. III-10]$$

The changes of η_D as a function of the cavity length (on the first decimal) and the other terms are well-known assuming to be independent of temperature. The terms $\eta_{D(0)}$ and $I_{th(0)}$ can be calculated as follows:

$$\eta_{D(0)} = \frac{n_i \alpha_m}{\alpha_i + \alpha_m} \quad \dots \quad I_{th(0)} = J_{tr} \cdot w \cdot L \cdot \exp\left(\frac{\alpha_i + \alpha_m}{\Gamma G_0}\right) \quad [Eq. III-11]$$

where α_m stands for the optical mirror losses, w is the ridge width and L represents the cavity length. The other parameters have been already defined in the “*Chapter II*”.

Using [Eq. III-8] and [Eq. III-10] recursively until the convergence, it is possible to find the optical output power of the LD for a given bias current.

As example, *Table III-1* gives the internal and external parameters for three cavity lengths of a LOC vertical structure and to calculate [Eq. III-11], we use the values of internal parameters extracted according our methodology developed in “*Chapter II-Electrical and optical characterizations*”.

L [mm]	w [μm]	η_i	R₁ [%]	R₂ [%]	α_i [cm ⁻¹]	η_d [W/A]	R_s [Ω]	V_{th} [V]	R_{th} [K/W]	T₀ [K]	T₁ [K]	I_{th} [A]
4						0,69	0,027	1,31	1,8	110	220	0,6
3	90	0,9	0,9	0,01	0,6	0,75	0,037	1,33	3,3	115	230	0,35
2						0,78	0,045	1,35	4,4	120	235	0,28

Table III-1: Internal and external parameters for three cavity lengths of a LOC vertical structure in order to predict L-I curves

Based on these internal and external parameters and the theoretical model, it is possible to predict the L-I curves for different cavity lengths as reported in *Figure III-2(a)* and compared them to experimental L-I curves. These results show a difference between experimental data and the

predicted ones using this first model. Experimentally, the L-I curves clearly show the well-known thermal roll-over effect since the optical power significantly decreases after 6A. *Figure III-2(a)* reports only L-I curves for two cavity lengths (3 and 4 mm) and *Figure III-2 (b)* plots the relative error between experimental and predicted L-I curves highlighting a large difference ($\sim 25\%$) at high bias current levels ($I > 10A$).

The difference between the simulated and experimental optical power clearly lies in the thermal behaviour considered in this model. For each iteration, we use the first calculated values of $\eta_{D(0)}$ and $I_{th(0)}$ and so the self-heating of the LD is not taken into account.

To improve the fit between the predicted and experimental L-I curves as far as possible, an alternative solution could consist in a modification of the overall thermal resistance and internal losses values into the first model. For instance, a value of 7 and 5 K/W for 3 and 4 mm cavity length respectively and internal losses of 1cm^{-1} have been used in *Figure III-3* for a fit improvement tentative. As demonstrated, the error is significantly lowered at high bias currents ($\sim 3\%$) whatever the considered cavity length but remains important at low bias current ($\sim 15\%$) for long cavity (4mm).

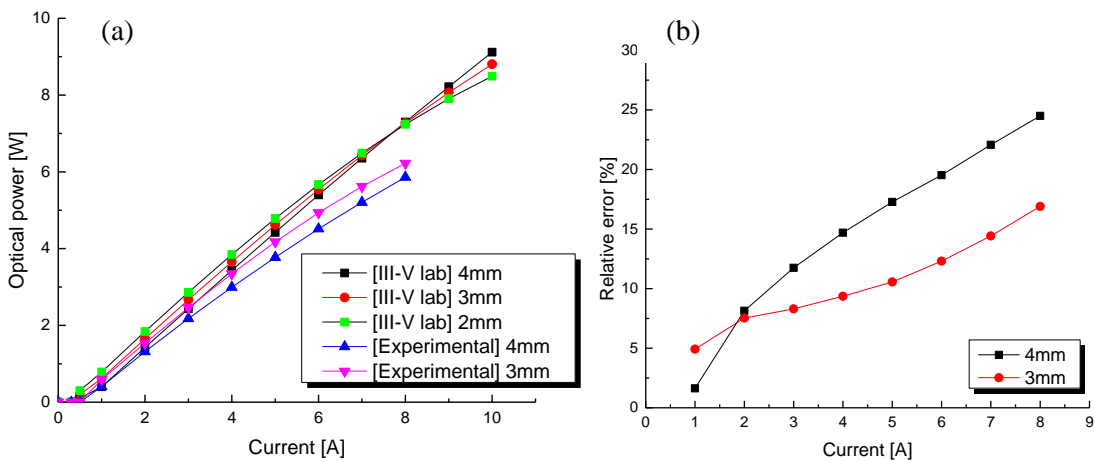


Figure III-2: (a) Predicted and experimental L-I curves versus cavity length. (b) Relative error between predicted and experimental L-I curves. [The experimental optical power shows the well-known thermal roll-over that is not considered in this first model].

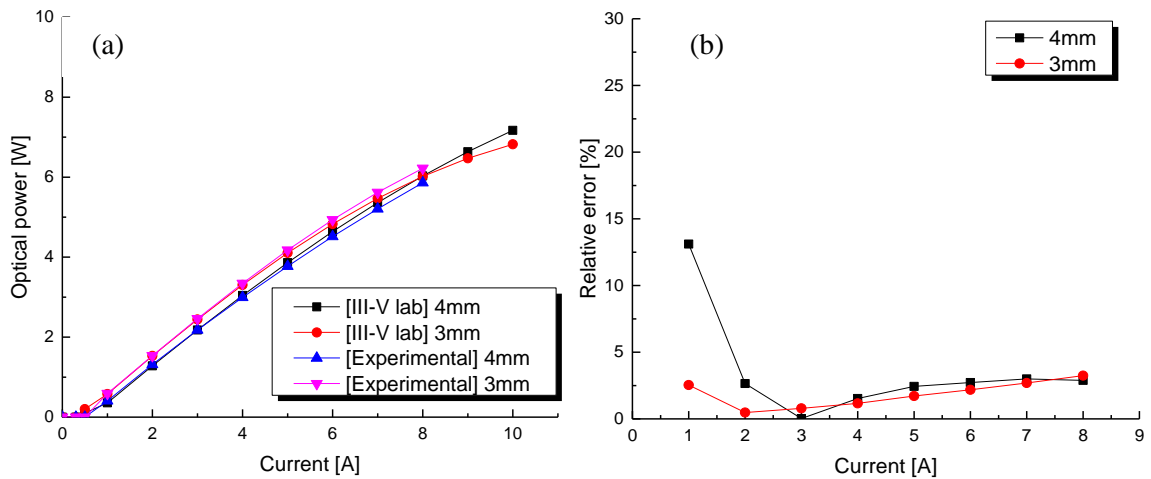


Figure III-3: (a) Predicted and experimental L-I curves versus cavity length. (b) Relative error between predicted and experimental L-I curves. [To improve the fit, the following values have been implemented in the first model: $R_{th} = 7-5$ K/W for 3-4mm cavity length LDs and $\alpha_i = 1\text{cm}^{-1}$].

The same accordance between experimental and predicted L-I curves can be achieved by modifying the series resistance or the characteristic temperatures. But for a good fit, the series resistance must be increased of one order of magnitude. Usually R_s ranges from 27 to 37m Ω and in order to obtain the same optical power, R_s was increased from a factor of 10 for the same cavity lengths. Clearly, these values are not similar to ones determined in “*Chapter II-Electrical and optical characterizations*”. With such high values of R_s , the Joule effect rapidly increases the temperature affecting the maximum optical power by a large thermal roll-over. A change in the characteristic temperatures ($T_0=50$ °C and $T_1=80$ °C for a 4mm LD cavity) leads to a better agreement between experimental and simulated optical power. Unfortunately, these two temperatures are one order of magnitude smaller than the experimental ones.

This first model is based on a main approximation since the optical power is calculated from the initial values of $\eta_{D(0)}$ and $I_{th(0)}$ without considering any other variations due to the heating process. So, an improved model must be established.

b. Model n° 2: the Simarjeet approach

From the methodology developed by S.S Simarjeet in 2007 [9], an improved analytical model is proposed. This last is derived from the III-V lab model but considers the self-heating of the LDs. For each iteration, the $\eta_{D(n)}$ and $I_{th(n)}$ are calculated using the previous values: $\eta_{D(n-1)}$ and $I_{th(n-1)}$. We just remind that the previous model calculated these values starting only from the first iteration since for each iteration, the $\eta_{D(n)}$ and $I_{th(n)}$ are constant and equal to $\eta_{D(0)}$ and $I_{th(0)}$.

First, the dissipated power must be calculated from [Eq. III-8]. Then, the optical power is calculated using a self-consistent method and the main difference between this second model and the model n°1 lies in $\eta_{D(n)}$ and $I_{th(n)}$, implemented in the expression of P_{opt} given below:

$$P_{opt(n+1)}(I) = \frac{1,24}{\lambda} \eta_{D(n)} \cdot \exp\left(\frac{\Delta T(n)}{T_1}\right) \cdot \left[I - I_{th(n)} \cdot \exp\left(\frac{\Delta T(n)}{T_0}\right) \right] \quad [Eq. III-12]$$

The values of $\eta_{D(n)}$ and $I_{th(n)}$ in [Eq. III-12] are calculated according to [Eq. III-11] for each iteration depending on the last iteration. The values of n_i and α_i are extracted for each iteration and are temperature dependent. This allows considering the thermal effects since both $\eta_{D(n)}$ and $I_{th(n)}$ values are related to the bias current and so temperature. Based on data given in Table III-1, it is possible to plot the predicted L-I curves as shown in Figure III-4. This analytical model clearly gives a better fit between experimental and simulated L-I curves compared to the previous one (in Figure III-4 (a)). The relative error between the experimental and simulation curves is reduced, in particular at bias current levels ($< 3\%$) without any modifications of R_s and characteristic temperatures. However, the relative error remains high at low bias current levels for long cavity ($\approx 18\%$) and so, a third model is proposed further.

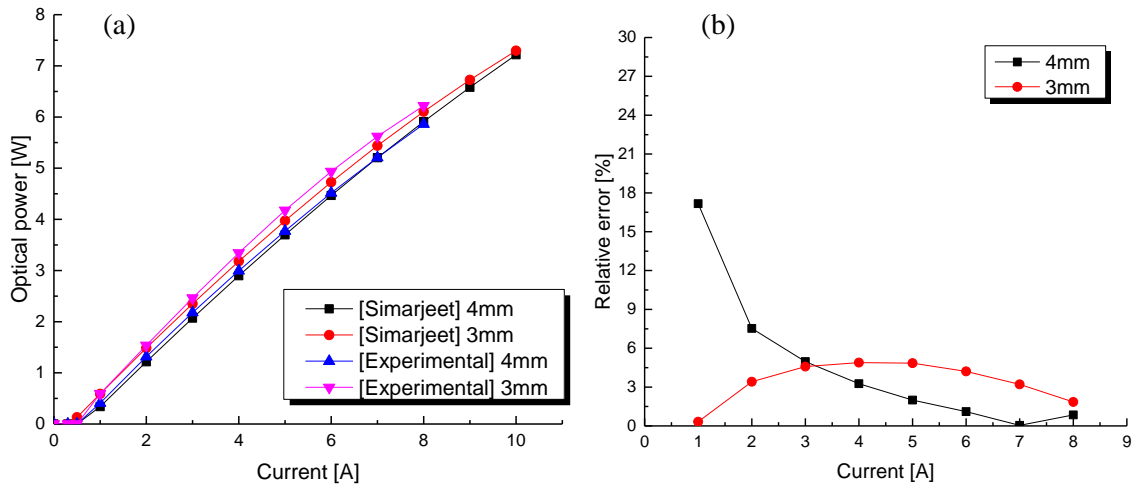


Figure III-4: (a) Predicted and experimental L-I curves versus cavity length. (b) Relative error between predicted and experimental L-I curves.

c. Model n° 3: the Behringer approach

The first model did not consider the thermal effects and the obtained results show a quite strong relative error between the predicted and experimental L-I curves. The second one assumes that η_i and α_i depend on temperature, hence the values of η_D and J_{th} change at each iteration. This

third model will take into account the drift of more parameters as a function of temperature such as: η_D , I_{th} and η_i , α_i and Γg_0 . From the methodology developed by M. Behringer in 2007 [10], it is possible to write the following set of equations for this model:

$$\begin{aligned}
 P_{opt}(\alpha_m, \Delta T, I) &= \eta_d(\alpha_m, \Delta T) \cdot [I - I_i - I_{th}(\alpha_m, \Delta T)] \\
 \eta_D(\alpha_m, \Delta T) &= \eta_i(\Delta T) \cdot \alpha_m [\alpha_i(\Delta T) + \alpha_m] \\
 J_{th}(\alpha_m, \Delta T) &= J_{tr}(\Delta T) \cdot \exp \frac{[\alpha_i(\Delta T) + \alpha_m]}{\Gamma g_0(\Delta T)}
 \end{aligned}
 \tag{Eq. III-13}$$

where:

$$\begin{aligned}
 \eta_i(\Delta T) &= \eta_i(0) \cdot \exp \left[-\frac{\Delta T}{T_\eta} \right] \\
 \alpha_i(\Delta T) &= \alpha_i(0) \cdot \exp \left[-\frac{\Delta T}{T_\alpha} \right] \\
 \Gamma g_0(\Delta T) &= \Gamma g_0(0) \exp[-\Delta T/T_g]
 \end{aligned}
 \tag{Eq. III-14}$$

In this model, the η_i , α_i are assumed to be dependent on temperature and, as a consequence, the n_D and J_{th} also depend on temperature as established in [11]. The parameters $T_\eta, T_\alpha, T_g, T_{tr}$ represent the characteristic temperatures as well as $\eta_i, \alpha_i, T_0, T_1$ are the mandatory inputs required to use this proposed model. In “*Chapter II-Electrical and optical characterizations*”, a methodology, enabling to extract all these parameters, has been described that is based on L-I-V pulsed and continuous measurements. *Table III-2* summarizes the different mathematical techniques to extract: $T_\eta, T_\alpha, T_g, T_{tr}$.

Input		Extracted parameters
X-axis	Y-axis	Slope
T_{HS}	$\ln[j_{tr}]$	T_{tr}
T_{HS}	$\ln[\alpha_i]$	T_α
T_{HS}	$-\ln[\eta_i]$	T_η
T_{HS}	$-\ln[g_0]$	T_g

Table III-2: General extraction methodology for the determination of the intrinsic optical parameters derived from pulsed L-I-V curves measurement.

where T_{HS} represents the heat sink temperature.

Table III-3 gives the complete set of extracted parameters and used in this model n°3 as a function of the cavity length.

Cavity length [mm]	w [μm]	η_i	R_1 [%]	R_2 [%]	α_i [cm^{-1}]	η_D	R_s [m Ω]	V_{th} [V]	R_{th} [K/W]
4					0,6	0,69	27	1,31	1,8
3	90	0,92	0,9	0,1	0,6	0,75	35	1,33	3,3
2					0,6	0,78	45	1,35	4,4

Cavity length [mm]	T_0	T_1	I_{th} [A]	J_{tr} [A/cm 2]	Γ_{g0} [cm $^{-1}$]	T_η	T_α	T_{tr}	T_{g0}	λ [μm]	α_m [cm $^{-1}$]
4	110	220	0,6		9						5,8
3	115	230	0,35	88	14	631	407	98	1000	0,975	7,8
2	120	235	0,28		16						11,7

Table III-3: Set of data used to calculate the L-I curve considering the third model.

Figure III-5(a) plots the difference between the predicted and experimental L-I curves a function of the cavity length and the model n^o3 clearly demonstrates the best fit between the predicted and experimental results with the lowest relative error (<5%) whatever the considered bias current.

Finally, this third model has been chosen to predict the optical power for bias current levels higher than those used for L-I-V curves measurement ($I > 10\text{A}$).

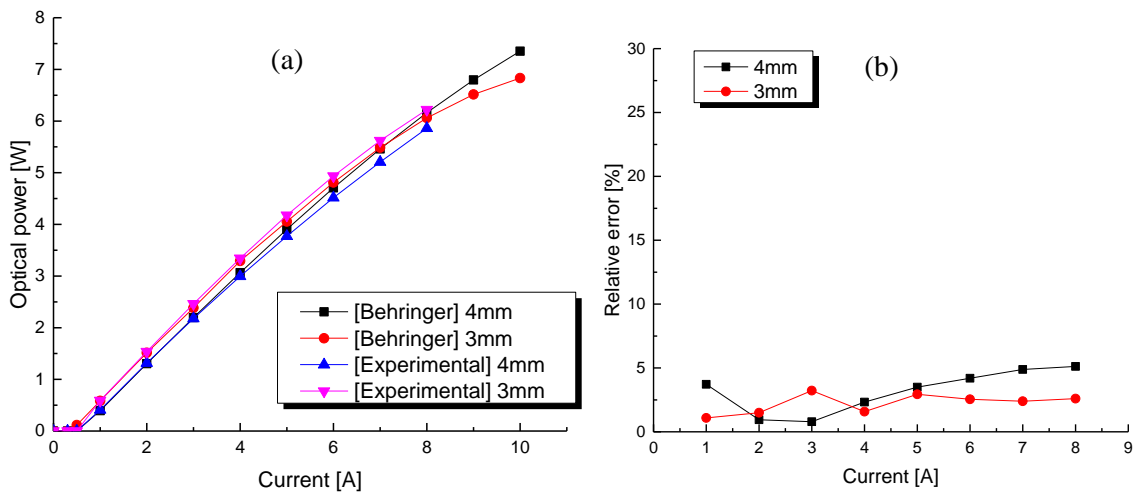


Figure III-5: (a) Predicted and experimental L-I curves versus cavity length. (b) Relative error between predicted and experimental L-I curves. [The relative error is significantly lower compared to ones calculated from the other models].

In particular, we will see its application in “Chapter III- Description of the modelling conditions in Comsol Multiphysics®” since using the predicted optical power at a specific bias current, it is possible to calculate the current density applied to the LD. In “Chapter III-Thermal and optical

analytical model”, this model will be used for the estimation of the heat sources located within the optical cavity.

3.2.2 Thermo-electrical modelling

In the previous section, we discussed the optical power models and we compared their ability to fit experimental L-I curves with the lowest error as possible. In this section and using the third model, we calculate the heat sources based on L-I-V curves measurement. The results of this model have been injected in the following thermo-electrical one, presented hereafter. This section focuses on the comparison of the results based on these two different inputs. Moreover, the results of such an analytical thermo-electrical model will be used in the “*Chapter III- Description of the modelling conditions in Comsol Multiphysics®*” to quantify the heat sources and set the boundary conditions.

Based on experimental data, the dissipated power is defined as given in [Eq. III-15]:

$$P_{TOT_diss} = (P_{ele_diss} - P_{opt}) = (V \cdot I - P_{opt}) \quad [Eq. III-15]$$

On the basis of the works of M. Kanskar, the heat contributions in a high power LD can be written as reported in [12]:

$$P_{TOT_diss} = (P_{joule} + P_{hj} + P_{carrier\ leakage} + P_{below\ threshold} + P_{absorption+scattering}) \quad [Eq. III-16]$$

and the different contributions are the following:

$$\begin{aligned} P_{joule} &= I^2 R_s \rightarrow \text{Joule heating} \\ P_{hj} &= I(V_{th} - V_F) \rightarrow \text{Thomson heating} \\ P_{carrier_leakage} &= P_{c_l} = IV_F(1 - \eta_i) \\ &\rightarrow \text{Electron - hole recombination heating} \\ P_{below_threshold} &= P_{b_th} = I_{th} V_F \eta_i \\ &\rightarrow \text{Auger and Shockley - Read - Hall heating} \\ P_{absorption+scattering} &= P_{abs+scat} = P_{stim} - P_{out} = V_F(I - I_{th})\eta_i \\ &\rightarrow \text{Absorption and scattering heating} \end{aligned} \quad [Eq. III-17]$$

I stands for the bias current applied at the LD, R_s represents the series resistance and V_{th} is the built-in voltage (or threshold voltage). Here, it is assumed that the built-in voltage does not change as a function of the cavity length since from our experiments, V_{th} changes are respective to the second decimal for LDs with the same vertical structure and with different cavity lengths (2/3/4

mm). For a semiconductor out of equilibrium (i.e. in the presence of an applied bias), the quasi-Fermi level represents the electron and hole concentrations at a non-equilibrium state. The term V_F represents the energy difference corresponding to the lasing transition:

$$\lambda[\mu m] = \frac{hc}{hv} = \frac{1,24}{hv(eV)} \rightarrow V_F(eV) = \frac{1,24}{\lambda} \quad [Eq. III-18]$$

This value is assumed to be constant for each laser structure.

P_{stim} represents the power occurring by the stimulated emission while P_{out} stands for the optical power measured at the AR facet. Based on experimental extrapolation of internal parameters and according to [Eq. III-17], it is possible to calculate each heating contribution for each cavity length and vertical structure. Therefore, as reported in Table III-4, we give the external parameters for LDs for each vertical structure with different cavity lengths but considering the same facet reflectivity and mounting process. The values of I_{th} can be calculated as follows:

$$I_{th} = N \cdot J_{tr} \cdot w \cdot L \cdot \exp\left(\frac{\alpha_i + \alpha_m}{\Gamma g_0}\right) \quad [Eq. III-19]$$

where w , L and N correspond to the width, length and number of QWs respectively. The terms J_{tr} , α_i , α_m and Γg_0 are described in “Chapter II-Electrical and optical characterizations”. The theoretical values of R_s are calculated from [Eq- II-5] and V_{th} is extracted from I-V curves.

Structure	Cavity length [mm]	I_{th} [A]	R_s [mΩ]	V_{th} [V]	η_i	Γg_0 [cm^{-1}]	J_{tr} [$A \cdot cm^{-2}$]	α_i [cm^{-1}]
LOC	2	0,288	55	1,32	0,92	9,76	73,6	0,62
	3	0,346	40	1,30				
	4	0,423	26,5	1,29				
SLOC	2	0,244	70	1,41	0,91	13,9	82,5	0,6
	3	0,316	60	1,38				
	4	0,5	38	1,37				
AOC	2	0,51	30	1,344	0,9	13,42	153	0,64
	3	0,645	21	1,319				
	4	0,85	16	1,31				

Table III-4: Main electro-optical parameters corresponding to the three vertical structures and calculated for each cavity length.

Figure III-6 plots the different heat contributions to the power dissipation for each vertical structure but only for a 4mm cavity length. It is clear that optical absorption and scattering phenomena are the dominant effects followed by the Joule effect as heating sources. In the case of LDs with 2 and

3 mm cavity length, the Joule effect is dominant because the R_s largely increases while the other contributions remain rather constant. The total experimental dissipated power is defined as: $P_{diss\ exp} = P_{opt} - I \cdot V$, where P_{opt} , I and V are the optical output power, the bias current and the applied voltage to the LD respectively. With such an analytical model, we obtain a low relative error ($< 7,5\%$) between the predicted and the experimental calculations of power dissipation in a large range of bias current (3-11A) and this error is low ($< 5\%$) even at high bias current levels ($I > 6A$). One can also note an increase of the error at low bias current ($< 3A$) reaching 22% and 15% for the SLOC and AOC structures at 1A while this error is low ($< 3\%$) for the LOC structure. We have calculated the contribution of the main heat sources for the high-power LD at 975nm for the three cavity lengths and for each vertical structure. From *Figure III-6*, one can deduce that the AOC vertical structure shows the lowest total dissipated power (7,5W at 11A) compared to the two other structures. This is due to a lower series resistance (lower Joule effect contribution) and lower optical reabsorption (benefit from its asymmetrical design).

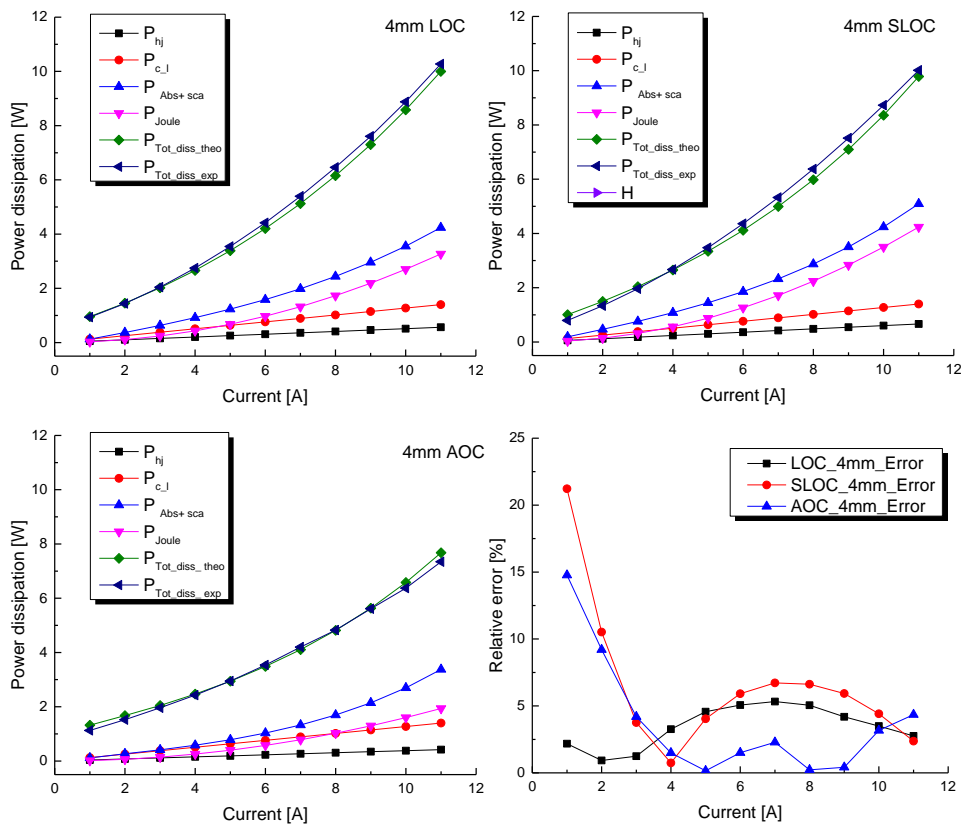


Figure III-6: Heat contributions and total power dissipation versus bias current for the three vertical structures (only for 4mm cavity length) and relative error between experimental and calculated results. The comparison between the experimental total dissipated power and the one calculated using the proposed thermo-electrical model shows a low relative error ($< 7,5\%$) for all the structures in a large range of bias current.

In *Table III-5*, we report values of theoretical and experimental dissipated power (this last is deduced from some calculations) for a 4mm cavity length LOC vertical structure.

Current [A]	$P_{\text{diss_theor.}}$ [W]	$P_{\text{diss_exp.}}$ [W]	Heat sources _{theor.} [W/m ³]	Heat sources _{exp.} [W/m ³]
1	0,957	0,93	$2,42 \cdot 10^{12}$	$2,36 \cdot 10^{12}$
2	1,45	1,43	$3,66 \cdot 10^{12}$	$3,63 \cdot 10^{12}$
3	2,02	2,04	$5,09 \cdot 10^{12}$	$5,16 \cdot 10^{12}$
4	2,66	2,75	$6,72 \cdot 10^{12}$	$6,94 \cdot 10^{12}$
5	3,39	3,54	$8,55 \cdot 10^{12}$	$8,94 \cdot 10^{12}$
6	4,2	4,42	$1,06 \cdot 10^{13}$	$1,12 \cdot 10^{13}$
7	5,12	5,39	$1,29 \cdot 10^{13}$	$1,36 \cdot 10^{13}$
8	6,15	6,46	$1,55 \cdot 10^{13}$	$1,63 \cdot 10^{13}$

Table III-5: Calculated and experimental heat source and dissipated power for a 4mm length laser LOC structure versus bias current.

Since FEM-based simulations will be performed further in order to analyze the heat flow propagation in our LDs, these predicted heat sources are of great interest since in section “*Chapter III - Description of the modelling conditions in Comsol Multiphysics®*”, the FEM model will use optical output power values as input data. If we want to predict the heat flow distribution at high values of current (i.e. values largely higher than the current maximum experimental bias current), we need to get free of the experimental output power measurement.

Short summary

In this section, we have carefully analyzed the main heat sources contributions in a high-power LD emitting at 975nm. We have demonstrated the great interest to propose a relevant analytical model to predict the optical output power as a function of the bias current. Referring to literature, it has been possible to extract relevant models and this section has presented and compared the obtained results using three models. The performances and the limits of each model have been discussed.

We found that the main heating sources due to optical re-absorption process and Joule heating are predominant. To calculate these heat sources, we use the experimental optical power, meaning that we can calculate the heat sources only for bias current up to 10A. Based on external and internal parameters of a LD, a first analytical model (III-V lab) was established enabling to predict the optical power (for different cavity lengths and for each vertical structure) as a function of bias current values and above all, largely higher than experimental ones ($\gg 10A$). Through an exhaustive literature review and derived from methodologies described in two other models (Simarjeet and Behringer), we have improved this analytical model and the relative error has been

drastically lowered <5% when predicted and experimental L-I curves are compared in particular at high bias current levels. Then with such results, a thermo-electrical model has been established that allows us to quantify the heat sources within a LD independently from the measured optical power.

3.3 DESCRIPTION OF THE MODELLING CONDITIONS IN COMSOL MULTIPHYSICS® ENVIRONMENT

The development of high power LDs emitting at 975nm capable to reach high levels of optical power (10W) with high values of WPE (> 60%), needs to accurately analyze the LD optical power limitations and optimize its packaging. The packaging process of such devices requires to overcome both optical, mechanical and electrical issues. These last are often highly interactive and the stability of devices is an essential factor to ensure high performances and develop reliable solutions [13]. In such a context, 2D stationary FEM-based multiphysics simulations appear as relevant tools.

The thermal management investigation is of major importance to scope these performances. Therefore, the study of each assembly part (submount and die-attach materials) as well as the geometry of the LD (etching depth of grooves, layer thicknesses) has been carried out with FEM simulations. Indeed, despite the great interest of analytical models such as previously developed, some local effects can only be analyzed through 2D or 3D simulations in particular based on FEM. For that, 2D stationary thermo-electrical simulations have been done to predict the thermal flow distribution within the micro assembled LD and paying particular attention to the following points:

- The impact of the etching depth of the grooves on the junction temperature depending on the bias current.
- The junction temperature versus current characteristics with different submounts (CuW or Diamond-copper composite) and different soldering thicknesses.

In literature, there are many studies regarding application of Finite Element Modelling (FEM) as an efficient tool addressing thermal management of semiconductor LDs but all are based on some particular assumptions:

- Without considering any Joule effect as reported in [14].
- Based on the solution of a two-dimensional model, the stationary heat conduction equation obtained by the separation-of-variables approach [15].
- Using a rate-equation approach and compared to FEM results [16].
- Investigation on steady-state thermal behavior of a semiconductor laser in CW regime [3].

- A 2D model according the longitudinal section [9].

In order to calculate the thermal gradient within a LD, the simulation must take care of three main points:

- Calculation of the bias voltage from the current density travelling the structure considering the application of the Ohm's law.
- Modelling of the different heat sources within the optical cavity.
- Prediction of the temperature distribution through the solution to the Fourier equation.

As these three equations are coupled via the thermal and electrical conductivity of each material, a COMSOL Multiphysics approach is mandatory. This software is a general-purpose platform, based on FEM, for modelling and simulating different coupled physical phenomena involved in the operation of a system.

Material properties versus temperature

The first step of our simulations needs to consider the physical properties of each material used for the epitaxial process of the different layers. These properties correspond to relevant input data for the model used in the FEM. For thermo-electrical simulations, it is assumed that all the physical properties are not dependent on temperature.

All the electrical and thermal properties of each material of the micro assembled LD have been extracted from literature and summarized in *Table III-6*.

	x	y	$W(x,y)$ $\left[\frac{W}{m \cdot k}\right]$	K $\left[\frac{W}{m \cdot k}\right]$	ρ $\left[\frac{Kg}{m^3}\right]$	Cp $\left[\frac{J}{Kg \cdot K}\right]$	ϵ_r	N $\left[\frac{1}{m^3}\right]$	μ_e $\left[\frac{m^2}{V \cdot s}\right]$	μ_h $\left[\frac{m^2}{V \cdot s}\right]$	σ $\left[\frac{S}{m}\right]$
[N]Al _x Ga _{1-x} As	0,33	---	8,93	11,2	4805	363,6	11,9	1,0·10 ²⁴	0,18	0,013	29264
[N] Ga _x In _{1-x} As _y P _{1-y}	0,75	0,51	21,67	4,6	5127	333,2	11,7	5,0·10 ²²	0,35	0,008	2800
[---] Ga _x In _{1-x} As	0,91	---	8,21	12,2	5343	310	13,0	1,0·10 ²²	0,65	0,092	1040
[P] Ga _x In _{1-x} As _y P _{1-y}	0,75	0,51	21,67	4,6	5127	333,2	11,7	5,0·10 ²²	0,35	0,008	61,6
[P]Ga _x In _{1-x} P	0,51	---	20,27	4,9	4468	371,2	11,7	1,5·10 ²³	0,35	0,15	8400
[P]Al _x Ga _{1-x} As	0,33	---	8,93	11,2	4805	363,7	11,9	1,5·10 ²³	0,18	0,013	313,2
GaAs	---	---	---	46	---	---	12,4	2,2·10 ²⁴	0,30	0	108036
Copper	---	---	---	---	---	---	---	---	---	---	---

Table III-6: Material properties used in our thermo-electrical models.

where x , y , W , K , ρ , C_p , ϵ_r , N , $\mu_{e/h}$, σ are the mole fraction, the lattice thermal resistivity, the thermal conductivity, the density, the heat capacity at constant pressure, the relative permittivity, the doping level, the electron/hole mobility and the electric conductivity respectively.

Among all these parameters, their thermal behaviour has been carefully analyzed as given in the following sub-sections. For further information on material properties and their temperature dependence, one can refer to *Annex n°3*.

3.4 THERMO-ELECTRICAL FEM SIMULATIONS - COMPARISON BETWEEN F-P AND DFB VERTICAL STRUCTURES

This section will present some results of two thermo-electrical simulations mainly based on the LOC vertical structure. Note that these results can be easily applied to the two other structures.

First, simulations performed in “*Chapter III - Results of thermo-electrical simulations along the transversal cross-section*” and “*Chapter III - Results of thermo-electrical simulations along the longitudinal cross-section*”, are done to understand the effects of the insulation channels etching and the NIM window processed at the front facet on the thermal management of the LD. Two different lengths of NIM window are considered. In this case, results from thermo-electrical simulations will be combined with those of optical simulations as detailed in “*Chapter II - Effects of a Non-Injected-Mirror (NIM) window*”, in order to determine the optimal NIM length. Only 2D simulations are addressed. Indeed, due to a size heterogeneity of the structure, the 3D meshing procedure of the overall structure becomes a huge challenge in a reasonable time. For instance, the QW has a thickness in the order of a few tens of nm while the cavity length is in the range of mm. Secondly, investigations on the grooves influence on the junction temperature does not required any specific 3D modelling.

3.4.1 Thermo-electrical steady-state simulations

a. Transverse and longitudinal cross-section models: materials and geometries

Two cross-section views (namely geometries), referred to the optical axis of the LD, are considered as shown in *Figure III-7*. We must note that considering the longitudinal cross-section, the drilled hole into the C-mount heat sink is not considered, leading to some quite optimistic results since the thermal resistance of the C-mount is certainly lower in comparison with that of the real device.

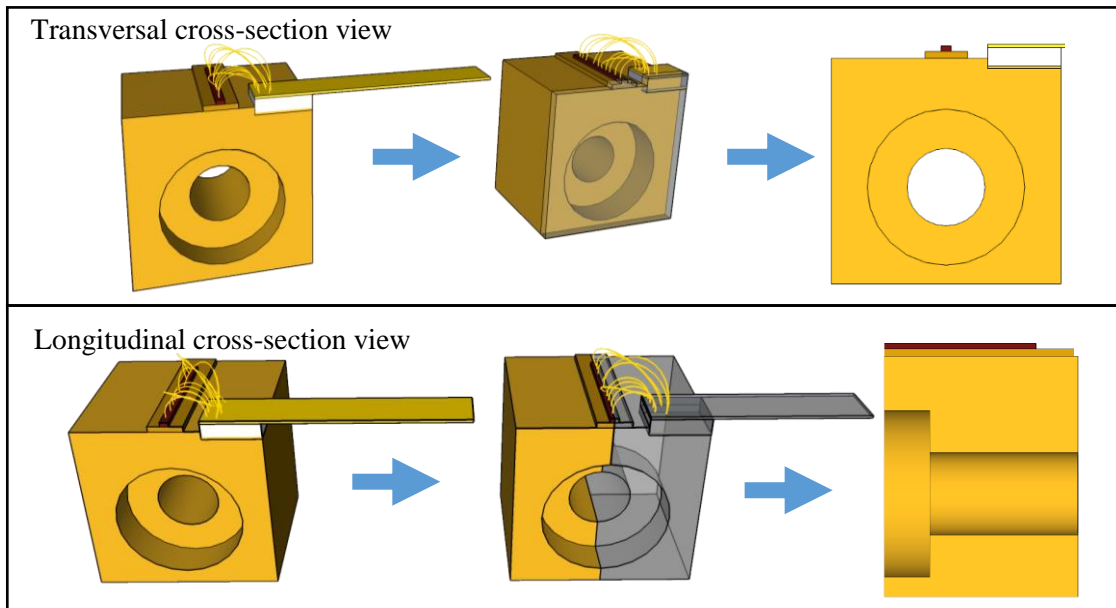


Figure III-7: Transverse and longitudinal cross-section views considered as the different geometries for the proposed thermo-electrical simulations.

Figure III-8 shows the double trench LOC structure considered for the modelling of the LD.

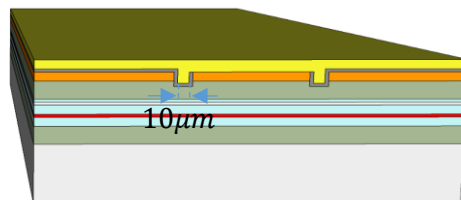


Figure III-8: Double trench LOC vertical structure considered for the thermo-electrical simulations.

The computations equipment used for the thermo-electrical simulations cannot mesh layers with a thickness below 0,1µm, hence we decide to use some approximation. *Table III-7* summarizes the difference between real and simulated LOC structure. In red, we highlight the main differences.

Layer	Material	Real thickness [μm]	Simulated thickness [μm]
Substrate	$GaAs$	150	150
Cladding	$Al_xGa_{1-x}As$	1,5	1,5
LOC	$Ga_xIn_{1-x}As_yP_{1-y}$	0,6	0,6
QW	$Ga_xIn_{1-x}As$	0,009	0,01
LOC	$Ga_xIn_{1-x}As_yP_{1-y}$	0,6	0,6
Spacer	$Ga_xIn_{1-x}P$	0,1	0,1
DFB grating	$Ga_xIn_{1-x}As_yP_{1-y}$	0,05	0,1
Spacer	$Ga_xIn_{1-x}P$	0,1	0,1
Cladding	$Al_xGa_{1-x}As$	1,5	1,5
Contact	$GaAs$	0,18	0,2
Metal	Au	0,4	0,4
Soldering	AuSn	4	4

Table III-7: Differences between the real and the simulated thicknesses used in our models for a DFB LOC LD. The F-P laser has the same structure but without spacer and DFB grating.

b. Modelling and boundary conditions

The LD mounted on a C-mount heat sink is fixed onto a dedicated copper mechanical support only used for L-I-V characterizations performed at the laboratory as shown in *Figure III-9*.

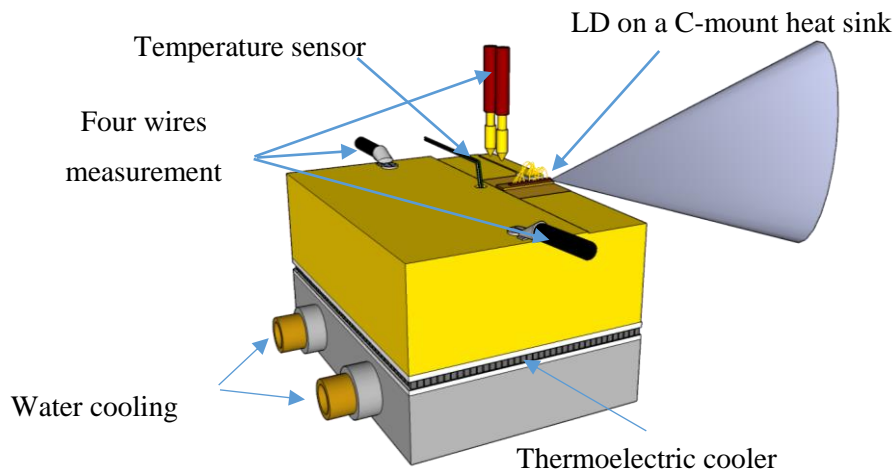


Figure III-9: LD on C-mount heat sink mounted onto a copper support.

Figure III–10 shows the simulated transversal and longitudinal cross-sections of the LD mounted on the C-mount heat sink. The modelling conditions are similar for all the investigated vertical structures (LOC, SLOC and AOC).

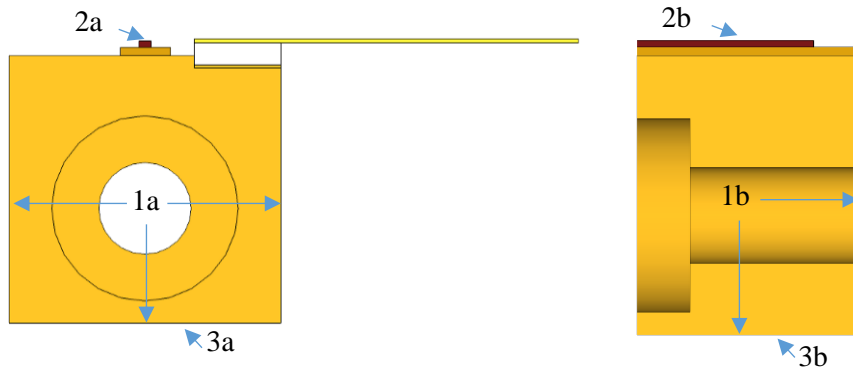


Figure III–10: Transversal and longitudinal cross-sections of the LD mounted on the C-mount heat sink.

Regarding Figure III–10, the boundary conditions are the following:

- The current density in the normal direction of the surface is applied to the LD substrate (2a, 2b).
- The ground connection is set to the bottom of the copper support (3a, 3b).
- A fixed temperature is applied along the plane 3 of the C-mount heat sink (1a,1b).
- No heat exchange between the air and the LD, except for the bottom of the heat sink (3a,3b) as reported in literature [9], [14].
- We assume a continuity between layers in the LD vertical structure: $\vec{n} \cdot (\vec{J}_1 - \vec{J}_2) = 0$.
- There is an electrical insulation along the external edge of the structure (heat sink and LD): $\vec{n} \cdot \vec{j} = 0$.
- There is no air movement close to the LD and no forced convection is assumed.

The thermo-electrical fields are calculated using the FEM. One can find an approximate solution with fields of discretization defined on sub-domain of global domain [13]. The field in each subdomain is determined by a finite number of fields values in arbitrary points called nodes. For 2D FEM simulations, it is essential to use coupled field elements since these last associate thermal and electrical simulations and both simulations are performed at the same time. The current density, used in these simulations, cannot correspond to the same current injected in the LD. Indeed, part of the injected current in a LD is converted into light above the optical threshold. Moreover, the Joule

heat contribution to the heating generation is linked to the differential quantum efficiency η_D that depends on temperature as described in [Eq. III-13] and [Eq. III-14]. The current density used in COMSOL Multiphysics® is calculated as follows:

$$J_{simul} = \frac{J_{injected} - (J_{injected} \cdot \eta_i(I))}{w \cdot L} \quad [Eq. III-20]$$

where w and L are the ridge width and the cavity length respectively while the $w \cdot L$ corresponds to the effective surface crossed by the current flow.

From values reported in *Table III-5*, the heat sources are applied into the volume of the optical cavity without considering the Joule heating (since this last is simulated for each material) as shows in *Table III-8*.

Current [A]	P_{diss_theory} [W]	Heat sources_Theory [W/m ³]	Heat sources_No Joule heating [W/m ³]
1	0,96	$2,42 \cdot 10^{12}$	$2,09 \cdot 10^{12}$
2	1,45	$3,66 \cdot 10^{12}$	$3,35 \cdot 10^{12}$
3	2,02	$5,09 \cdot 10^{12}$	$4,71 \cdot 10^{12}$
4	2,66	$6,72 \cdot 10^{12}$	$6,20 \cdot 10^{12}$
5	3,39	$8,55 \cdot 10^{12}$	$7,81 \cdot 10^{12}$
6	4,20	$1,06 \cdot 10^{13}$	$9,55 \cdot 10^{12}$
7	5,12	$1,29 \cdot 10^{13}$	$1,14 \cdot 10^{13}$
8	6,15	$1,55 \cdot 10^{13}$	$1,29 \cdot 10^{13}$

Table III-8: Calculated dissipated power and heat sources versus bias current for a 4mm length laser LOC structure.

c. Methodology for an optimal meshing process

In COMSOL Multiphysics®, it is possible to use different type of meshing elements as a square or a triangle and set many boundary conditions as the number of the nodes in each line. The number of nodes and the calculation time are compared using the same boundary conditions and focusing mainly on the LOC vertical structure. To force a gradual meshing of the geometry, we add complementary lines to the geometry as shown in *Figure III-11* and *Figure III-12*. Rather than use the automatic meshing process, each layer is meshed using different boundary conditions. Hence, COMSOL Multiphysics® requires performing a regular meshing in each layer and to use a progressive increase of meshing elements in the C-mount heat sink.

Meshing of the transversal cross-section

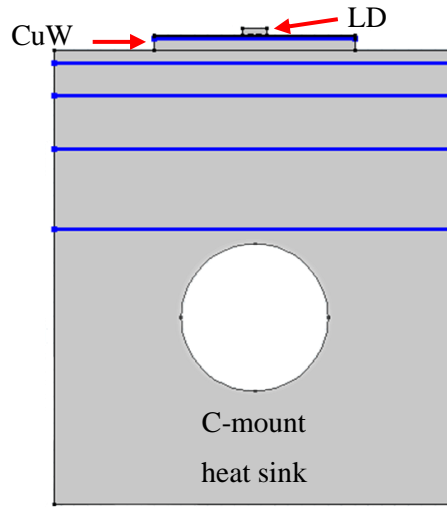


Figure III–11: Geometrical model used for thermo-electrical simulations of the transversal cross-section. The blue lines are used to set the boundary conditions during the meshing process. In these lines, it is possible to set the total number of intersection points used in the meshing.

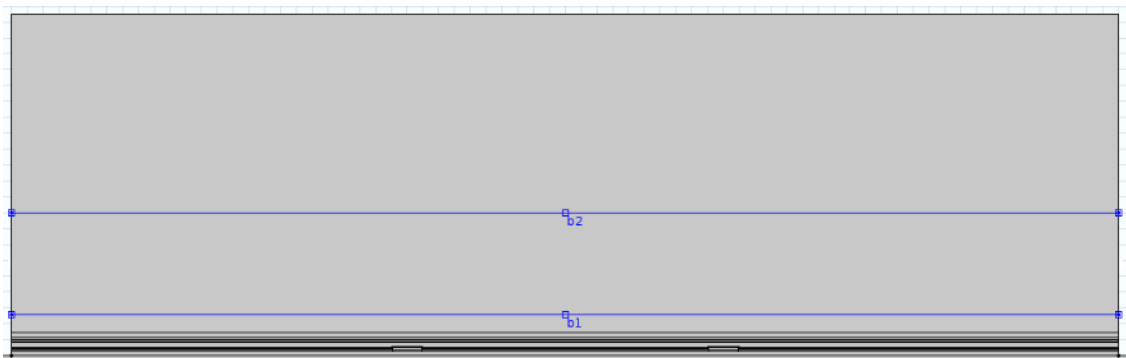


Figure III–12: Zoom of the complementary lines used within the LD. These lines allow dividing the substrate layer that has a higher thickness ($150\mu\text{m}$) than the other layers ($0,5\mu\text{m}$) and force a gradual meshing.

From Figure III–13 to Figure III–15, we show the results using a meshing based on square elements. The use of layers with progressive thickness combined with boundary conditions at interfaces, allows us to mesh the geometry. For all interfaces, the number of nodes is set so as the same number of nodes is obtained with the same spacing between two different domains.

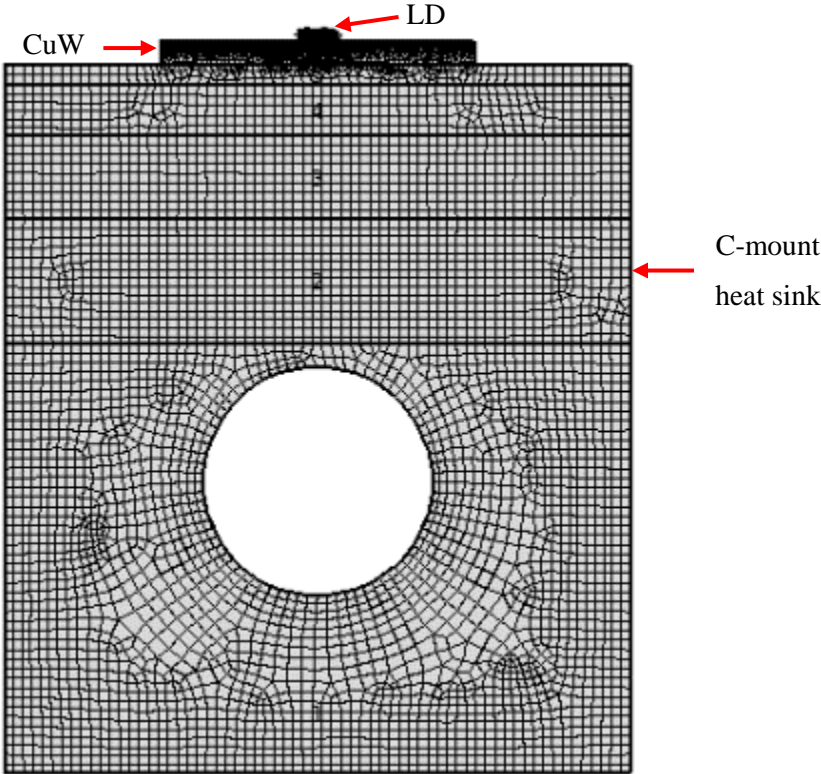


Figure III-13: Meshing of the overall device with square elements (transversal cross-section). The gradual meshing is dense near the LD.

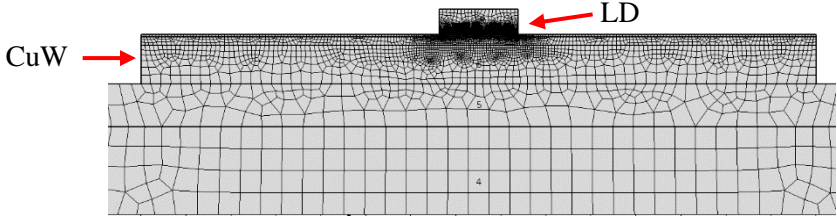


Figure III-14: Enlarged view of the LD-CuW heat spreader interface.

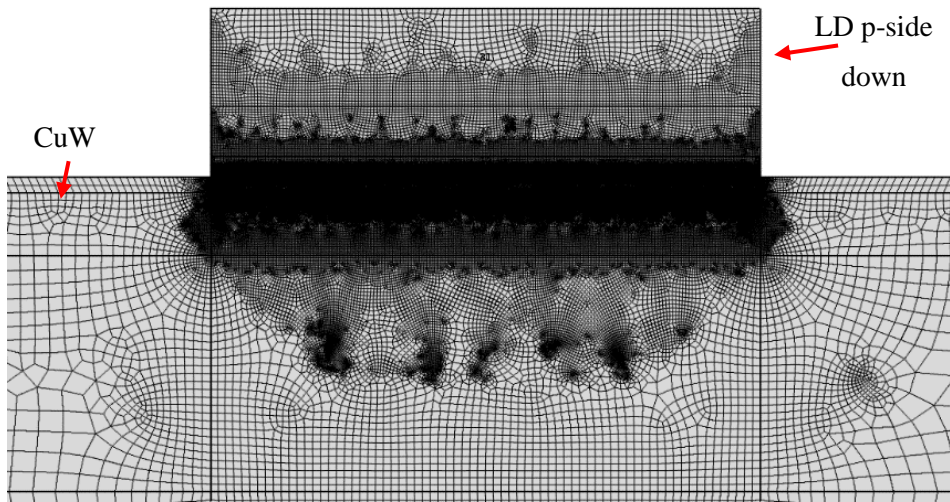


Figure III–15: Enlarged view of the LD-CuW heat spreader interface.

The thinner part of the geometry corresponds to the quantum well and a node was positioned each $0,2\mu\text{m}$ over a total width of $350\mu\text{m}$. The other parts of the geometry are meshed starting from the QW. In order to compare two performances of meshing based on triangular and square elements, we use the same boundary conditions already described in *Figure III–11* and *Figure III–12*. *Figure III–16* and *Figure III–17* show the meshed structure.

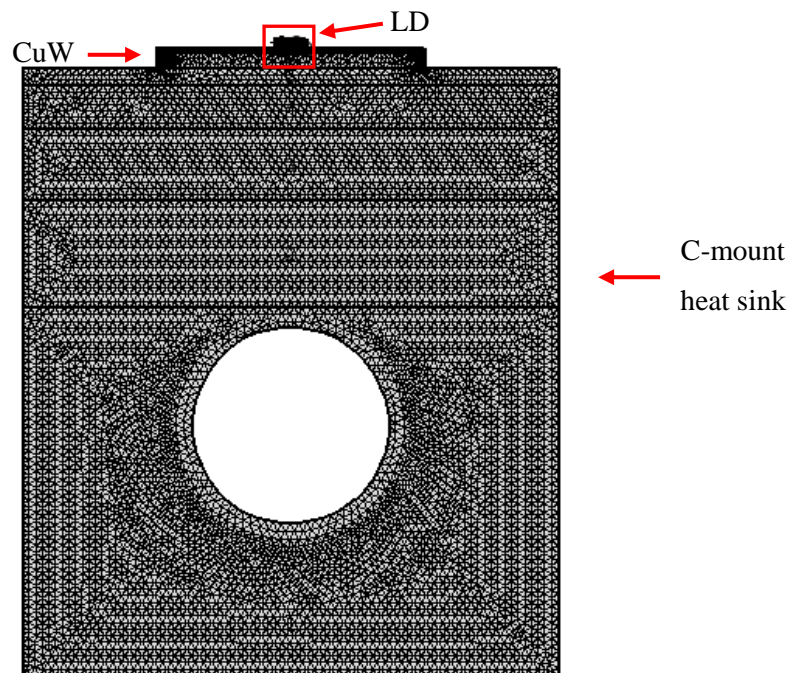


Figure III–16: Meshing of the overall device with triangle elements (transversal cross-section). The number of elements is lower compared to the previous meshing using square elements and so the number of nodes is consequently reduced resulting in a lower time of computations.

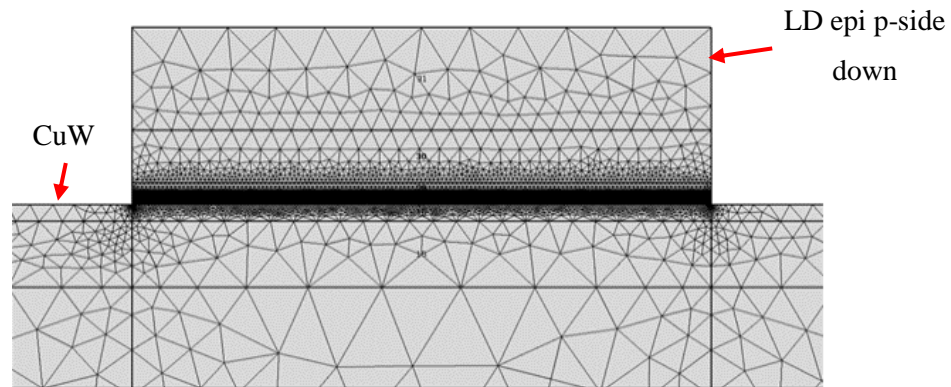


Figure III-17: Zoom of the red square area in Figure III-16. It is possible to see the LD epi p-side down on top of the CuW submount.

Table III-9 compares computational performances (meshing and solver times) using both square and triangle elements of the transversal cross-section.

Meshing element	n° of nodes	Meshing time	Solver time
		[min]	[min]
Square	393430	50	40
Triangle	298810	10	2

Table III-9: Comparison of computational performances using square and triangle elements for the meshing process of the transversal cross-section.

Meshing of the longitudinal cross-section

Regarding the longitudinal cross-section, the situation is rather different. As an example, our model includes a 50nm thick QW with a length of 4000 μm which means a difference of five orders of magnitude resulting in a more complex meshing process. In comparison with the transversal cross-section, finally a meshing process based on triangle elements ($> 10^6$) was chosen. The FEM solver takes two iterations before reaching the solution with a convergence of 10^{-5} . Figure III-18 shows the meshing distribution of the overall device.

The value of the junction temperature obtained with two different meshing operations does not change drastically. With different scenarios (multiple bias currents and heat sources in the QW), the temperature changes are not significant (first decimal). This means a temperature difference of $\approx 0,3\%$ between a meshing considering square and triangular elements. Finally, a meshing process using triangular elements (~ 300000 nodes) has been selected.

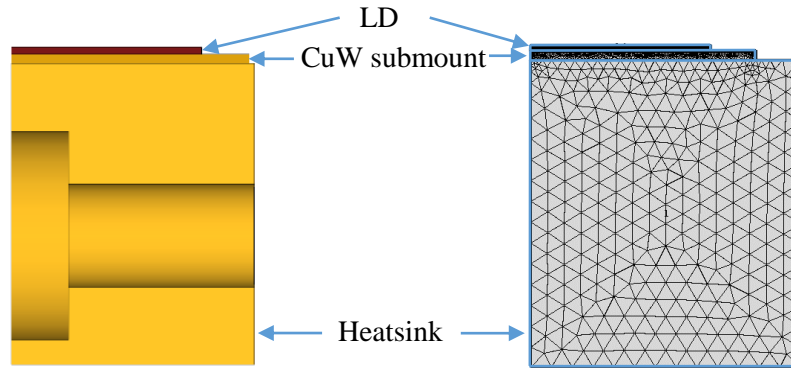


Figure III-18: Meshing of the overall device with triangle elements (longitudinal cross-section).

d. Results of thermo-electrical simulations along the transversal cross-section

Junction temperature variations versus bias current

From the thermal point of view, one can assume that no significant difference should occur between the F-P and DFB vertical structures. Indeed, a DFB structure has two additional layers compared to the F-P one in the p-side (grating/ $-Ga_xIn_{1-x}As_yP_{1-y}$ and spacer/ $-Ga_xIn_{1-x}P$) and though these layers have a low thermal and electrical conductivity as reported in *Table III-6*, no real difference is expected on the temperature distribution between the two structures. Such a result assumes that no concentration of defects is taken into consideration after the second step of the epitaxial process.

For a DFB architecture, it is possible to compare the experimental and simulated junction temperature in the QW during CW operation. Here, the considered vertical structure is based on a 4mm cavity length LOC vertical structure mounted on a C-mount heat sink. *Figure III-19(a)* compares the junction temperature (T_J) deduced from thermo-electrical simulations and the one from experiments showing a maximal difference of 5% over the bias current range.

The junction temperature, deduced from experiments, is determined from the well-known formula:

$$T_J = T_{HS} + R_{th}(P_{ele_diss} - P_{opt}) \quad [Eq. III-21]$$

where T_{HS} , R_{th} , P_{ele_diss} and P_{opt} are respectively the TEC temperature, the thermal resistance of the LD, the total dissipated power within the LD and the optical output power.

Note that all these parameters have been experimentally determined and the technique to determine the thermal resistance (R_{th}) is detailed in the first part of “*Chapter IV*”.

In order to achieve the best agreement between the experimental and the simulated results, the resistivity of the QW had to be modified and particularly decreased from $19 \Omega \cdot m$ to $4,1 \Omega \cdot m$ that corresponds to the residual doping level of the QW (the residual doping of the n-side GaInAsP layer grown). Similar results have been obtained for the SLOC and AOC vertical structures.

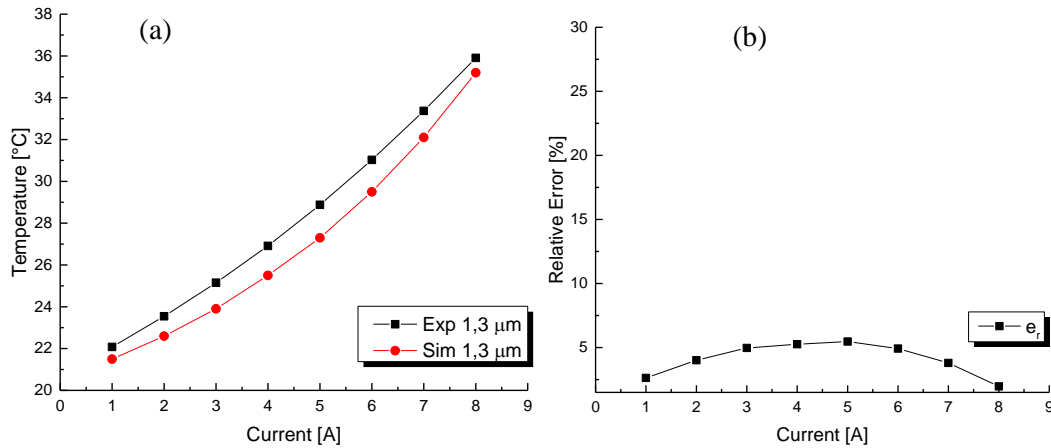


Figure III-19:(a) Comparison between experimental and simulated junction temperature versus the bias current for a 4mm cavity length DFB structure mounted on a C-mount heat sink. (b) Relative error between experimental and simulated results. This accordance between simulated and experimental junction temperature has been achieved modifying the QW resistivity.

Independently from the vertical structure (LOC, SLOC or AOC), the LD can be fabricated from two different designs (single ridge and double trench) as presented in *Figure III-20*. Compared to the double trench technology, the “single ridge” is realized by removing the p-side contact layer (orange colour) and part of the cladding layer (green colour) everywhere except in the emission area. Then, everything is covered with the metallization layer (yellow). The Schottky barrier guarantees the insulation of the left and right side of the LD.

Because the LD is soldered epi-p side down, such a configuration has a huge negative influence on the thermal dissipation. Because of the small area of contact, approximately $90\mu m$ of the central ridge, the LD can be mounted with a possible tilt (teta) resulting from the soldering process. To avoid such a problem, a new configuration has been developed, namely the “double trench” process. Each trench has a width of $10\mu m$. In this configuration, the deposition of the metallization is uniform all over the device. Hence, during the soldering, the occurrence of such a tilt is lesser. The great interest of the “double trench” process is to provide a good planarization of the LD onto the heat sink. With the help of simulations, it is possible to analyse these two configurations from a

thermal point of view. For such a study, we choose to use the same vertical structure (LOC), with the same depth of the etching ($0,7\mu\text{m}$) and the same cavity length (4mm). The same methodology can be easily extended to either the two other vertical structures (SLOC and AOC) or different cavity lengths.

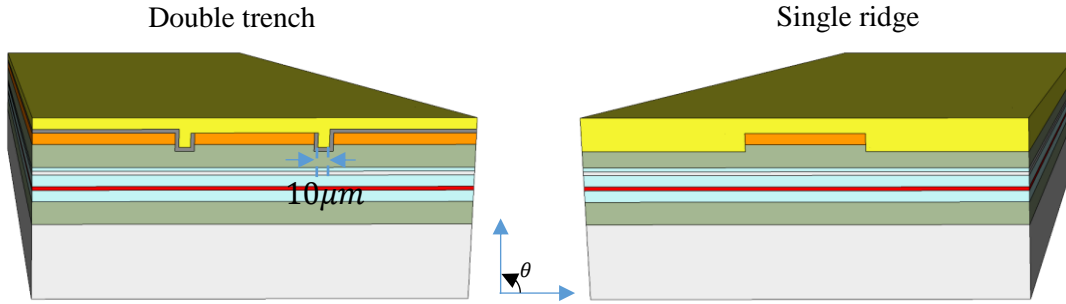


Figure III–20: 3D view of the “double trench” and the “single ridge” designs.

Figure III–21 plots the comparison between the junction temperature of the QW extracted from [Eq. III-21] and predicted by FEM simulations on the two designs. The experimental values of junction temperature refer to $R_{th} = 1\text{K/W}$ and $T_{HS} = 293,15\text{ K}$. Figure III–21 clearly shows that the variations of the simulated junction temperature versus bias current for the “single ridge” and the “double trench” are quite similar. One can conclude that the presence of the oxide in the “double trench” does not significantly affect the thermal dissipation. For this design, changing the oxide width does not have a significant impact on the heat flow within the vertical structure. The “double trench” design demonstrates a slight benefit at high bias currents (few % of T_j reduction) compared to the “single ridge” one.

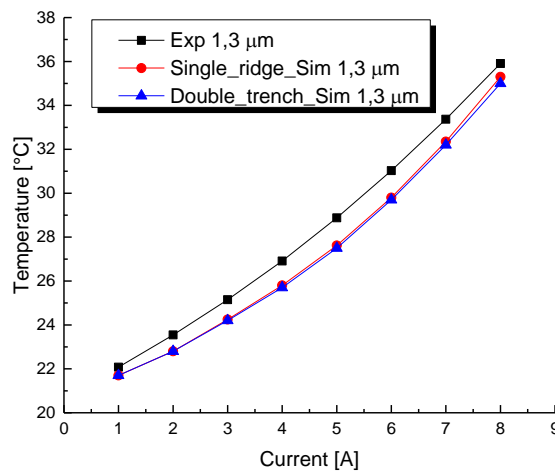


Figure III–21: Comparison between experimental and predicted junction temperature for the two designs (single and double trench).

The results also demonstrate a quite optimistic behaviour of the simulations since the predicted junction temperature is continuously lower than the experimental one over the bias current range (~ 5%). This can be due to both:

- The overestimated thermal resistance of the micro assembled LD used in [Eq. III-21].
- Physical parameters of the LD model have been set based on data given in Table III-6 and these values have been extracted from literature that can be rather different from the materials used in our technology.

Figure III-22 shows the current density distribution into the LD vertical structure distribution for a 4 mm LOC LD under a bias current of 8A and by the well-known electro-thermal analogy, we can clearly assume that the heat generation is in the central ridge. As the current density distribution in the device is mostly concentrated in the central ridge, it is obvious that the heating sources are also concentrated in the same region. Because of that, the areas outside the central ridge are slightly concerned by the heat transfer.

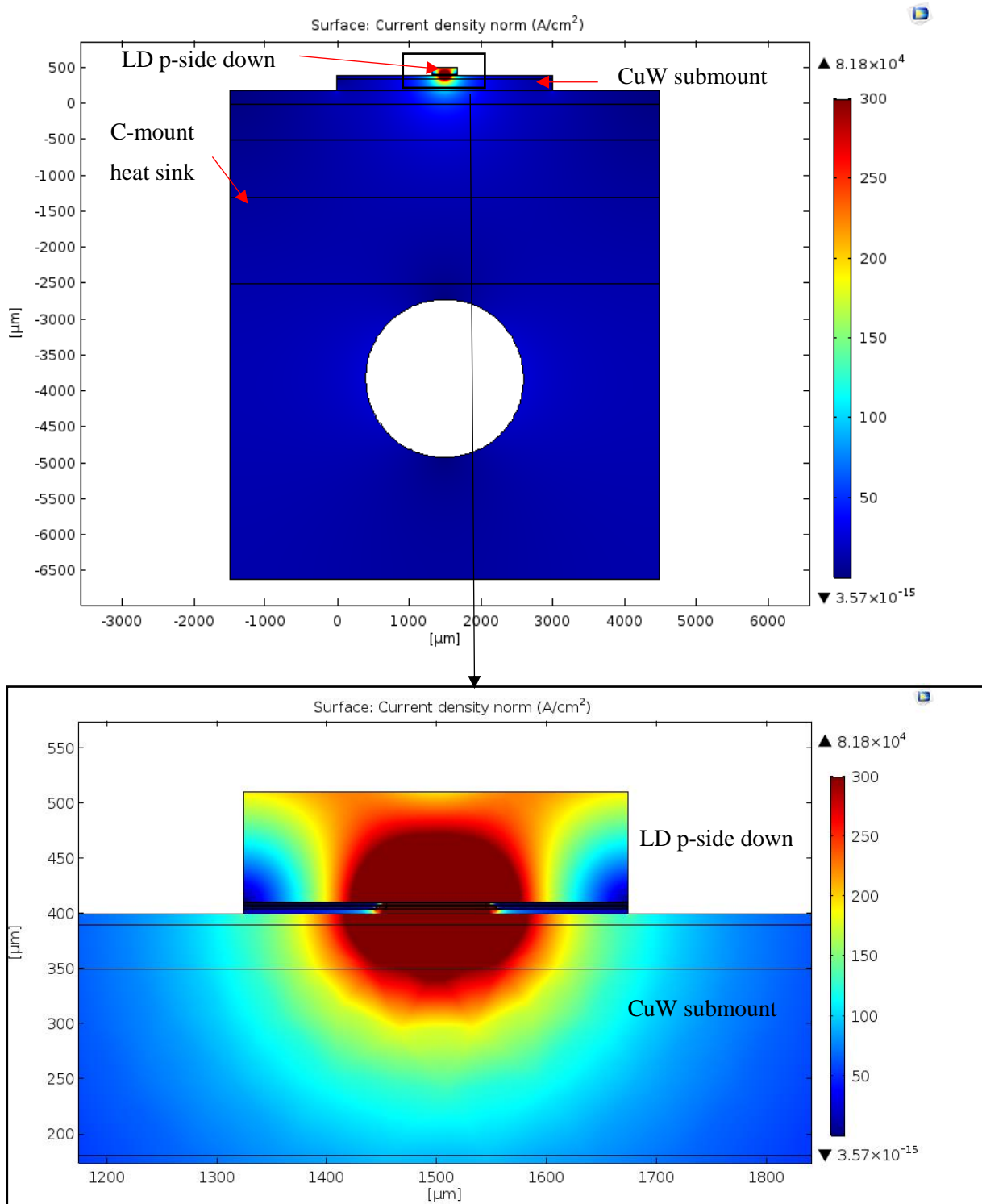


Figure III-22: Density current distribution for a 4 mm LOC LD under a bias current of 8A.

Influence of the etched grooves depth on the junction temperature (“double-trench” design)

With such 2D thermo-electrical simulations, it is possible to optimize the electrical lateral confinement in the LD. Moreover, we have investigated on the effect of the grooves etching depth on the thermal management of the LD (double-trench” design). A generic cross-section view of the etched grooves located at the front facet is given in *Figure III–23*.

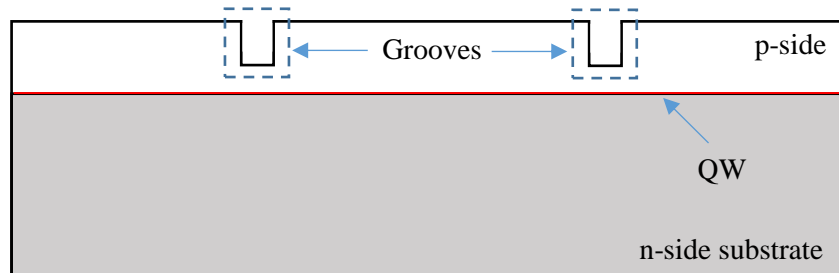


Figure III–23: Generic cross-section view of the LD (not mounted on the CuW submount) with the etched grooves (depth not at the scale)

Figure III–24 plots the simulation results of the current density variations in the QW as a function of the grooves etching depth for a 4mm cavity length LOC structure. These simulations have been done considering a bias current equal to 8A. A change in the etching depth of the grooves significantly affects the confinement of the current density in the central ridge. Higher is the depth and stronger will be this confinement.

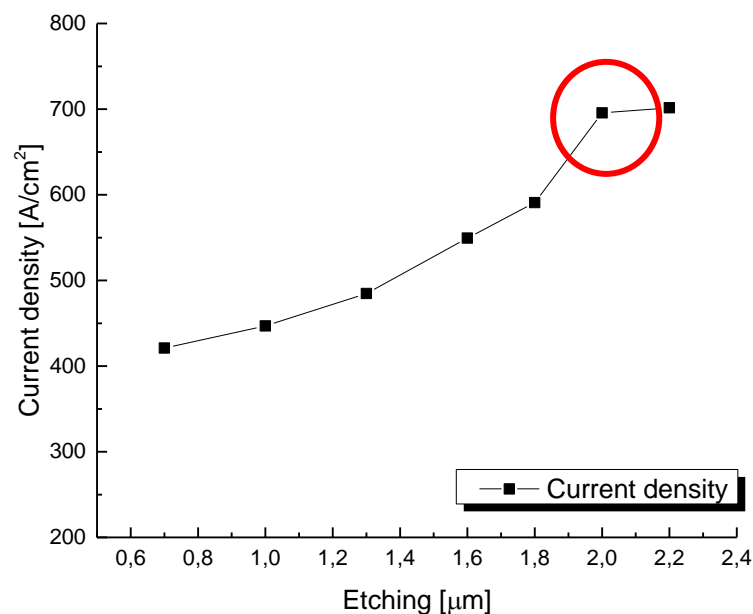


Figure III–24: Variations of current density in the QW as function of the grooves etching depth for a 4mm cavity length LOC structure. The knee point (red circle) corresponds to the limit of the cladding layer thickness. The AlGaAs layer is highly doped, compared to the optical confinement layer (GaInAsP).

The current density increases according the etching of the grooves in particular up to $1,8 \mu\text{m}$. In this range, the etching depth does not reach the p-side AlGaAs layer. This layer is highly-doped compared to the other layers within the structure (almost three orders of magnitude higher) and the current spreading increases in such a layer. The knee point highlighted with a red circle in *Figure III-24*, corresponds to the end of the AlGaAs layer thickness.

Similar results have been obtained with different cavity lengths and vertical structures. The only difference for the two other structures (SLOC and AOC) lies in the knee point that occurs at different etching depths. For the SLOC, that has a cladding layer thickness bigger than the LOC structure, the knee point appears at higher values of etching depth while for the AOC structure, with a cladding layer thickness smaller than the LOC one, the knee point appears at lower values of etching depth.

Figure III-25 plots variations of the predicted junction temperature as a function of the bias current of the 4mm cavity length LOC structure mounted on the C-mount heat sink. For a comparison with experimental junction temperature extracted from [Eq. III-21], variations are also plotted for the particular etching depth of $1,3\mu\text{m}$.

Optical simulations reported in “*Chapter II*” show that the optical modes in the waveguide depend of the etching grooves depth and an etching depth ideally close to the QW allows obtaining the maximum number of guided modes. Nevertheless, thermo-electrical simulations show that the temperature in the QW increases as increases the grooves depth and preferably, the etching depth must be closer to the p-side GaAs contact layer as far as possible. So, we highlight that a compromise can be reached between the number of guided modes and the etching depth of the grooves.

In order to compare the previous results for the DFB LOC structure (*Figure III-25*) with those considering the F-P LOC structure, simulations based on the same conditions have been done and the results are given in *Figure III-26*. We demonstrate that only a minor augmentation of the temperature ($0,2^\circ\text{C}$ @ 5A) occurs that is mainly due to the addition of two layers in the vertical structure of the LD (spacer and grating).

To summarize, thermo-electrical simulations considering the transversal section in combination with optical simulations allowed determining the optimal grooves etching depth that is established at $1,2 \mu\text{m}$. This value results from a compromise targeting the best optical confinement as well as the best thermal management. With such a value, it is possible to increase the thermal roll-over threshold and, potentially, the lifetime of the LD for the targeted application field.

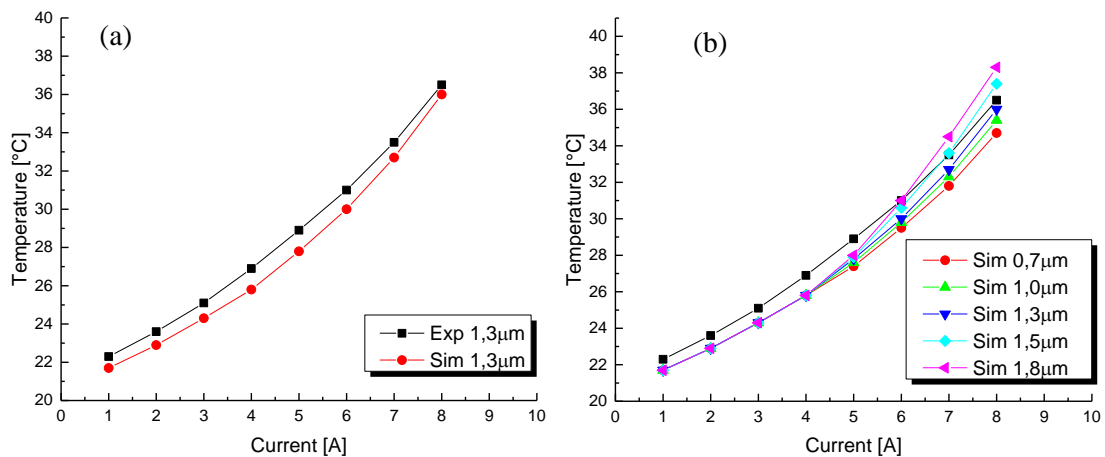


Figure III-25: (a) Comparison between simulated and experimental junction temperature variations in the QW versus bias current for a 4mm cavity length DFB-based LOC structure and the particular etching depth of 1,3µm. (b) Simulation results for different depths of etching grooves.

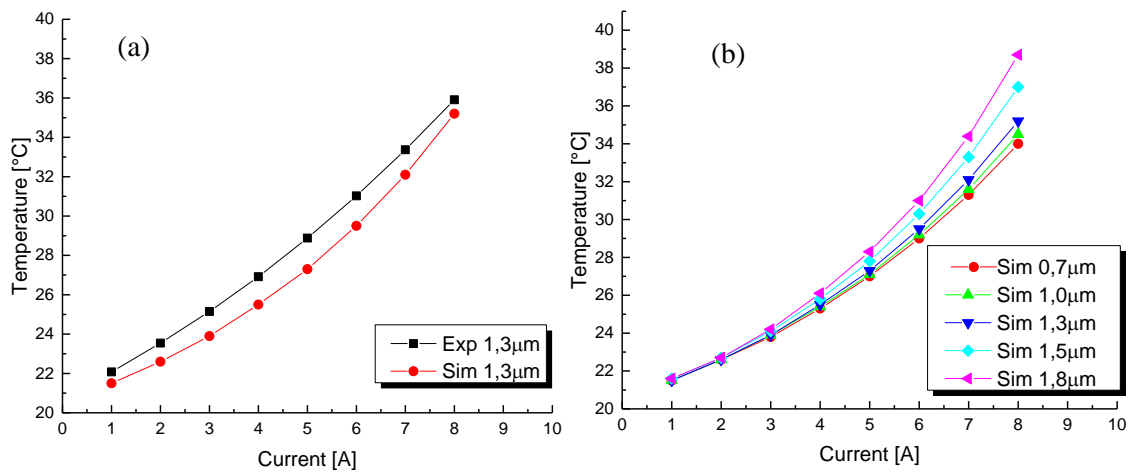


Figure III-26: (a) Comparison between simulated and experimental junction temperature variations in the QW versus bias current for a 4mm cavity length F-P-based LOC structure and the particular etching depth of 1,3µm. (b) Simulation results for different depths of etching grooves.

e. Results of thermo-electrical simulations along the longitudinal cross-section

In this section, we present thermo-electrical simulations considering the longitudinal cross-section (see Figure III-27). With such simulations, it is possible to give some results addressing:

- The temperature distribution along the cavity,
- The influence of the NIM structure located at the front facet.

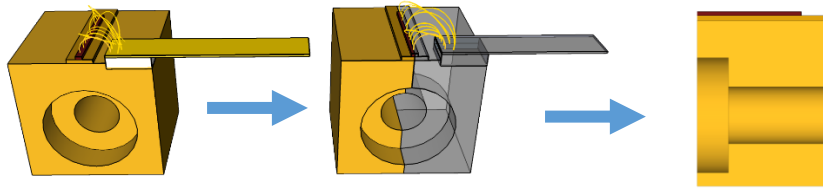


Figure III-27: Longitudinal cross-section of the LD mounted on the C-mount heat sink. The cross-section is assumed to cut the geometry of the model in the middle of the LD.

Distribution of temperature along the cavity

As studied in “*Chapter II -Effects of a Non-Injected-Mirror (NIM) window*”, there is a term of heat generation at the emission surface of the LD. Because of that, we use an additional experimental term of surface heating generation at the front facet. *Figure III-28* plots the temperature distribution within the overall structure composed of a 4mm cavity length DFB LOC LD mounted on a C-mount heat sink, under a bias current of 4A. At the emission facet, the temperature is the same than the ones predicted by simulations considering the transversal section. This simulation points out that the emission facet corresponds to the area affected by the highest temperature that agrees with literature [16]-[18]. The temperature of the front facet is higher than the other parts of the LD because of both surface carriers-recombination corresponding to a non-radiative process and the copper mass underneath the LD that is lower compared to the rear facet, thus reducing the thermal spreading path. The heat flow is supposed to go from the front facet to the rear facet. Same results have been obtained for all the vertical structures of the LD and each cavity length as described in “*Chapter II -Effects of a Non-Injected-Mirror (NIM) window*”.

Influence of the NIM window length

In “*Chapter II -Effects of a Non-Injected-Mirror (NIM) window*”, we have presented the interest of a NIM window from an optical point of view that allows to decrease the surface recombination heating process by reducing the electrical pumping on a short zone just above the front facet. With the transversal cross-section simulations, it is possible to analyse the current density flow in the LD. Hence, we have investigated on the impact of the NIM length allowing to decrease the current density in the vicinity of the front facet surface as far as possible. Based on a literature review, two lengths have been considered: 30 and 50 μm . *Figure III-28* shows the thermal profile of the DFB LOC LD with 4mm cavity length on a C-mount heatsink. At the emission facet, the blue arrow, the temperature is the same as the simulation of transversal section. *Figure III-29*

shows the cross-section view of the LD without the NIM-(a) and with the NIM-(b). The last view is given to see the detailed structure-(c).

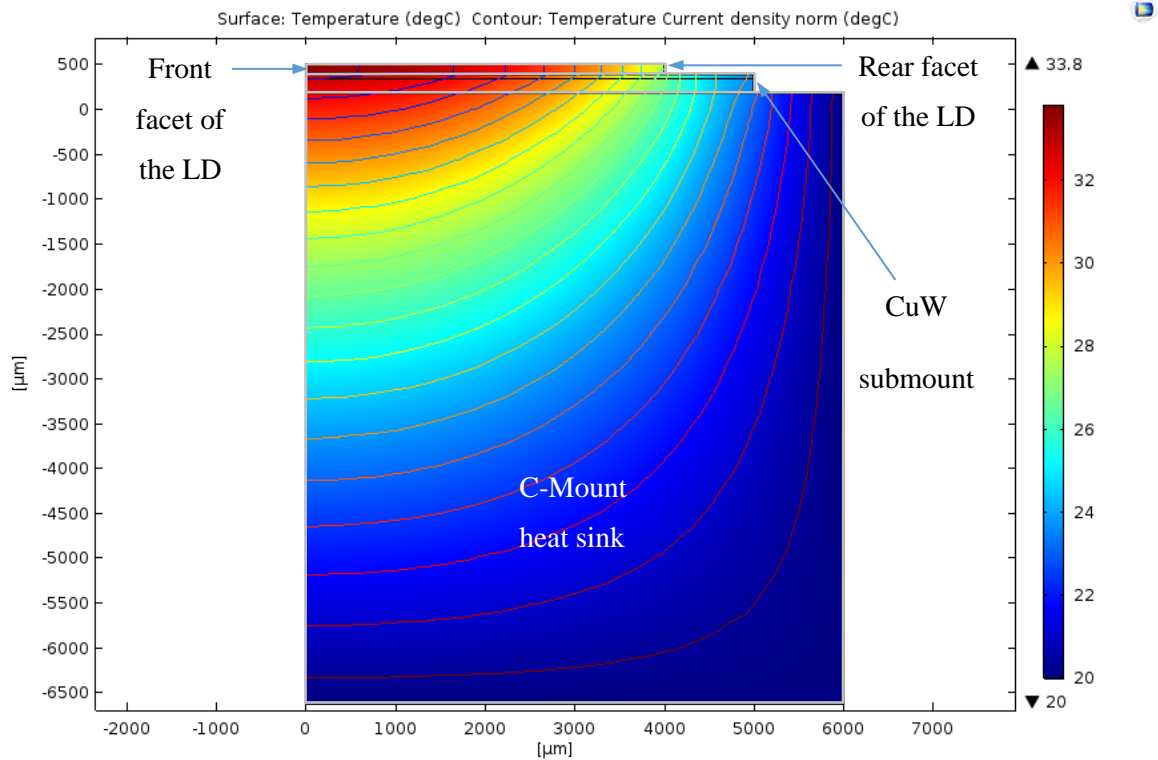


Figure III-28: Temperature distribution along the longitudinal axis of a 4 mm LOC-based LD under a bias current of 4A (longitudinal cross-section).

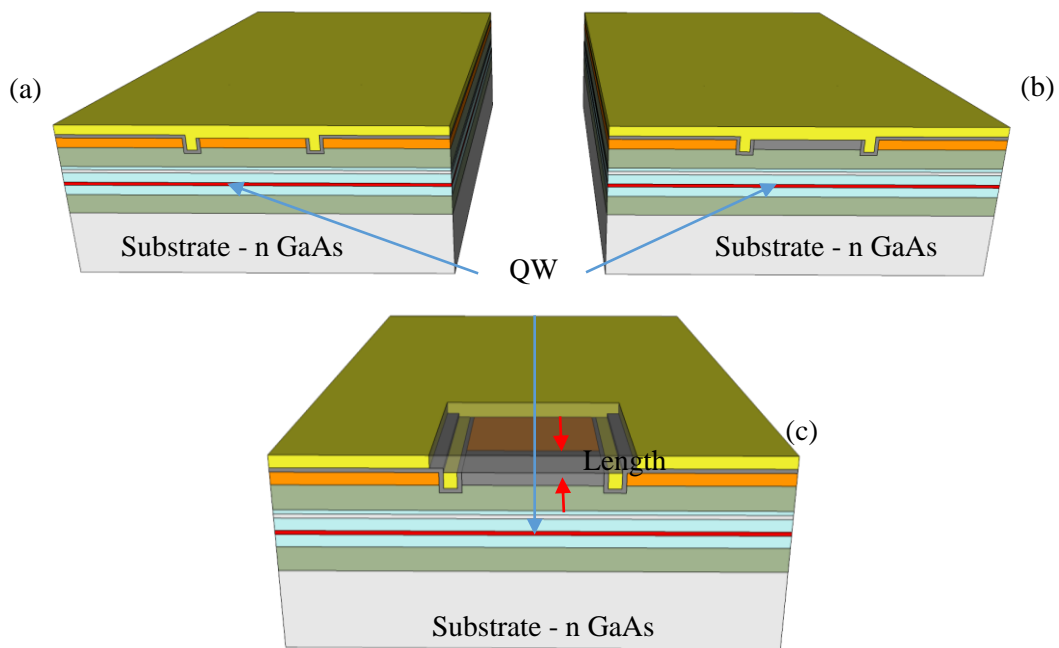


Figure III-29: Cross-section view of a LD without (a) and with the NIM (b). The noticeable difference lies in the presence of the oxide (grey layer) instead of the GaAs contact layer (orange layer). A detailed view of the NIM structure and length is drawn in (c).

For the study of the NIM windows length effect, it is of interest to focus on current density distribution in the LD rather than the temperature distribution. The NIM length must be the highest as possible to avoid the pumping of the emissive region and for this reason, simulation results only focus on the current density distribution in the vicinity of this region.

Figure III–30 and *Figure III–31* present the results of relevant thermo-electrical simulations along the longitudinal cross-section for two NIM lengths on a SLOC vertical structure under a bias current equal to 8A. We choose to use such a high value of bias current in order to investigate on the magnitude of current density at the front facet. One can remind that such a structure has the higher distance between the QW and the p-side GaAs contact layer compared to the two other vertical ones. Higher thickness means larger spreading in the LD vertical structure and for this reason, the results can be extended to the other structures that have a lower thickness between the QW and the p-side GaAs.

From *Figure III–30* and *Figure III–31*, we can conclude that the current density in the QW close to the emission facet is lower than in the other regions along the cavity and the role of the NIM length is clearly highlighted since a decrease of 45% has been obtained at the front facet. Table III-10 summarizes the results. In addition, the optical simulations do not show significant difference regarding the optical field characteristics (i.e. near and far fields) considering these two lengths of NIM. One can expect that the COMD threshold will increase as increases the NIM length.

NIM length [μm]	Current density [A/cm^2]	
	Along the cavity	At the front facet
30	190	119
50	190	65

Table III-10: Effect of the NIM length on the current density at two different locations of a DFB SLOC-based LD (4mm cavity length).

To summarize, based on optical and thermo-electrical simulations, the main outcomes are the following:

- An optimal etching depth of 0,5 μm starting from the GaAs contact layer to fabricate the NIM.
- An optimal NIM length equal to 50 μm .

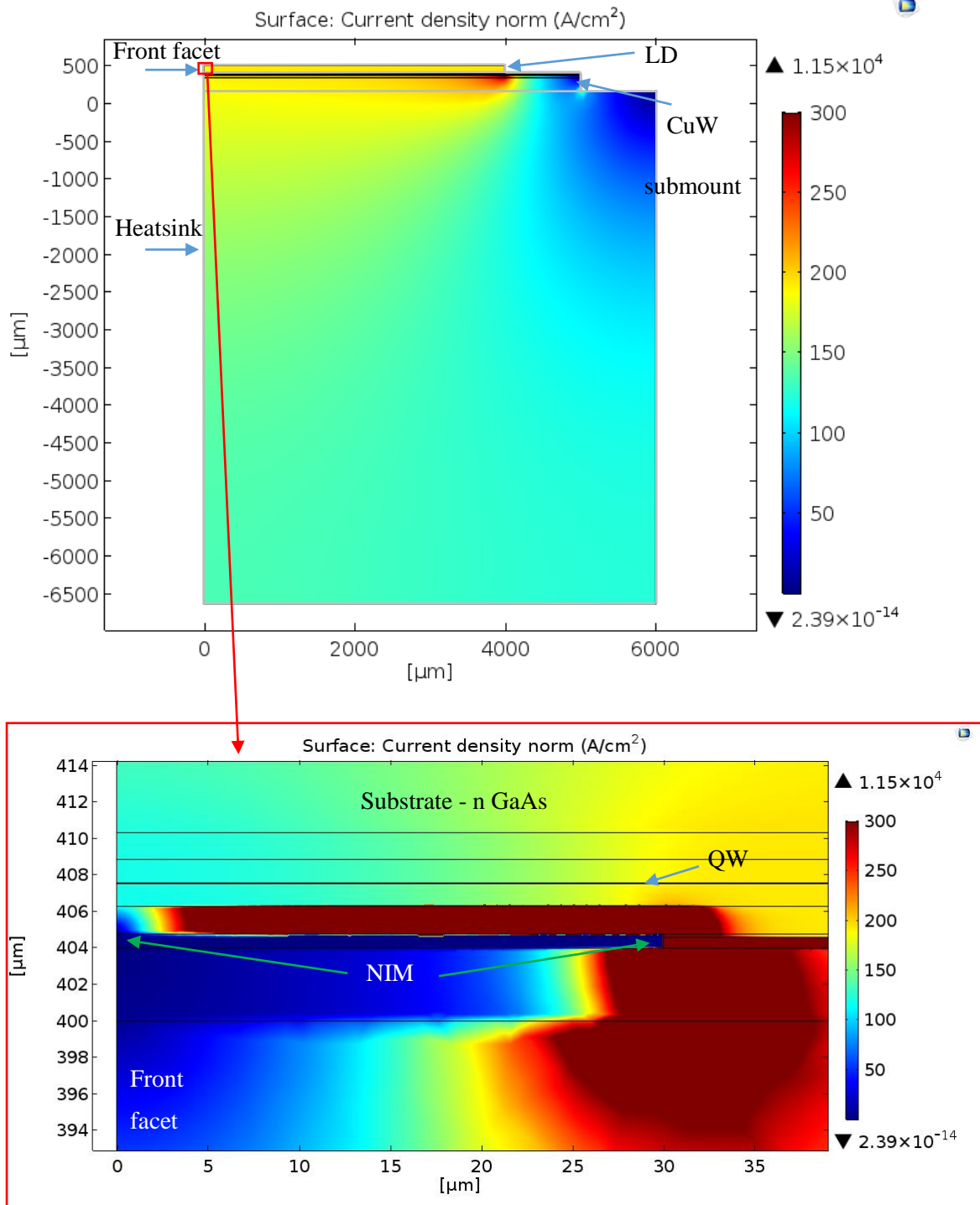


Figure III-30: Effect of a 30μm length NIM window on the current density distribution within a 4mm cavity length DFB SLOC structure (longitudinal cross-section) under a bias current of 8A.

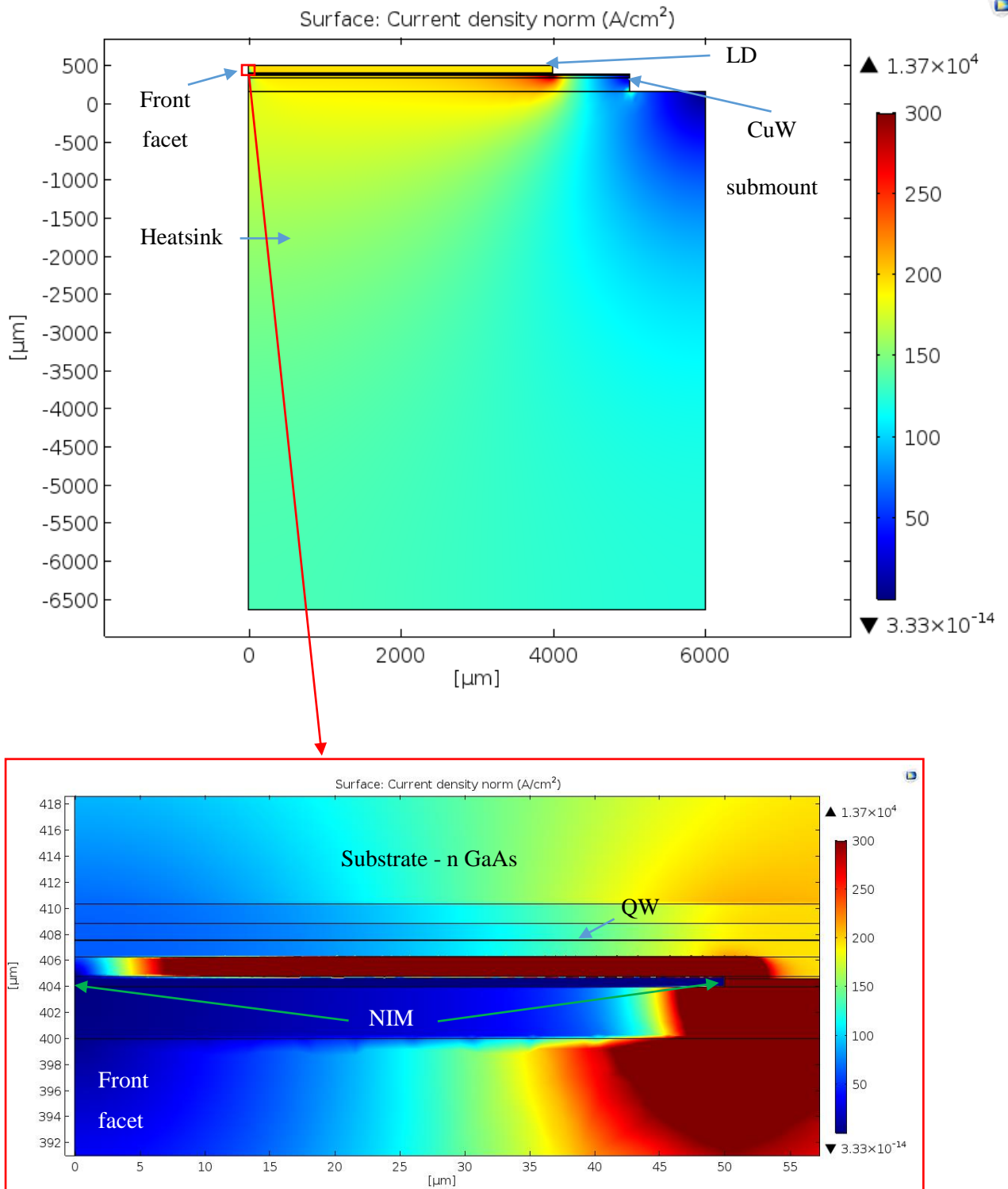


Figure III-31: Effect of a 50 μm length NIM window on the current density distribution for a 4mm cavity length DFB SLOC structure (longitudinal cross-section) under a bias current of 8A.

CONCLUSION

Thermal management investigation is of great importance in order to reach high levels of optical output power and the study of each assembly part (different submount or soldering materials) as well as the impact of the LD design (geometry, etched regions, unpumped window...) needs to be deeply investigated. **This chapter** aimed to bring a comprehension of the heat propagation in our LD technology through different tools using both analytical calculations and FEM simulations.

A first section has given a brief overview of the different heat sources in a high-power LD including well-established processes such as: Joule, Auger, SRH, re-absorption and scattering effects. However, calculations of these heat contributions lead inevitably to some approximations. For high power LD at 975nm, optical re-absorption and Joule effect are clearly the most important heat sources. In addition, these heat sources can be estimated through the optical power experimentally measured but restricted to a limited range of bias current (10A) due to the dedicated test bench.

The **second section** has described the implementation methodology of a relevant analytical model enabling to estimate these heat sources. For that, we proposed an analytical thermo-electrical model derived from three models already reported in literature, the data achieved by experimental measurements and theoretical L-I-V curves. This model can predict any L-I curve of a LD over a large range of bias current, knowing the external and the internal parameters as well as establishing a simple relationship between the structure design of the LDs and their optical performances. For that, three models (III-V lab, Simarjeet, Beringer) have been considered and main limitations from each of them have been highlighted. In particular, the first model (III-V lab) did not consider the thermal effects and the obtained results show a quite strong relative error ($\sim 25\%$ at high bias current levels) between the predicted and experimental L-I curves. The second model (from S.S. Simarjeet) assumes that $\eta_{D(n)}$ and $I_{th(n)}$ are temperature-dependent, hence the values of η_D and J_{th} change after each iteration. This third model (M. Behringer) will take into account the drift of more parameters as a function of temperature (complete self-heating) such as: η_D , I_{th} and η_i , α_i and Γg_0 . From this methodology, L-I curves can be plotted over a large range of bias current ($> 10A$) with the best fit (error $< 5\%$) obtained between experiments and calculations whatever the vertical structure and the cavity length. Using these L-I curves, it is possible to calculate the current density applied to the LD and then estimate the heat sources located within the optical cavity. For that, each heat contribution in a high-power LD has been carefully taken into account from works of M. Kansar and predictions of the overall dissipated power have been done. In order to analyze the heat

flow propagation in the micro assembled LD through FEM-based simulations, these predicted heat sources are of major interest for the input data of the model.

The development of high power LDs emitting at 975nm capable to reach high levels of optical power (10W) needs to accurately analyze optical power limitations and optimize its packaging. The packaging process requires to overcome both optical, mechanical and electrical issues. These last are often highly interactive and the stability of devices is an essential factor to ensure high performances and develop reliable applications. In such a context, time dependent FEM-based multiphysics simulations appear as a relevant tool. Indeed, despite the great interest of such analytical models, some local effects can only be analyzed through 2D or 3D simulations in particular based on FEM.

The third section described, analyzed and discussed the results achieved from stationary thermo-electrical simulations considering the transversal section (parallel to the front facet plane) and longitudinal section (parallel to the longitudinal axis of the LD) with specific boundary conditions. Because of the size heterogeneity of the structure, the 3D meshing procedure of the overall structure has represented a huge challenge and only 2D simulations have been addressed. These last have been performed with the COMSOL© software using a necessary Multiphysics approach, to predict the thermal flow distribution in F-P and DFB LDs under a specific bias current. Then, the effect of grooves etching depth defining the stripe width (90 μ m) and the length of Non-Injected Mirror (NIM) window were also discussed in terms of current density and heat distribution both at the emissive front facet and along the longitudinal axis of the LD.

Optical simulations highlighted that the optical modes in the waveguide depend of the etching grooves depth and an etching depth ideally close to the QW allows obtaining the maximum number of guided modes. Nevertheless, thermo-electrical simulations have also reported that the temperature in the QW increases as increases the grooves depth and preferably, the etching depth must be closer to the p-side GaAs contact layer as far as possible. A compromise is necessary to consider between the number of guided modes and the etching depth of the grooves. Between the DFB and the F-P design (LOC-vertical structure), it is demonstrated that only a minor augmentation of the temperature (0,2°C @ 5A) occurs that is mainly due to the addition of two layers in the vertical structure (spacer and grating). Simulations considering the transversal section in combination with optical simulations allowed determining the optimal grooves etching depth that is established at 1,2 μ m and corresponds to the middle of the cladding layer. This value results from a compromise targeting the best optical confinement as well as the best thermal management. Then, it is possible to increase the thermal roll-over threshold and potentially, the lifetime of the LD for the targeted application field. A best fit was obtained when experimental and simulated junction

temperatures in the QW are compared ($< 5\%$). For the LOC-based DFB device (4mm cavity length), the junction temperature reaches 37°C @ 8A. Finally, the influence of the NIM window length was investigated and the following optimized design rules are proposed:

- An etching depth of $0,5\mu\text{m}$ starting from the GaAs contact layer to fabricate the NIM.
- A NIM length equal to $50\mu\text{m}$ allowing a decrease of 45% of the current density at the front facet compared to a $30\mu\text{m}$ length.

CHAPTER III REFERENCES:

- [1] X. Liu, M. H. Hu, C. G. Caneau, R. Bhat, and Chung-en Zah, "Thermal Management Strategies for High Power Semiconductor Pump Lasers," in *IEEE Transactions on Components and Packaging Technologies*, vol. 29–2, pp. 268–276, 2006.
- [2] J. Piprek, "Non-radioactive recombination," in *Semiconductor Optoelectronic devices Introduction to physics and simulation*, Academic press publication, pp. 69–71, 2003.
- [3] E. Suhir, J. Wang, Z. Yuan, X. Chen, and X. Liu, "Modeling of Thermal Phenomena in a High Power Diode Laser Package," in *International Conference on Electronic Packaging Technology & High-Density Packaging*, vol. 1, pp. 438–432, 2009.
- [4] M. Szymanski, M. Zbroszczyk, and B. Mroziwicz, "The influence of different heat sources on temperature distribution in broad-area diode lasers," in *Advanced Optoelectronics and Lasers, proceedings of CAOL*, vol. 1, pp. 252–254, 2003.
- [5] M. Takahiro, "Current versus light output characteristics," in *Fundamentals of semiconductor Laser*, 2nd ed., Japan: William T. Rhodes, pp. 89–186, 2015.
- [6] Y. C. Chen, R. G. Waters, J. J. Coleman, D. P. Bour, P. Wang, "Carrier Recombination Rates in GaAs/AlGaAs and Strained InGaAs/GaAs Quantum Wells Under High Levels of Excitation," in *12th IEEE International Conference on Semiconductor Laser*, vol. 1, pp. 182–183, 1990.
- [7] A. Fily, "Chapter 6 Aspects de thermique de la diode laser de puissance," in *Thèse de doctorat Modèles pour diodes laser de puissance*, Université Paris XI, pp. 183–191, 1998.
- [8] T. E. Nee, C. C. Cheng, and M. Lin, "Phonon-Assisted Auger Recombination Processes in InGaAs/GaAs Single-Quantum-Well Lasers," in *Japan Journal of Applied Physics*, vol. 43, no. 3, pp. 890–893, 2004.
- [9] S. S. Simarjeet, C. Si Hyung, and D. Mario, "Thermal considerations in high power lasers and SOAs," in *SPIE proceedings Photonics Packaging, Integration, and Interconnects VII*, vol. 6475, p. 15, 2007.
- [10] B. Martin, G. Erbert, M. Reinhard, B. Konstantin, T. Jens W., and K. Mark, "High-Power Diode Laser: Fundamentals, Technology, Application," in *High-Power Diode Lasers*, Springer/Verlag., vol. 128, pp. 5–74, 2007.
- [11] U. Menzel, A. Bärwolff, P. Enders, D. Ackermann, R. Puchert, and M. Voss, "Modelling the temperature dependence of threshold current, external differential efficiency and lasing wavelength in QW laser diodes," in *Semiconductors Science Technology*, vol. 10, pp. 1382–1392, 1995.
- [12] M. Kanskar, J. Cai, C. Galstad, Y. He, S.H. Macomber, E. Stiers, S.R. Tatavarti-Bharatam, D. Botez, L. J. Mawst, "High power conversion efficiency and wavelength stabilized, narrow bandwidth 975nm diode laser pumps," in *SPIE proceedings Laser Source and System Technology for Defense and Security II*, vol. 6216, 2006.

- [13] Y. Deshayes, Y. Ousten, and L. Bechou, “Chapter 10 - Techniques Three-Dimensional FEM Simulations in Laser Modules and Their Applications,” in *Mems/Nems Handbook techniques and applications*, Springer., vol. Medical applications and MOEMS, Leondes, Cornelius T.
 - [14] A. Bärwolff, R. Puchert, P. Enders, U. Menzel, and D. Ackermann, “Analysis of thermal behaviour of high power semiconductor laser arrays by means of the finite element method (FEM),” in *Journal of Thermal Analysis and Calorimetry*, vol. 45, no. 3, pp. 417–436, 1995.
 - [15] M. Szymanski, “Two-dimensional model of heat flow in broad-area laser diode: Discussion of the upper boundary condition,” in *Microelectronics Journal*, vol. 38, pp. 771–776, 2007.
 - [16] G. Erbert, A. Barwolff, J. Sebastian, and J. Tomm, “High power Broad area diode laser and laser bars,” in *High-Power Diode Lasers*, vol. 78, Springer Berlin Heidelberg, pp. 173–223, 2000.
 - [17] W. B. Joyce and R. W. Dixon, “Thermal resistance of heterostructure lasers,” in *Journal of Applied Physics*, vol. 46, no. 2, pp. 855–862, 1974.
 - [18] F. Rinner, M. Kelemen, M. Mikulla, G. Weimann, J. Tomm, and R. Poprawe, “Facet temperature reduction by a current blocking layer at the front facets of high-power InGaAs/AlGaAs lasers,” in *Journal of Applied Physics*, vol. 93, no. 3, pp. 1848–1850, 2003.
-

CHAPTER IV

LASER DIODE THERMAL RESISTANCE MEASUREMENT AND PACKAGING- INDUCED STRESS ANALYSIS

INTRODUCTION

Through analytical calculations and thermo-electrical FEM simulations, the previous chapter has addressed the thermal management of the fabricated devices operating in CW regime. An important parameter to quantify it lies in the determination of the thermal resistance of the micro assembled device since a low value of this parameter allows to reduce the junction temperature by an optimized thermal dissipation path (by 1D conduction and spreading effect), ensuring long-term operation especially when high output optical power is foreseen ($> 10\text{W}$).

Moreover, the surface mounting of a high-power LD by solder joint represents a critical step since it has been already demonstrated that the soldering process induces residual mechanical strain/stress in particular due to CTE mismatch between the different materials and their temperature-dependent thermomechanical behaviour (i.e. stress-strain curves versus temperature). Time and temperature-dependent relaxation phenomenon of such a residual stress can lead to formation of point defects and dislocations in the active region as well as delamination and/or crack along interfaces (for example between the chip and the solder joint) that can be responsible for a large increase in thermal resistance and consequently an occurrence of hot spots, reducing the lifetime of the LD or bring sudden catastrophic failures with very little possibility to detect early failure signatures.

This chapter 4 is divided into two main parts. **A first part** deals with a methodology enabling to extract the thermal resistance not only of the micro assembled device, as usually given by the measurement of the central wavelength drift versus both temperature (at constant bias current) and bias current (at constant temperature), but also of each material forming the overall assembly using transient thermal testing. To our knowledge, very few results are currently available in literature particularly addressing this technique for thermal resistance extraction of unpackaged high-power

DFB LDs emitting at 975nm. We will show that such a methodology can give relevant information about the thermal flow propagation along the vertical axis. Certainly, recent progress on long length cavity DFB LDs structures makes difficult to use the optical spectrum analyser due to the intrinsic multimodal nature of the LD and expected resolution. This can lead to a wrong extraction of the thermal resistance measurement (so the junction temperature) and accordingly the lifetime of the micro assembled device in operating conditions. From transient thermal testing, we will propose an optimized procedure to ensure repeatability and reproducibility of measurements that remains a key point in the case of very low thermal resistance ($< 2\text{K/W}$). We will point out the results of both methodologies and we will conclude on the benefit provided by the transient technique compared with the one derived from the optical spectrum.

A second part investigates on two mechanical configurations used to mount the LD onto the C-mount heatsink. The standard configuration will be compared with the new one; this last consists in a different placement of the chip. Thermo-electro-mechanical FEM simulations will be performed to analyse the stress distribution on the front facet (transversal section) as well as along the cavity length (longitudinal section). Finally, stress distribution analysis as well as Catastrophic optical damage (COD) threshold determination will be achieved and discussed on LDs with different vertical structures (mainly SLOC and AOC) using four dedicated techniques (micro photoluminescence, photocurrent spectroscopy, time-resolved photoluminescence and high current pulsed measurements) in collaboration with the Max-Born-Institut in Berlin. Indeed, COD corresponds to a sudden degradation mechanism that affects edge-emitting LDs in particular when operated at elevated levels of emission power. In most cases, COD starts at one of the cavity mirrors (i.e. facets) while sometimes defects within the gain medium inside the cavity also initiate the COD process. Numerous papers reported on COD effects and kinetics but most of them relying on the analysis of the resulting damage pattern once the COD is initiated. Nevertheless and even though technological improvements, COD is still a major concern thus limiting performances and operating reliability of high-power Laser devices since the COD threshold is more and more rejected towards very high current values (only achievable in pulse regime) and COD sensitivity is more and more difficult to predict on fresh devices. **This project has received funding from the EU's H2020 research and innovation programme under GA no. 654148 Laserlab-Europe.**

4.1 MEASUREMENT OF THERMAL RESISTANCE DERIVED FROM OPTICAL SPECTRUM

Since the early 1970s, the impact of the thermal dissipation in the LD has been extensively studied and particularly W. B. Joyce and R. W. Dixon has reported on the background for comprehension of thermal propagation and effects on the thermal resistance of p-side down mount LDs [1]. Later, others works from C. Amann confirmed the importance of p-side down mount [2]. However, until 1990 years, it was difficult to analyse the impact of the different soldering materials and the different sub mount on the thermal behaviour of the LDs. To characterize the thermal behaviour of high power LDs, it is convenient to introduce the thermal resistance R_{th} . Basically, this parameter is defined as the ratio of the temperature difference (i.e. between the junction and the case of the device) over the dissipated power (i.e. for two bias conditions), ($R_{th} = \frac{\Delta T}{\Delta P}$). It is well-established that the R_{th} measurement derived from the extraction of the central wavelength drift versus both temperature (at constant bias current) and bias current (at constant temperature) [3]. From now, we will refer to the R_{th} relative to micro assembled LD, soldering and heatsink. In 1998, it is possible to see the first remarkable achievement in the optical power [4]. Because of the great importance related to various fields (pump source for Er/Yb fiber, medical application, material processing), more and more studies appear over the years. JDS Uniphase in 2004 as well as nLight in 2014 reported relevant results on their 4 mm cavity length F-P LD technologies but without any information about values of their intrinsic thermal resistance [5]-[6]. Since 2010, FBH worked on F-P, DFB, and DBR broad area LDs emitting at 975 nm. The obtained value of R_{th} was about 4,6 K/W for a 3 mm DFB LD [7]-[8]. In 2012, FBH has significantly reduced the thermal resistance achieving $R_{th} \approx 2 K/W$ for a 4 mm F-P LD [9] and $R_{th} \approx 4 K/W$ for a 3 mm DFB LD [10]. In the same year, FBH has investigated on the effect of high order of DFB gratings and shows how this parameter affects the thermal resistance $R_{th} \approx 8 K/W$ or $4K/W$ [11]. In 2013, FBH and Jenoptik have stated on the achievement of low thermal resistances $R_{th} \approx 1,2 K/W$ and $0,8K/W$ for a 6 and 9 mm F-P LD [12]. Finally in 2014, FBH has demonstrated a thermal resistance of 3,5K/W and 2K/W for a 3 and 4 mm respectively whatever the considered structure (F-P, DFB, DBR) [13]-[14]. *Figure IV-1* summarizes the different thermal resistance values reached since 2008 by different research groups, for high power 975nm LDs considering only the LOC and SLOC vertical architectures.

Using the well-known technique of measurement of R_{th} previously described, we measured DFB-LDs of 4mm cavity length mounted epi p-side down on a CuW submount and over a C-mount

heatsink. The methodology used in this study is described hereafter and we obtained values of R_{th} among the best currently given in literature.

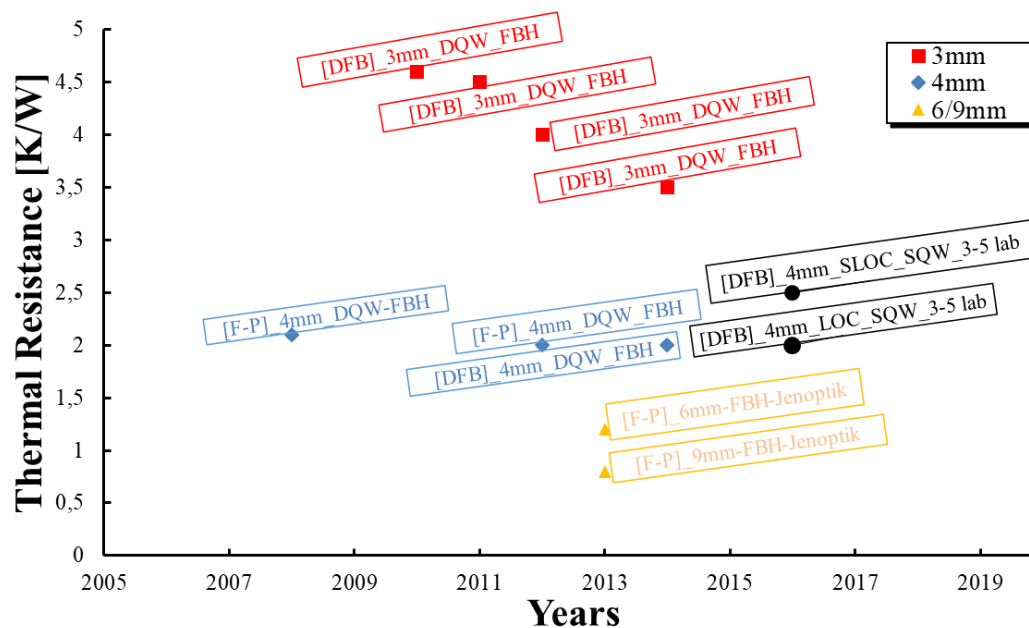


Figure IV-1: Reported values of thermal resistance for high power 975nm LDs in literature since 2008 [7]-[8]-[11]-[12]-[14]-[15]-[16]-[17]-[18]-[19]-[20]-[10]-[21]-[22]-[23]-[24].

From *Figure IV-1*, it is obvious that an estimation of the thermal resistance is somewhat difficult. Indeed, all the thermal resistance measurements are performed with the well-known technique based on the optical spectrum and the values during the years did not change drastically and do not show a real trend. Moreover, based on this measurement technique, the extraction of the thermal resistance remains an issue particularly due to the intrinsically multimodal nature of the optical spectrum.

In addition, research teams began to investigate on new ways for optimization of the thermal management. In order to reduce elevated facet temperatures, unpumped window has been implemented near the facet as presented in the previous chapter. The more the LD reaches its limits (in terms of optical power beam dimension or divergence), the more the studies pay attention on the package as well as the bonding quality of the LD [25]. Since 2009, the scientific community in the field focuses on laser bars as reported in [26]-[27] but there are still many studies to do in the field of high power Laser diodes operating near of 980nm, as shown in a recent published book [28].

4.1.1 Principle of measurement

The measurement of R_{th} is based on the well-established technique consisting on the estimation of the central wavelength drift versus both temperature, $\frac{\Delta\lambda}{\Delta T}$, (at constant bias current) and bias current, $\frac{\Delta\lambda}{\Delta P}$, (at constant temperature) [3]:

$$R_{th} = \frac{\Delta T}{\Delta P} = \frac{1}{\frac{\Delta\lambda}{\Delta T}} \cdot \frac{\Delta\lambda}{\Delta(P_{ele_diss} - P_{opt})} \quad [Eq. IV-1]$$

where P_{ele_diss} and P_{opt} represent the dissipated power and the optical output power of the LD. This technique is suitable for LDs with a low spectral width (typically $<1\text{nm}$) and it is applicable to LD on a heatsink or packaged. For the purpose of this study, such a technique gives information about the R_{th} of the entire device that include LD/submount/C-mount heatsink. It is not possible to distinguish each part of this assembly as well as each epitaxial layer of the LD. Furthermore, it remains an issue for broad area ($90\mu\text{m}$ width stripe) LDs since it is extremely difficult to discriminate the different optical modes within the gain envelop and find the exact wavelength corresponding to the maximal magnitude. In addition, it is also rather difficult to follow the drift of one mode versus the temperature or the current.

As an example, *Figure IV-2* shows the optical spectrum of a high-power DFB SLOC 4mm cavity length LD at 975nm. These measurements were taken at different heatsink temperatures (35°C and 45°C) under a bias current equal to 5A.

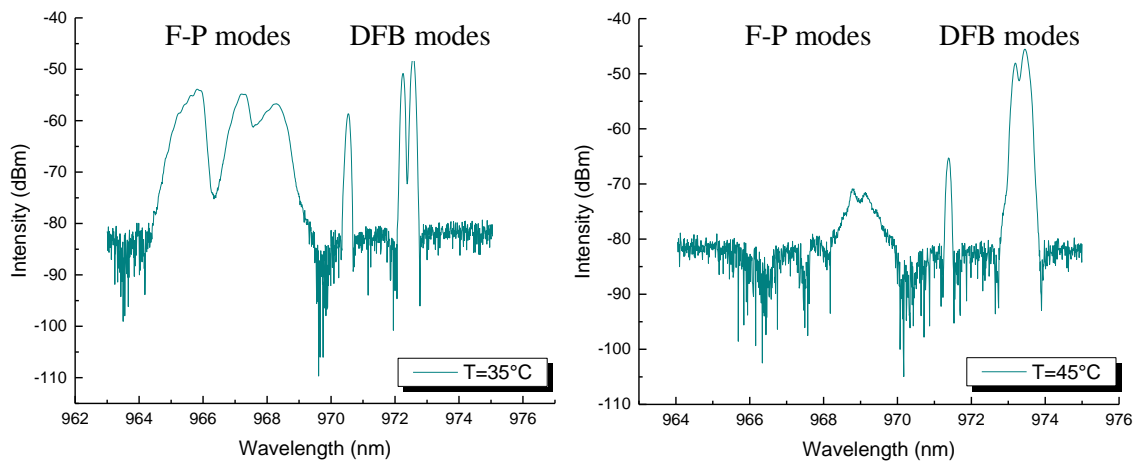


Figure IV-2: Optical spectra of a 975nm DFB high-power LD measured at different temperatures and under a bias current of 5A. With these images, it is possible to clearly understand that not only the F-P but also the DFB spectrum is intrinsically multimode.

There are numerous F-P modes in the first envelope as well as in the considered DFB one. For such a measurement, the setup already described in “*Chapter II-Electrical and optical characterizations*”, was used. The temperature sensor is a thermistor CTN with an accuracy of $\pm 0,3\%$. This thermistor is located near of the rear side of the C-mount heatsink. *Figure IV-3* shows a picture of the LIV setup used for the R_{th} measurement.

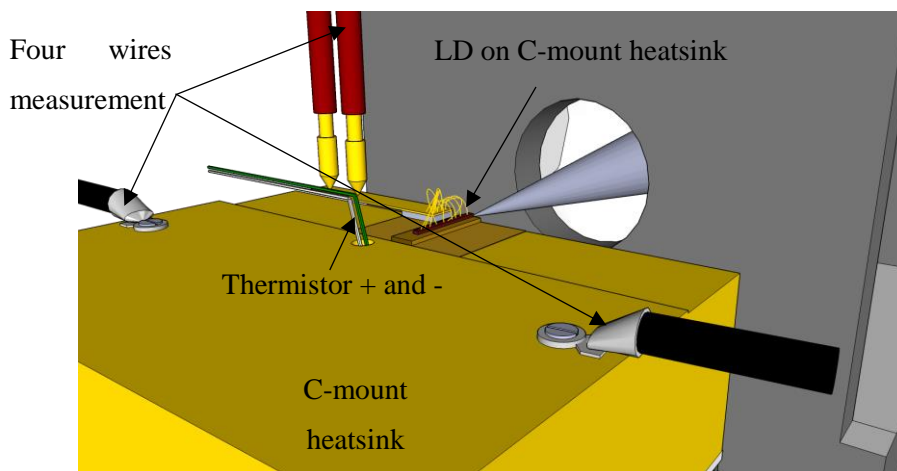


Figure IV-3: Schematics of the L-I-V setup already described in Chapter II. The thermistor is located near the rear of the C-mount heatsink.

4.1.2 Experimental results and discussion

Here, the measurements addressing LOC, SLOC and AOC structures are presented. *Table IV-1* summarizes the values of R_{th} extracted for the three vertical structures. The LDs have the same cavity length (4mm), the same coating (HR 95% and AR 1%) and have been mounted on a C-mount heatsink. Because of the weak number of measured LDs, a substantial statistical analysis is not possible but we report hereafter the minimum and maximum values of R_{th} for each F-P vertical structure.

LD structure	R_{th} [K/W] LD on heatsink
LOC_4mm	$R_{th_min} \approx 0,7$
LOC_4mm	$R_{th_max} \approx 1,4$
SLOC_4mm	$R_{th_min} \approx 0,7$
SLOC_4mm	$R_{th_max} \approx 1,2$
AOC_4mm	$R_{th_min} \approx 0,8$
AOC_4mm	$R_{th_max} \approx 1,2$

Table IV-1: Minimum and maximum values of R_{th} obtained for the three vertical structures (LOC, SLOC and AOC).

These values are in good agreement with the best values reported in literature (see *Figure IV-1*). One can see that there is a quite high dispersion of the results since for the same cavity length, the R_{th} have a difference of almost 100% between the maximum and the minimum values.

In conclusion, because of the intrinsic multimodal emission of the LD, we clearly demonstrate that it is too difficult to monitor correctly the drift of a single mode as a function of the bias current or temperature and thus extract the real value of R_{th} especially for low values ($< 1\text{K/W}$). Moreover, with this technique, it is not possible to discriminate the different contributions from each part of the assembly to the total R_{th} since we obtained only an overall value of R_{th} .

Because of that, hereafter we introduce a new technique based on transient thermal testing of the LDs enabling to obtain the overall value of the thermal resistance as well as the one corresponding to each sub-part of the assembly.

4.2 MEASUREMENT OF THERMAL RESISTANCE DERIVED FROM TRANSIENT THERMAL TESTING

The transient thermal testing method is well-known for extraction of thermal resistance of electronic devices and LEDs, being a crucial technique for understanding both the thermal management of the structure and its improvement through design for reliability. This technique is based on the transient thermal testing, the direct monitoring of the temperature distribution into the whole micro assembled device through an equivalent one-dimensional (R-C) Cauer circuit and the measurement procedure is described in the next section.

4.2.1 Principle of measurement

Through a thermal transient test, the T3STER®, proposed by the Mentor Graphics company, allows characterizing the heat propagation through a packaged device from the active region to the case.

Many papers focusing on such an approach have been recently published, especially in the field of the thermal resistance extraction of GaN-based high-power LEDs [29]-[30]-[31]. However, to the best of our knowledge and using this technique, no results are currently available in the literature for chip on submount optical devices and particularly for high-power LDs emitting at 975nm. The measurement is based on two main steps:

- The determination of a so-called “K-factor” for the calibration.
- Thermal transient measurements of the device under test.

The “K-factor” calibration step consists in the measurement of the drift of the LD voltage (V_{dri}) as a function of temperature. This calibration is done at low bias current ($I_{dri} = 300mA$ and $I_{sens} = 1mA$) because reducing self-heating of the device. The device was thermally calibrated using a dry thermostat and T3STER® as the power supply. The product of K and the difference in temperature sensing voltage (ΔV_S) produces the rise in the device junction temperature [31]:

$$\Delta V_S = -\Delta T_J \cdot K \quad \rightarrow \quad K = -\Delta V_S / \Delta T_J \quad [Eq IV-2]$$

This “K-factor” corresponds to the ratio of difference temperature sensing voltage (ΔV_S) and the rise in the device junction temperature (ΔT_J).

The voltage drop across the junction is measured once the LD reaches the thermal equilibrium and the temperature of the chamber decreases from 75°C to 25°C with a step of 10°C (*Figure IV-4(a)*). The “K-factor” is then calculated from the slope of the linear curve plotted in *Figure IV-4(b)*. Such a calibration step must be done for each device under test.

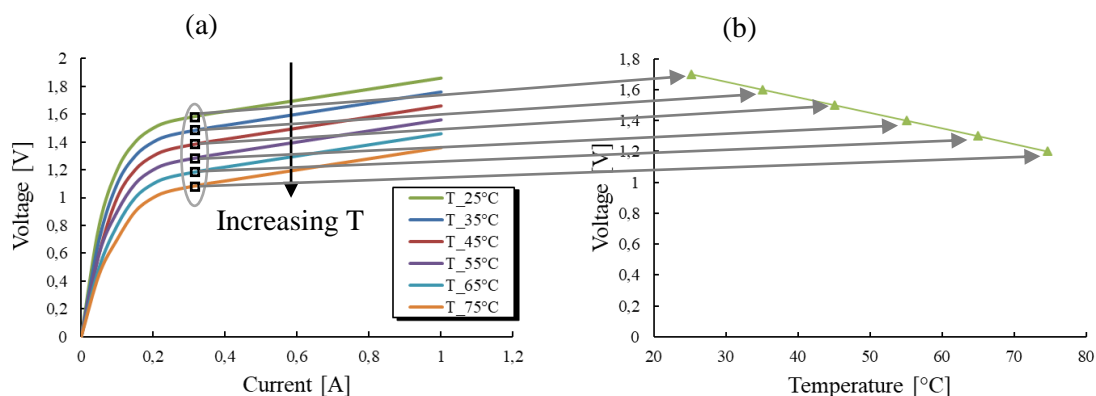


Figure IV-4: Determination procedure of the "K factor" for each LD under test.

Transient thermal measurements rely on the Electrical Test Method as standardized 20 years ago by JEDEC as described in [47]. Measurements are mostly realized as thermal transient measurements on a system after application of a power step (see *Figure IV-5*). T3STER© equipment monitors directly heating or cooling curves for data processing. Junction temperature of the LD is achievable, depending on voltage variations as a function of temperature when a constant probe current gets through the device. When the power step is applied on a single point of the device, an equivalent one-dimensional circuit (Cauer type circuit) can be built up, from the network theory, which gives the same temperature response [33]. The calculation of the temperature from the drift of the built-in voltage is done following the detailed procedure in [34].

This technique allows obtaining a specific curve called "cumulative structure function" of the thermal capacity versus thermal resistance. It gives a detailed overview of the heat flow spreading into the whole micro assembled device, including LD, submount heatsink and all interfaces (solders).

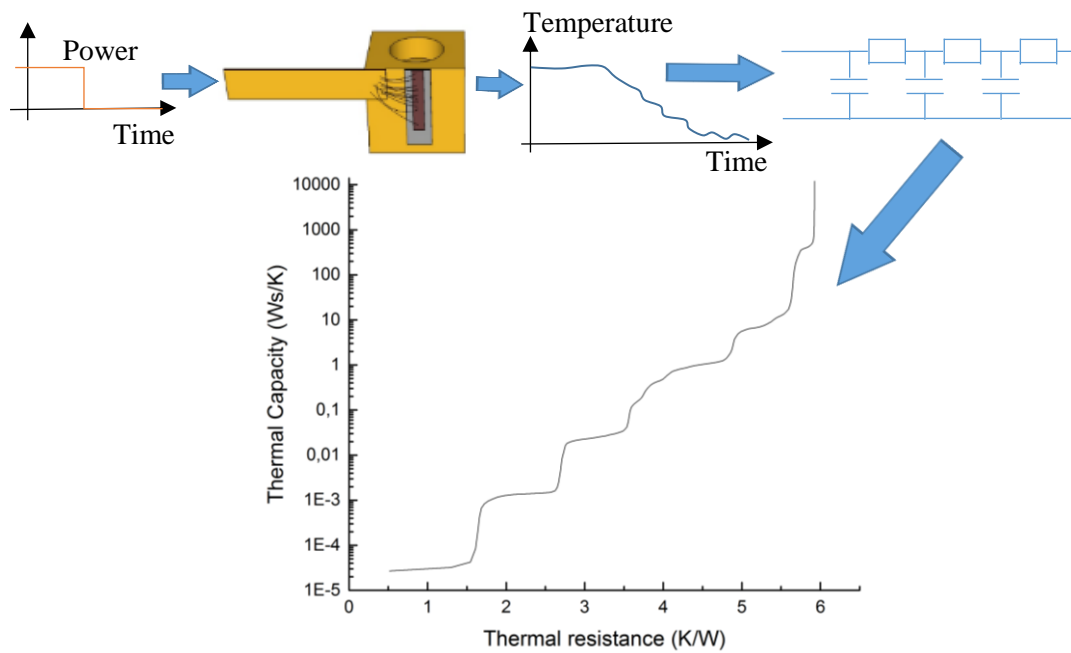


Figure IV-5: Thermal transient testing of a laser diode on a C-mount heatsink. The excitation due to the power step gives a temperature versus time response and from this, it is possible to build a Cauer circuit. From the Cauer circuit it is possible to obtain the cumulative structure function of thermal capacity versus thermal resistance.

Figure IV-6 provides the scheme of the dedicated mechanical interface for the location of the laser diode and the thermal characterization of the LD mounted on a C-mount heatsink and fixed on the hot plate of the T3STER©. A specific procedure is used to ensure repeatability and reproducibility of measurement [31]-[33].

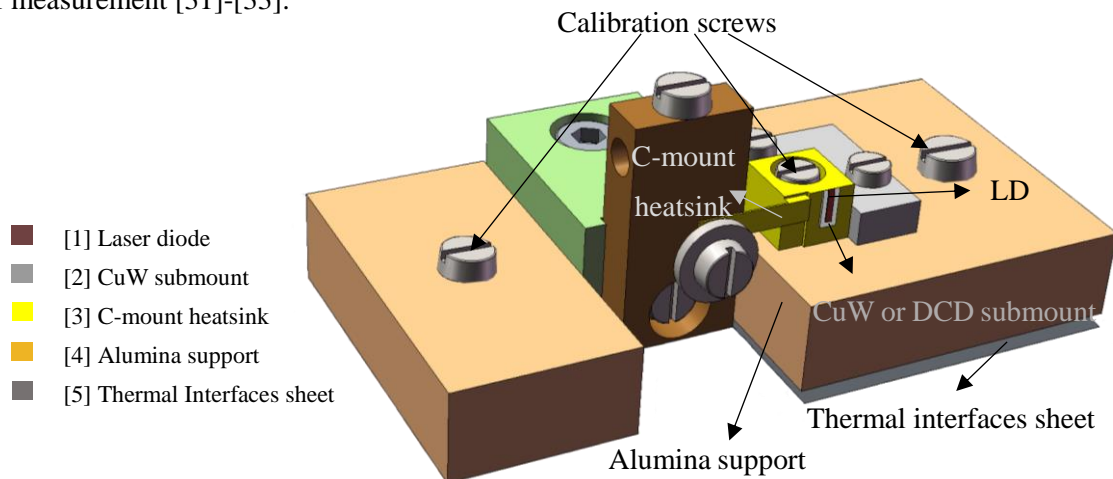


Figure IV-6: Dedicated mechanical interface for the thermal characterization of the LD mounted on the C-mount heatsink and fixed on the hot plate of the T3STER©. The hot plate of the T3STER© is not visible in this figure.

4.2.2 Calibration and measurement procedures

The soldering process of the device is a key issue in order to obtain an accurate determination of the thermal resistance. Different materials have been considered for mechanical attachment of the heatsink and alumina support, each other having its own thermal conductivity and thickness to assess the best thermal interface ensuring the highest repeatability as possible:

- thermal PAD ($1,6 \text{ Wm}^{-1} \text{ K}^{-1}$, $230\mu\text{m}$)
- graphite sheet ($1000 \text{ Wm}^{-1} \text{ K}^{-1}$, $70\mu\text{m}$)
- indium sheet ($81 \text{ Wm}^{-1} \text{ K}^{-1}$, $100\mu\text{m}$)

Those materials are necessary to guarantee a good thermal contact between the device and the thermal cooler platform during the measurement procedure. From our experience, the thermal PAD showed the worst results of R_{th} (more than 10 K/W for a 4mm cavity length), due to bad heat propagation. The graphite and the indium sheet demonstrated a good repeatability in terms of device placement on the thermal cooler and a value of R_{th} in line with classic measurements ($R_{th} \approx 2\text{K/W}$).

Different steps drive the measurement of the thermal impedance as follows:

Measurement time: This parameter can affect the results since the heat flow must cross the whole structure from the junction of the LD to the bottom of C-Mount copper heat sink (representing the steady-state regime). Different measurement times ranging from 200 to 2400 seconds have been used and finally considering that steady-state regime is acquired for a temperature below $0,25^\circ\text{C}$, an “ON-state” duration of 800 sec is enough to reach the steady state when the electrical power drops from the ON to the OFF regime as reported in *Figure IV-7*.

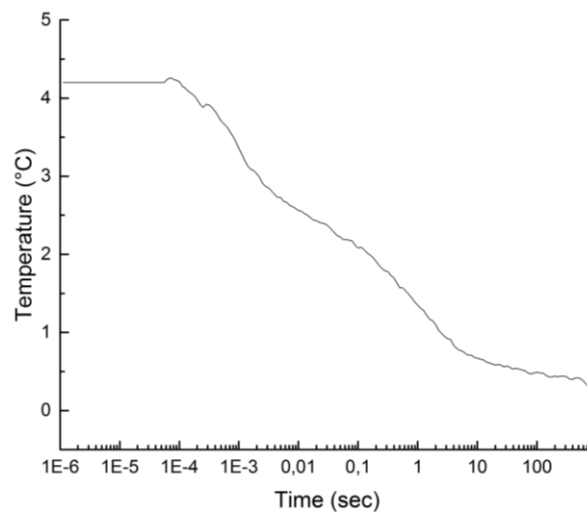


Figure IV-7: Temperature variations versus time after electrical power drops from the On to the Off regime. At 800 seconds the device has reach a steady state and the temperature is above 0,25°C. For measurement times bigger than 800 seconds, we obtain the same results of using 800s.

The power step: The current value (I_{sens}) can have an impact on the heat generation in the LD especially if this value is too low. A bias current ranging from 100 to 800 mA has been used for a 4mm cavity length LD. From our observation, after the optical threshold, it is quite difficult to extrapolate a good thermal transient analysis since the thermal interfaces are no longer discernible. Therefore, we assumed that the I_{drive} must be lower or equal than optical threshold and big enough to heat the device. *Table IV-2* summarizes the final operating bias current depending on the cavity length of the LD.

Cavity length [mm]	Bias current [mA]
2	300
3	450
4	600

Table IV-2: Operating bias current versus cavity length of the LD.

Calibration screws: The screws are also responsible of the thermal interface quality. A too strong tightening torque will distort the mechanical interfaces and a too low one will not ensure a good contact between interfaces. In both cases, the quality of thermal interfaces can change from one measurement to another. Hence, in order to ensure the repeatability of the measurement, the influence of the tightening torque for the three calibration screws has been studied. Using a 4mm SLOC LD, three measurements have been done using different tightening torques: 0,2, 0,25 and 0,3N.m. For each measurement, the following protocol has been used:

- The same measurement conditions are applied: 600mA of bias current and 800sec measurement time,
- After each measurement, the LD was unplugged.
- After 45 minutes, the LD was plugged into the alumina support for another measurement.

Each cumulative structure function is composed of 171 points of measurement and *Figure IV–8* shows the standard variation (for each measurement point) for the three tightening torques.

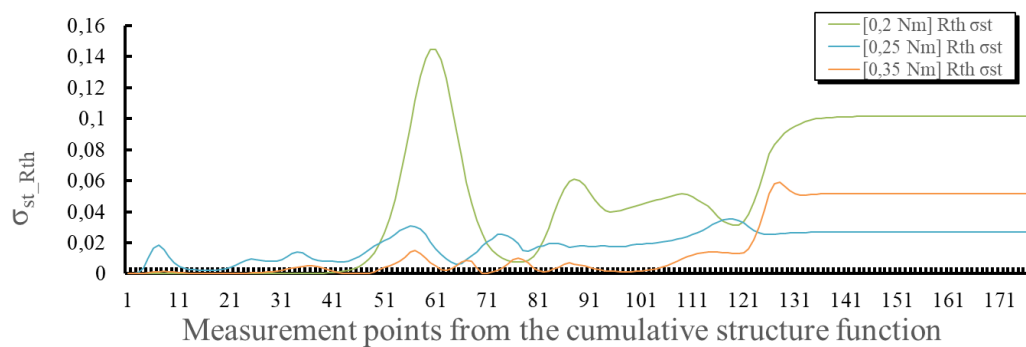


Figure IV–8: Standard deviation extraction for three tightening torques.

According to these results and to ensure the best metrology as possible, the following protocol has been chosen for the measurement of the different cumulative structure functions:

- A graphite sheet is used to guarantee an optimal thermal contact between the heat sink and the alumina support.
- A tightening torque of 0,25 Nm for the three calibration screws shown in *Figure IV–6*.
- The bias current depends on the cavity length and sets to the following values: 600mA, 450mA and 300mA for 4mm, 3mm and 2mm respectively.
- The equipment monitors the transient cooling curve of heat flow over the micro assembled device for an “OFF-state” duration of 800s. After the ON/OFF regime, the obtained cooling profile is then processed using the T3STER© Master Software for the calculation of the structure function considering the boundary conditions.

4.2.3 Experimental results and discussion

From the cumulative structure function of *Figure IV-5*, one can extrapolate the overall thermal resistance of the whole micro assembled device for each cavity length. *Figure IV-9* shows a cross-section of a LD mounted on a heatsink and the heat spreading into the micro assembled device.

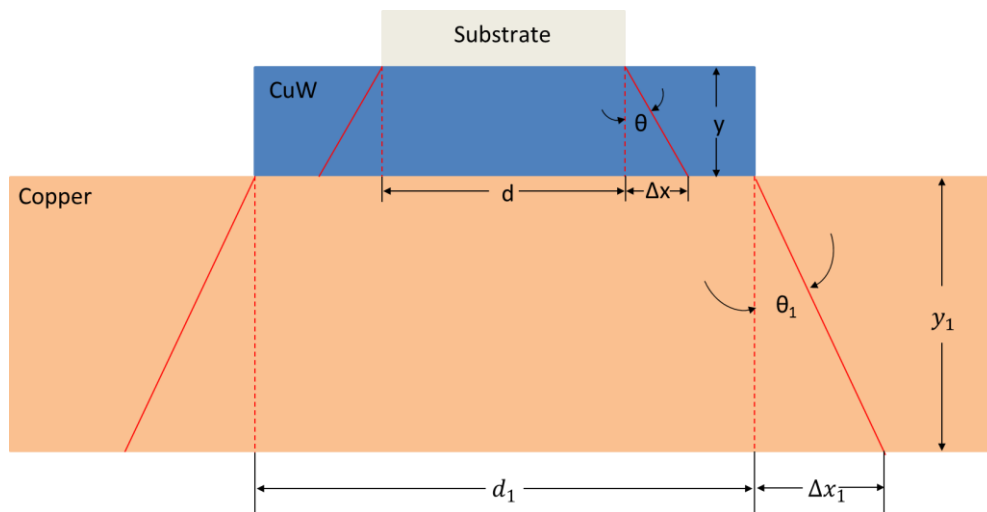


Figure IV-9: Geometrical representation of the heat path spreading effect in a stack formed by three layers with different areas.

The analytical model for the thermal capacity and the thermal resistance is realized in order to compare these results with the T3STER measurements [35]. For that, we used a theoretical approach based on the estimation of the different thermal resistance contributions for each part of the assembly. Both 1D thermal and spreading resistances have been calculated from the methodology derived from the works of A. Jamnia and based on physical properties of each material [36]. Indeed, it is well-established now that the available surface for the heat path increases along the cross-sectional direction of a micro assembled device. As an example, the surface of the heat sink is bigger than that of the chip and thus, the thermal resistance could not only result from a “1D approach” since the heat flow is not perpendicular to the crossed surface. It is necessary to take into account the “spreading” effect responsible of the lateral heat diffusion along the vertical axis. The definition of thermal resistance quantifies the ability of a material to prevent heat from flowing through it. It is equal to the difference between the temperatures of opposite faces of the material divided by the rate of heat flow.

$$R_{th} = (T_1 - T_2)/Q \quad [Eq IV-3]$$

where the $T_{1/2}$ represent the temperatures at two surfaces of the material and Q is the heat flux.

Since the heat flux is defined as: $Q = kS/L(T_1 - T_2)$, hence, the 1D thermal resistance is given by:

$$R_{th\ 1D} = kS/L \quad [Eq\ IV-4]$$

where k is the thermal conductivity of each material, S and L represent the section and the length respectively. The model of A. Jammia predicts the angle θ due to the spreading effect and the total amount of material Δx to add in the calculation:

$$\theta = 90 \tanh \left[0,355 \left(\frac{\pi \cdot K}{180} \right)^{0,6} \right] \quad \Delta x = d \cdot tg \left(\theta \cdot \frac{\pi}{180} \right) \quad [Eq\ IV-5]$$

Considering the spreading effect, the total thermal resistance is equal to:

$$R_{th} = R_{th\ 1D} + R_{th\ spreading} \quad [Eq\ IV-6]$$

The thermal capacity (also called heat capacity), describes the amount of heat per unit mass required to raise the temperature by 1°C.

$$C_{th} = \frac{Q}{\Delta T} = \rho V C_p \quad [Eq\ IV-7]$$

where ΔT corresponds to the temperature difference between the initial and the final state (measured in °C). It is possible to use the equivalent formula with ρ the density, the volume V and C_p heat capacity at constant pressure.

Table IV-3 summarizes the calculated values. For that, only the GaAs substrate is considered because the other layers are too thin to bring some significant changes detected by the T3STER©.

	C_{th} [J.s/K]	R_{th} [K/W]
GaAs 2mm cavity length	$1,91 \cdot 10^{-4}$	3,90
GaAs 3mm cavity length	$2,86 \cdot 10^{-4}$	2,60
GaAs 4mm cavity length	$3,81 \cdot 10^{-4}$	1,95
AuSn	$1,49 \cdot 10^{-5}$	0,063
CuW submount 2mm cavity length LD	$4,59 \cdot 10^{-3}$	0,535
CuW submount 3mm cavity length LD	$6,83 \cdot 10^{-3}$	0,356
CuW submount 4mm cavity length LD	$9,07 \cdot 10^{-3}$	0,267
Copper heatsink 2mm cavity length LD	$3 \cdot 10^{-1}$	0,861
Copper heatsink 3mm cavity length LD	$2,98 \cdot 10^{-1}$	0,574
Copper heatsink 4mm cavity length LD	$2,97 \cdot 10^{-1}$	0,430

Table IV-3: Calculated values of thermal resistance and thermal capacity for each main part of a micro assembled LD.

With the values in *Table IV-3*, it is possible to plot the predicted cumulative structure functions calculated from the theory previously detailed (*Figure IV-10*).

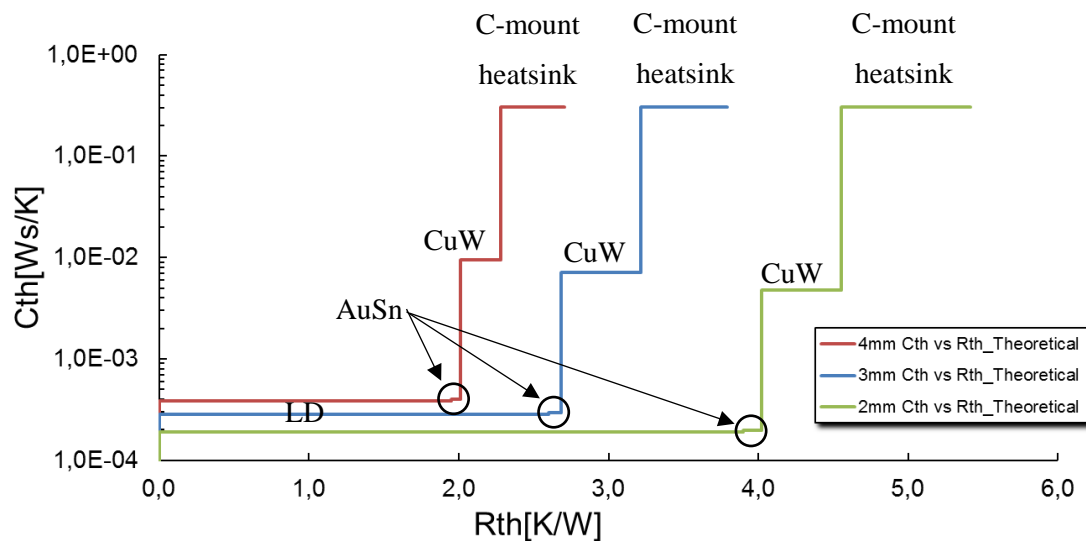


Figure IV-10: Theoretical cumulative structure functions calculated from 1D and spreading contributions of each part of the micro assembled device for different cavity lengths of a high-power DFB LD.

Figure IV-11 plots the experimental cumulative structure functions for three different cavity lengths for high-power DFB SLOC LDs, considering 800sec of measurement time and 600/300/200mA of bias current for 2, 3 and 4mm cavity lengths (Figure IV-11).

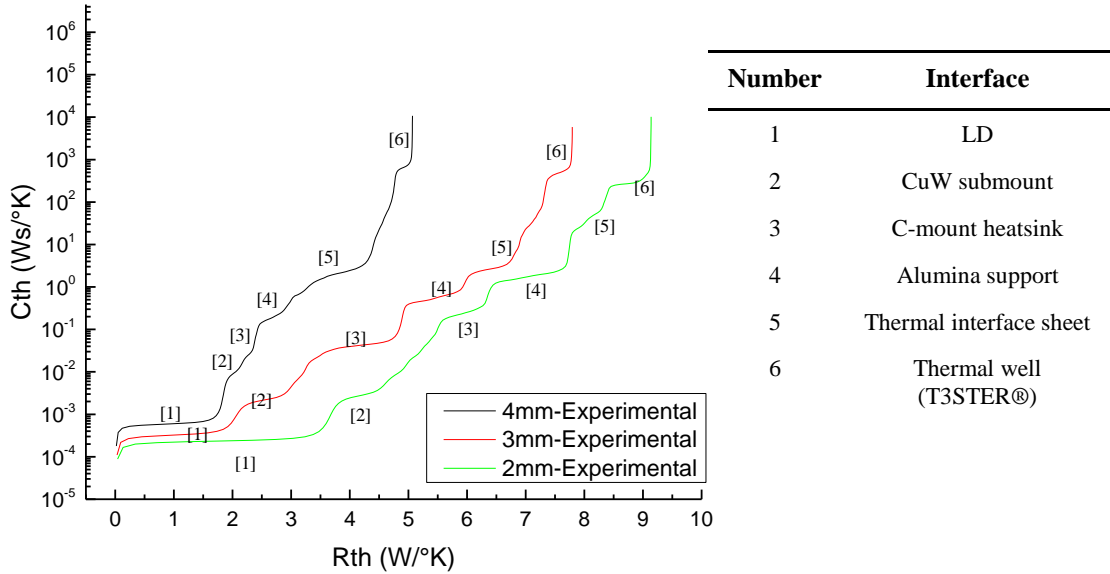


Figure IV-11: Experimental cumulative structure functions measured with the T3STER© equipment according to the optimized protocol for different cavity lengths of DFB LDs. The numbers refer to the interfaces as reported in Figure IV-6.

Based on Figure IV-11, one can extrapolate the values of R_{th} for the LD chip and the whole micro assembled device that are given in Table IV-4. Experimental and calculated values are in very good agreement for short lengths (< 12%) but the error increases up to 28% for the highest length since the thermal resistance decreases.

	Cavity length [mm]	R_{th} of the LD chip [K/W]	R_{th} of the whole micro assembled device [K/W]
Experimental	2	3,4	6,4
Experimental	3	2,9	5,5
Experimental	4	1,4	2,85
Calculated	2	3,9	5,5
Calculated	3	2,6	3,9
Calculated	4	1,95	2,7

Table IV-4: Experimental and theoretical R_{th} versus cavity length for the SLOC DFB LD vertical structure.

The T3STER© enables to measure only the R_{th} contribution coming from the substrate of the LD, which is the same for the three vertical structures. Hence, the measured R_{th} of the whole micro

assembled device for a SLOC, LOC and AOC is almost the same. The difference between the values of R_{th} for different vertical structures lies in the second decimal. Because of that, we choose to not show the experimental cumulative structure functions measured for the LOC and AOC structures.

Table IV-5 shows a comparison of the thermal resistance values obtained via T3STER© for the three vertical structures (4mm cavity length) including two DFB LDs (LOC and SLOC) and one F-P LD (AOC). The values of R_{th} for the LD chip only are very close because the T3STER© cannot discriminate the different layers composing the vertical structure of the chip.

LD structure	R_{th} of the LD chip [K/W]	R_{th} of the whole micro assembled device [K/W]
DFB LOC	1,38	2,82
DFB SLOC	1,41	2,85
F-P AOC	1,45	2,55

Table IV-5: Experimental R_{th} for the three vertical structures (4mm cavity length).

As the values of the whole micro assembled device are also quite equal whatever the considered vertical structure, we can conclude that the mounting process of the LDs on the submount is reproducible and perfectly well-mastered.

From the cumulative structure functions shown in *Figure IV-11*, *Table IV-6* allows to compare the thermal resistance of laser/heatsink structure for LDs with different cavity lengths extracted with the two techniques.

Cavity length (mm)	R_{th} obtained with T3STER© [K/W]	R_{th} obtained with optical spectrum [K/W]
2	~ 3,2	~ 2,6
3	~ 2,8	~ 1,7
4	~ 1,5	~ 0,7

Table IV-6: Comparison of typical thermal resistance values obtained via T3STER© and optical spectrum measurements for SLOC-based LDs versus cavity length.

The values obtained with the T3STER© are usually bigger than the values obtained by the optical spectrum measurement. These values are more reliable than the previous estimation using the optical spectrum technique, the LDs are intrinsically multimode and the extrapolation of the modal drift is quite difficult. Moreover, the T3STER© considers the effective power dissipation of the

device. Such a technique gives the opportunity to discriminate an atypical thermal behaviour of the device as a degradation of an interface for instance.

4.2.4 Comparison with other substrate materials

The heat transfer problem between the LD and the heatsink, involves the matching of the thermal expansion coefficients inside the hybrid design of laser diode chip mounted epi p-side down on the heatsink. The problem is defined by a sufficient difference of thermal and mechanical properties of semiconductor and the heat diffusion materials. This appears as an issue due to thermo-elastic strain in hybrid configuration as micro assembled LDs. Commonly used thermo-compensators are produced from dielectrics AlN, BeO, SiC as well as from current conducting composites CuW and CuMo. However, the range of thermal conductivity remains quite low ($150\text{--}250\text{ W}\cdot\text{m}^{-1}\cdot\text{K}^{-1}$) responsible of unsafe operation of high-power LD for output power levels more than 10W in CW regime [37]-[38]-[39].

Diamond and diamond-based composites are the best candidates to overcome these limitations. The main advantage of pure diamond is the very highest thermal conductivity among known materials, up to $2400\text{ W}\cdot\text{m}^{-1}\cdot\text{K}^{-1}$ for special type pure diamond and even up to $3600\text{ W}\cdot\text{m}^{-1}\cdot\text{K}^{-1}$ for isotropic clean material [40]. However, because of the mismatch of the CTE between the diamond and the semiconductor, the composite diamond is preferred.

A specific bonding process on diamond-copper composite (DCD) has been developed and optimized for the DFB LD technology at III-V lab. *Figure IV-12* plots cumulative structure functions achieved under a drive current and a transient cooling duration of 500mA and 800s respectively for two submount materials. Particularly, we demonstrate the benefit of the DCD material since a reduction of 22% is reached for the whole thermal resistance.

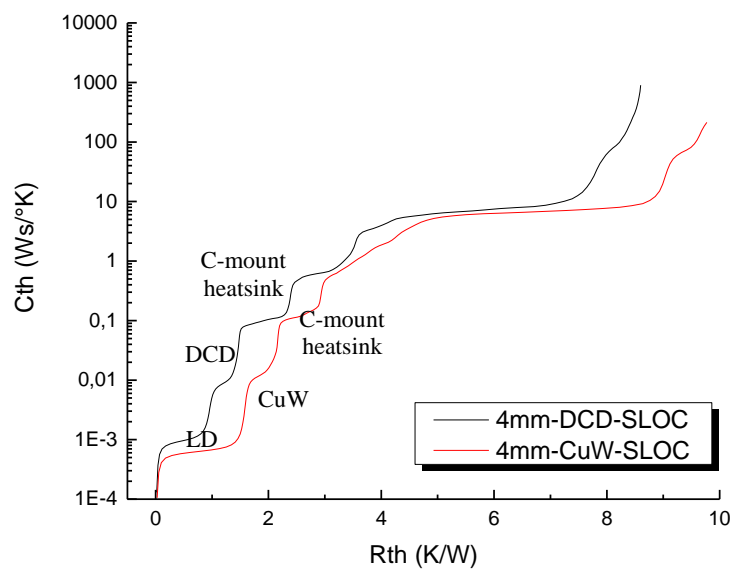


Figure IV-12: Comparison of experimental cumulative structures functions measured with the T3STER© according the optimized protocol for two submount materials of a 4mm cavity length high-power DFB laser diode (ON/OFF regime 500mA-800s).

Figure IV-13 gives the L-I and WPE curves at 20°C in order to compare the benefit carried out by DCD for three devices based on 4mm cavity length: two F-P LDs mounted on CuW and DCD submount and a DFB LD mounted on CuW submount. From this figure, the enhancement carried out by the DCD submount is somewhat more moderated than anticipated particularly with F-P devices. The substantial gain on WPE of a few % with DCD is obtained at 3A instead of 3,15A with CuW (see Table IV-7). The difference between DFB and F-P laser is more significant. Another tangible interest of DCD material appears at high current (> 5,5A) on both the maximum output optical power (3%) and the more linear behavior of the L-I curve predicting a lower self-heating of the laser chip at 9A. DFB devices manufactured with new fabrication runs are currently characterized up to the maximum current as possible (> 10A) to confirm these outcomes.

Submount material	Laser diode structure	P_{\max} [W] @ I_{\max}	WPE_{\max} [%] @ I	P-I slope [W/A] [from I_{th} to I_{\max}]
Copper-Tungsten (CuW)	F-P	6,19 @ 9A	52,9 @ 3,15A	0,722
	DFB	5,55 @ 8A	43,3 @ 4,4A	0,756
Diamond-copper composite (DCD)	F-P	6,27 @ 9A	53,5 @ 3,02A	0,731

Table IV-7: Optical performances of 4mm cavity length high power F-P and DFB laser diodes versus submount material.

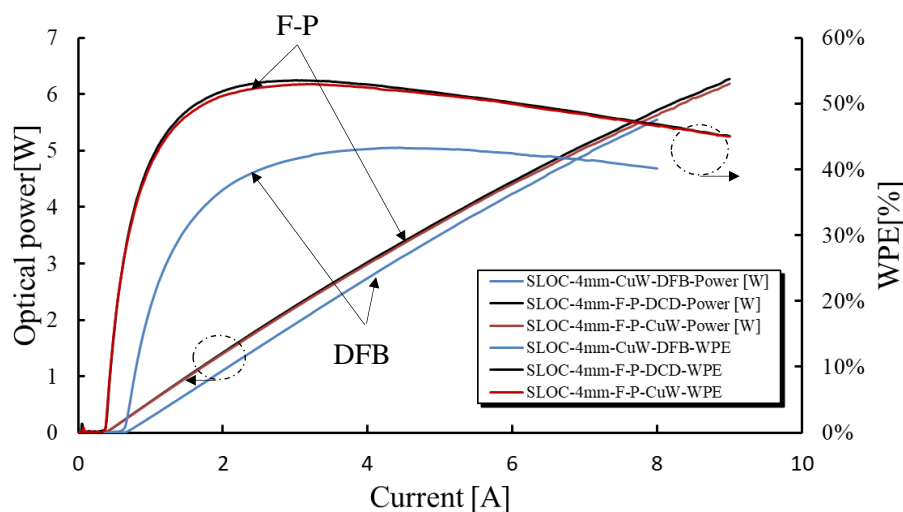


Figure IV-13: CW L-I and WPE curves at 20°C of 4mm cavity length LDs (F-P and DFB) mounted on CuW and DCD submounts.

4.3 PACKAGING-INDUCED STRESS ANALYSIS: FEM SIMULATIONS AND EXPERIMENTS

4.3.1 Standard and new mechanical mounting configurations

Soldering is the ultimate but the most cost-consuming step connecting the device to its final environment. However, soldering induces mechanical strain on the active region and, depends on the amplitude of such mechanical strain, may leads to premature COD. The choice of the soldering temperature and pressure profile combined with the submount is a key point. During this study, we observed that COD-like failure occurs regularly at the same current level for LDs of 4mm cavity length without any facets coating. For that, multiple LDs (more than 10) have been tested under CW operation and the COD thresholds have been extracted at 14-12-10 A for the SLOC, LOC and AOC vertical structures respectively.

Without facet coating, the optical power density is equal at both facets and one can assume that, statistically, a COD can occur at both facets with a probability of 50%.

Experimentally, after the CW L-I-V characterizations of more than 10 LDs, all the COD are located at the front facet. Our first assumption lies in a non uniform distribution of mechanical stress along the cavity length of the LDs. To understand the origin of this mechanical stress (during the soldering of the LD on the C-mount heatsink) a thermo-electro-mechanical simulation has been done and

more details are given in the next sections “*Chapter IV - Modelling and boundary conditions*” and “*Chapter IV - Results of 3D thermo-electro-mechanical simulations*”.

Moreover, we have experimentally investigated on the longitudinal cross-section of failed LDs using Destructive Physical Analysis (DPA). Such a technique requires a specific preparation of the device under test. The LD mounted on a C-mount heatsink is immersed into a bowl with resin. When the resin is dry, it is possible to proceed to the erosion via abrasion. This technique enables to erode part of the LD mounted on C-mount heatsink and allows to analyze the longitudinal section in the middle of the waveguide as shown in *Figure IV–14(a)*. Two COD-like failed SLOC LDs of 4mm were analyzed with such a technique and *Figure IV–14(b)* gives a SEM view showing the different interfaces.

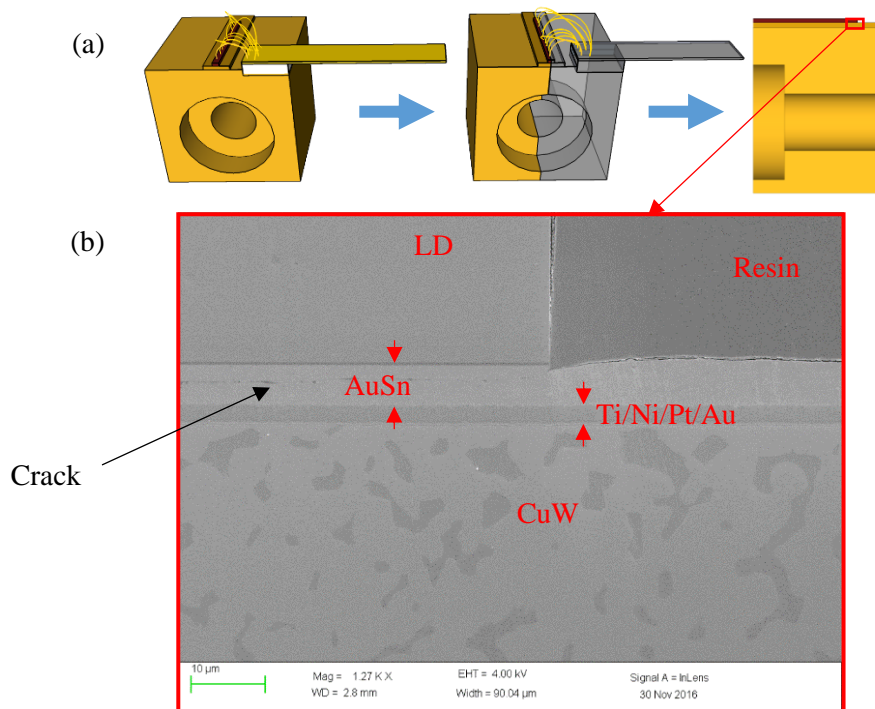


Figure IV–14: (a) Section used for the DPA. (b) SEM cross-section view of the LD mounted onto the CuW submount obtained after the polishing process.

For each LD, a crack has been observed from the front facet up to rear facet along the interface between the AuSn solder and the LD (see zoom of the rear facet in *Figure IV–14(b)*).

Considering the FEM simulations reported in “*Chapter IV -Results of 3D thermo-electro-mechanical simulations*”, it has been proved that there is a significant difference of mechanical stress between the front and the rear facets, in particular due to the soldering process of the LD on the C-mount heatsink.

During the soldering, the C-mount heatsink is placed in a chamber and heated, using a convection flow, up to 290°C in order to make liquid the AuSn preform. The LD is then introduced into the chamber and is put physically in contact with the C-mount heatsink. After this operation, the cooling down soldering profile starts. During these steps, the LD is not submitted to the same boundary conditions at the rear and the front facet since in particular, the area of materials (and so the thermal path) under each facet is different. For example, for the standard configuration, under the front facet, one can find immediately below the submount and the C-mount heatsink while the rear facet is quite far from the edge of the submount. So, the front facet of the LD is located at the exact edge of the submount that leads to an asymmetric configuration from a thermomechanical point of view as shown in *Figure IV–15*. In order to reduce the mechanical stress between the front and the rear facet, a new mechanical placement of the LD is proposed and used for the mounting process as shown in *Figure IV–15*. The temperature and pressure profile used during the soldering process remains the same for the standard configuration and the new one, but the new location of the LD permits to better balance the thermal path as well as the thermomechanical stress distribution along its longitudinal axis compared with the previous one.

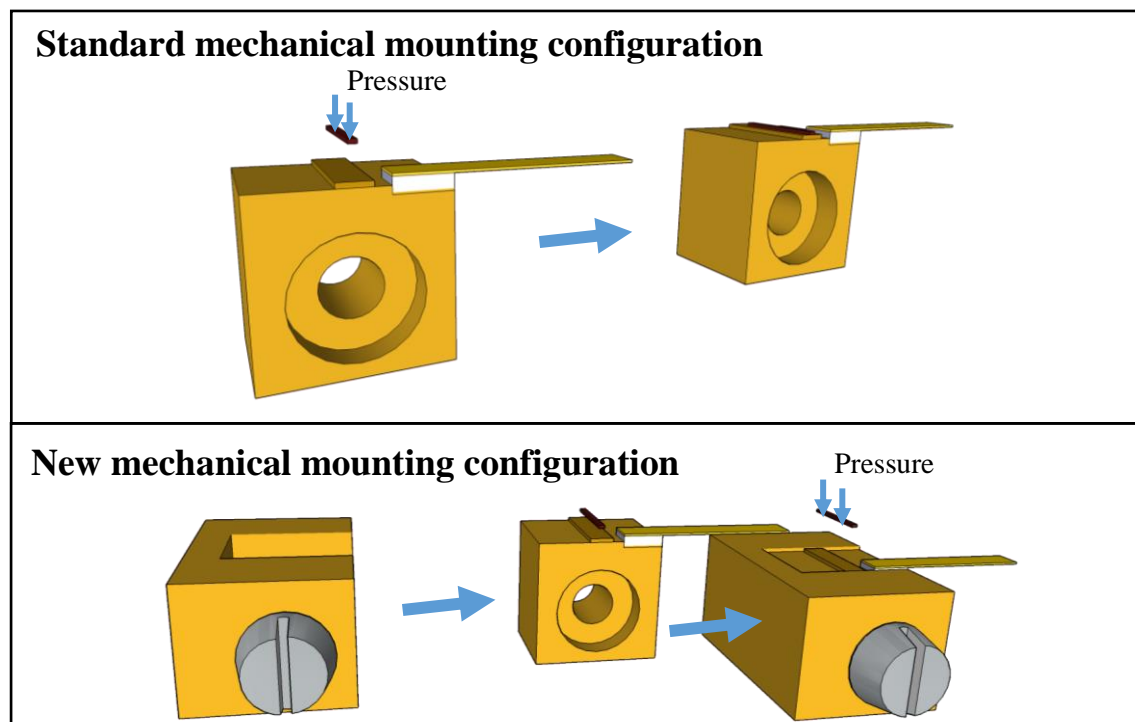


Figure IV–15: Standard and new mechanical mounting configurations used for the soldering process of the LDs onto the CuW submount and the C-mount heat sink.

Because of the different boundary conditions applied to front and rear facets during the soldering process, the die-attach material tends to curve inwards, in the space between the CuW submount and the LD at the level of the front facet after the cooling down (see *Figure IV–16(a)*). In contrast, with the new mechanical mounting configuration, the die-attach material does not return to the inner part (see *Figure IV–16(b)*). *Figure IV–16* highlights some differences at the level of the front facet. The new configuration allows to better fill the grooves and the AuSn soldering does not curve inwards. Hence, one can consider that the LD has a better thermal interface near the front facet.

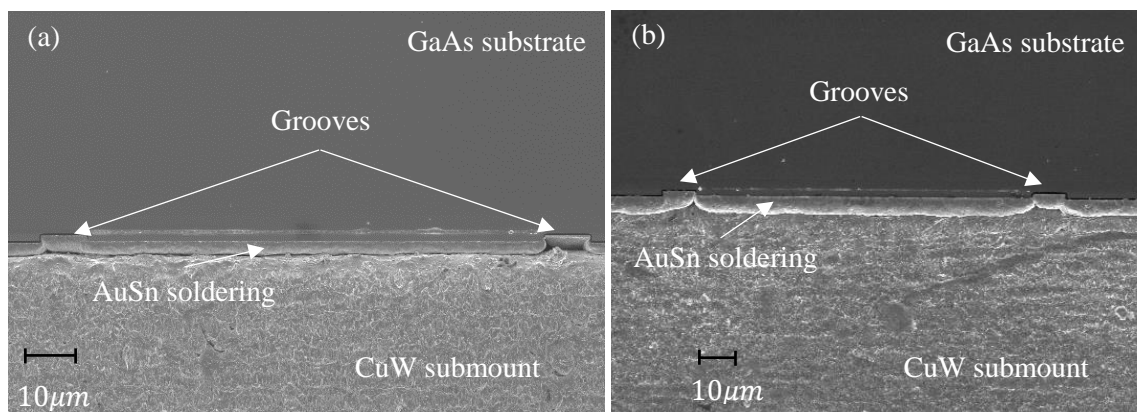


Figure IV–16: SEM views of the front facet of two LD soldered with standard (left) and new mechanical mounting configurations (right).

The section “*Chapter IV - Standard and new mechanical mounting configurations*” introduces a new mechanical mounting configuration for the LD. During the cooling down of the soldering process and considering that the front and the rear facets of the LD do not have the same amount of copper below as shown in *Figure IV–17*, one can assume that different thermomechanical strain affecting the front and rear facets will occur. In order to verify such a statement, time-dependent 3D thermo-electro-mechanical modelling and simulations by FEM of the soldering process as well as packaging-induced stress/strain analysis have been conducted. These simulations reproduce as close as possible the soldering conditions of the LD and allows estimating residual stress/strain due to the soldering process. The experimental measurement of residual stresses/strains are presented at the end of this section.

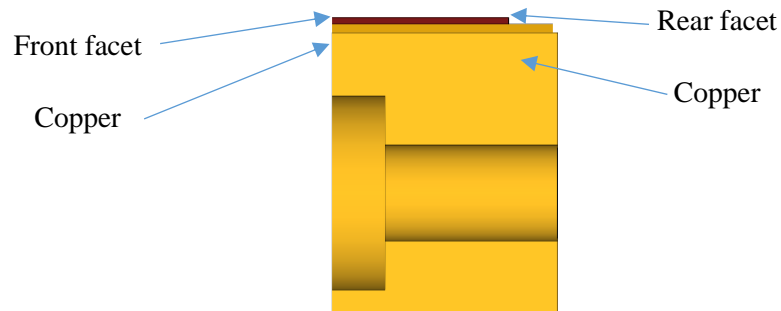


Figure IV-17: Longitudinal section of a LD soldered on a CuW submount and mounted onto the C-mount heatsink showing the different geometries below the front facet and the rear one.

a. Modelling and boundary conditions

Because of the meshing complexity in particular due to the multiple thin epitaxial layers, a simplified structure has been considered for the LD as reported in *Figure IV-18*. The modelled structure is composed of 150 μm thick GaAs substrate with an oxide layer (SiO_2) used to delimit the central ridge and 4 μm thick AuSn layer. Indeed, the oxide layer does not exist in the real structure and it is only used to simulate the energy barrier between the soldering and the metal. It is assumed that such a layer has the same thermo-mechanical characteristics than the metal and the only difference lies in the electrical conductivity equal to zero.

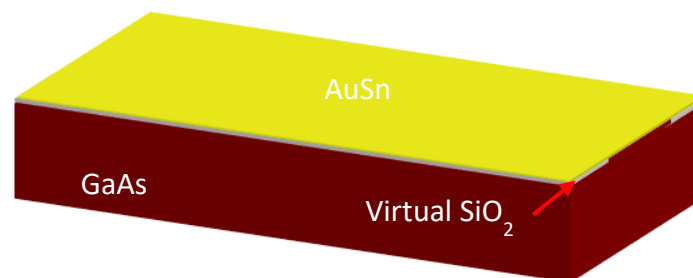


Figure IV-18: Simplified LD structure used for time-dependent thermo-electro-mechanical simulations. The LD is composed of 150 μm of GaAs substrate and a SiO_2 layer delimiting the central ridge and the 4 μm thickness AuSn layer.

Figure IV-19 shows the simulated structure of the LD mounted onto the heatsink.

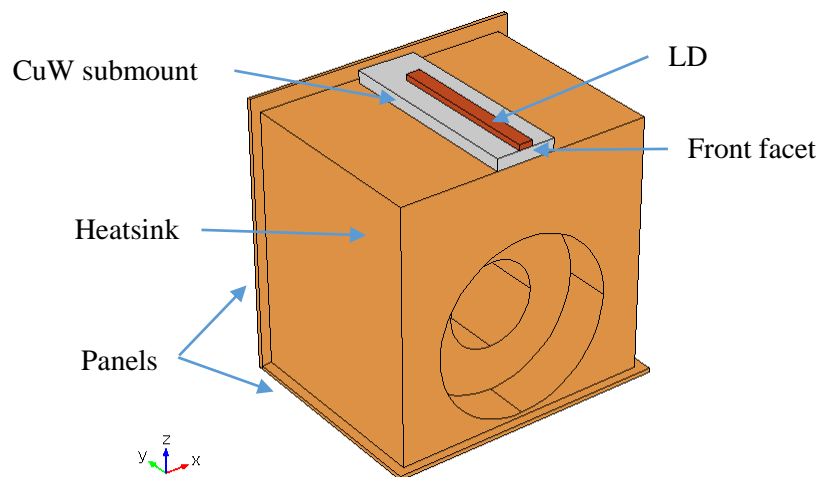


Figure IV–19: Simulated geometry considering a 4mm cavity length LD and the heatsink.

The boundary conditions are the same than the ones used for the previous 2D thermo-electrical simulations.

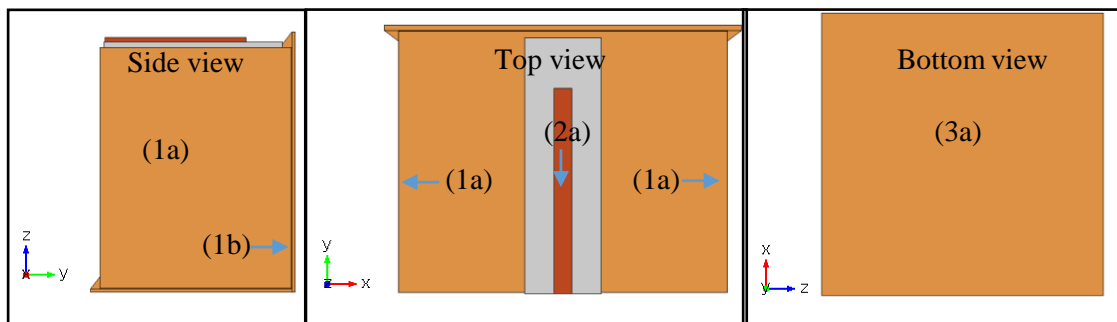


Figure IV–20: Different views of the LD mounted onto the C-mount heatsink.

In the geometry described in *Figure IV–19*, two panels have been added and used as boundary conditions. The bottom panel (3a in *Figure IV–20*) represents the stage where the C-mount heatsink is fixed during the soldering. This boundary condition is used only during the soldering operation of the LD on the C-mount heatsink. The rear panel (1b in *Figure IV–20*) represents the copper support used in the setup for L-I-V characterizations and already presented in “*Chapter II*”. This boundary condition is set only for simulation of operating conditions.

Considering the orthogonal projection as represented in *Figure IV–20*, the final boundary conditions for thermo-electro-mechanical simulations are the following:

- The injection of a current density is connected to the top of the LD at the level of the n-substrate surface (2a).

- The ground voltage is connected to the bottom of the C-mount copper heatsink (3a).
- A fixed temperature is considered along 4 side of the C-mount heatsink (1a, 1b, 3a).
- No forced convection is applied assuming that there is no air movement close to the LD.

Additional boundary conditions have been also added:

- Gravity is applied on all the surfaces.
- The temperature profile for the soldering is not applied by using forced convection but only considering thermal conduction and a fixed temperature is set to all the materials because of the small dimension of the device.
- A pressure profile is applied during the soldering process of the LD onto the C-mount heatsink (2a).
- A fixed pressure is applied to simulate the mechanically-drilled holes that keeps the heatsink blocked (3a) during CW operation.

Regarding the meshing process, we choose to use tetrahedral elements with a total number of elements equal to 323354 as displayed in *Figure IV–21*.

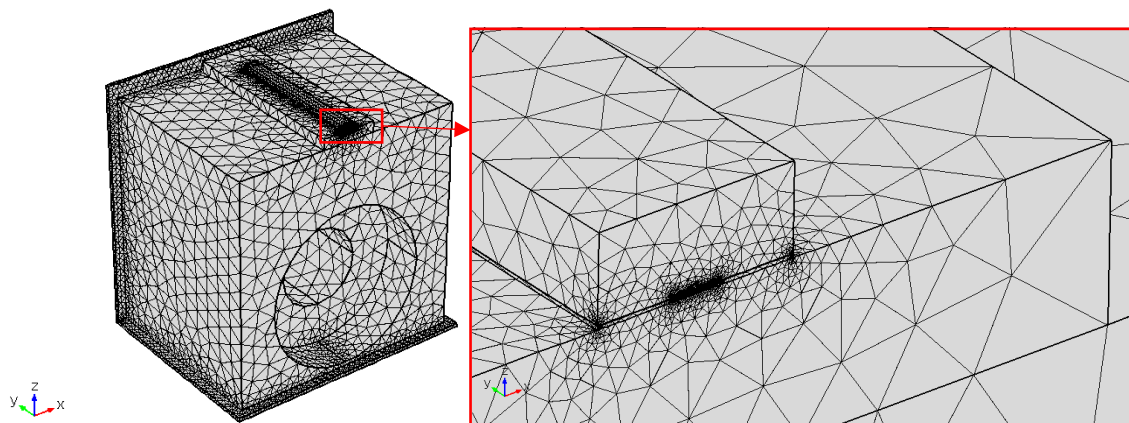


Figure IV–21: Meshing of the simulated geometry based on triangle elements.

b. Results of 3D thermo-electro-mechanical simulations

Time-dependent 3D thermo-electro-mechanical simulations have been carried out to reproduce the standard mechanical mounting configuration of the LD onto the C-mount heatsink and for that, experimental data of temperature and pressure profile have been taken into account. Due to the complexity of such simulation and we did not have enough time to reproduce the 3D

time-dependent 3D thermo-electro-mechanical simulation using the new mechanical mounting configuration.

These simulations particularly focus on the mechanical stress induced by the soldering and its material properties as a function of temperature. *Figure IV–22* shows the simulation results. The zero of the x-axis represents the front facet while the 4mm stands for the rear facet. One can conclude on the large asymmetry of the Von-Mises stress predicted by FEM simulations along the longitudinal axis of the LD. The highest stress is clearly located at the level of the front facet (up to 4MPa) while reaching 1,5MPa at the rear facet.

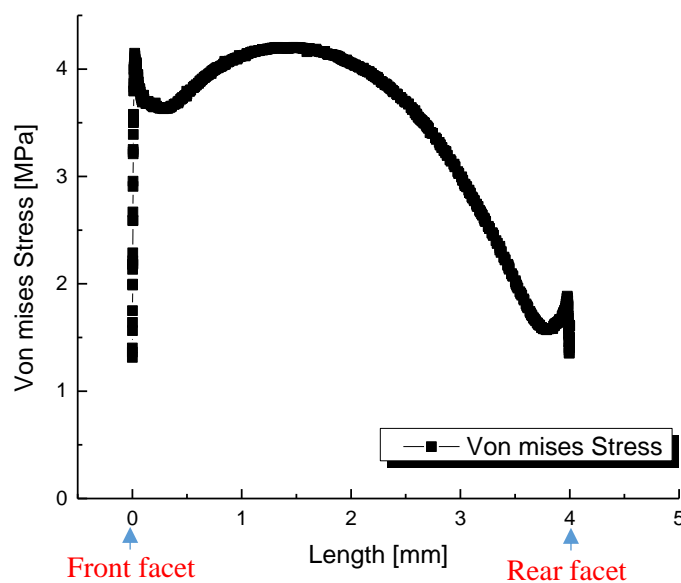


Figure IV–22: Predicted Von Mises stress along the GaAs substrate for a 4mm LD and considering the standard mechanical mounting configuration.

4.3.2 Techniques for packaging-induced stress analysis

To deeply investigate on the residual mechanical stress occurring from the two mechanical mounting configurations, the following sections will present the obtained results in order to quantify the amplitude and distribution of this residual stress as well as the COD robustness regarding the different vertical structures in particular focusing on SLOC and AOC ones. For that, different non-destructive techniques performed at MBI (Berlin), have been used for characterization and analysis of the residual stress distribution:

- Micro-photoluminescence (μ PL),
- Photocurrent spectroscopy (PCS),
- Time-resolved photoluminescence (TRPL).

A second technique (destructive) has been used allowing to extract the COD threshold in pulsed current regime.

Each analysis brings results on different parts of the micro assembled LD. The μ PL and PCS measurements can quantify the mechanical stresses induced by the soldering process while the TR-PL technique investigates the potential defects related to the recombination centres at the front facet. Finally, the pulse COD measurement can give relevant information when vertical structure designs, thermal management and mounting quality are compared.

Different vertical structures (SLOC, AOC), different facet coatings (90% with 3 layers of $\text{SiO}_2/\text{TiO}_2$ and 95% with 4 layers of $\text{SiO}_2/\text{TiO}_2$) and different mechanical mounting configurations (Standard and New) have been investigated. All the LDs under investigation are mounted onto a CuW submount on top of a C-mount heatsink. *Table IV-8* summarizes the LDs technological characteristics used for these investigations.

The last column of this table refers to the nitrogen time, representing the atmosphere used between the cleaving step and the coating of facets. This last allows the passivation of the facets and avoid the oxidation of the layers with Al elements as already described in “*Chapter II – Properties of the facets coating*”.

Vertical structure	Number of devices	AR [%]	HR [%]	Mechanical mounting configuration	Nitrogen time (min)
SLOC	2	1x	3x	Standard	1,5
SLOC	2	1x	3x	Standard	9
SLOC	2	1x	3x	New	9
SLOC	2	1x	4x	Standard	1,5
AOC	3	1x	3x	Standard	1,5
AOC	3	1x	3x	Standard	9
AOC	3	1x	3x	New	1,5
AOC	1	1x	3x	New	9

Table IV-8: Technological characteristics of the LDs used for non-destructive and destructive experiments.

4.3.3 Micro-photoluminescence measurements

a. Principle and setup description

Such a technique consists in the measurement of the radiative recombination rate extracting from a semiconductor layer. A laser beam, with a specific wavelength, excites the electrons in the

valence band of the device under test. A relatively small number of photons emerges from the sample establishing the luminescence. Many numerous papers and books have described the main advantages and drawbacks of this technique [41]-[42]. *Figure IV-23* shows the dedicated setup implemented for μ PL measurements.

For reliability investigations, the μ PL technique is mainly used to assess the fabrication quality of semiconductors such as thickness of the QW, intrinsic luminescent properties of the layers, presence of impurities and defects reducing the produced luminescence intensity [43]. In our case, we used μ PL to characterize the relative residual packaging-induced stress by the mechanical mounting configuration of the LD on the heatsink. The excitation source supplies a laser beam that passes through a microscope stage enabling to obtain resolution in the micron range. The residual reflected luminescence signal passes through the optics and collected by the spectrometer. Then, the signal is processed via a dedicated computing interface.

In a first step, the laser beam scans the device line by line covering mainly the front facet and a spectral analysis is performed for each point. Three lines are used during the measurement as displayed in *Figure IV-24*. These three measurements have been preferentially done on front facet and at the level of the GaAs substrate. At the first order, the measured spectral shift of the GaAs substrate can be converted into an hydrostatic stress or strain as follows [42]:

$$\left. \frac{d\lambda_{PL}}{dP} \right|_{GaAs} = 0,07nm/MPa \quad [Eq IV-8]$$

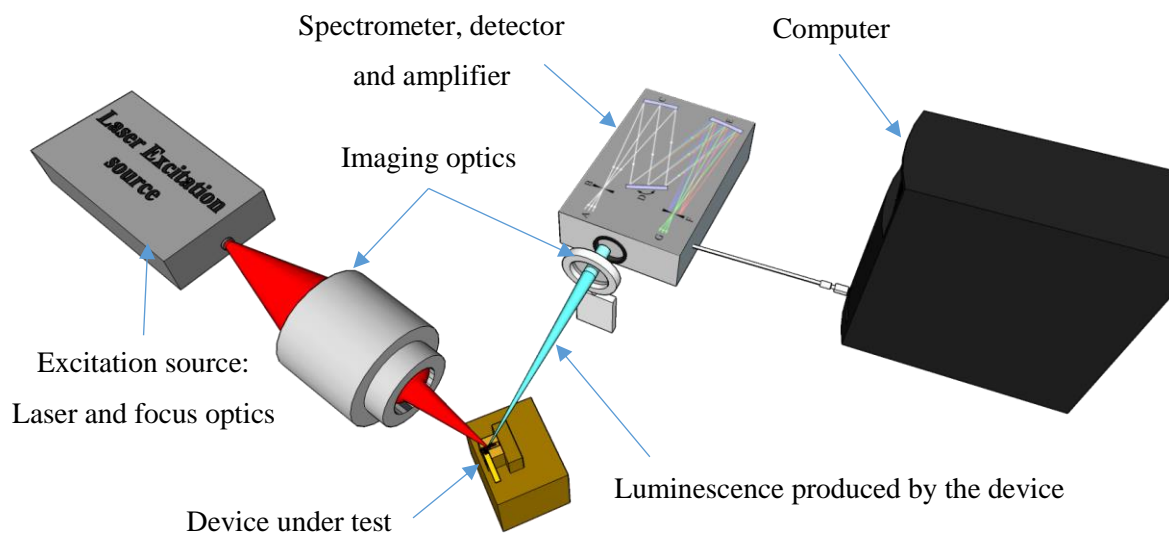


Figure IV-23: Dedicated setup implemented for μ PL measurements.

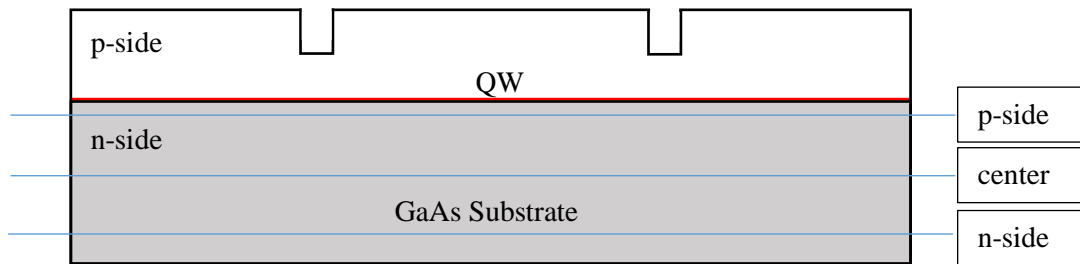


Figure IV-24: Front facet cross-section view of the LD and identified scanning lines for μ PL measurement at the level of the GaAs substrate namely p-side, center and n-side. The lines are separated of $\sim 40\mu\text{m}$ from each other and the p-side line is $\sim 20\mu\text{m}$ from the QW.

Two types of measurement have been realized as shown in *Figure IV-25*. One measurement is along the front facet (x-axis with green arrows) while the other one is done along the longitudinal side (y-axis with blue arrows). Both measurements have a precision step of $1\mu\text{m}$. The longitudinal μ PL is measured to characterize the mechanical stress distribution along the cavity from the front facet to the rear one.

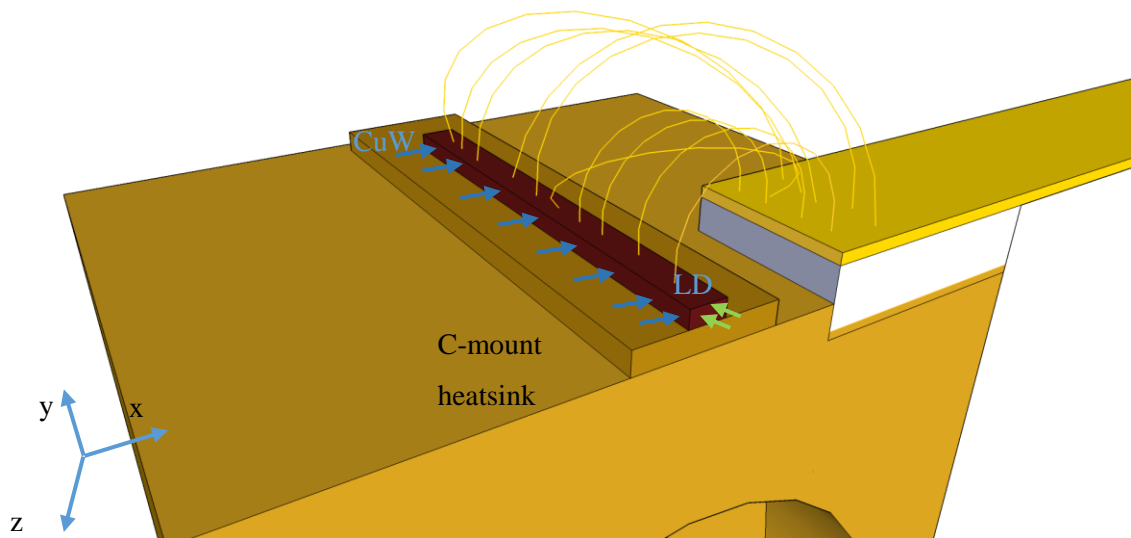


Figure IV-25: Location of areas used for μ PL measurements. The green arrows represent the front facet region while the blue arrows show the longitudinal region.

b. Experimental results and discussion

For this study, investigations have been performed only on four LDs (2 SLOC and 2 AOC vertical structures). *Table IV-9* summarizes the main characteristics of the LDs under investigation.

All the LDs have the same cavity length (4mm) and are soldered onto a C-mount heatsink with the two mounting mechanical configurations previously described.

Vertical structure	n°	AR (%)	HR (%)	Mounting configuration	Nitrogen time (min)
SLOC	C0542	1x	3x	Standard	1,5 min
SLOC	C0596	1x	3x	New	1,5 min
AOC	C0578	1x	3x	Standard	1,5 min
AOC	C0598	1x	3x	New	1,5 min

Table IV-9 : Characteristics of the LDs used for μ PL measurements.

Because of its vertical configuration, the AOC structure has the optical cavity closer to the heatsink compared with the SLOC or LOC ones, particularly due to the thinner layer p-side of the GaInAsP resulting in a high strain into the QW. Table IV-10 recalls the different layers of the two vertical structures, especially highlighting the difference (quoted in red) between the thickness of the p-side GaInAsP for the AOC and the SLOC vertical structure.

AOC vertical structure			SLOC vertical structure		
Layer	Material	Thickness [μ m]	Layer	Material	Thickness [μ m]
Substrate	GaAs	150	Substrate	GaAs	150
Cladding	$Al_xGa_{1-x}As$	2,8	Cladding	$Al_xGa_{1-x}As$	2,8
LOC	$Ga_xIn_{1-x}As_yP_{1-y}$	0,9	LOC	$Ga_xIn_{1-x}As_yP_{1-y}$	1,25
QW	$Ga_xIn_{1-x}As$	0,009	QW	$Ga_xIn_{1-x}As$	0,009
Barrier	$Ga_xIn_{1-x}As_yP_{1-y}$	0,012	LOC	$Ga_xIn_{1-x}As_yP_{1-y}$	1,25
QW	$Ga_xIn_{1-x}As$	0,009	Cladding	$Al_xGa_{1-x}As$	1,1
LOC	$Ga_xIn_{1-x}As_yP_{1-y}$	0,1	Contact	GaAs	0,18
Cladding	$Al_xGa_{1-x}As$	0,4			
Cladding	$Al_xGa_{1-x}As$	1,1			
Contact	GaAs	0,18			

Table IV-10: Details of the AOC and SLOC vertical structures.

c. Front facet spatially-resolved μ PL measurements

The μ PL measurement strongly depends on the alignment of the optics and because of that, we cannot strictly compare the absolute values obtained from the different devices under test. The

absolute PL signal reproducibility often fluctuates by a factor of 10–30 %, in particular if the sample is removed and newly aligned for a next step of characterization [44].

Figure IV–26 compares the transversal (x axis) μ PL results for the AOC vertical structure with the standard and the new mechanical mounting configurations. The three curves represent the gradual changes of the strain in the GaAs substrate associated with the n-side, center and p-side scanning lines. The orange curve represents the front facet waveguide structure with the grooves and the central ridge emissive area as previously presented in *Figure IV–24*.

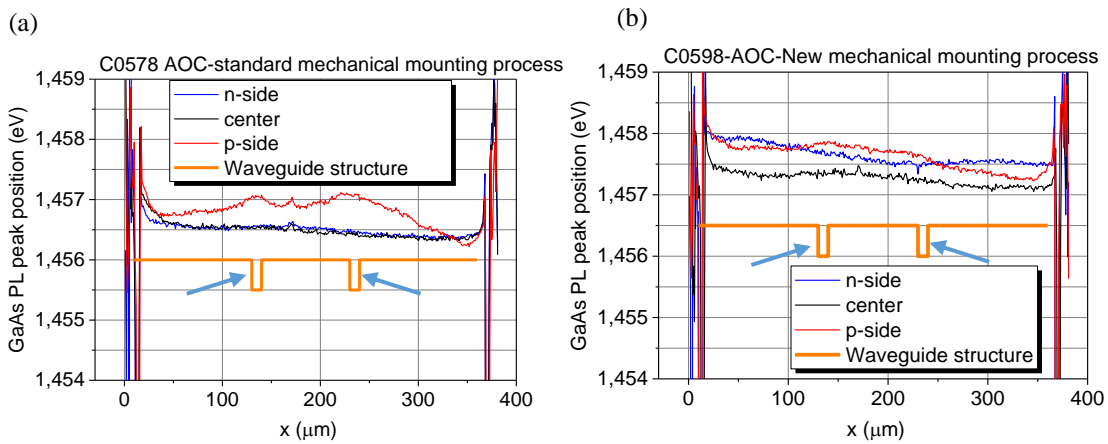


Figure IV–26: Front facet spatially-resolved μ PL measurements for two AOC-based LDs (4mm cavity length) mounted with (a) standard and (b) new mechanical mounting configurations.

The standard mechanical mounting configuration shows a compression state in the p-side while a tension state in the n-side due to the soldering process (*Figure IV–26(a)*). Moreover, two peaks occur on the p-side scan. These peaks are probably related to the waveguide vertical structure corresponding exactly to the position of the ridge grooves. Even if the “p-side” curve corresponds to a measurement done in the substrate, the signature of the LD grooves clearly appear as shown by the blue arrows in *Figure IV–26*. In contrast, with the new mechanical mounting configuration, these previous peaks detected in the “p-side” curve disappeared that can be related to a lower residual strain compared with the standard mechanical mounting (*Figure IV–26(b)*). Moreover, the strain seems to be more uniform and homogeneous whatever the considered scanning line and in particular close to the QW region (see “p-side” curve).

Figure IV–27 plots on a same graph, the spatially-resolved μ PL measurements at the level of the front facet performed on AOC-based LDs mounted with the two configurations (standard-C0578 and new-C0598).

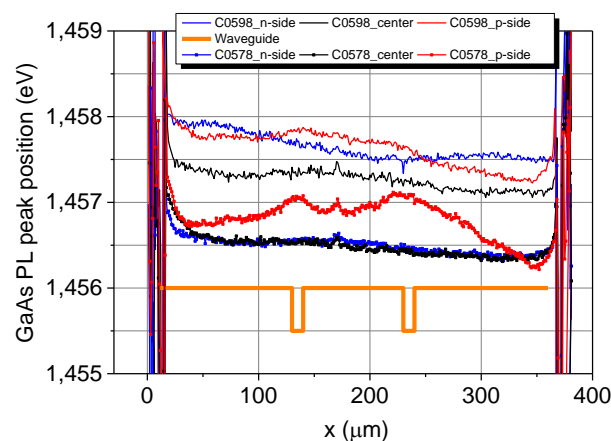


Figure IV–27: Comparison of spatially-resolved μ PL measurements at the level of the front facet performed on the two mounting configurations (standard-C0578 and new-C0598) for two AOC-based LDs.

Figure IV–28 gives the results obtained from the spatially-resolved μ PL measurements at the level of the front facet performed on the two mounting configurations for two SLOC-based structures. The standard one shows a compression state on the p-side waveguide while a tension state on the n-side. The negative peak (black arrow in Figure IV–28) observed in the standard soldering could be the signature of a defect along the front facet. With an optical microscope, the front facet was investigated and nothing unusual was observed. It seems that the new mounting configuration allows to reduce the difference between the compression state and the tension state from the n-side region to the p-side region. In Figure IV–29, it is possible to compare the overall results for the two devices on a same graph. For the SLOC vertical structure, the standard mechanical mounting process shows a more uniform strain compared with the new mounting process that is drastically different from the previous results obtained with AOC-based LDs.

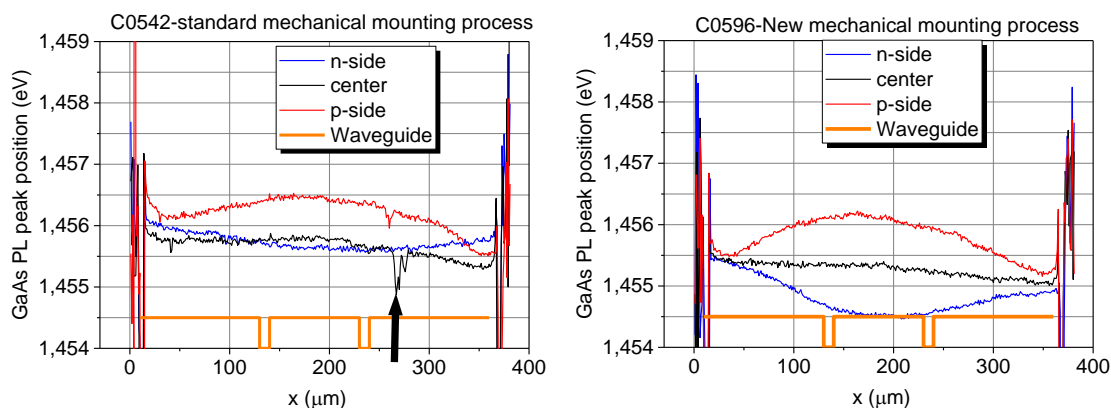


Figure IV–28: Front facet spatially-resolved μ PL measurements for two SLOC-based LDs (4mm cavity length) mounted with (a) standard and (b) new configurations.

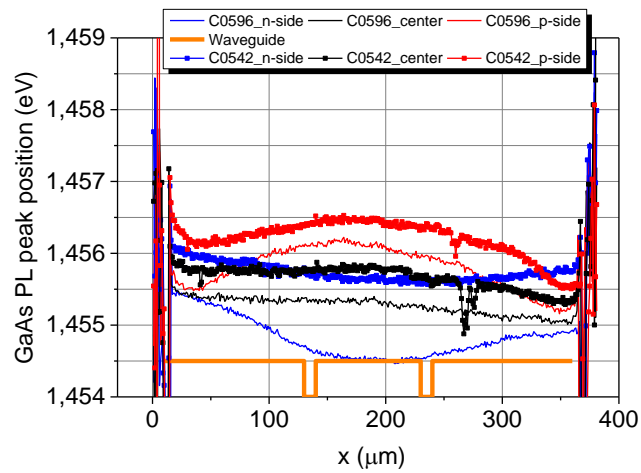


Figure IV-29 : Comparison of spatially-resolved μ PL measurements at the level of the front facet performed on the two mounting configurations (standard-C0542 and new-C0596) for two SLOC-based LDs.

When all these results are compared, the benefit coming from the new mounting process configuration is not so obvious whatever the vertical structure considered. A large increase of the strain difference is highlighted between the n- and p-side scanning lines that is 40% higher than that of the one induced by the standard mounting process especially for the AOC structure. As reported in *Table IV-10*, the optical cavity thickness of the SLOC structure is twice compared with the AOC one, and so, the distance from the QW to the CuW submount is higher than for the AOC structure. We believe that a shorter distance between the QW and the CuW submount will lead to a higher strain in the AOC structure.

d. Longitudinal spatially-resolved μ PL measurements

Some additional interesting results arise from the longitudinal μ PL measurements performed along the length of the same LDs starting from the front facet up to the rear facet. One can assume that from an ideal point of view, the mechanical strain should be almost the same along the optical cavity but *Figure IV-30* shows an asymmetric and non-uniform residual strain along the optical cavity.

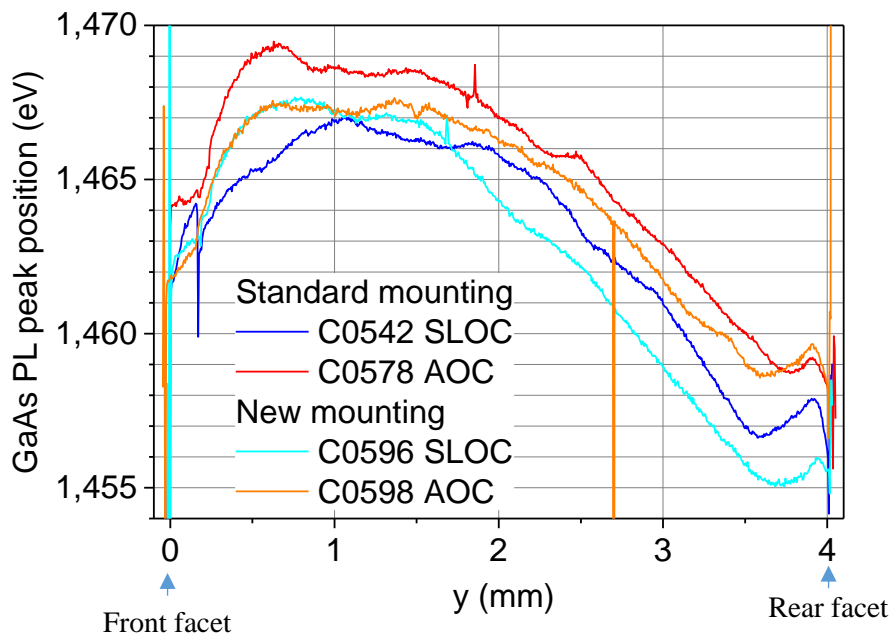


Figure IV-30 : Comparison of longitudinal spatially-resolved μ PL measurements performed on the whole mounting configurations (standard-C0542, C0578 and new-C0596, C0598) for the two vertical structures (AOC and SLOC).

The band-structure parameters, such as the band gap and effective mass, are dependent on both temperature and pressure. It is well-established that increasing the hydrostatic pressure (p [GPa]) usually increases the band-gap energy [45] and at the first order, the hydrostatic pressure corresponds to the isotropic stress. Based on [Eq IV-9], it is possible to estimate the stress magnitude:

$$E_g(p) = 1,9 - 1,15 \cdot 10^{-2} \cdot p \quad [\text{Eq IV-9}]$$

where p represents the stress and $E_g(p)$ is the shift of the band gap as a function of the stress.

From [Eq IV-8] and [Eq IV-9], the measured stress along the cavity length of each LD can be predicted and plotted in Figure IV-31.

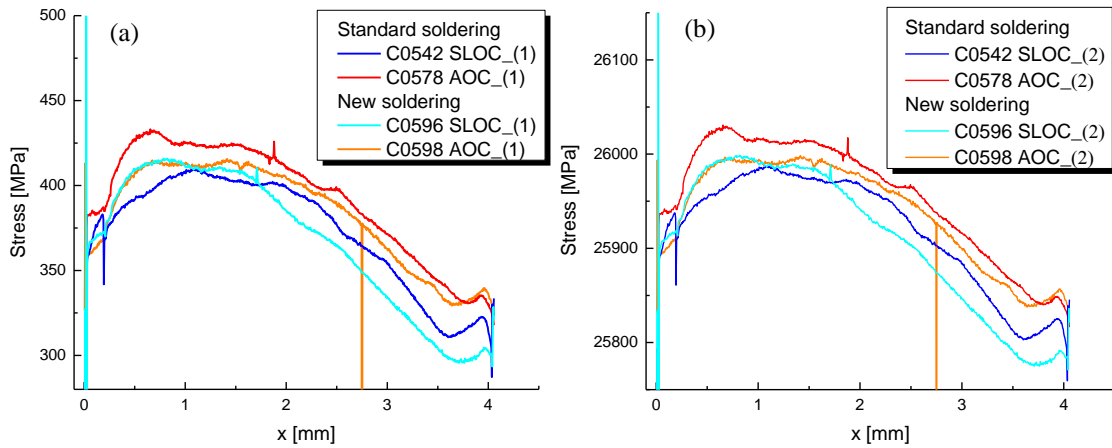


Figure IV-31: Predicted stress from the μ PL measurements along the cavity length using [Eq IV-9] for (a) and [Eq IV-8] for (b).

With these two approaches and although the magnitude is different using the two equations, we can clearly see that the shape of the stress remains nearly the same. These results are also in good agreement with those given in *Figure IV-22* (predicted Von-Mises stress) obtained from 3D thermo-electro-mechanical simulations. The vertical structure used in these simulations is considered as an approximation of the real structure since in order to obtain reasonable computation times, the vertical structure has been modelled only by the GaAs substrate. This may explain the different values for the resulting stress amplitude between experiments and simulations. However, thermo-electro-mechanical simulations confirmed the longitudinal μ PL experiments and particularly the overall variations of the stress along the cavity.

Since the difference in stress magnitude obtained from [Eq IV-8] and [Eq IV-9] reported in *Figure IV-31* is quite large, we have chosen to use the units in eV. In this case, the variations of the μ PL measurements remain almost equal for the two vertical structures. The strain difference between the two facets is in the order of 10^{-2} eV. Such a weak difference can be considered as negligible but it has been reported that a stress difference of 10^{-3} eV less may lead to reliability issues during CW operation. The following points can be highlighted:

- The predicted variations of the stress along the longitudinal axis are very similar whatever the chosen equation.
- The weaker stress magnitude is achieved with the SLOC-based structure whatever the mechanical mounting configuration compared with the AOC-based one.
- The new mechanical mounting configuration has a positive impact since the stress difference between front and rear facet is reduced compared with the standard one whatever the considered vertical structure.

The only thing that is similar in all cases is the soldering process. Hence, this phase can be addressed as the root cause for premature COD of all LDs. We have previously shown that after a COD failure, a crack appears at the interface between the LD and the AuSn solder along the cavity length. This crack appears after a COD event, we investigate a good LD, the AuSn solder interface is uniform and without a crack. The cause of the COD of all the LDs lies in the residual mechanical stress due to the mounting configuration. The new configuration reduces the mechanical stress particularly for the AOC structure resulting in a higher COD threshold (up to 14A in CW operation) for the AOC structure compared with the SLOC structure (10A). The μ PL experiments allowed us to quantify the surface strain due to mechanical mounting process but it is also of interest to assess the strain inside the LD structure. For that, in the next section, photocurrent spectroscopy characterizations have been performed.

4.3.4 Photocurrent Spectroscopy measurement (PCS)

a. Principle and setup description

The PCS technique can quantify the residual mechanical strain due to a soldering process by measuring the strain inside the device under test. Hence, the PCS technique is fully complementary to the previous one since this last enables to determine only the surface or sub-surface strain. As described for the first time by Henry et al., this technique is based on the use of the LD as a photodiode [46]. An excitation light reaches the front facet of the LD and it is absorbed then creating non-equilibrium electron-hole pairs. The excitation light goes through the LD and the penetration depth depends on the wavelength of the source. If the excitation photon energy is higher than the bandgap of the material, the absorption occurs predominantly close to the surface of the LD. Using lower photon energies, the light will travel deeper in the LD structure [42]. For high-power LDs emitting at 975nm, the analysis depth is in the range of $100\mu m$. The excitation photons produce electrical carriers giving the photocurrent. An ammeter connected to the LD, completes the measurement setup. Even though the whole front facet is illuminated, the main information comes from the depletion region around the p-n junction. The photo-generated carriers are produced in a region without voltage gradients, the substrate cannot contribute to the PCS unless these carriers are able to diffuse to the regions of the LD that have a voltage gradient [42].

Figure IV–32 shows the dedicated setup implemented for PCS measurements. The Bruker optics IFS 66V/S is a Fourier Transform Infrared Spectrometer having a wavenumber ranging from 7500 to 370 cm^{-1} with a resolution equal to $0,25\text{cm}^{-1}$.

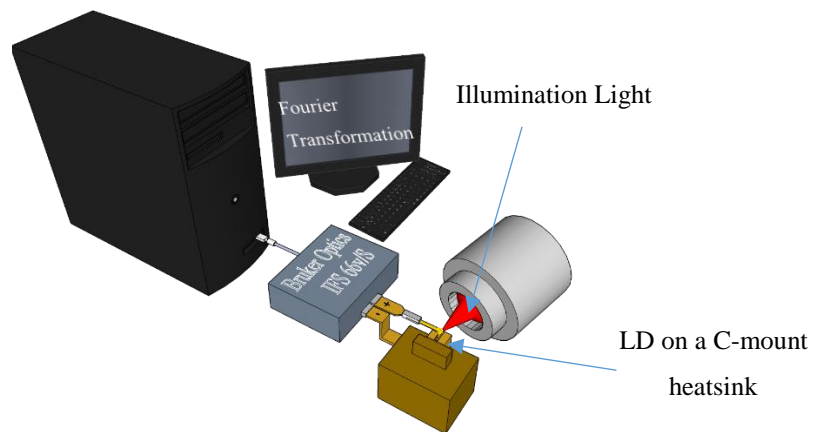


Figure IV–32: Dedicated setup implemented for PCS measurements. The “Illumination light” lights up the front facet of the LD that generates the photocurrent. This last is measured with the “Bruker Optics IFS 66V/S” that is a Fourier Transform Infrared Instrument Technology.

Figure IV–33 shows an example of PCS spectrum achieved from a SLOC-based structure LD (4mm cavity length). The three blue dashed arrows represent the main emission wavelengths of the LD. The first and second transitions are related to the photon absorption at the barriers of the QW and the GaAsInP quaternary layer respectively. These two transitions have quite the same photocurrent level. The third transition corresponds to the QW emission wavelength.

Beyond 975nm, there are only weak PCS contributions probably caused by defects and impurities that can be located within the waveguide or the QW [42].

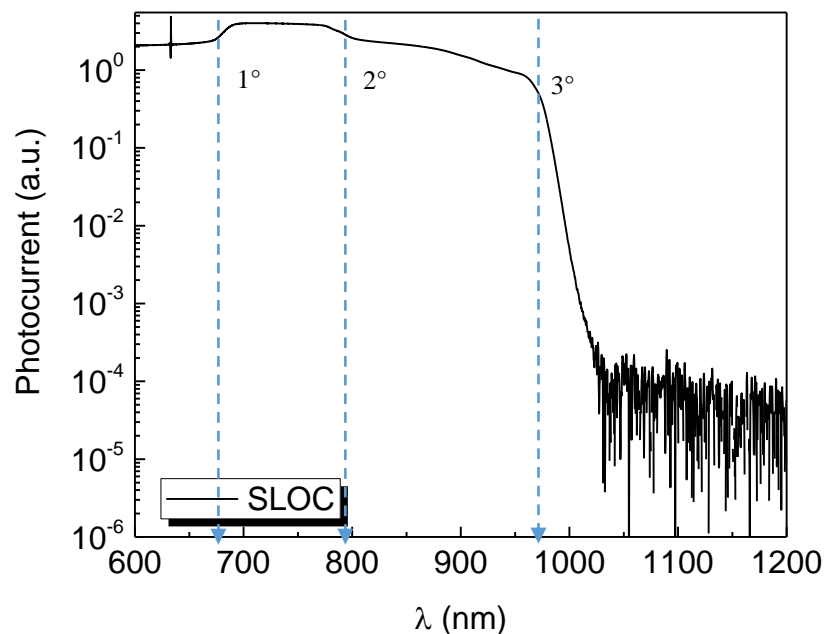


Figure IV–33: Example of PCS measurement achieved from a SLOC-based structure LD (4mm cavity length).

It is known that the spectral position of the optical transition within a QW depends on its intrinsic epitaxial process-dependent mechanical strain [42]. From PCS spectra, it is possible to quantify the strain in the QW. The PCS spectra can also give some relevant information about the absorption coefficient of the waveguide. The absorption coefficient in the QW is assumed to have a step-like spectral dependence. If one differentiates even a broadened step function, the first derivative will show its maximum at the onset of the steps. If the broadening is symmetric, the position of the maximum is not affected. The first derivative curve highlights the spectral position of each optical transition within the QW [42]. A drift in the emission spectrum corresponds to a different strain in the QW. The great interest of such a first derivative graph is highlighted in the following section.

b. Experimental results and discussion

In order to compare the effects of standard and new mechanical mounting configurations on the strain, four LDs (4mm cavity length) were analyzed and their characteristics are summarized in *Table IV-11*.

Vertical structure	Mounting configuration	Coating
SLOC	Standard	HR95%-AR1%
SLOC	New	HR95%-AR1%
AOC	Standard	HR95%-AR1%
AOC	New	HR95%-AR1%

Table IV-11: Characteristics of the LDs used for PCS experiments.

Figure IV-34(a) shows the photocurrent spectra for the two mechanical mounting configurations for wavelengths ranging from 600 to 1200nm. The difference in the magnitude of the signals in *Figure IV-34(a)*, mainly lies in the optical alignment since each device under test may be subjected to a different alignment and the magnitude of the measured spectra can differ from a LD to another. *Figure IV-34(b)* plots the first derivative of the spectra in the same range of wavelengths while *Figure IV-34(c)* gives an enlargement of the photocurrent variations around 980nm in the QW region. One can clearly see the shift of the minimum of the photocurrent between standard and new mechanical mounting configurations for both SLOC and AOC structures. For the SLOC structure, the difference in the QW absorption wavelength (minimum of the photocurrent) between the two mounting configurations is equal to $\sim 2,6\text{nm}$ while for the AOC structure, the same difference is largely reduced to $\sim 0,4\text{nm}$.

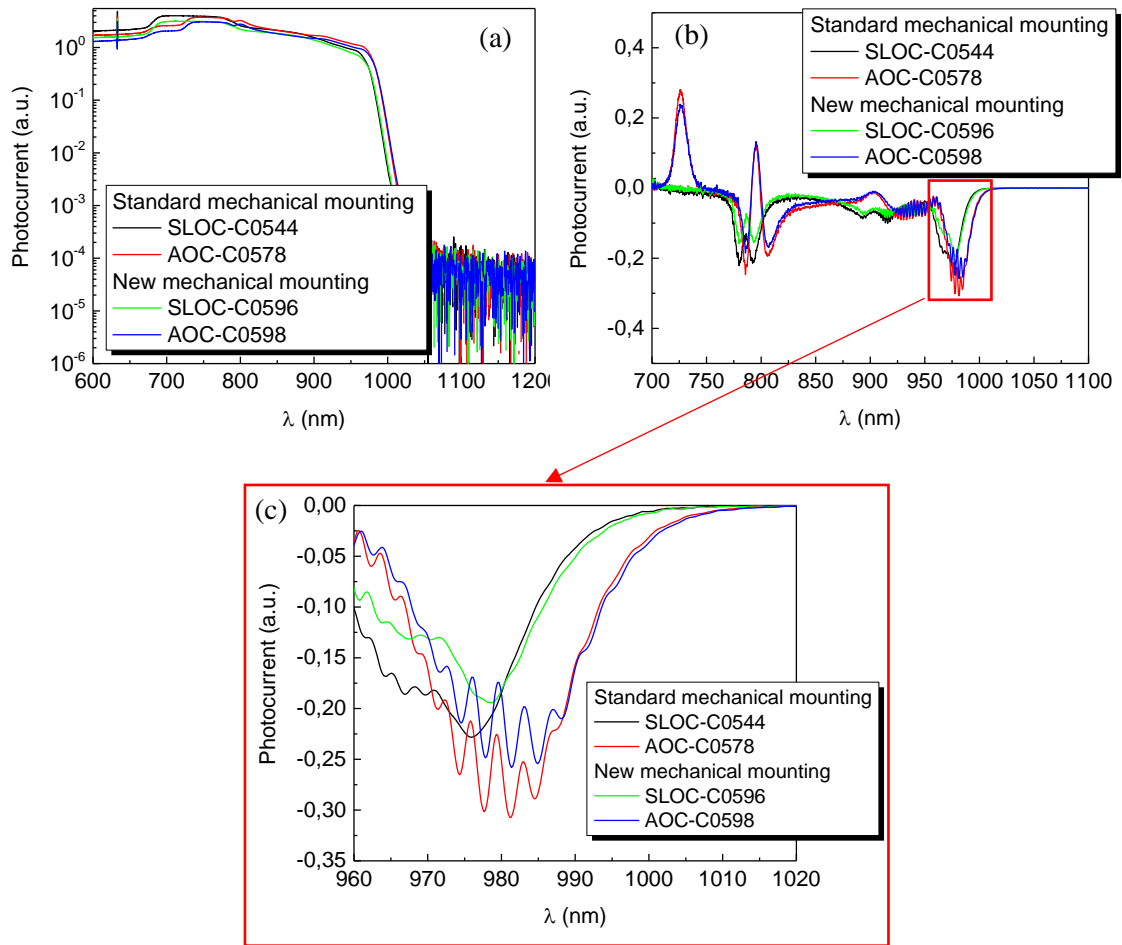


Figure IV-34: (a) PCS measurements for the 4 LDs considering the two vertical structures and the two mounting configurations. (b) First derivative of the measurements. (c) Enlargement of the emission peak of the QW emission.

This measurement demonstrates that the new mechanical mounting process configuration modifies the QW absorption wavelength and so the residual strain (as reported by M. Hempel et al. in [47]) due to a different location of the LD onto the C-mount. In particular, we see the different strain variations in the QW in the two cases and for the two vertical structures. *Table IV-12* summarizes the QW spectral absorption for the four LDs under measurement.

Device under test	Mounting configuration	Min wavelength [nm]
SLOC-C0544	Standard	975,80
SLOC-C0596	New	978,38
AOC-C0578	Standard	981,15
AOC-C0598	New	981,52

Table IV-12: QW spectral absorption for SLOC and AOC LDs with standard and new mechanical mounting configurations.

The two peaks extracted at 725 and 880 nm correspond to the AlGaAs and GaInAsP layers.

Although the modification of QW spectral absorption is more pronounced for the SLOC structure compared with the AOC one and even if μ PL and PCS provided quantitative information, it remains quite difficult to really conclude on the most suitable mechanical mounting configuration for our LD technology and especially its robustness to COD failure. For that, another technique based on pulse measurements has been used and described hereafter.

4.3.5 Extraction of COD threshold in pulsed current conditions

a. Principle and setup description

The COD phenomenon represents one of the most important example of degradation process in high-power LDs and it becomes of relevance when we aim to reach high levels of output power (> 10 W in CW regime). Generally, the COD starts at the emission facet or within the active region (emissive waveguide) where the temperature and the optical power density are the highest and is strongly related to the level of residual stress in particular due to the mounting process. Pulse COD measurements have been performed in order to avoid self-heating and acceleration of the device aging. Of course, such a technique is considered as destructive since the COD failure is an irreversible process.

The setup is described in *Figure IV-35*. A dedicated supply provides a current pulsed magnitude in the range of 0-60 A and a width of 2, 3 and 4 μ s with a repetition rate of 1Hz. The optical response of the LD is measured through a photodiode connected to a resistor and an oscilloscope monitors the produced voltage along this resistor. This signal is used to determine when the LD does not emit light anymore. A CCD camera gets some images of the spontaneous emission along the cavity length (longitudinal axis of the LD). The pulsed current generator triggers bot the CCD camera and the oscilloscope.

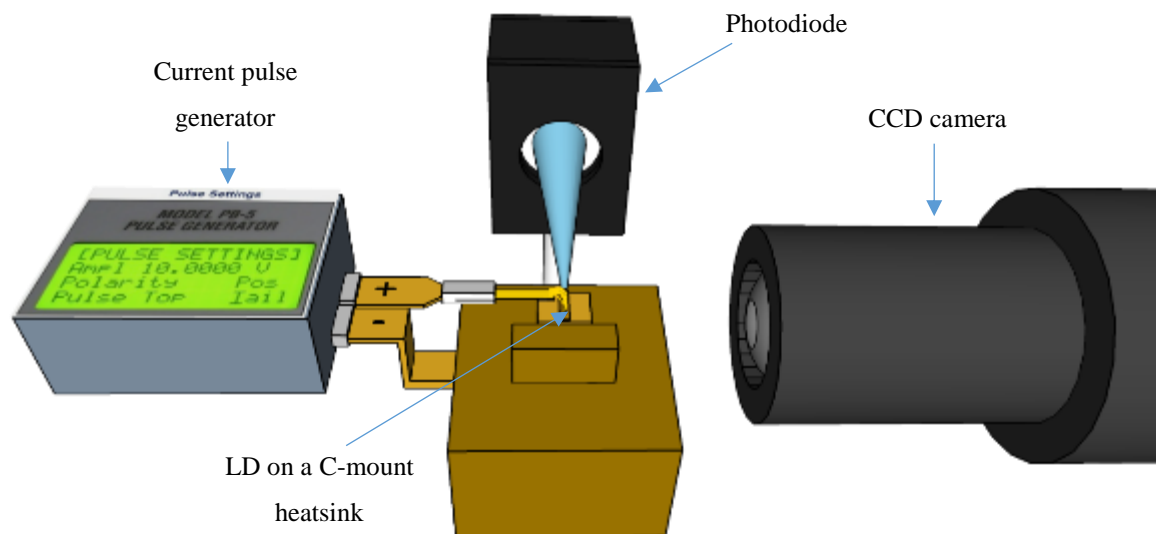


Figure IV–35: Dedicated setup implemented for pulsed COD measurements.

For broad-area LDs, this approach is suitable to generate the same type of damage pattern as already observed for COD developed during long-term CW aging experiments [47]. Such a measurement can reveal problems related to lithography, vertical structure design as well as soldering process. For each LD under investigation, the measurement protocol is the following:

- An optical inspection of the front facet is made before starting the measurements.
- A sequence of bias current pulses (2 μ s duration) and reference current up to the COD occurrence of the LD is set.
- For each pulse of current, the CCD camera takes an image of the spontaneous emission along the cavity while, through the photodiode, the oscilloscope monitors the optical power emitted by the front facet.

Figure IV–36 shows the sequence of bias current pulses as a function of time. A duration of 50s has been set between two pulses corresponding to the time necessary to charge the capacitors necessary for pulses generation.

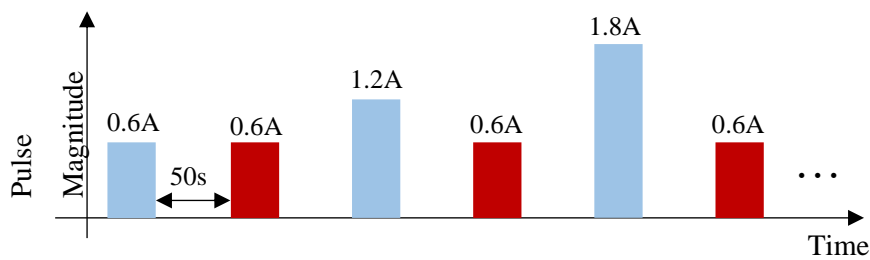


Figure IV-36: Example of sequence of bias current pulses applied to the LDs. After each increment pulse (blue), a reference measurement is done (red). This reference measurement is used to demonstrate that a COD occurs due to the considered pulse and not due to the others applied before.

The sequence starts with a low magnitude of pulsed current (0,6A) and this magnitude increases by step of 0,6A for each pulse until the COD happens. Between two incremental pulses, a reference value of constant magnitude (0,6A) is applied. This reference measurement value allows to determine the exact COD threshold current and to demonstrate that there is no any aging effect. The COD is supposed to occur only because of the last current pulse triggering the LD.

Figure IV-37 gives the result of a pulsed COD measurement, it is almost representative of all the measurements done for the LDs. Two images of the emitted spontaneous emission can be extracted:

- The first image is related to the application of incremental pulses (Figure IV-37(a))
- The second one referred to the application of reference pulses (Figure IV-37(b))

Each image is processed and the intensity of the spontaneous emission is calculated.

In Figure IV-37, the x-axis represents the position along the cavity of the LD where “0” is the front facet and “4mm” is the rear facet. The y-axis represents the pulsed current at which each measurement is done. The y-axis in Figure IV-37(a) represents the value of the current pulses at which the measurement is done while in Figure IV-37(b), the y-axis represents the values at which the measurement is done after the increment value equal to 0,6A. For instance, in Figure IV-37(b), the current value of 50A stands for the reference measurement at 0,6A taken after the application of a 50A peak pulse and 2 μ s duration. Each line in Figure IV-37 represents the spontaneous emission along the cavity length of the LD.

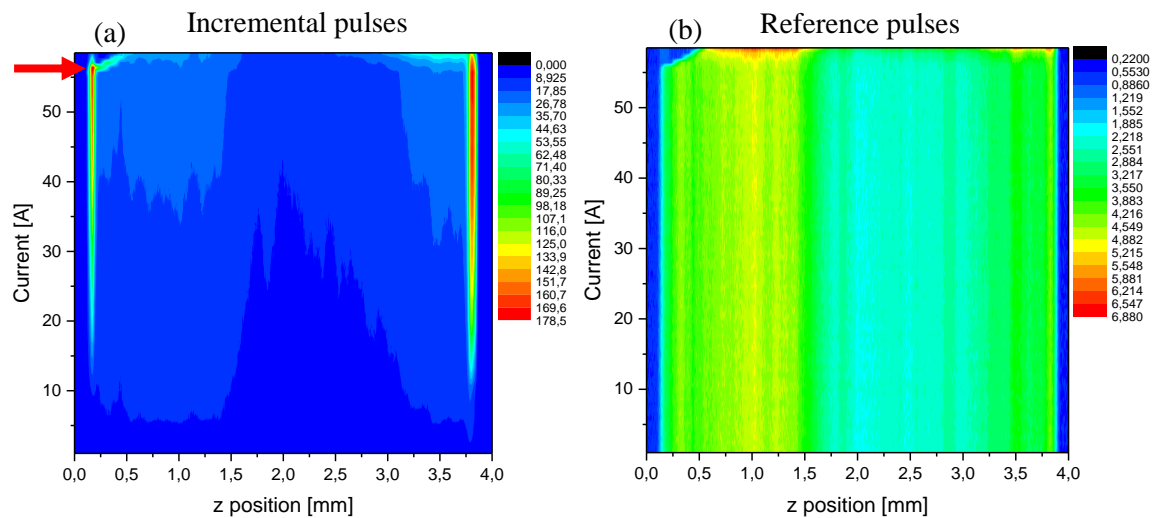


Figure IV-37: Example of spontaneous emission cartography in pulsed current conditions along the longitudinal axis of the LD. On the left, the incremental pulses image and on the right the reference pulses one. The colour code represents the spontaneous emission amplitude related to an arbitrary unit.

From the incremental pulses image on the left, it is possible to clearly see the beginning of the COD process initiated at 57A, located close to the front facet and highlighted by a red arrow on the left of *Figure IV-37(a)*. We notice a huge increase of the spontaneous emission (red colour) and as increases the current magnitude, this “hot-spot” travels inside the cavity. The reference pulses image shows that up to 57A, no clear difference is highlighted in the spontaneous emission of the LD along the cavity. The COD arises at the front facet (0 mm) and the spontaneous emission immediately downs to zero demonstrating that the COD results from the last applied pulse. There is no aging due to previous pulses.

b. Experimental results and discussion

For this measurement, two vertical structures (SLOC and AOC) have been considered. All the LDs (4mm cavity length) are soldered onto a CuW submount on top of a C-mount heatsink. The impact of two different HR coatings and the mounting process is also considered. Technological characteristics of the LDs and the COD threshold current for each vertical structure are summarized in *Table IV-13* and *Table IV-14*.

Vertical structure	Mounting configuration	Nitrogen time	HR	AR	COD threshold current (A)
SLOC	Standard	1,5 min	3x	1x	53,3
SLOC	Standard	1,5 min	3x	1x	53,9
SLOC	Standard	1,5 min	4x	1x	59,5
SLOC	Standard	1,5 min	4x	1x	58,3
SLOC	New	1,5 min	3x	1x	42
SLOC	New	1,5 min	4x	1x	62

$\langle I_{\text{COD}} \rangle = 54,8\text{A}$ and $\sigma_{\text{COD}} = 7,1\text{A}$

Table IV-13: Technological characteristics of SLOC-based LDs and extracted COD threshold currents versus the mounting configuration and the HR coatings.

Table IV-14 summarizes the AOC LDs population used for the COD measurement.

Vertical structure	Mounting configuration	Nitrogen time	HR	AR	COD threshold current (A)
AOC	Standard	9 min	3x	1x	60,8
AOC	Standard	1,5 min	3x	1x	52
AOC	New	1,5 min	3x	1x	58,9
AOC	New	1,5 min	3x	1x	53,9
AOC	New	9 min	3x	1x	60,1
AOC	New	1,5 min	3x	1x	61,4

$\langle I_{\text{COD}} \rangle = 57,85\text{A}$ and $\sigma_{\text{COD}} = 3,9\text{A}$

Table IV-14: Technological characteristics of AOC-based LDs and extracted COD threshold currents versus the mounting configuration and the HR coatings.

From the results presented in the previous sections regarding μPL and PCS measurements, we have concluded that no huge difference appears in residual stress whatever the vertical structures and the standard and new mounting configurations considered.

With these experiments, the key issue is to identify the location of the COD in the region of the front facet. Using an optical microscope, we have demonstrated that the COD happens recurrently on the left side of the LD (close to the groove) and sometimes, on the right side (also close to the groove) whatever the considered vertical structure as shown in *Figure IV-38*.

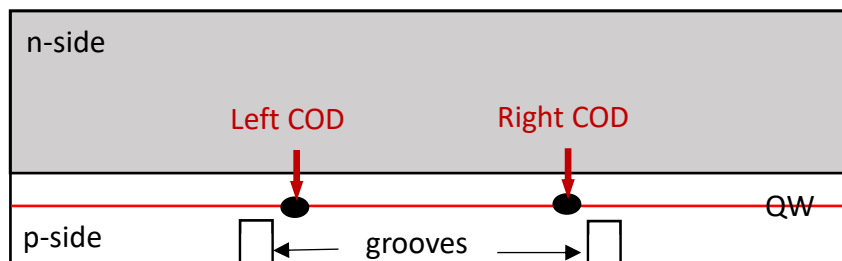


Figure IV-38: Location of the COD in the region of the front facet.

Table IV-15 summarizes the results of the COD threshold and the location of the COD spots for all the LDs under test. The last AOC-based LD was tested with a pulse duration of $3\mu\text{s}$ because the LD reaches the maximum available current delivered by the supply (60A) with a $2\mu\text{s}$ pulse duration.

LD structure	Mechanical mounting configuration	COD (A)	Location of the COD spot
SLOC	Standard	53,3	Left and right grooves
SLOC	Standard	53,9	Left groove
SLOC	Standard	59,5	Right groove
SLOC	Standard	58,3	Left groove
SLOC	New	42	Right groove
SLOC	New	62	Left groove
AOC	Standard	52	Left groove
AOC	Standard	60,8	Left groove
AOC	New	58,9	Left groove
AOC	New	53,9	Right groove
AOC	New	60,1	Left groove
AOC	New	61,4 A ($3\mu\text{s}$ duration)	Left groove

Table IV-15: Results of COD pulsed measurements giving the location of the COD spots.

Table IV-16 gives a comparison between the maximal COD threshold obtained in pulse conditions for the two vertical structures and the two mounting configurations.

LD structure	Mounting configuration	Maximal COD threshold in pulsed conditions [A]
SLOC	Standard	59,5 (2 μ s)
SLOC	New	62 (2 μ s)
AOC	Standard	60,8 (2 μ s)
AOC	New	61,4 (3 μ s)

Table IV-16: Maximal COD threshold obtained in pulsed conditions for the two vertical structures and the two mounting configurations.

Figure IV-39 shows an example of the front facet before and after COD pulsed measurements. All the LDs under test present the same signature of COD.

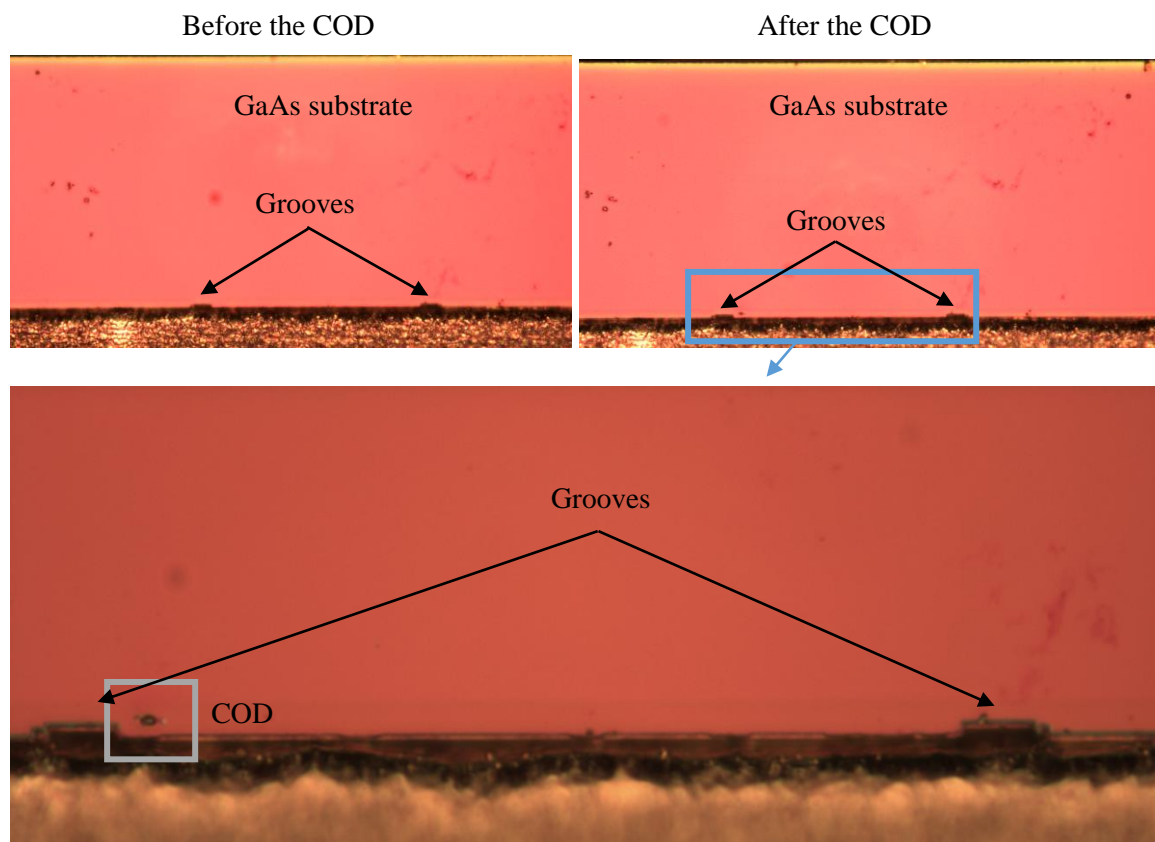


Figure IV-39: Front facet optical view of a LD before and after the pulsed current measurements. The COD is located on the left side (see grey square).

Because the optical power density is the highest in the centre of the emissive area compared with the other parts between the grooves, generally the COD appears in this region as reported in most of recent literature. In our case, we demonstrate that the situation is rather different and this failure signature could originate from the following points:

- a problem related to the vertical structure design, lithography or etching processes,
- a vertical multimode emission,
- the nitrogen time used between the cleaving step and the facets coating,

The COD appears in the same region whatever the vertical structures considered. This may be due to a problem of structure design. If this assumption is true, both the structures should have a low optical confinement into the cavity that can be detected through the L-I-V curves, underlying a well-known “kink effect” and indicating a switching process between lateral or axial modes. Such an effect can be also highlighted with far-field characterizations. Such measurements have been performed in “*Chapter II*”. If a vertical multimode emission occurs, two lobes would have appeared in the far-field pattern. However, after measurement of many LDs with different vertical structures, no real variations of this parameter have been observed meaning that the vertical confinement is not affected.

The second origin lies in a problem during the lithography steps, in particular due to the grooves patterning defining the emissive area that is considered as a critical issue of the overall fabrication process. The devices derived from the SLOC and AOC-based wafers have been processed at different times and the fabrication of the grooves is strictly the same for the left and right sides. Hence, we do believe that a problem in the lithography process is not responsible for the COD occurrence.

The last origin could be related with the nitrogen time. For that, TPRL technique was used and the results are given hereafter.

4.3.6 Time-Resolved Photoluminescence measurement (TRPL)

This technique allows to analyse the effect of different nitrogen times before the coating procedure of the facets. Such a process is used to prevent oxidation of the facets. The standard procedure developed at III-V lab for high-power LDs is to expose facets to nitrogen during 1,5min.

The non-equilibrium carrier dynamics in semiconductors directly reflect the nature and the quality of materials. For particular classes of semiconductors, the characteristic of the non-

equilibrium carriers recombination lifetime, τ , is highly dependent on the nature of the materials and interfaces between the layers of a LD. The parameter τ describes the kinetics of a non-equilibrium population decay provided that the number of recombining carriers pairs is proportional to the total number of excited carriers pairs. This situation is called linear recombination and is described by an exponential law for which τ represents the decay time constant. A non-linearity in this curve is mainly caused by Auger recombination, carrier transport and recombination, including excitonic and defect-related processes as perfectly detailed in [44]. The radiative recombination mechanism, creating the PL signal, is proportional to the total number of carriers pairs ($\delta\eta$). Hence, TRPL allows to measure the non-equilibrium carriers population that decays.

The TRPL setup is based on a pulsed laser as excitation source and a fast detection system enables to measure the PL transient as shown in *Figure IV-40*. For a detailed description of the setup, more data are available in [44].

The blue square of *Figure IV-40* represents the excitation source that is typically a laser source. The excitation wavelength goes from UV to IR and the repetition rate is 80 MHz (representing 12 ns between each pulse). The pulse duration is 80 fs and the excitation spot is $\varnothing \sim 100 \mu\text{m}$. Neutral density filters are typically placed between the laser source and the free-space optics, required for an adjustment of the laser power. The mode-locked laser reaches the sub ps-range. In the red square of *Figure IV-40*, a monochromator is used to separate the fluorescence signal from the excitation light. The streak camera detects and collects the fluorescence signal while the data are then processed with a dedicated computer [44].

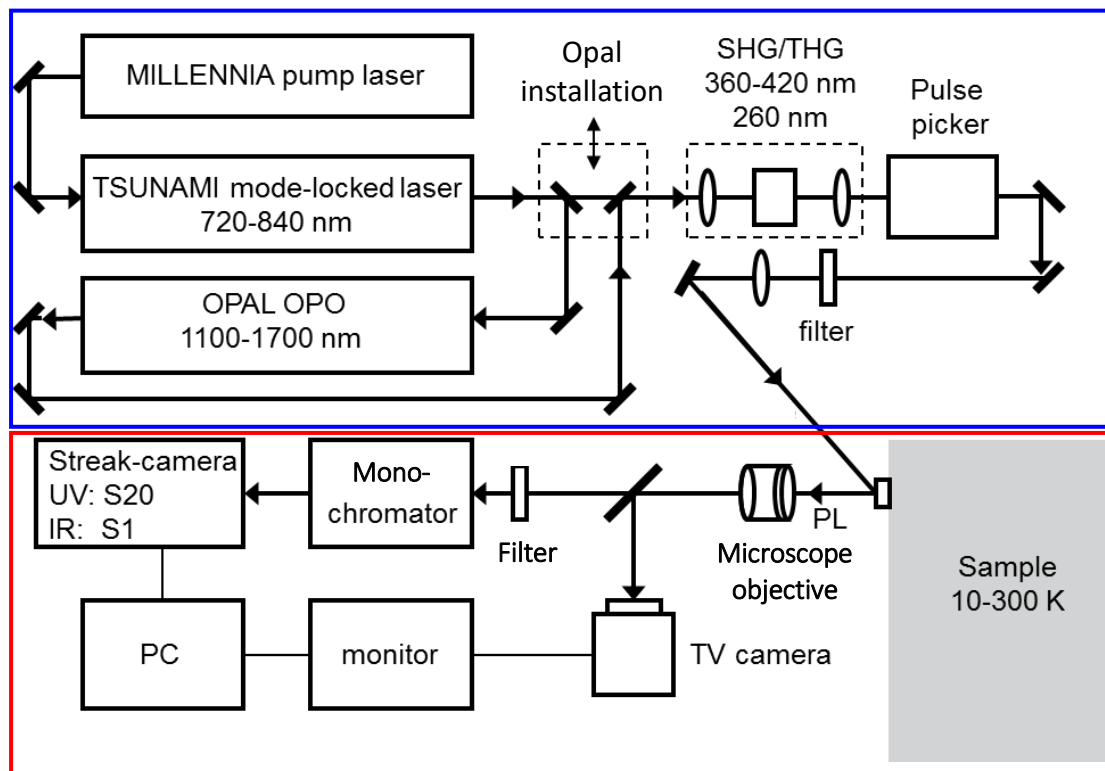


Figure IV-40: Dedicated setup implemented for TRPL experiments already reported in [44].

At III-V lab, it was demonstrated that a nitrogen time lower than 1,5min cannot provide an oxidation prevention of the facet. Therefore, for our study, higher exposition times have been set (1,5 and 9min) and we compare the results using TRPL analysis in the region of the front facet. All the previous 15 LDs presented in *Table IV-8* were tested and the overall results are summarized in *Figure IV-41*. Twelve LDs were tested after the COD appears and the results are compared with three goods LDs.

The slope of the curves in *Figure IV-41* allows obtaining information about the time of carriers decay and presence of potential defects located at the front facet and related to recombination centers. One can see that the slope remains the same whatever the nitrogen time considered for all the devices. We can conclude on the repeatability and the quality of the coating process since no particular signatures (mainly sudden changes of the slope) in the PL decay have been observed. So, regarding our assumptions previously proposed and based on these results, one can assume that the mechanical mounting of the LDs is certainly the main origin of COD. Of course, our conclusion must be weighted by a weak population of devices and it will be of interest to going-on with μ PL measurements on larger batches of LDs appearing as one of the best technique to characterize mechanical mounting efficiency.

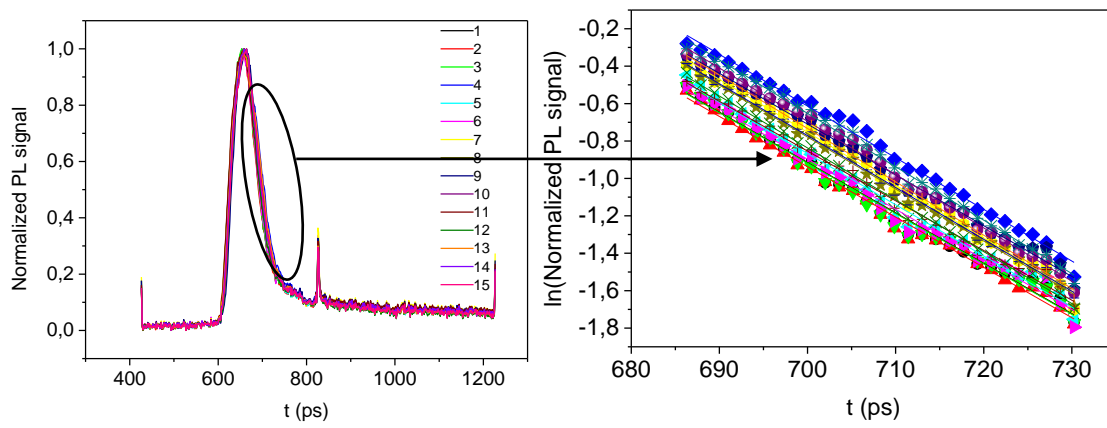


Figure IV-41: Results of TRPL measurements for 15 LDs coated under two nitrogen times (1,5 and 9 min).

CONCLUSION

Results reported in **chapter 4** have mainly focused on the extraction of thermal resistance of the micro assembled LDs (F-P and DFB architectures) and analysis of stress distribution considering different mechanical mounting configurations as well as its impact on the COD threshold.

A first part of this chapter dealt with a methodology enabling to extract the thermal resistance not only of the micro assembled device but also of each material forming the overall assembly using transient thermal testing. Indeed, thermal resistance remains also a critical issue leading to a reduced junction temperature rise within the chip, especially targeting high optical output power ($> 10\text{W}$).

We demonstrated that thermal resistance can be efficiently evaluated using a dedicated technique namely T3STER[®] that is based on the direct monitoring of the temperature distribution into the whole micro assembled device through a pulsed bias testing. Such an equipment gives a detailed overview of the heat flow spreading into the whole device including laser chip, solder, submount and heatsink. A specific effort to validate a metrology procedure has been carried out to deduce the optimized setup parameters for the determination of cumulative structure functions. The final protocol is the following:

- A graphite sheet is used to guarantee an optimal thermal contact between the heat sink and the alumina support. A tightening torque of 0,25 Nm for the three calibration screws.
- The bias current depends on the cavity length and sets to the following values: 600mA, 450mA and 300mA for 4mm, 3mm and 2mm respectively.
- The equipment monitors the transient cooling curve of heat flow over the micro assembled device for an “OFF-state” duration of 800s. After the ON/OFF regime, the obtained cooling profile is then processed using the T3STER[®] Master Software for the calculation of the structure function considering the boundary conditions.

With the help of theoretical calculations taking into account both 1D contribution and spreading effects of the thermal flow, experimental thermal resistances have been extracted on both F-P and DFB LDs with different cavity lengths. The thermal resistance of a 4mm DFB laser device is equal to 2,85K/W while the thermal resistance of the chip itself is around 1,4K/W, agreeing with state-of-the-art. In comparison, a 4mm F-P laser device demonstrates a slightly lower thermal resistance near of 2,5K/W. The interest to use diamond-copper composite (DCD) as thermo-compensators submount has been also investigated and compared with CuW. Although the results are not as

impressive as expected, since only a gain of 3% has been highlighted for the maximum current on a 4mm cavity length F-P LD, DCD clearly appears as an interesting solution to push back the thermal “roll-off” threshold and optical power saturation over 10A.

The second part of this chapter investigated on surface mounting effects of a high-power LD by solder joint that represents a critical step since it has been already demonstrated that the soldering process induces residual mechanical stress and strain in particular due to CTE mismatch between the different materials and their temperature-dependent thermomechanical behaviour. In particular, two mechanical configurations used to mount the LD onto the C-mount heatsink have been considered and their efficiency was compared. The standard configuration has been compared with the new one; this last consisting in a different placement of the chip.

Stress distribution analysis as well as Catastrophic optical damage (COD) threshold determination has been achieved and discussed on LDs with different vertical structures (mainly SLOC and AOC) using four dedicated techniques (microphotoluminescence, photocurrent spectroscopy, time-resolved photoluminescence and high current pulsed measurements) in collaboration with the Max-Born-Institut in Berlin.

First, time-dependent 3D thermo-electro-mechanical simulations (FEM) have been performed to reproduce the standard mechanical mounting configuration of the LD onto the C-mount heatsink taking into account experimental data of temperature and pressure profile and to analyze the stress distribution on the front facet (transversal section) as well as along the cavity length (longitudinal section). For the standard configuration currently used at III-V lab, the front facet of the LD is located at the exact edge of the submount that leads to an asymmetric configuration from a thermomechanical point of view. In order to reduce the mechanical stress between the front and the rear facet, a new mechanical placement of the LD has been proposed and used for the mounting process with the same soldering conditions. The new location of the LD aims to better balance the thermal path as well as the thermomechanical stress distribution along its longitudinal axis compared with the previous one.

Because of the meshing complexity in particular due to the multiple thin epitaxial layers, a simplified structure has been considered to model the LD. The structure is composed of 150 μ m thick GaAs substrate with an oxide layer (SiO₂) used to delimit the central ridge and 4 μ m thick AuSn layer. These simulations particularly focused on the mechanical stress induced by the soldering. One can conclude on the large asymmetry of the Von-Mises stress predicted by FEM simulations along the longitudinal axis of the LD. The highest stress is clearly located at the level of the front facet (up to 4MPa) while reaching 1,5MPa at the rear facet.

Secondly, measurements have been performed using the four previous techniques on a batch of LDs considering two vertical structures, different facet coatings, nitrogen time and the previous mechanical mounting configurations (standard and new). The main highlights are the following:

- Spatially-resolved μ PL characterizations: From front facet results, the benefit coming from the new mounting process configuration is not so obvious whatever the vertical structure considered. A large increase in the strain difference is highlighted between the n- and p-side scanning lines that is 40% higher than that of the one induced by the standard mounting process especially for the AOC structure. We believe that a shorter distance between the QW and the CuW submount leads to a higher stress in the AOC structure. From longitudinal measurements along the cavity, one can deduce that:
 - * the predicted variations of the stress along the longitudinal axis are very similar whatever the chosen model,
 - * the weaker stress magnitude is achieved with the SLOC-based structure whatever the mechanical mounting configuration compared with the AOC-based one,
 - * the new mechanical mounting configuration has a positive impact since the stress is reduced compared with the standard one whatever the considered vertical structure.
- PCS characterizations: The photocurrent spectra for the two mechanical mounting configurations for wavelengths ranging from 600 to 1200nm have been analyzed and we show the interest of the first derivative of the spectra. One can clearly see the shift of the minimum of the photocurrent between standard and new mechanical mounting configurations for both SLOC and AOC structures. This measurement demonstrates that the new mechanical mounting process configuration modifies the QW absorption wavelength and so the residual strain due to a different location of the LD onto the C-mount. In particular, we see the different strain variations of the QW in the two cases and for the two vertical structures. Although this modification is more pronounced for the SLOC structure compared with the AOC one and even if μ PL and PCS provided quantitative information, it remains quite difficult to really conclude on the most suitable mechanical mounting configuration for our LD technology.
- COD threshold measurements: A specific procedure has been proposed based on a reference measurement allowing to determine the exact COD threshold current and to demonstrate that there is no any aging effect. The COD is supposed to occur only because of the last current pulse triggering the LD. We have demonstrated that the COD happens recurrently on the left side of the LD and sometimes on the right side (close to the groove

in both cases) whatever the considered vertical structure. Such a situation is rather different from literature and this failure signature could originate from different points that have been discussed.

- Finally, TRPL technique has been performed to analyse the effect of different nitrogen times before the coating procedure of the facets. Such a process is used to prevent oxidation of the facets. The standard procedure developed at III-V lab consists in exposing facets to nitrogen during 1,5min but a higher exposition time has been also considered (9min). We conclude on the repeatability and the quality of the coating process since no particular signatures (mainly sudden changes of the slope) in the PL decay have been observed. This result agrees with the COD pulsed measurement.

Based on these results, one can assume that the mechanical mounting of the LDs is certainly the main origin of COD occurrence. Of course, our conclusion must be weighted by a weak population of devices and it will be of interest to going-on with μ PL measurements on larger batches of LDs appearing as one of the best technique to characterize mechanical mounting efficiency.

CHAPTER IV REFERENCES:

- [1] W. B. Joyce, R. W. Dixon, "Thermal resistance of heterostructure lasers," in *Journal of Applied Physics*, vol. 46, no. 2, pp. 855–862, 1974.
- [2] M. C. Amann, "Thermal resistance of ridge waveguide lasers mounted upside down," in *Applied Applied Physics*, vol. 50, no. 4, pp. 4–6, 1987.
- [3] D. Veyrié, O. Gilard, K. Sanchez, S. Lhuillier, B. Levrier, L. Béchou, "New methodology for the assessment of the thermal resistance of laser diodes and light emitting diodes," in *Microelectronics Reliability*, vol. 50, pp. 456–461, 2009.
- [4] A. Al-Muhanna, L. J. Mawst, D. Botez, D. Z. Garbuzov, R. U. Martinelli, and J. C. Connolly, "High-power (>10 W) continuous-wave operation from 100- μm -aperture 0.97- μm -emitting Al-free diode lasers," in *Applied Physics*, vol. 73, no. 9, pp. 1182–1184, 1998.
- [5] M. Kanskar, L. Bao, J. Bai, Z. Chen, D. Dahlen, M. DeVito, W. Dong, M. Grimshaw, J. Haden, X. Guan, M. Hemenway, K. Kennedy, R. Martinsen, J. Tibbals, W. Urbanek, S. Zhang, "High Reliability of High Power and High Brightness Diode Lasers," in *SPIE proceedings High-power diode laser technology and applications XII*, vol. 8965, pp. 01–10, 2014.
- [6] V. Rossin, E. Zucker, M. Peters, M. Everett, B. Acklin, "High power High efficiency 910-980 nm broad area laser diodes," in *SPIE proceedings High-power diode laser technology and application*, vol. 5336, pp. 196–203, 2004.
- [7] P. Crump, C. M. Schultz, H. Wenzel, S. Knigge, O. Brox, A. Maaßdorf, F. Bugge, G. Erbert, "Reliable operation of 976nm High Power DFB Broad Area Diode Lasers with over 60% Power Conversion Efficiency," in *SPIE proceedings Novel in-plane semiconductor lasers X*, vol. 7953, pp. 1G, 2011.
- [8] C. M. Schultz, P. Crump, H. Wenzel, O. Brox, A. Maaßdorf, G. Erbert G. Trankle, "11W broad area 976 nm DFB lasers with 58% power conversion efficiency," in *Electronics Letters*, vol. 46, no. 8, pp. 580–581, 2010.
- [9] P. Crump, H. Wenzel, G. Erbert, G. Trankle, "Progress in increasing the maximum achievable output power of broad area diode lasers," in *SPIE proceedings High-Power diode laser technology and applications X*, vol. 8241, pp. 0U, 2012.
- [10] A. Maaßdorf, C.M. Schultz, O. Brox, H. Wenzel, P. Crump, F. Bugge, A. Mogilatenko, G. Erbert, M. Weyers, G. Trankle, "In-situ etching of patterned GaAs/InGaP surfaces for highly efficient 975nm DFB – BA diode lasers," in *Journal of Crystal Growth*, vol. 370, pp. 226–229, 2012.
- [11] J. Fricke, H. Wenzel, F. Bugge, O. P. Brox, A. Ginolas, W. John, P. Ressel, L. Weixelbaum, G. Erbert, "High-Power Distributed Feedback Lasers With Surface Gratings," in *IEEE Photonics Technology Letters*, vol. 24, no. 16, pp. 1443–1445, 2012.
- [12] A. Pietrzak, R. Hülsewede, M. Zorn, O. Hirsekorn, J. Sebastian, J. Meusel, P. Hennig, P. Crump, H. Wenzel, S. Knigge, A. Maaßdorf, F. Bugge, G. Erbert, "Progress in efficiency-optimized high-power diode lasers," in *SPIE proceedings Technologies for optical countermeasures X and High power lasers*, vol. 8898, pp. 08–22, 2013.
- [13] K. H. Hasler, H. Wenzel, P. Crump, S. Knigge, A. Maasdorf, R. Platz, R. Staske, G. Erbert, "Comparative theoretical and experimental studies of two designs of high-power diode lasers," in *Semiconductor Science and Technology*, vol. 29, no. 045010, pp. 01–06, 2014.
- [14] P. Crump, J. Fricke, C. M. Schultz, H. Wenzel, S. Knigge, O. Brox, A. Maaßdorf, F. Bugge, G. Erbert, "10W-reliable 90 μm -wide broad area lasers with internal grating stabilization," in *SPIE proceedings High-Power diode laser technology and applications X*, vol. 8241, pp. 10N, 2012.
- [15] P. Crump, G. Blume, K. Paschke, R. Staske, A. Pietrzak, U. Zeimer, S. Einfeldt, A. Ginolas, F. Bugge, K. Häusler, P. Ressel, H. Wenzel, G. Erbert, "20W continuous wave reliable operation of 980nm broad-area single emitter diode lasers with an aperture of 96 μm ," in *SPIE proceedings High-Power diode laser technology application VII*, vol. 7198, no. 14, p. 9, 2009.

- [16] J. Fricke, A. Ginolas, F. Bugge W. John, A. Klehr, M. Matalla, P. Ressel, H. Wenzel, G. Erber, "High-Power 980 nm Broad Area Laser Spectrally Stabilized by Surface Bragg Gratings," in *IEEE Photonics Technology Letters*, vol. 22, no. 5, pp. 284–286, 2010.
- [17] M. Kanskar, Y. He, J. Cai, C. Galstad, S.H. Macomber, E. Stiers, D. Botez, L.J. Mawst, "53% wallplug efficiency 975 nm distributed feedback broad area laser," in *Electronics Letters*, vol. 42, no. 25, 2006.
- [18] M. Kanskar, M. Nesnidal, S. Meassick, A. Goulakov, E. Stiers, Z. Dai, T. Earles, D. Forbes, D. Hansen, P. Corbett, L. Zhang, T. Goodnough, L. LeClair, N. Holehouse, D. Botez, L.J. Mawst, "Performance and Reliability of ARROW Single Mode & 100 μ m Laser Diode and the Use of NAM in Al-free Lasers," in *SPIE proceedings Novel in-plane semiconductor lasers II*, vol. 4995, pp. 196–208, 2003.
- [19] K. Kosiel, J. Muszalski, A. Szerling, M. Bugajski, "High power (>1 W) room-temperature (300 K) 980 nm continuous-wave AlGaAs/InGaAs/GaAs semiconductor lasers," in *Optica Applicata*, vol. 37, no. 4, pp. 423–431, 2007.
- [20] J. J. Lee, L. J. Mawst, and D. Botez, "Asymmetric Broad Waveguide Diode Lasers ($\lambda = 980$ nm) of Large Equivalent Transverse Spot Size and Low Temperature Sensitivity," in *IEEE Photonics Technology Letters*, vol. 14, no. 8, pp. 1046–1048, 2002.
- [21] L. J. Mawst, A. Bhattacharya, J. Lopez, and D. Botez, D. Z. Garbuzov, L. DeMarco, J. C. Connolly, M. Jansen, F. Fang, and R. F. Nabiev, "8 W continuous wave front-facet power from broad-waveguide," in *Applied Physics Letters*, vol. 69, no. 11, pp. 1532–1534, 1996.
- [22] K. Paschke, S. Einfeldt, A. Ginolas, K. Häusler, P. Ressel, B. Sumpf, H. Wenzel, G. Erbert, "15-W reliable operation of 96- μ m aperture broad-area diode lasers emitting at 980 nm," in *Lasers and Electro-Optics/Quantum Electronics and Laser Science Conference and Photonic Application System Technologies*, vol. CMN4, 2008.
- [23] V. Rossin, E. Zucker, M. Peters, M. Everett, and B. Acklin, "High power High efficiency 910-980 nm Broad area laser diodes," in *SPIE proceedings High power Laser Technology and applications*, vol. 5336, pp. 27–35, 2004.
- [24] M. Zorn, R. Hülsewede, O. Hirsekorn, J. Sebastian, and P. Hennig, "High-Power single emitters and Diode Laser bars with improved performance developed at JENOPTIK," in *SPIE proceedings High power diode laser Technology and applications X*, vol. 8241, pp. 824110/1-824110/10, 2012.
- [25] M. Leers, K. Boucke1, M. Götz, A. Meyer, M. Kelemen, N. Lehmann, F. Monti di Sopra, "Thermal resistance in dependence of diode laser packages," in *SPIE proceeding High-Power Diode Laser Technology and Applications VI*, vol. 687609–1, 2008.
- [26] Y. Qiao, S. Feng, C. Xiong, and H. Zhu, "Working Thermal Stresses in AlGaAs/GaAs High-Power Laser Diode Bars Using Infrared Thermography," in *IEEE Transactions on Device and Materials Reliability*, vol. 14, no. 1, pp. 413–417, 2013.
- [27] E. Suhir, J. Wang, Z. Yuan, X. Chen, and X. Liu, "Modeling of Thermal Phenomena in a High Power Diode Laser Package," in *International conference on electronic packaging technology & high density packaging - Electronic packaging technology & high density packaging*, vol. 1, pp. 438–432, 2009.
- [28] T. Gin, W. Ronnie, "Advances in high power laser diode packaging," in <http://www.intechopen.com/books/semiconductor-laser-diode-technology-andapplications/advances-in-high-power-laser-diode-packaging>, 2012.
- [29] C. Jong Hwa, S. Moo Whan, "Thermal investigation of LED lighting module," in *Microelectronics Reliability*, vol. 52, no. 5, pp. 830–835, 2012.
- [30] S. Shanmugan, D. Mutharasu, "Thermal transient analysis of high power led tested on Al₂O₃ thin film coated Al substrate," in *International Journal of Engineering Trends and Technology*, vol. 30, no. 6, pp. 6, 2015.
- [31] S. Shanmugan and D. Mutharasu, "Thermal transient analysis of high power led employing spin coated silver doped ZnO thin film on al substrates as heat sink," in *Journal of Optoelectronics and Biomedical Materials*, vol. 7, no. 1, pp. 1–9, 2015.

- [32] “JESD51-1, Integrated Circuits Thermal Measurement Method – Electrical Test Method (Single Semiconductor Device),” 1995.
- [33] M. Renez, V. Székely, A. Poppe, G. Farkas, and B. Courtois, “New Methods and Supporting Tools for the Thermal Transient Testing of Packages,” in *International Conference on Advanced Packaging*, vol. 1, pp. 407–4016, 2001.
- [34] A. HanB, M. Schmid, E. Liu, and G. Elger, “Transient thermal analysis as measurement method for IC package structural integrity,” in *Chinese Physical society and IOP publishing Ltd*, vol. 24, no. 6, pp. 18, 2015.
- [35] B. Chambion, “Présentation des composants étudiés, outils et méthodes d’analyses mises en œuvre,” in *Fiabilité de diodes laser de forte puissance 808 nm microassemblées pour des applications spatiales*, Thèse de doctorat, Université Bordeaux, 2014.
- [36] A. Jamnia, “Thermal and Mechanical Design and Analysis,” 2nd Edition, vol. 1. CRC Press, pp 18-20, 2008.
- [37] L. He, C. Zhao, W. Liu, S. Wu, B. Qiu, M. Hu, Y. Liu, “Effects of heatsink on the performance of high power semiconductor lasers,” in *16th International Conference on Electronic Packaging Technology*, pp. 997–1000, 2015.
- [38] G. Jiang, L. Diao, and K. Kuang, “Understanding Lasers, Laser Diodes, Laser Diode Packaging and Their Relationship to Tungsten Copper,” in *Advanced Thermal Management Materials*, Springer Science and Business Media, pp. 154, 2013.
- [39] X. Liu, L. C. Hughes, M. H. Rasmussen, M. H. Hu, V. A. Bhagavatula, R. W. Davis, C. G. Caneau, R. Bhat and C. Zah, “Packaging and Performance of High Power Semiconductor Lasers of High Heat Flux up to 2000 W/cm²,” in *Electronics Components and Technology*, vol. 1, pp. 251–258, 2005.
- [40] V. Bezotosnyi, O. N. Krokhin, V. A. Oleshchenko, V. F. Pevtsov, Y. M. Popov, and E. A. Cheshev, “Thermal regime of high-power laser diodes,” in *Physics Procedia*, vol. 72, pp. 399–404, 2015.
- [41] G. D. Gilliland, “Photoluminescence spectroscopy of crystalline semiconductors,” in *Materials Sciences and Engineering*, vol. 18, no. 3–6, pp. 99–399, 1997.
- [42] J. W. Tomm, J. Jimenez, “Strain measurement,” in *Quantum-well laser array packaging*, pp. 65–144, 2007.
- [43] L. Pavesi, M. Guzzi, “Photoluminescence of Al_xGa_{1-x}As Alloys,” in *Applied Physics Letters*, vol. 75, pp. 4779–4842, 1994.
- [44] J. Jimenez, J. W. Tomm, “Photoluminescence (PL) Techniques,” in *Spectroscopy analysis of optoelectronics semiconductors*, vol. 202, Springer -Verlag Berlin Heidelberg, pp. 317, 2016.
- [45] S. Adachi, “Energy-band structure: energy-band gaps of bulk materials,” in *GaAs and related materials*, Word scientific, 1994.
- [46] C. H. Henry, P. M. Petroff, R. A. Logan, and F. R. Merrit, “catastrophic damage of AlGaAs double heterostructure laser material,” in *Journal of Applied Physics*, vol. 50, pp. 3721–3732, 1979.
- [47] M. Hempel, J.W. Tomm, F. La Mattina, I. Ratschinski, M. Schade, I. Shorubalko, M. Stiefel, H.S. Leipner, F. M. Kießling, T. Elsaesser, “Microscopic Origins of Catastrophic Optical Damage in Diode Lasers,” in *IEEE Journal of Selected Topics in Quantum Electronics*, vol. 19, no. 4, p. 8, 2013.
- [48] IOFFE Physico-Tecnical Institute, “Optical properties of Ga_xIn_{1-x}As.” <http://www.ioffe.ru/SVA/NSM/Semicond/GaInAs/optic.html>, 2000.
- [49] S. Adachi, *Properties of semiconductor alloy group IV, III-V, II-VI semiconductors*. John Wiley and Sons, Inc. Publication, 2009.
- [50] S. Adachi, “GaAs, AlAs, and Al_xGa_{1-x}As Material parameters for use in research and device applications,” in *Journal of Applied Physics*, vol. 58, no. R1, pp. R1–R29, 1985.
- [51] S. Adachi, *Properties of Group-IV, III–V and II–VI Semiconductors*, 2005th ed., vol. 1, John Wiley & Sons, Inc. Publication, 2005.
- [52] S. Adachi, *Properties of Aluminium Gallium Arsenide*, vol. 1, INSPEC, the Institution of Electrical Engineers, 1993.

- [53] R. Brozel and G. E. Stillman, Properties of Gallium Arsenide, 3rd edition. INSPEC, the Institution of Electrical Engineers, 1996.
- [54] J. Piprek, “Non-radioactive recombination,” in *Semiconductor Optoelectronic Devices Introduction to physics and simulation*, Academic press publication, pp. 69–71, 2003.
- [55] S. M. Sze and M. K. Lee, *Semiconductor devices*, 3rd ed. John Wiley & Sons, Inc. Publication, 2010.
- [56] S. Dimitrijević, *Principles of semiconductor devices*, 2nd Edition, Oxford university press, 2012.

GENERAL CONCLUSION

This “CIFRE” PhD study, supervised by IMS Laboratory and III-V lab, takes part of a large project, funded by the French Ministry of Defense (DGA), namely “LAFIP SOMUST” (Laser à Fibre Pulsé à base de SOurce semi-conductrice Multimode STabilisée en longueur d’onde). The main goal of this project was to develop a pulsed fiber laser Er/Yb at 1,55 μm through an active collaboration between Thales Research and Technology (TRT), III-V lab for the development of the pump source and the KEOPSYS company in charge of the integration of the pump source in the fiber laser. This study has developed, fabricated and characterized a distributed feedback architecture (DFB) high-power LD (90 μm cavity width including a patterned 2nd order grating layer) emitting at 975nm to fulfill the requirements of the “LAFIP SOMUST” project. **A significant step-forward** has been highlighted with the realization of Al-free high-power LDs operating in a DFB mode and capable to reach at least 10W in CW regime with a Wall-Plug Efficiency (WPE) higher than 50% for the development of such a pulsed fiber laser delivering a pulsed peak optical power over 1kW at 25°C. The fiber laser must operate without thermal regulation and a high spectral stability is required for the pump source. Regarding the targeted application, it was demonstrated that most of the requirements must be fully covered with a LD pump source including DFB grating.

Chapter 1 has introduced the general context, the motivation and the objectives of this study. Firstly, a brief state-of-the-art of infrared Laser diode technologies has been given and in particular the different vertical structures reported by the major research and industrial leaders in the field. The objective was to emphasize on the advantages bringing by the III-V lab technology regarding the other competitors. Indeed, most of the published works referred to high-power LDs with Al-based compounds composing the optical cavity. With this technology, reliability remains an issue since a faster aging process of the device has been observed due to Al oxidation. From literature and up to now, only the FBH has demonstrated reliable high-power LDs with a grating layer. General background on semiconductor Laser heterostructures and description of optical resonators including a DFB, have been given. The different electro-optical parameters and in particular related to DFB laser resonators have been presented and discussed. High-power LDs with a ridge of 90 μm width have a typical spectral linewidth higher than 3nm but regarding the application, the spectral width must be lower than 1nm. Moreover, for a F-P LD, the detuning of the spectrum as a function of temperature is in the range of 0,5nm/°C. For these reasons, the integration of an optical grating into the resonator is necessary allowing to reach less than 0,1nm/°C. The different technological

parameters have been presented and the coupling factor as well as the reduction factor (depending on the geometry of the gratings) are critical parameters since directly related to the vertical single mode selectivity. The main electro-optical parameters have been also stated for a high-power LD. We demonstrated that the output optical power and WPE are related to internal quantum efficiency (at the first order) depending on physical effects that play a major role in performance drift. The maximum output power can be also limited by the temperature rise of the active region. Important parameters of LDs deal with the series resistance and a power-dependent limiting process resulting in the occurrence of well-known failure modes: Catastrophic Optical Damage (COD) or Catastrophic Optical Mirror Damage (COMD). So, different trade-offs need to be considered for the optimal design of high-power LDs ensuring to push back their COD limit and increase as far as possible their operating lifetime. Finally, a last section has addressed a brief overview of the LDs global market and in particular, a state-of-the-art performances review of high-power LDs emitting at 975nm is given over the last 20 years. From an exhaustive evaluation of literature, we have reported the different values of the main electro-optical parameters over the year only for LDs with 4mm cavity length and for comparison, the values obtained with the different III-V lab devices are also indicated ahead of time.

Chapter 2 aimed to describe the proposed LDs from a technological point of view and report on the results of electrical and optical characterizations enabling to determine their main intrinsic performances. Three vertical structures, developed in the cleanrooms of III-V lab (LOC, SLOC and AOC) have been studied. Taking benefit from its solid experience in the development of high-power LDs in the IR band, the considered devices are grown in one (for F-P LD) or two (for DFB LD) steps using a metal-organic vapor phase epitaxy (MOVPE) on 2" GaAs wafers. The overall structure of the LD is based on the edge double trench planar structure and an "Al-free" optical cavity with a 90 μ m wide strip. Each design has been described with a specific emphasize on the main differences in terms of materials, thickness and doping levels of each layer. Through dedicated optical simulations, some key parameters of the LDs have been determined: series resistance, optical losses, coupling factor, far field divergence and spectral width of DFB versus F-P architectures.

The effect of the cavity length is clearly shown on the series resistance that represents the main source of thermal dissipation at high levels of bias current. Considering this effect, the innovative AOC structure reveals one of its main advantage, demonstrating a very low series resistance (ex. $\sim 10\text{m}\Omega$ for a 4mm cavity length) but the highest value of internal losses ($\sim 0,6\text{ cm}^{-1}$) whatever the cavity length, in comparison with the two other structures (LOC and SLOC). For the AOC structure,

the vertical refractive index profile has been also calculated, predicting an excellent optical confinement factor ($> 2\%$).

Because of the performance requirements for the targeted application, a DFB structure has been processed (only for the LOC and SLOC structures) that remains a challenge for high-power LDs since only few research centers succeeded in this development. From optical simulations, the properties of the DFB vertical structure have been studied to predict the theoretical coupling factor and the spectral width as well as analyse the influence of the grooves depth on the optical confinement properties. Clearly, the second-order grating is the most affected by variations of the relative mark length compared to the first-order grating. However, a second-order grating was chosen because of the main difficulties to pattern a first-order grating using the e-beam technique that requires a very short pitch ($\Lambda \approx 100\text{nm}$). We used the second-order square shape grating with a relative mark length equal to 25% allowing to obtain: $\kappa L \approx 0,92$ or $\kappa L \approx 1,3$. A grating pitch equal to 290nm has been successfully implemented that is more compatible with e-beam resolution of III-V lab facilities.

The emission facet of the LD is subjected to huge local heating effect due to a recombination process at the GaAs-air interface and the reabsorption phenomenon of the emitted light. To prevent the LDs and enhance their robustness to COD, a Non-Injecting Mirror (NIM) window has been proposed and its effect on the far field divergence has been particularly analyzed since the near field does not change significantly. An optimized design of the NIM window has been proposed leading to a vertical position and an etching depth equal to 0,4 μm and 0,5 μm respectively.

A second section has given the complete description of the vertical structure fabrication process. The device mounting process is also detailed including the study of different die-attach materials, the nature of the submount acting as a thermomechanical compensator and then mounted on a C-mount heat sink. The mechanical mounting is a key step to optimize the heat flow across the whole device that depends on the overall thermal resistance and its thermal management allowing to reduce the junction temperature.

A last section was devoted to electrical and optical characterizations based on the measurement of the L-I-V curves in pulsed and CW regimes enabling to extract the external and internal parameters for each vertical structure and compared with simulation results. After the development of dedicated test benches, our characterizations have also addressed the extraction of WPE, far field and vertical divergence playing a significant role in the coupling efficiency during the beam collimation as well as the spectral properties. The experimental external parameters of the three structures have been compared with the literature showing state-of-the-art results. Calculation of internal parameters via pulsed L-I measurements allowed us to compare experimental and simulated values of optical

parameters as well as the series resistance. Finally, measurements of the optical spectrum for a DFB LD validate simulation results.

Because, thermal management investigation is of great importance to reach high levels of optical output power, **chapter 3** aimed to bring a comprehension of the heat propagation in our LD technology through different tools using both analytical calculations and FEM simulations. A first section has given a brief overview of the different heat sources in a high-power LD but calculations of these heat contributions lead inevitably to some approximations. Optical re-absorption and Joule effect are clearly the most important heat sources. A second section has described the implementation methodology of a relevant analytical model enabling to estimate these heat sources. For that, we proposed an analytical thermo-electrical model derived from three models already reported in literature (III-V lab, Simarjeet, Beringher), the data achieved by experimental measurements and theoretical L-I-V curves. This model can predict any L-I curve of a LD over a large range of bias current, from external and internal parameters as well as establishing a simple relationship between the structure design of the LDs and their optical performances. Using these L-I curves, it is possible to calculate the current density applied to the LD and then estimate the heat sources located within the optical cavity. For that, each heat contribution can be carefully taken into account from works of M. Kansar et al. and predictions of the overall dissipated power have been done. In order to analyse the heat flow propagation in the micro assembled LD through FEM simulations, these predicted heat sources are of major interest as input data of the model.

The development of high power LDs emitting at 975nm capable to reach high levels of optical power (10W) needs to accurately analyse optical power limitations and optimize its packaging. The packaging process requires to overcome both optical, mechanical and electrical issues. These last are often highly interactive and the stability of devices is an essential factor to ensure high performances and develop reliable applications. In such a context, time dependent FEM-based Multiphysics simulations are relevant tool. Indeed, despite the great interest of analytical models, some local effects can only be analyzed through 2D or 3D simulations in particular based on FEM.

The third section described and discussed the results achieved from stationary thermo-electrical simulations, in COMSOL© environment using a necessary Multiphysics approach, considering the transversal section (parallel to the front facet plane) and longitudinal section (parallel to the longitudinal axis of the LD) with specific boundary conditions. Because of the size heterogeneity of the structure, the 3D meshing procedure of the overall structure has represented a huge challenge and only 2D simulations have been addressed. Then, the effect of grooves etching depth defining the stripe width (90µm) and the length of Non-Injected Mirror (NIM) window were also discussed

in terms of current density and heat distribution both at the emissive front facet and along the longitudinal axis of the LD.

Optical simulations highlighted that the number of modes propagating in the waveguide depend of the etching grooves depth and an etching depth ideally close to the QW, allows obtaining the maximum number of guided modes. Nevertheless, thermo-electrical simulations have also reported that the temperature in the QW increases as the grooves depth increases and preferably, the etching depth must be closer to the p-side GaAs contact layer as far as possible. A compromise is necessary to consider between the number of guided modes and the etching depth of the grooves. Between the DFB and the F-P design (LOC vertical structure), it was demonstrated that only a minor augmentation of the temperature ($0,2^{\circ}\text{C}$ @ 5A) occurs, mainly due to the addition of two layers in the DFB structure (spacer and grating). Simulations considering the transversal section in combination with optical simulations allowed determining the optimal grooves etching depth that is established at $1,2\mu\text{m}$ and corresponds to the middle of the cladding layer. This value results from a compromise targeting the best optical confinement as well as the best thermal management. Then, it is possible to increase the thermal roll-over threshold and potentially, the lifetime of the LD for the targeted application field. A best fit was obtained when experimental and simulated junction temperatures in the QW are compared ($< 5\%$). Finally, the influence of the NIM window length was investigated and some optimized design rules have been specified.

Results reported in **chapter 4** have mainly focused on the extraction of thermal resistance of the micro assembled LDs (F-P and DFB architectures) and analysis of stress distribution considering different mechanical mounting configurations as well as its impact on the COD threshold. A first part dealt with a methodology enabling to extract the thermal resistance not only of the micro assembled device but also of each material forming the overall assembly using transient thermal testing. We demonstrated that thermal resistance can be efficiently evaluated using a dedicated technique namely T3STER[®] that is based on the direct monitoring of the temperature distribution into the whole micro assembled device through a pulsed bias current. Such an equipment gives a detailed overview of the heat flow spreading into the whole device including laser chip, solder, submount and heatsink. A specific effort to offer a metrology procedure has been carried out to deduce the optimized setup parameters for the determination of cumulative structure functions. With the help of theoretical calculations taking into account both 1D contribution and spreading effects of the thermal flow, experimental thermal resistances have been extracted on both F-P and DFB LDs with different cavity lengths. The thermal resistance of a 4mm DFB laser device is equal to $2,85\text{K/W}$ while the thermal resistance of the chip itself is around $1,4\text{K/W}$, agreeing with

state-of-the-art. In comparison, a 4mm F-P laser device demonstrates a slightly lower thermal resistance near of 2,5K/W. The interest to use diamond-copper composite (DCD) as novel thermo-compensator submount has been also investigated and compared with CuW.

A second part has studied surface mounting effects of a high-power LD by solder joint that represents a critical step since it has been already demonstrated that the soldering process induces residual mechanical stress and strain, in particular due to TCE mismatch between the different materials and their temperature-dependent thermomechanical behaviour. Two mechanical configurations (standard and new) used to mount the LD onto the C-mount heatsink have been considered and their efficiency was compared. The new one consists in a different placement of the chip. Stress distribution analysis as well as COD threshold determination have been achieved and discussed on LDs with different vertical structures (mainly SLOC and AOC) using four dedicated techniques (micro photoluminescence, photocurrent spectroscopy, time-resolved photoluminescence and high current pulsed measurements) in collaboration with the Max-Born-Institut in Berlin.

First, time-dependent 3D thermo-electro-mechanical simulations (FEM) have been performed to reproduce the standard mechanical mounting configuration of the LD onto the C-mount heatsink taking into account experimental data of temperature and pressure profile. Then, the stress distribution on the front facet as well as along the cavity length was analyzed. In order to reduce the mechanical stress between the front and the rear facet, a new mechanical placement of the LD has been proposed and used for its mounting with the same soldering conditions. This new location allows to better balance the thermal path as well as the thermomechanical stress distribution along its longitudinal axis compared with the standard one. It was concluded on the large asymmetry of the Von-Mises stress predicted by FEM simulations along the longitudinal axis of the LD. The highest stress is clearly located at the level of the front facet (up to 4MPa) while reaching 1,5MPa at the rear facet.

Secondly, measurements have been performed using the four previous techniques on a batch of fifteen LDs considering two vertical structures (SLOC and AOC), different facet coatings, nitrogen exposition times and the previous mechanical mounting configurations (standard and new). Based on these results, one can assume that the mechanical mounting of the LDs is certainly the main origin of premature COD occurrence. Of course, our conclusion must be weighted by a weak population of devices under test and it will be of interest to going-on with μ PL measurements on larger batches of LDs appearing as one of the best technique to characterize mechanical mounting efficiency.

Looking at short-term, future works will address the following points:

- Improve the AOC vertical structure electro-optical performances. Considering the decomposition of the WPE into three efficiency (related to the threshold current, the differential quantum efficiency and the bias of the LD) the AOC vertical structure reaches the max WPE for high level of current. The WPE_{max} for the AOC vertical structure is lower compared to the LOC and SLOC vertical structures, for the same cavity length. This because the AOC vertical structure reaches the maximum of the threshold current efficiency for high level of current, when the differential quantum efficiency has already decrease of 20%. In order to increase the WPE_{max} , the development of the AOC F-P vertical structure must address the decrease of the threshold current, in order to increase the efficiency related to the I_{th} and increase the WPE_{max} achievable.
- Develop a DFB LD based on AOC vertical structure which allows to obtain the best optical performance (in terms of optical power and spectral stability) and increase the COD threshold.
- Develop an optimized soldering process onto a DCD submount that, compared to the CuW one, has a bigger thermal conductivity and thus enables to improve the heat dissipation. Hence, it will be possible to reach both higher operating current ($\gg 14A$) and optical power ($> 10W$).
- Strengthen the strain measurements (in particular μPL) by increasing the number of LDs under investigation.
- Increase the cavity length of the LD in order to achieve higher output level (20W in CW) that will give an advantage over the other competitors.

APPENDIXES

Annex n°1

Starting from the rate equation as given in [3]:

$$\begin{aligned} \frac{dn}{dt} &= \frac{J}{ed} - G(n)S - \frac{n}{\tau_n} \\ \frac{dS}{dt} &= G(n)S - \frac{S}{\tau_{ph}} + \beta_{sp} \cdot \frac{n}{\tau_r} \end{aligned} \quad [Eq. 1]$$

where e is the elementary charge, d is the active layer thickness, $G(n)$ is the amplification rate due to stimulated emission, S is the photon density, τ_n and τ_{ph} are the carrier (electron and hole) lifetime, β_{sp} represents the spontaneous emission coupling factor and n is the carrier concentration.

In steady state, below and at threshold, it is considered that $S=0$ and hence from [Eq. 1], one can write:

$$0 = \frac{J}{ed} - \frac{n}{\tau_n} \rightarrow J_{th} = \frac{edn_{th}}{\tau_n} \quad [Eq. 2]$$

From this equation, one can evaluate the carrier concentration at the optical threshold. Below the optical threshold, the $\beta_{sp} \ll 1$ and so from [Eq. 1], one can write:

$$0 = G(n)S - \frac{S}{\tau_{ph}} \rightarrow G(n) = \Gamma_a g_0 (n - n_0) = \frac{1}{\tau_{ph}} \quad [Eq. 3]$$

where Γ_a is the optical confinement factor and g_0 is the differential gain coefficient.

From [Eq. 3]:

$$n = \frac{1}{\tau_{ph}\Gamma_a g_0} + n_0 \quad [Eq. 4]$$

The carrier concentration depends on cavity length, facet reflectivity and refractive index. The carrier concentration is clamped to the value obtained at the optical threshold.

Annex n°2

The photon flux density is given by:

$$\Phi_{ph} = \frac{I_{opt}}{\hbar\omega} \quad [Eq. 5]$$

where I_{opt} is the intensity of optical wave, \hbar is the Planck constant and ω the angular frequency.

I_{opt} is given by:

$$I_{opt} = \sqrt{\frac{\epsilon_{opt}\epsilon_0}{4\mu_0}} |\vec{E}_0|^2 \quad [Eq. 6]$$

with ϵ_{opt} represents the optical dielectric constant.

From [7], one can estimate the ϵ_{opt} , ϵ_0 is the vacuum permittivity ($8,85 \cdot 10^{-12}$ [F/m]), μ_0 vacuum permeability ($1,256 \cdot 10^{-6}$ [H/m]), and $|\vec{E}_0|^2$ is the amplitude of TE mode.

Annex n°3

Thermal resistivity

The thermal resistivity of each layer into the LD vertical structure is calculated on the basis of Sadao Adachi works [4] and [1], using two different equations regarding ternary (A-B-C) and quaternary alloys (A-B-C-D):

$$\begin{aligned} W(x) &= xW_{AC} + (1-x)W_{BC} + C_{A-B}x(1-x) \\ W(x) &= xyW_{AC} + x(1-y)W_{AD} + y(1-x)W_{BC} + (1-x)(1-y)W_{BD} \\ &\quad + C_{A-B}x(1-x) + C_{C-D}y(1-y) \end{aligned} \quad [Eq. 7]$$

Density, heat capacity at constant pressure, relative permittivity and electron/hole mobility depend on the mole fraction x and y , as reported by IOFFE and S. Adachi works [4] and [3]:

$$\begin{aligned} \rho &= C_1 - C_2 \cdot x; \quad \rho = C_3 - C_4 \cdot y + C_5 y^2 \\ C_p &= C_7 + C_8 \cdot x; \quad C_p = C_9 + C_{10} \cdot y - C_{11} y^2 \\ \epsilon_r &= C_{11} - C_{12} \cdot x \\ \mu_{e/h} &= C_{13} - C_{14} \cdot y + C_{15} y^2 \end{aligned} \quad [Eq. 8]$$

where each coefficient (from C_1 to C_{14}) is assumed to be constant.

The electron conductivity is calculated based on the following equation:

$$\sigma = e \cdot (N_e \cdot \mu_e + N_h \cdot \mu_h) \quad [\text{Eq. 9}]$$

Generally, all physical parameters are temperature dependent. In our study, we focused our simulations in a specific range of temperature (300K-400K) and we have assumed two different points:

- Variations of the physical properties in the temperature range are low enough to consider that the material properties are constant.
- Variations of the physical properties are strong in the temperature range and so, we must consider the temperature dependence of the material properties.

Heat capacity

The heat capacity at constant pressure (C_p) is given by:

$$C_p = \left(\frac{\Delta Q}{\Delta T} \right) \quad [\text{Eq. 10}]$$

where ΔQ and ΔT are the heat source and the corresponding change in temperature respectively. For III-V compounds, the temperature dependence can be expressed as follows [4]:

$$C_p = c_1 + c_2 T - c_3 T^{-2} \left[\frac{J}{g \cdot K} \right] \quad [\text{Eq. 11}]$$

where c_1, c_2 and c_3 represent constant values different for each semiconductor compound. *Figure 1* shows the dependence of the heat capacity C_p versus temperature for the GaAs based on calculations using [Eq. 11]. The LD junction temperature, even at high levels of bias current, will never reach 600K. Here, one can see that the heat capacity at constant pressure does not change dramatically (7%) in the range of 300-600K. Hence, a constant value for heat capacity of all materials has been introduced in our COMSOL Multiphysics® simulated model.

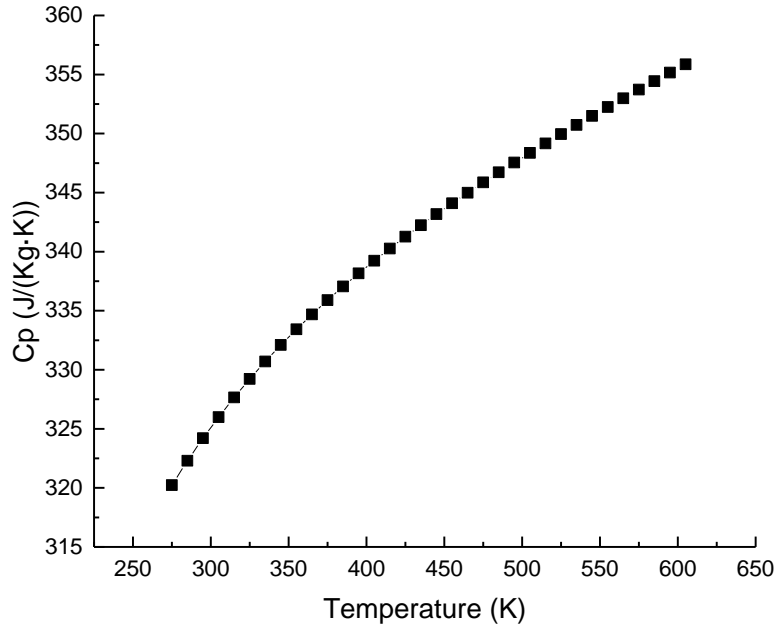


Figure 1: Predicted variations of the heat capacity versus temperature for GaAs (at constant pressure).

Thermal conductivity

The thermal conductivity results from interactions between phonons and from the scattering of phonons by crystalline imperfections. The theoretical calculation is highly approximated, due to the difficulty of an exact solution of phonons-phonons interactions. This is exacerbated in the case of alloy compounds, basically because of the random distribution of constituent atoms in sub-lattice sites [2]. Based on S. Adachi works, the thermal conductivity is given by:

$$K(T) = K_{300K} \cdot \left(\frac{T}{300K}\right)^\alpha \quad [\text{Eq. 12}]$$

where K_{300K} is the thermal conductivity at environment temperature and α is a linearly interpolated parameter because of the lack of experimental data.

The α parameter is different for each compound and an exhaustive literature has already addressed it [3]-[5]. In *Figure 2*, one can see the typical predicted variations of the thermal conductivity as a function of temperature calculated from [Eq. 12].

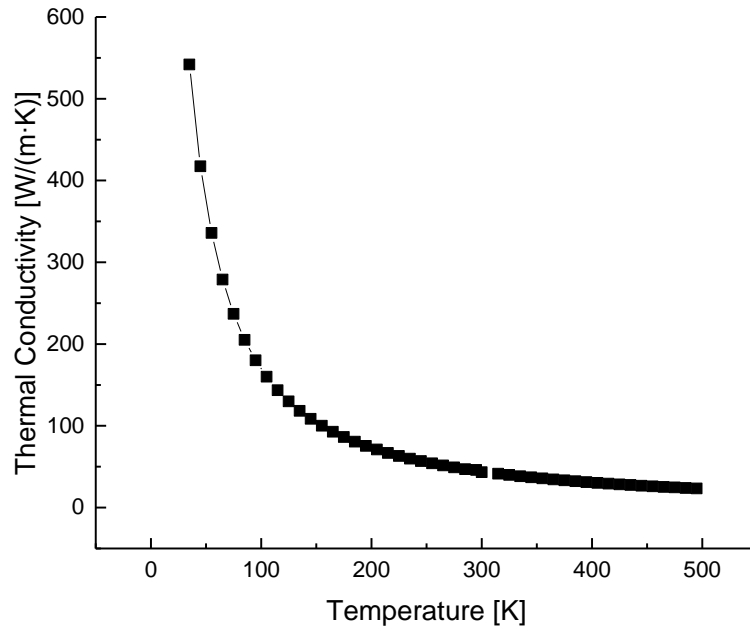


Figure 2: Predicted temperature dependence of thermal conductivity for GaAs.

In the case of the semiconductor alloy, only few experimental results are available and the value of K_{300K}^{AB} can be calculated using the harmonic average [3]:

$$K_{300K}^{AB} = \frac{1}{\left(\frac{1-x}{K_{300K}^A} + \frac{x}{K_{300K}^B} \frac{(1-x) \cdot x}{C_K} \right)} \quad [\text{Eq. 13}]$$

where C_K represents the bowing factor that considers the drastic reduction of the thermal conductivity with the increase of material composition x .

The α parameter is linearly interpolated as follows:

$$\alpha = (1-x) \cdot \alpha^A + x \cdot \alpha^B \quad [\text{Eq. 14}]$$

Table 1 summarizes the parameter values for the alloys used in each vertical structure of the LDs:

	$K_{300} [W/m \cdot K]$	α	$C_k [W/m \cdot K]$
AlGaAs	12,91	-1,28	3,3
GaInAsP	4,61	-1,41	3,0
GaInAs	12,17	-1,11	1,4

Table 1: Parameter values for the calculation of the thermal conductivity and the bowing factor.

Carriers mobility and electrical resistivity

From Ohm's law, it is possible to express the current density in a semi-conductor [8]:

$$j = q\mu_n nE = -qn v_{dr} \text{ or } j = q\mu_p pE = qp v_{dr} \quad [\text{Eq. 15}]$$

where E is the applied field and the v_{dr} represents the drift velocity of the free carriers.

The Ohm's law derives from the experimental observation that the current density depends linearly on the applied electric field. The electron, or hole, mobility is the proportional constant introduced in order to maintain the linear dependence.

$$v_{dr} = -\mu_n E \text{ or } v_{dr} = \mu_p E \quad [\text{Eq. 16}]$$

From [Eq. 15] and [Eq. 16] it is possible to define the carrier mobility. This last, is a proportional coefficient in the dependence of drift velocity on the applied field. The Ohm's law [Eq. 15], assumes a linear relationship between the v_{dr} and E, but this is valid only for small electric field, the mobility cannot be constant over a large range of electric field values.

Electrons into an electric field E are subjected to a force $F=-qE$ and this force accelerate them $F = m \cdot \frac{dv}{dt} \rightarrow -qE = m^* v_{dr} / \tau_c$.

$$v_{dr} = -\frac{q\tau_c}{m^*} E \quad [\text{Eq. 17}]$$

where The τ_c and m^* stand for the average scattering time and the effective mass. Combining [Eq. 16] with [Eq. 17], it is possible to write:

$$\mu_n = \frac{q\tau_c}{m^*} \quad [\text{Eq. 18}]$$

From [Eq. 18] it is evident that carrier mobility depends on the effective mass and the mean free time. This last is determined by the various scattering mechanisms [9]. The principal scattering mechanisms are lattice scattering and impurities. The lattice scattering is the ratio between the scattering length and the average thermal velocity of the carrier, v_{th} . The radius of the atom vibration increases with temperature and the probability of collisions increases. Consequently, the phonon mobility decreases with temperature.

Because the semiconductors are regularly doped, the introduced impurity (ionized particles) repel or attract electrons or hole in the vicinity, changing consequently the direction of their motion. This

is referred to the well-known Coulomb scattering effect and such a phenomenon is more pronounced at low temperature [6].

On the base of the Mathieson's rule it is possible to combine the scattering effects:

$$\frac{1}{\tau} = \frac{1}{\tau_{c-ph}} + \frac{1}{\tau_{c-c}} \rightarrow \frac{1}{\mu} = \frac{1}{\mu_{c-ph}} + \frac{1}{\mu_{c-c}} \quad [\text{Eq. 19}]$$

Mobility is a temperature dependent parameter and the dependence can be written as follows:

$$\mu_{c-ph} = A_{ph} T^{\alpha_{ph}} \quad \mu_{c-c} = A_c T^{\alpha_c} \quad [\text{Eq. 20}]$$

The values of $A_{ph}, A_c, \alpha_{ph}, \alpha_c$ depend on semiconductor compounds. The equivalent mobility is:

$$\frac{1}{\mu} = \frac{1}{\mu_{c-ph}} + \frac{1}{\mu_{c-c}} \rightarrow \mu = \frac{\mu_{c-ph} \cdot \mu_{c-c}}{\mu_{c-ph} + \mu_{c-c}} = \frac{A_{ph} A_c T^{\alpha_c} T^{\alpha_{ph}}}{A_c T^{\alpha_c} + A_{ph} T^{\alpha_{ph}}} \quad [\text{Eq. 21}]$$

Figure 3 shows the temperature dependence of the free carriers mobility for different semiconductor alloy compounds reported in [3].

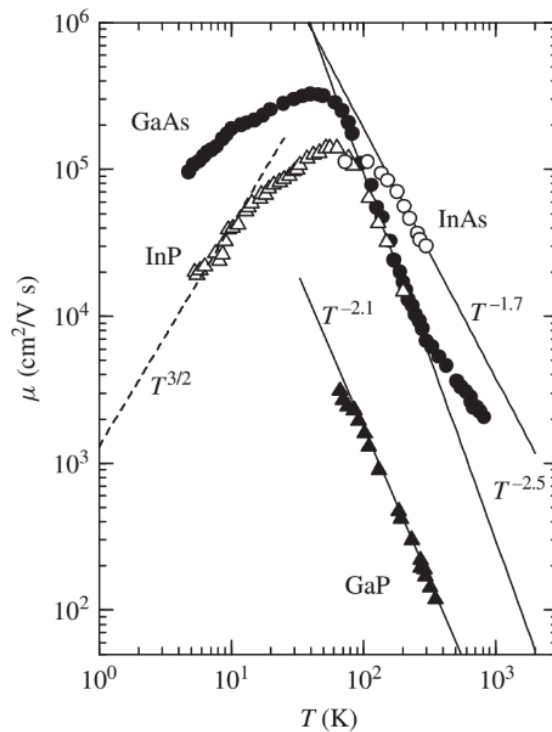


Figure 3: Variations of electron mobility versus temperature for relatively pure n-type III-V alloys [3].

From [Eq. 9], we can predict the temperature dependence of the electrical conductivity, reminding that the electrical resistivity is given by $\rho = 1/\sigma$.

Then, it is possible to calculate the temperature dependence for all the layers of each vertical structure and, as example; *Figure 4* plots the calculated temperature dependence for the N-doped GaAs material.

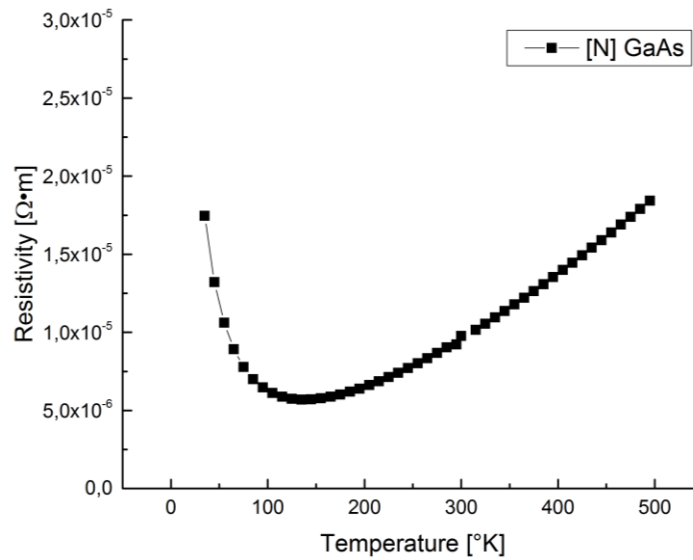


Figure 4: Predicted temperature dependence of the electrical resistivity for GaAs. The shape results from two contributions to the total carrier mobility.

The thermal dependence of each parameter, previously described, was estimated for each layer of the LD vertical structure and these values have been used for our FEM simulations.

REFERENCES

- [1] S. Adachi, "GaAs, AlAs, and Al_xGa_{1-x}As@B: Material parameters for use in research and device applications" in *Journal of Applied Physics*, pp. R1–R29, 1985.
- [2] S. Adachi, "*Properties of Aluminium Gallium Arsenide*" INSPEC, the Institution of Electrical Engineers, 1993.
- [3] S. Adachi, "*Properties of Group-IV, III–V and II–VI Semiconductors*," a John Wiley & Sons, Inc. Publication, 2005.
- [4] S. Adachi, "Properties of semiconductor alloy group IV, III-V, II-VI semiconductors," John Wiley and Sons Inc. Publication, 2009.
- [5] R. Brozel and G. E. Stillman, "*Properties of Gallium Arsenide*," 3rd edition. INSPEC, the Institution of Electrical Engineers, 1996.
- [6] S. Dimitrijević. "*Principles of semiconductor devices*" 2nd Edition. Oxford university press, 2012.
- [7] IOFFE Physico-Technical Institute, "Optical properties of Ga_xIn_{1-x}As" in <http://www.ioffe.ru/SVA/NSM/Semicond/GaInAs/optic.html>, 2000.
- [8] J. Piprek, "Non-radioactive recombination", in *Semiconductor Optoelectronic Devices Introduction to Physics and Simulation*. Academic press publication, pp. 69–71, 2003.
- [9] S.M. Sze and M. K. Lee, "*Semiconductor devices*" 3rd Edition John Wiley & Sons, Inc., 2010.

PUBLICATIONS

INTERNATIONAL CONFERENCES

(2017) R. Mostallino, M. Garcia, Y. Deshayes, A. Larrue, Y. Robert, E. Vinet, M. Krakowski, M. Lecomte, O. Parillaud, L. Bechou. Thermal Management Characterization of Microassembled High Power Distributed-Feedback Broad Area Lasers Emitting at 975nm. San Diego, United States. **ECTC Electronic Components and Technology Conference**, pages 563-574.

(2016) R. Mostallino, M. Garcia, Y. Deshayes, A. Larrue, Y. Robert, E. Vinet, M. Krakowski, M. Lecomte, O. Parillaud, L. Bechou. Thermal management of high power DFB broad area lasers at 975nm with 55% efficiency. Warsaw, Poland. ISROS 2016, **International Symposium on Reliability of Optoelectronics for Systems**.

(2016) R. Mostallino, M. Garcia, Y. Deshayes, A. Larrue, Y. Robert, E. Vinet, L. Bechou, M. Lecomte, O. Parillaud, M. Krakowski. Thermal investigation on high power DFB broad area lasers at 975nm, with 60% efficiency. San Francisco, United States. **SPIE, High-power diode laser technology and application XIV**, Volume 9733.

NATIONAL CONFERENCES

(2015) R. Mostallino, M. Garcia, Y. Deshayes, A. Larrue, Y. Robert, E. Vinet, L. Bechou, M. Lecomte, O. Parillaud, M. Krakowski. Développement et caractérisation de diode laser de pompe DFB, de puissance et rendement à la prise élevés à 975nm. Rennes, France. **JNOG, Journées National d'Optique Guidée**.

JOURNAL

(2016) R. Mostallino, M. Garcia, Y. Deshayes, A. Larrue, Y. Robert, E. Vinet, M. Krakowski, M. Lecomte, O. Parillaud, L. Bechou. Achieving a 60% efficient laser diode design with optimized thermal management. **Engineering Edge of Mentor Graphics**, Volume 05 Issue 02, pages 66-69.

Résumé substantiel en français

Cette thèse « CIFRE », codirigée par le laboratoire IMS de l'Université de Bordeaux et le GIE III-V Lab, s'inscrit dans le cadre du projet LAFIP-SOMUST (Laser à Fibre Pulsé à base de Sources semi-conductrices Multimodes Stabilisées en longueur d'onde), financé par la DGA. Ce projet ambitionnait de développer un laser à fibre pulsée Er/Yb à 1,55 μm en collaboration active avec THALES Research and Technology (TRT), pour le développement de la source de pompage et la société LUMIBIRD (ex KEOPSYS-QUANTEL), en charge de l'intégration de la source de pompage dans le laser à fibre final.

Dans ce contexte, le travail de thèse s'est attaché à développer des diodes laser de pompe :

- avec une émission stabilisée en longueur d'onde à 975nm (SMSR > 40 dB) et une faible largeur spectrale (< 1nm) en utilisant une architecture à contre-réaction répartie (DFB),
- fonctionnant en régime continu,
- développant une puissance optique de sortie supérieure à 10W avec un rendement à la prise élevé (Wall-Plug Efficiency-WPE > 60%).

À l'heure actuelle, il n'existe pas de filière industrielle établie pour les diodes laser de pompe de forte puissance et émettant à 975nm. Ce projet a souhaité répondre à cette exigence en apportant une certaine indépendance par rapport aux acteurs internationaux du domaine et en visant à développer un nouveau type de laser à fibre Er/Yb impulsionnel à 1,55 μm . Ce dernier doit être pompé par une diode de puissance à fort rendement à la prise (> 60%), émettant à 975nm avec une largeur spectrale réduite (\sim 1nm) et stabilisée thermiquement en longueur d'onde (dérive inférieure à 0,1nm. $^{\circ}\text{C}^{-1}$), en s'appuyant sur une technologie « Al-free » pour la zone active, fruit de l'expertise du III-V Lab. Plusieurs applications sont visées : la télémétrie, le guidage de drones, la détection d'obstacles, le développement de systèmes de contre-mesures optroniques.... Ce type de diode laser est à ce jour le plus utilisé, notamment de par son rendement élevé de conversion.

Avec un objectif d'intégration de la fiabilité au plus tôt de la conception (« Design for Reliability »), cette thèse a abordé la fabrication et la caractérisation électro-optique fine de lasers à cavité Fabry-Pérot (F-P) et à contre-réaction répartie (DFB), basés sur plusieurs structures verticales : LOC (« Large Optical Cavity »), SLOC (« Super Large Optical Cavity ») et AOC (« Asymmetric Optical Cavity »).

Quatre principaux chapitres composent ce manuscrit :

Le **chapitre 1** introduit le contexte général, la motivation et les objectifs de l'étude. Premièrement, les technologies de diodes laser infrarouge sont présentées avec une focalisation sur les différentes structures verticales décrites par les principaux leaders de la recherche et de l'industrie

dans le domaine. L'objectif est de mettre en lumière les avantages apportés par la technologie III-V Lab par rapport aux autres compétiteurs ; la plupart des travaux publiés dans la littérature, se référant à des structures verticales avec des composés à base d'Aluminium dans la cavité optique. Avec cette technologie, la fiabilité reste un point névralgique car un processus de vieillissement plus rapide du dispositif a été observé en raison de l'oxydation de l'aluminium. Jusqu'à présent, seul l'Institut Ferdinand-Braun (FBH) a démontré des diodes laser robustes sous forte puissance et stabilisées en longueur d'onde (DFB).

Dans un second temps, ce chapitre rappelle les principes physiques qui décrivent le fonctionnement des hétérostructures à base de semi-conducteurs avec une attention particulière sur la sélection de longueurs d'onde grâce à un réseau de type DFB. Les performances en termes de puissance optique de sortie et de WPE sont liées, au premier ordre, au rendement quantique interne. Par conséquent, différents compromis doivent être considérés pour optimiser la conception de diodes laser à haute puissance.

Une dernière partie propose un bref aperçu du marché mondial des diodes laser et en particulier une analyse des meilleures performances des diodes laser haute puissance émettant à 975 nm, obtenues au cours des 20 dernières années. Enfin, à partir d'une évaluation bibliographique exhaustive, les différentes valeurs des principaux paramètres électro-optiques très récemment mis en lumière, ont été recensés uniquement pour les diodes laser de longueur de cavité égale à 4mm.

Le **chapitre II** s'est attaché à décrire, d'un point de vue technologique, chaque structure verticale proposée pour répondre au besoin de lasers de pompe à 975nm : LOC et SLOC en F-P et DFB, et AOC uniquement en F-P. Les résultats des caractérisations électriques et optiques permettant de déterminer leurs principales performances intrinsèques, sont ensuite présentés. Les trois structures sont étudiées et une comparaison a été effectuée concernant les paramètres électro-optiques, le champ lointain et le confinement optique. La diode laser est basée sur une structure plane à double tranchée et développée en une étape (FP) ou en deux étapes (DFB) en utilisant une technique de croissance cristalline par épitaxie en phase vapeur aux organométalliques (MOVPE) sur des plaques 2" en GaAs. Les étapes de lithographie, en particulier la fabrication de réseaux de Bragg par la technique de faisceau d'électrons (e-beam), et le traitement aux facettes, pour prévenir une défaillance de type Catastrophic Optical Damage (COD), sont détaillées. Chaque structure verticale est décrite en tenant compte des principales différences en termes de matériaux, d'épaisseurs et de niveaux de dopage de chaque couche. Les simulations optiques dédiées ont permis de déterminer certains paramètres clés des diodes laser (résistance en série, pertes optiques, facteur de couplage, divergence en champ lointain et largeur spectrale) pour les architectures DFB en les comparant aux architectures F-P.

En raison des exigences de performance pour l'application ciblée, la structure DFB a été considérée en priorité (uniquement pour les structures LOC et SLOC), ce qui reste un défi pour les diodes laser de forte puissance car seuls quelques centres de recherche ont réussi ce développement. À partir de simulations optiques, les propriétés de la structure verticale du DFB ont été étudiées pour prévoir le facteur de couplage théorique ($\kappa.L \approx 0,92$ et $\kappa.L \approx 1,3$) et la largeur spectrale, mais également pour analyser l'influence de la profondeur des gravures sur les propriétés du confinement optique. Un réseau à profil carré de second ordre ($\approx 290\text{nm}$) a été choisi en raison des principales difficultés rencontrées pour structurer un réseau de premier ordre nécessitant un pas beaucoup plus court ($\approx 100\text{nm}$).

La facette d'émission de la diode laser est soumise à un fort échauffement local en raison d'un processus de recombinaisons à l'interface GaAs-air et du phénomène de réabsorption de la lumière émise. Pour améliorer la robustesse de la diode laser au COD, une fenêtre non pompée « Non-Injecting Mirror » (NIM) a été proposée et son influence sur la divergence du champ lointain a été particulièrement analysée, car le champ proche ne change pas de manière significative.

La brasure est un des principaux points critiques pour ce type de diode laser, compte tenu de la gestion de l'écoulement thermique (de par la valeur de la résistance thermique) et de la différence des coefficients d'expansion thermique (CTE) des matériaux, à l'origine de contraintes thermomécaniques susceptibles de provoquer un stress résiduel. Une bonne qualité de brasage permet de diminuer la température de jonction du laser, ainsi que la contrainte résiduelle induite par le procédé utilisé.

Une dernière partie est consacrée aux caractérisations électriques et optiques basées sur la mesure des courbes L-I-V en régime pulsé et CW, permettant d'extraire les paramètres externes et internes de chaque structure verticale et de les comparer aux résultats de simulation. Après le développement de bancs dédiés de mesure, les caractérisations ont également permis l'extraction du WPE. La divergence en champ lointain joue aussi un rôle significatif dans l'efficacité du couplage lors de la collimation du faisceau ainsi que dans les propriétés spectrales. Les paramètres externes expérimentaux des trois structures ont été comparés aux valeurs reportées dans la bibliographie. Le calcul des paramètres internes via les mesures L-I pulsées nous a permis de comparer les valeurs expérimentales et simulées des principaux paramètres optiques ainsi que de la résistance série. Enfin, les mesures expérimentales du spectre optique pour les diodes laser DFB ont également permis de valider les résultats de simulation.

Le **chapitre III** vise à comprendre la propagation de la chaleur au sein de la diode laser microassemblée, au moyen de différents outils combinant des calculs analytiques et des simulations par éléments finis (FEM). Une première partie a recensé les différentes sources de chaleur dans une diode laser de haute puissance à 975nm. La réabsorption optique et l'effet Joule sont clairement les contributions les plus importantes. Une deuxième partie décrit la méthodologie de mise en œuvre d'un modèle analytique permettant d'estimer ces sources de chaleur. Pour cela, un modèle thermoélectrique analytique, dérivé de trois modèles déjà rapportés dans la littérature (III-V Lab, Simarjeet, Beringher), a été proposé. Il permet de prédire la caractéristique L-I d'une diode laser sur une large plage de courant de polarisation, à partir des paramètres internes et externes, ainsi qu'en établissant une relation simple entre la structure des diodes laser et leurs performances optiques.

Le développement de la diode laser à haute puissance capable d'atteindre des niveaux élevés de puissance optique (10W) nécessite d'évaluer avec précision leurs limitations et d'optimiser la phase de brasage. Malgré le grand intérêt de tels modèles analytiques, certains effets locaux ne peuvent être compris que par des simulations FEM. Ce chapitre décrit et analyse les résultats issus des simulations thermoélectriques stationnaires en 2D, implémentées en environnement COMSOL© et utilisant une approche multiphysique indispensable, pour prédire la distribution du flux thermique dans les diodes laser F-P et DFB en fonction du courant de polarisation.

Les simulations optiques ont montré que le nombre de modes qui se propagent dans le guide d'ondes dépend de la profondeur de gravure des tranchées, définissant le ruban central d'émission. Il ressort qu'une profondeur de gravure proche du puits quantique permet d'obtenir le nombre maximal de modes guidés. Néanmoins, des simulations thermoélectriques ont également montré que la température dans le puits quantique augmente en fonction de la profondeur de gravure. Il est conclu que, dans la mesure du possible, la profondeur de gravure doit être proche de la couche de contact GaAs du côté p ; un compromis étant nécessaire entre le nombre de modes guidés et la profondeur de gravure.

Le **chapitre IV** décrit une méthodologie permettant d'extraire la résistance thermique de la diode laser microassemblée, mais également de chaque matériau à l'aide d'essais thermiques transitoires. Un paramètre important pour quantifier la gestion thermique des dispositifs fabriqués fonctionnant en régime d'onde CW réside dans la détermination de la résistance thermique du dispositif microassemblé. Une valeur faible de ce paramètre permet de réduire la température de jonction par un chemin de dissipation thermique optimisé, garantissant un fonctionnement optimal à long terme, en particulier lorsqu'une puissance optique de sortie élevée est envisagée (> 10W).

Les diodes laser à haute puissance (à cavité longue) rendent difficile l'utilisation de l'analyseur de spectre optique en raison de la nature multimodale intrinsèque de la diode laser et de la résolution attendue. Cela peut entraîner une mesure erronée de la résistance thermique (donc de la température de jonction) et par conséquent de la durée de vie du dispositif microassemblé dans des conditions de fonctionnement long-terme. À partir d'essais thermiques transitoires, une procédure optimisée pour l'extraction de la résistance thermique est proposée. Cette dernière, peut-être efficacement évaluée à l'aide d'une technique et d'un équipement dédiés (T3STER©), qui repose sur la mesure directe de la répartition de la température dans l'ensemble du dispositif microassemblé par le biais d'un courant de polarisation pulsé. Un tel équipement donne un aperçu détaillé du flux de chaleur qui diffuse dans l'ensemble du dispositif, y compris la puce laser, la brasure, le support et le dissipateur thermique. Une procédure de métrologie a été mise en place afin d'en déduire les paramètres de configuration optimisés pour la détermination des fonctions de structure cumulatives $C_{th} = f(R_{th})$.

Une seconde partie a étudié les effets de la brasure des diodes laser à haute puissance, qui représente une étape critique dans la mesure où il a déjà été démontré que le processus de brasage induit des contraintes thermomécaniques résiduelles, dues en particulier au déséquilibre de CTE entre les différents matériaux (diode laser, brasure, embase...etc). Des simulations FEM thermo-électromécaniques ont été effectuées pour analyser la répartition des contraintes sur la facette avant (section transversale) ainsi que le long de la cavité (section longitudinale). Une analyse de la répartition de ces contraintes et la détermination du seuil de dommage optique catastrophique (COD) ont été effectuées et discutées sur des diodes laser en particulier pour deux structures verticales différentes (SLOC et AOC) en utilisant quatre techniques dédiées : microphotoluminescence, spectroscopie de photocourant, photoluminescence résolue dans le temps et mesures pulsées sous incrément de courant en collaboration avec le Max Born Institut (Berlin).

Sur la base de ces résultats, on peut supposer que le montage mécanique des diodes laser est certainement la principale cause d'apparition prématurée d'un COD. Bien entendu, ce résultat doit être pondéré par la faible population de dispositifs testés. En perspective, il sera intéressant de poursuivre les mesures en microphotoluminescence à partir d'un plus grand nombre d'échantillons ; cette dernière étant clairement l'une des meilleures techniques pour caractériser l'efficacité du montage mécanique.